Framatome Inc. Non-Proprietary
Westinghouse Non-Proprietary Class 3

WCAP-17788-NP
Volume 6, Revision 1

December 2019

Comprehensive Analysis and Test Program for GSI-191 Closure (PA-SEE-1090) – Subscale Head Loss Test Program Report

Westinghouse

framatome

WCAP-17788-NP
Volume 6, Revision 1

Comprehensive Analysis and Test Program for GSI-191 Closure (PA-SEE-1090) – Subscale Head Loss Test Program Report

Matt M.Swartz	Westinghouse
James P. Spring	Westinghouse

December 2019

Prepared by: Danial Utley*
LOCA Integrated Services II

Reviewer: Kevin F. McNamee*
Operating Plant Fluid Systems and Procedures

Approved: Timothy D. Croyle*, Manager
Operating Plant Fluid Systems and Procedures

Approved: Jay D. Boardman*, Program Director
PWR Owner's Group PMO

This work was performed under PWR Owners Group Project Authorization PA-SEE-1090.

*Electronically approved records are authenticated in the electronic document management system.

Westinghouse Electric Company LLC
1000 Westinghouse Drive
Cranberry Township, PA 16066, USA

Framatome Inc.
3315 Old Forest Road
Lynchburg, VA 24501

ACKNOWLEDGEMENTS

This report was developed and funded by the PWR Owners Group under the leadership of the participating utility representatives of the Systems & Equipment Engineering Committee. The authors thank the PWR Owners Group GSI-191 Technical Integration Group Engaged in Research (TIGER) Team for their support and contributions to this program; Mr. Jeffrey Brown, the late Mr. Phillip Grissom, Mr. Dana Knee, Mr. Ernie Kee, Mr. Kenneth Greenwood, Mr. Timothy Croyle, and associate members; Mr. Kurt Flaig and Mr. Paul Leonard. The authors also gratefully acknowledge and recognize Mr. Jay Boardman, PWR Owners Group Program Manager, and Mr. Paul Stevenson, Ms. Danielle Page Blair, Mr. John Maruschak and Mr. David C. Kovacic, Project Managers, for their guidance and encouragement throughout the process of developing this report. The authors also gratefully acknowledge all the members of the Churchill staff for their efforts in making this test program a success. The authors also acknowledge and recognize the Framatome technical team who supported this effort; Mr. Adam Spontarelli and Mr. Gordon Wissinger.

LEGAL NOTICE

This report was prepared as an account of work performed by both Framatome Inc. and Westinghouse Electric Company LLC. Neither Framatome Inc., nor Westinghouse Electric Company LLC, nor any person acting on its behalf:

1. Makes any warranty or representation, express or implied including the warranties of fitness for a particular purpose or merchantability, with respect to the accuracy, completeness, or usefulness of the information contained in this report, or that the use of any information, apparatus, method, or process disclosed in this report may not infringe privately owned rights; or

2. Assumes any liabilities with respect to the use of, or for damages resulting from the use of, any information, apparatus, method, or process disclosed in this report.

COPYRIGHT NOTICE

DISTRIBUTION NOTICE

This report was prepared for the PWR Owners Group. This Distribution Notice is intended to establish guidance for access to this information. This report (including proprietary and non-proprietary versions) is not to be provided to any individual or organization outside of the PWR Owners Group program participants without prior written approval of the PWR Owners Group Program Management Office. However, prior written approval is not required for program participants to provide copies of Class 3 Non-Proprietary reports to third parties that are supporting implementation at their plant, and for submittals to the NRC.

PWR Owners Group
United States Member Participation* for WCAP-17788

Utility Member	Plant Site(s)	Participant	
		Yes	No
Ameren Missouri	Callaway (W)	X	
American Electric Power	D.C. Cook 1 & 2 (W)	X	
Arizona Public Service	Palo Verde Unit 1, 2, & 3 (CE)	X	
Dominion Energy	Millstone 2 (CE)	X	
	Millstone 3 (W)	X	
	North Anna 1 & 2 (W)	X	
	Surry 1 & 2 (W)	X	
	V.C. Summer (W)	X	
Duke Energy Carolinas	Catawba 1 & 2 (W)	X	
	McGuire 1 & 2 (W)	X	
	Oconee 1, 2, & 3 (B&W)	X	
Duke Energy Progress	Robinson 2 (W)	X	
	Shearon Harris (W)	X	
Entergy Palisades	Palisades (CE)	X	
Entergy Nuclear Northeast	Indian Point 2 & 3 (W)	X	
Entergy Operations South	Arkansas 1 (B&W)	X	
	Arkansas 2 (CE)	X	
	Waterford 3 (CE)	X	
Exelon Generation Co. LLC	Braidwood 1 & 2 (W)	X	
	Byron 1 & 2 (W)	X	
	Calvert Cliffs 1 & 2 (CE)	X	
	Ginna (W)	X	
FirstEnergy Nuclear Operating Co.	Beaver Valley 1 & 2 (W)	X	
	Davis-Besse (B&W)	X	
Florida Power & Light \ NextEra	St. Lucie 1 & 2 (CE)	X	
	Turkey Point 3 & 4 (W)	X	
	Seabrook (W)	X	
	Pt. Beach 1 & 2 (W)	X	

PWR Owners Group
United States Member Participation* for WCAP-17788

Utility Member	Plant Site(s)	Participant	
		Yes	No
Luminant Power	Comanche Peak 1 & 2 (W)	X	
Pacific Gas & Electric	Diablo Canyon 1 & 2 (W)	X	
PSEG – Nuclear	Salem 1 & 2 (W)	X	
So. Texas Project Nuclear Operating Co.	South Texas Project 1 & 2 (W)	X	
Southern Nuclear Operating Co.	Farley 1 & 2 (W)	X	
	Vogtle 1 & 2 (W)	X	
Tennessee Valley Authority	Sequoyah 1 & 2 (W)	X	
	Watts Bar 1 & 2 (W)	X	
Wolf Creek Nuclear Operating Co.	Wolf Creek (W)	X	
Xcel Energy	Prairie Island 1 & 2 (W)	X	

*** Project participants as of the date the final deliverable was completed. On occasion, additional members will join a project. Please contact the PWR Owners Group Program Management Office to verify participation before sending this document to participants not listed above.**

PWR Owners Group
International Member Participation* for WCAP-17788

Utility Member	Plant Site(s)	Participant	
		Yes	No
Asociación Nuclear Ascó-Vandellòs	Asco 1 & 2 (W)	X	
	Vandellos 2 (W)	X	
Centrales Nucleares Almaraz-Trillo	Almaraz 1 & 2 (W)	X	
EDF Energy	Sizewell B (W)	X	
Electrabel	Doel 1, 2 & 4 (W)	X	
	Tihange 1 & 3 (W)	X	
Electricite de France	58 Units	X	
Elektriciteits Produktiemaatschappij Zuid-Nederland	Borssele 1 (Siemens)	X	
Eletronuclear-Eletrobras	Angra 1 (W)	X	
Emirates Nuclear Energy Corporation	Barakah 1 & 2	X	
Hokkaido	Tomari 1, 2 & 3 (MHI)	X	
Japan Atomic Power Company	Tsuruga 2 (MHI)	X	
Kansai Electric Co., LTD	Mihama 3 (W)	X	
	Ohi 1, 2, 3 & 4 (W & MHI)	X	
	Takahama 1, 2, 3 & 4 (W & MHI)	X	
Korea Hydro & Nuclear Power Corp.	Kori 1, 2, 3 & 4 (W)	X	
	Hanbit 1 & 2 (W)	X	
	Hanbit 3, 4, 5 & 6 (CE)	X	
	Hanul 3, 4 , 5 & 6 (CE)	X	
Kyushu	Genkai 2, 3 & 4 (MHI)	X	
	Sendai 1 & 2 (MHI)	X	
Nuklearna Electrarna KRSKO	Krsko (W)	X	
Ringhals AB	Ringhals 2, 3 & 4 (W)	X	
Shikoku	Ikata 2 & 3 (MHI)	X	
Taiwan Power Co.	Maanshan 1 & 2 (W)	X	

*** Project participants as of the date the final deliverable was completed. On occasion, additional members will join a project. Please contact the PWR Owners Group Program Management Office to verify participation before sending this document to participants not listed above.**

USE OF TECHNICAL REPORT WCAP-17788
BY
MEMBERS OF THE PRESSURIZED WATER REACTOR OWNERS GROUP

WCAP-17788 is comprised of six volumes. All six volumes of Revision 0 of the technical report were submitted to the U.S. Nuclear Regulatory Commission (US NRC) with the objective of obtaining a Safety Evaluation (SE) on the complete report (all six volumes). The US NRC initiated a review of the technical report and issued a number of Requests for Additional Information (RAIs). A number of RAI questions were also asked for this technical report. Responses to those RAIs were prepared and submitted. In the middle of 2019, the US NRC informed the PWROG that an SE would not be issued on WCAP-17788. Rather, the US NRC would accept licensees referring to WCAP-17788 in their response submittals to Generic Letter (GL) 2004-02 (ADAMS Accession Number ML042360586), accompanied by a statement demonstrating the applicability of the referenced portion of WCAP-17788 to their specific PWR unit.

Additionally, the US NRC has used information contained in WCAP-17788, along with other information, to prepare a Technical Evaluation Report (TER) that concludes in-vessel debris effects are of low safety significance. The US NRC has used the TER to support closure of GSI-191 (ADAMS Accession Number ML19203A303). In lieu of an SE, the TER was published in Volume 1 of WCAP-17788, Revision 1.

To support use of WCAP-17788 by PWROG members, Revision 1 of this technical report was prepared and includes the TER, all RAIs and their responses, as well as modifications to the text of the report committed to in the RAI responses. As noted previously, WCAP-17788 has not received an US NRC SE. However, all six volumes of WCAP-17788 have been amended to Revision 1 and are made available to participating PWROG members for their use in responding to GL 2004-02 for the PWR units they operate.

All RAIs and their responses are included in an appendix to the applicable volumes. It is noted that Volume 2 was not reviewed in detail by the US NRC, and as a result, an RAI was not provided for this volume of the technical report. It is also noted that sections of technical report PWROG-15091 Revision 0, "Subscale Brine Test Program Report" were reviewed as supporting information to WCAP-17788. RAIs and their responses related to PWROG-15091 are included in the applicable Volume 1 appendix. Revision 1 of PWROG-15091 was also prepared and includes a modification committed to in the RAI response.

This report may reference AREVA. Since revision 0 of this report was generated, AREVA has changed their name to Framatome Inc.

1. PWROG-15091-NP, Revision 1, "Subscale Brine Test Program Report," November 2019. (Non-Proprietary)
2. NRC Generic Letter 2004-02, "Potential Impact of Debris Blockage on Emergency Recirculation during Design Basis Accidents at Pressurized-Water Reactors," ADAMS Accession Number ML042360586, September 13, 2004.
3. NRC Memorandum from R. V. Furstenau to H. K. Nieh, "Closure of Generic Issue GI-191, 'Assessment of Debris Accumulation on PWR Sump Performance,'" ADAMS Accession Number ML19203A303, July 23, 2019

TABLE OF CONTENTS

LIST OF TABLES

LIST OF FIGURES

LIST OF ACRONYMS AND ABBREVIATIONS

ACRS	Advisory Committee on Reactor Safeguards
AFP	Alternate Flow Path
BB	Barrel/Baffle
BN	Bottom Nozzle
CFR	Code of Federal Regulations
CSS	Containment Spray System
DI	De-Ionized
DIS	Debris Injection System
ECCS	Emergency Core Cooling System
FA	Fuel Assembly
FEP	Fluorinated Ethylene Propylene
GSI	Generic Safety Issue
GL	Generic Letter
H_3BO_3	Boric Acid
HCT	High Concentration Tank
HLB	Hot Leg Break
HMP	AREVA High Mechanical Performance Fuel Assembly Grid
ID	Inner Diameter
L/D	Length-to-Diameter Ratio
LCT	Low Concentration Tank
LOCA	Loss-of-Coolant Accident
LTCC	Long-Term Core Cooling
NaOH	Sodium Hydroxide
NaTB	Sodium Tetraborate
NEI	Nuclear Energy Institute
NRC	Nuclear Regulatory Commission
OFA	Westinghouse Optimized Fuel Assembly
p:f	Particle-to-Fiber
P-Grid	Westinghouse Protective Grid
PCI	Performance Contracting Inc.
PWR	Pressurized Water Reactor(s)
PWROG	Pressurized Water Reactor Owners Group
RCS	Reactor Coolant System
RFA	Robust Fuel Assembly
RHS	Right Hand Side
RV	Reactor Vessel(s)
SEM	Scanning Electron Microscope

LIST OF ACRONYMS AND ABBREVIATIONS

TH	Thermal-Hydraulic(s)
TSP	Trisodium Phosphate
UFA	Westinghouse Upgraded Fuel Assembly
UHSN	Upper Head Spray Nozzle(s)
U.S.	United States
WCAP	Westinghouse Technical Report Number Preface (formerly Westinghouse Commercial Atomic Power)

1 EXECUTIVE SUMMARY

The Pressurized Water Reactor Owners Group (PWROG) has undertaken a comprehensive test and analysis program as part of the resolution to Generic Safety Issue (GSI) 191 to increase the fibrous debris limits per fuel assembly (FA). An important part of this effort is associated with determining the pressure drop due to collection of fibrous and particulate debris at the core inlet following a postulated large hot leg break (HLB) loss-of-coolant accident (LOCA).

In order to assess the pressure drop due to a debris bed at the core inlet, fiber and particulate head loss testing was performed. The range of conditions examined specifically focused on HLB scenarios for the United States (U.S.) pressurized water reactor (PWR) operating fleet with traditional forced emergency core cooling system (ECCS) injection from the cold leg side of the reactor vessel. Furthermore, the testing effort did not consider the effects of chemical debris resulting from dissolution and corrosion of sump materials. Volume 5 provides the testing basis for the expected arrival timing of chemical debris. Results of this report are not applicable following the arrival of significant chemical debris.

Given the range of possible debris loads and core inlet geometry combinations, the test program included extensive parametric studies that encompassed a wide range of thermal-hydraulic (TH) and geometric conditions. The flow boundary conditions for this study were defined based on trends observed in the TH analyses presented in Volume 4. Other parameters investigated included fuel geometry, debris size, debris mass, debris concentration and water chemistry. In addition to investigating blockage of various FA inlet components, the experimental effort also investigated the potential for blockage of alternate flow paths (AFPs) that consist of flow holes located in the core bypass channels of a PWR reactor vessel. These AFP flow holes are credited as part of this program to provide adequate core cooling, should the core inlet become blocked with debris.

Section 2 of this report provides relevant background for completing the head loss testing and includes results of the literature review used to develop the test program. Section 3 provides a description of the experimental facility. Section 4 documents the test matrix. Section 5 provides analysis and discussion of the test results. Section 6 documents the basis for selection of test geometric scale and includes scaled test results that can be used to develop fibrous debris limits. Section 7 provides conclusions and summarizes the information that will be used in subsequent work.

Results from the parametric studies performed as part of this program were used as the basis to define limiting conditions for the collection of debris on inlet fuel components. A series of core inlet geometry experiments were performed at the limiting conditions. Results from the core inlet testing will be used as input to the overall methodology described in detail in Volume 1 that allows PWR licensees to calculate a plant-specific in-vessel fibrous debris limit.

2 INTRODUCTION

2.1 BACKGROUND

The Nuclear Regulatory Commission (NRC) issued generic letter (GL) 2004-02 (Reference 2-1) requesting that licensees of PWRs perform evaluations of the ECCS and containment spray system (CSS) based on the identified potential susceptibility of PWR recirculation sump screens to debris blockage during design basis accidents requiring recirculation operation of ECCS or CSS and on the potential for additional adverse effects due to debris blockage of flow paths necessary for ECCS and CSS recirculation. In addition, Reference 2-1 states, "Debris blockage at flow restrictions within the ECCS recirculation flow path downstream of the sump screen is a potential concern for PWRs. Debris that is capable of passing through the recirculation sump screen may have the potential to become lodged at a downstream flow restriction, such as a high pressure injection throttle valve or FA inlet debris screen. Debris blockage at such flow restrictions in the ECCS flow path could impede or prevent the recirculation of coolant to the reactor core, thereby leading to inadequate core cooling." The overall objective of the evaluation by the licensees is to assure long-term core cooling (LTCC), thus, satisfying the requirements of 10 Code of Federal Regulation (CFR) 50.46 (Reference 2-2).

To support this objective FA testing was performed under the initial PWROG program to quantify the amount of post-LOCA debris that can be tolerated in the reactor vessel (RV) and core. The work completed under that program is summarized in WCAP-16793-NP-A, Revision 2 (Reference 2-3). The FA testing showed that fibrous debris could accumulate and form debris beds at the core inlet and upstream edges of spacer grids near the core inlet that are within the region of the core containing single-phase liquid. When chemical precipitates were introduced during testing, the precipitates collected in the fibrous debris beds and, for certain debris loadings, stopped flow through the debris bed entirely. This result implied that flow to the core through the normal flow path may be impeded under certain post-LOCA scenarios. Consequently, additional work has been completed to examine the effectiveness of alternate flow paths (AFPs) to remove decay heat from the core when the core inlet is blocked by debris.

All U.S. PWRs have design flow paths in the RV that allow fluid to bypass the heated core during normal operations. Examples include the barrel/baffle (BB) channel, for upflow BB plants, and the upper head spray nozzles (UHSNs). Both the BB channel and the UHSNs provide a path for coolant to reach the core in the event that the core inlet becomes blocked with debris. In this context, these are termed AFPs as they provide an alternate path for coolant to bypass the core inlet and reach the core.

At some point after the postulated LOCA, when decay heat removal requirements are lower, AFPs can provide sufficient flow to maintain core cooling considering a completely blocked core inlet. The overall approach used to evaluate this scenario, considering flow through AFPs, is described in Volume 1. As a simplification, the approach assumes complete core inlet blockage at the time chemical debris arrives. This requires knowledge of the timing associated with corrosion, dissolution and precipitation of materials within the containment sump. The basis for chemical debris arrival timing is documented in Volume 5.

Demonstration of LTCC considering flow through AFPs is also predicated upon establishing the core conditions and timing of flow distribution through the core and AFPs. Volume 4 describes details of TH analyses for different PWR plant configurations. The TH analyses simulated the RCS following a large HLB and modeled debris resistance at the core inlet using a dimensionless form-loss coefficient. The outcome of the simulations confirms that LTCC can be maintained for all plant types considered when post-LOCA debris is modeled. When a debris bed of uniform resistance is modeled at the core inlet, the simulations predict that, while flow through the core inlet decreases, removal of decay heat continues since sufficient flow is able to bypass the core inlet and reach the core region. Debris testing provides the link between what was modeled in the analysis and a physical debris limit.

The subscale facility was designed to conduct systematic, separate effects tests under well-controlled laboratory conditions in order to generate debris bed resistance data as a function of debris mass. The facility is capable of operating over a wide range of conditions representative of those expected in a PWR during the post-LOCA phase of a postulated accident. Debris bed resistance data collected in the subscale facility is used to relate a physical debris quantity to the limiting core inlet resistances determined in the TH analyses as described in Volume 1.

The motivation for initial subscale facility phenomenological studies was aimed at addressing concerns raised by the Advisory Committee on Reactor Safeguards (ACRS) related to various parameter impacts that were not studied as part of the Reference 2-3 program. The ACRS concerns are documented in Reference 2-4. To guide resolution of these concerns, a literature review was conducted in Section 2.2. Results of the literature review were used to develop the test matrix.

Given the significant parametric study necessary to resolve ACRS concerns, the subscale facility was designed for rapid test turnaround. The subscale facility represents approximately one-quarter of a full-area FA. This is a significant downscale from the Reference 2-3 full-area FA test program. The basis for the reduced facility scale, which conservatively simplifies the problem by promoting uniform debris bed formation, is provided in Section 6. This reduced scale minimized resource requirements associated with completing individual experiments. Other design features that promote quick cleanup allowed up to 4 to 5 experiments to be completed within a working day. This represents a substantial increase in throughput compared to the Reference 2-3 program. This increased throughput allowed a rigorous characterization of experimental uncertainty and thorough investigation of parameter impacts. Implementation of filtration added efficiency to post-test cleanup activities, while also providing information to evaluate debris retention within the facility and valuable insights into the debris bed morphology through direct measurement of debris penetration.

Initial phenomenological studies considered debris beds formed on FA grids. The single grid was selected for initial investigations to ensure uniform debris bed formation at a single location. These studies provided valuable insights into the debris bed morphology and mechanisms resulting in debris penetration. After completing the grid studies, more realistic core inlet geometry was examined to compare to the acceptance criteria defined by the TH analyses. For this program, the core inlet region is defined as the region extending downstream of the lower core plate to the first spacer grid. This region includes the FA lower end fitting and any additional filtering grids specific to a fuel design (e.g., Westinghouse P-grid) below the first spacer grid. This region is assumed to be part of the non-boiling region of the core and consists of single phase liquid. The facility design also incorporated features that

allowed for investigation of possible AFP flow hole blockage, considering the overall approach requires that flow be maintained through these paths should complete core inlet blockage occur.

2.2 LITERATURE REVIEW

A review of open literature was performed to support design of the test facility and development of the test matrix. First, governing equations and published correlations for flow through particulate and fibrous media are reviewed to provide insights into the mechanisms resulting in head loss through a debris bed. This is followed by a review of debris capture and penetration mechanisms. Finally, a discussion of re-entrainment and breakthrough phenomena is included due to their importance as observed in the Reference 2-3 program.

2.2.1 Flow through Particulate Media

Pressure loss through a debris bed takes the general form defined for one-dimensional flow through porous media:

$$\frac{\Delta P}{L} = AU + BU^2 \qquad \text{Equation 2-1}$$

where U is the superficial fluid velocity, ΔP is the pressure difference across a layer of porous media of length L, and A and B are constants dependent on the fluid properties of the flow and the media composition. The first term on the right hand side (RHS) of Equation 2-1 represents energy losses through the debris bed due to viscous effects and the second term represents the inertial losses through the bed.

For conditions in which viscous effects dominate, the Blake-Kozeny equation is commonly used to represent the first term on the RHS of Equation 2-1 (Reference 2-5):

$$\frac{\Delta P}{L} = k\frac{\mu}{d_p^2}\frac{(1-\varepsilon)^2}{\varepsilon^3}U \qquad \text{Equation 2-2}$$

where ε is the bed porosity, μ is the fluid viscosity, d_p is the particle diameter and k is a constant with a value of 150 for particulate beds. The bed porosity is defined as the ratio of void volume (pores) to total bed volume:

$$\varepsilon = \frac{V_v}{V_T} \qquad \text{Equation 2-3}$$

where V_v is the voided volume and V_T is the total volume.

For conditions in which inertial effects dominate, the Burke-Plummer equation is typically used to represent the second term on the RHS of Equation 2-1 (Reference 2-5):

$$\frac{\Delta P}{L} = b\frac{\rho}{d_p}\left(\frac{1-\varepsilon}{\varepsilon}\right)U^2 \qquad \text{Equation 2-4}$$

where ρ is the fluid density and b is a constant with a value of 1.75.

Combining the viscous and inertial terms from Equation 2-2 and Equation 2-4 yields the widely-accepted Ergun equation (Reference 2-5) for pressure loss through porous media:

$$\frac{\Delta P}{L} = k\frac{\mu}{d_p^2}\frac{(1-\varepsilon)^2}{\varepsilon^3}U + b\frac{\rho}{d_p}\left(\frac{1-\varepsilon}{\varepsilon}\right)U^2 \qquad \text{Equation 2-5}$$

Niven, Reference 2-6, provides some physical insights into the Ergun equation by performing dimensional analysis using interstitial velocity and length scales to define a dimensionless Reynolds Number and Galileo number. For a packed bed consisting of non-spherical particles, Niven defines the void length scale as:

$$l_\varepsilon = \frac{\varepsilon d_p}{6(1-\varepsilon)} \qquad \text{Equation 2-6}$$

For particles of arbitrary shape d_p is typically approximated using:

$$d_p = \frac{6V_p}{A_p} \qquad \text{Equation 2-7}$$

where V_p is the volume of a single, non-spherical, particle and A_p is its surface area. The interstitial velocity scale, U_l, can be defined in terms of the superficial velocity as follows:

$$U_l = \frac{U}{\varepsilon} \qquad \text{Equation 2-8}$$

Using the Equation 2-6 and Equation 2-8 length and velocity scales, the dimensionless Reynolds and Galileo numbers are defined:

$$Re = \frac{\rho l_\varepsilon U_l}{\mu} \qquad \text{Equation 2-9}$$

$$Ga = \frac{\rho^2 g l_\varepsilon^3}{\mu^2} \qquad \text{Equation 2-10}$$

Rewriting the Ergun equation, Equation 2-5, in terms of these dimensionless parameters yields:

$$\frac{\Delta P/L}{\rho g} = \frac{1}{Ga}[kRe + bRe^2] \quad \text{Equation 2-11}$$

As defined above, the values for k and b are 150 and 1.75, respectively, for the Ergun equation, which is typical for particulate beds.

2.2.2 Flow through Fibrous Media

Davies, Reference 2-7, redefined the value of k, which acts on the viscous term in Equation 2-11, to consider flow through a fibrous bed:

$$k = a\frac{\varepsilon^3}{(1-\varepsilon)^{0.5}}[1 + a_0(1-\varepsilon)^3] \quad \text{Equation 2-12}$$

where a and a_0 are constants. Ingmanson, Reference 2-8, documented a rigorous study of the variation in k for various types of fiber mats, including glass fibers. Ingmanson found values for a and a_0 of 3.5 and 57, respectively, based on experimental data. Using these results, a general equation for flow through fibrous debris beds can be obtained:

$$\frac{\Delta P/L}{\rho g} = \frac{1}{Ga}\left[3.5\frac{\varepsilon^3}{(1-\varepsilon)^{0.5}}[1 + 57(1-\varepsilon)^3]Re + 1.75Re^2\right] \quad \text{Equation 2-13}$$

For uniform diameter fibers, Equation 2-7 can be used to define d_p in terms of the fiber diameter, d_f:

$$d_p = \frac{6}{4}d_f \quad \text{Equation 2-14}$$

For a debris bed formed from uniform diameter fibers, combining Equation 2-6 and Equation 2-14, the void length scale can be defined as:

$$l_\varepsilon = \frac{\varepsilon}{(1-\varepsilon)}\frac{d_f}{4} \quad \text{Equation 2-15}$$

This result demonstrates that the void length scale, and consequently the definition of Re and Ga, are independent of fiber length for uniform diameter fibers. Correspondingly, it would be expected that energy loss due to viscous and inertial effects are only functions of fiber diameter and not fiber length. Figure 2-1 graphically depicts the results of Equation 2-15 for various fiber diameters.

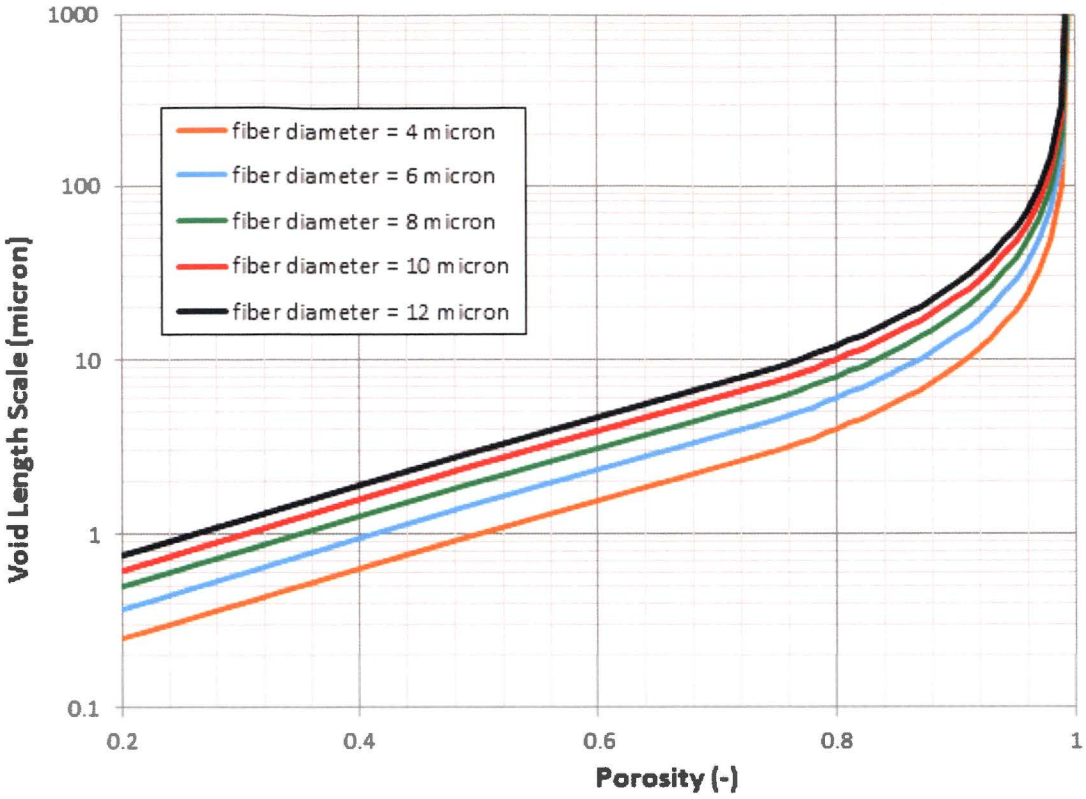

Figure 2-1 Void Length Scale as a Function of Bed Porosity for Various Fiber Diameters

2.2.3 Fiber Capture and Penetration

As fibrous debris transports to a screen or other capture geometry, such as a fuel grid, there is some potential for the fiber to collect on the capture geometry and reduce the effective opening size. This effect builds on itself and, if enough fibers are present, a thin fiber bed will form with openings that are small enough to begin to collect particulate debris that is very small compared to the capture geometry opening. At that point, penetration of fibers through the capture geometry would be greatly reduced. Of course, this simple description does not preclude mechanisms such as fiber re-entrainment that may lead to some continued shedding of fibrous debris as discussed in Reference 2-9.

The majority of fibers that pass through the capture geometry occur during the early stages of this process. While typical sump strainers are designed with small openings to preclude debris penetration that could result in blockage of core components, one of the sump strainer design requirements is that the pressure loss across the strainer should be low enough that the net positive suction head requirements of ECCS pumps are still met. This has resulted in sump strainer surface areas that are one to two orders of magnitude greater than the core cross sectional area. As a result, the small overall percentage of fibers that could penetrate the sump strainer during the early stages of bed development could result in potential core blockage scenarios.

Similar to penetration that occurs at the sump strainer, penetration of fiber through the core can also occur. This was observed during the Reference 2-3 FA test program, in which several debris beds were observed to form at different elevations (grids and lower end fitting) within the FA test geometry. The test geometry used for the Reference 2-3 testing included a wall boundary with a long narrow gap formed between the wall and capture geometry (grids and lower end fitting). This geometry is less susceptible to capture of fiber than the conditions in a PWR core, considering two grids or lower end fittings located adjacent to each other with a narrow gap formed between them. The core condition provides a ledge on either side of the gap for debris collection, while the tested flat-wall condition would promote penetration.

Intuitively, there should be a functional relationship between length of fibers entering the screen versus capture efficiency and length of fibers which penetrate the screen. However, very little work has been done to characterize this functional relationship. References 2-10 and 2-11 document the most comprehensive study of these functional relationships for sump strainer conditions over a range of screen velocities and opening diameters. For a given fiber type, these studies found a statistically significant functional relationship between length of fibers that penetrated the screen, velocity and opening size. Results from the Reference 2-10 and 2-11 studies were used as input to this program to define an appropriate range of fiber lengths to investigate fiber penetration through fuel components.

Given the narrow range of conditions tested as part of the Reference 2-10 and 2-11 studies, it is not possible to extend these fiber penetration conclusions to conditions in the core, where velocities and capture geometry are significantly different. Therefore, further investigation into the effect of fiber length distribution on fiber capture efficiency and penetration through core components was considered as part of this program.

2.2.4 Particulate Capture and Retention

Once a fibrous debris bed has formed, it is possible for the debris bed to collect small particulates. Reference 2-12 classifies particulate capture mechanisms into seven categories: straining, sedimentation, interception, inertial impaction, diffusion, hydrodynamic interaction and electrostatic interaction. Several of these mechanisms are discussed in the following paragraphs.

Straining occurs when particles are larger than the pore through which the fluid passes. Interception occurs when particles move with the fluid streamlines to within approximately one particle diameter of the filtering media. For increasing particle diameters, interception becomes the dominant capture mechanism. For particle diameters approaching the characteristic pore dimension, straining becomes the dominant mechanism. These effects can be characterized with the dimensionless ratio of particle diameter to pore length, α, where pore length, l_ε, is defined by Equation 2-15 for fibrous beds:

$$\alpha = \frac{d_p}{l_\varepsilon} = \frac{4(1-\varepsilon)}{\varepsilon}\frac{d_p}{d_f} \qquad \text{Equation 2-16}$$

Inertial impaction is a result of particles that are of different density than the fluid transporting them. When the fluid streamlines pass through the porous media, the particles may not follow the streamlines, resulting in impact. This effect is typically characterized with the dimensionless Stokes, St, number as defined in Reference 2-13:

$$St = \frac{2\rho_p U_i d_p^2}{9\mu l_v} \quad \text{Equation 2-17}$$

where ρ_p is the particle density.

Electrostatic interaction is caused by electric potential (zeta potential) due to charge on the surface of the particle and filter media. In colloidal suspensions, the pH and ionic strength, which are functions of the water chemistry, play an important role in electrostatic interaction. These properties of the solution impact the ability for particulates to agglomerate and their ability to "stick" to other solids like fiber due to electric potential of the particulate.

Reference 2-13 provides a simplistic classification of filtration types based on particle capture and retention mechanisms. For large particles, greater than 30 μm in diameter, mechanical filtration occurs and volume phenomena are dominant. For small particles, on the order of 1 μm, surface phenomena such as electrostatic interaction prevail. For colloidal particles, on the order of 0.1 μm or less, the laws of physical chemistry and colloids are most important. Reference 2-13 also defines a transition range from 1 μm to 30 μm in which volume and surface phenomena can have effects of similar magnitude.

Reference 2-14 provides a more recent reference to the classification of various capture mechanisms and divides the mechanisms into transport and attachment, where transport mechanisms act to move particles in the flow stream into contact with debris bed and attachment mechanisms are what hold the particles on the surface. Reference 2-14 provides theoretical bases that could be used to predict transport mechanisms, but states that attachment mechanisms are almost exclusively modeled empirically.

Since the smallest particulate debris postulated to reach the core inlet, in significant quantities, during the early stages of recirculation mode is expected to be on the order of 10 μm (Reference 2-15), it is clear that a number of the mechanisms described above could be important for the initial capture and possible re-entrainment of particulate debris collected in a fiber bed. As a result of the large number of important capture and retention mechanisms, some simplifications are necessary to develop an engineering assessment of the core inlet blockage scenario.

2.2.5 Re-entrainment and Breakthrough Mechanisms

Reference 2-13 provides a description of different mechanisms that can lead to re-entrainment of captured particulate. The mechanisms are divided into spontaneous and provoked. Provoked re-entrainment is a result of sudden changes in the flow or pressure through the debris bed. During a post-LOCA scenario, this could occur due to operator action, such as switching to hot leg injection or stopping and starting a pump. In addition, boiling instabilities in the core and other instabilities in the RCS, such as loop seal clearing and re-filling, could result in substantial provoked re-entrainment of captured debris.

Spontaneous re-entrainment occurs due to local variations in pressure or flow in the vicinity of captured particulate. Reference 2-10 refers to the spontaneous (localized) re-entrainment phenomenon as scouring. Scouring can occur as particulates are filtered by a fibrous debris bed, resulting in an increase in interstitial velocity. The increased interstitial velocity increases shear stress in the pores and on the

particles. This can cause the particles to dislodge and re-entrain. Typically, scouring is accounted for empirically.

Scouring can be considered a static instability in the debris bed. Once a critical shear stress is reached, and particle re-entrainment becomes pronounced enough locally to reduce the local porosity, the local resistance will decrease. This will drive a localized increase in flow and the process will build on itself until a new equilibrium is reached. This implies that the scouring phenomenon would behave very differently if the flow was controlled by a constant-head or a constant-flow process. Considering the complex response of the reactor coolant system to a HLB, which involves downcomer filling, forced ECCS flow and several other mechanisms that impact the response to a debris bed, it is not possible to model the scouring phenomena without considering the integral effects of the RCS. However, onset of the scouring instability can be investigated separately. Furthermore, the scouring instability will always result in a reduction in the overall debris bed resistance.

Re-entrainment phenomena are complex and cannot be considered independently of continued debris transport and concentration of debris transport to the bed. Depending on the bed inlet condition, as local re-entrainment becomes pronounced, continued debris delivery may dampen the scouring instability. On the other hand, local scouring may reach a large enough scale to promote re-entrainment of fibrous debris trapped in the bed, resulting in breakthrough and physical holes (boreholes) in the debris bed, as were observed in the Reference 2-3 program. Of course, it is possible that fiber penetration due to this mechanism is a function of fiber length in addition to other properties of the fiber and capture geometry.

2.2.6 Literature Review Summary

Presentation of the results of this program in terms of the dimensionless Reynolds and Galileo numbers, as defined by Equation 2-9 and Equation 2-10 using published correlations for flow through fibrous media, will provide insights into the mechanisms resulting in head loss through the debris bed. Section 5.4 discusses this evaluation using test results from this program.

Review of the governing equations indicates that fiber length is not an important parameter for evaluating pressure drop through a debris bed, but fiber diameter directly influences the pressure drop since it has a direct influence on the length scale of pores within the debris bed. Section 3.9.1.2 of this report documents the fiber diameters used as input for this program and Section 5.5 provides an evaluation of length distribution measurements as they relate to the results of this program.

The mechanisms of particle capture and retention are complex and involve both physical and chemical attachment mechanisms. The importance of straining and interception can be understood by considering the dimensionless parameter particle diameter divided by the void length scale. The mechanism of inertial impaction can be understood by considering the dimensionless Stokes number as defined in Equation 2-17. Investigation of these parameters, for a given type of fibrous debris bed, requires variation of the particle diameter. Section 5.2.6 documents testing conducted over a wide range particle sizes and summarizes conclusions in terms of straining / capture efficiency and particle packing density.

Water chemistry, and its impact on electrostatic interaction, can have a significant effect on the ability to collect and hold particulate on a fibrous debris bed, thus having a direct impact on head loss. Generally, these effects are considered negligible for particles with diameters greater than about 30 μm. For small

particles, less than about 1μm in diameter, chemical effects are the dominant mechanism. For particles in the range 1 to 30 μm, both physical and chemical processes may be important for particle capture and re-entrainment. The effects of water chemistry on debris bed blockage are almost exclusively dealt with experimentally due to the lack of theoretical models that describe this behavior within a porous media. Some investigation into the water chemistry effect was warranted since particulate debris transported to the core may approach the range of particle sizes in which water chemistry may have an influence (Reference 2-15). Section 5.2.4 documents the results of a pH and buffering agent study to evaluate the influence of these parameters for a range of expected sump coolant chemistries.

Re-entrainment and debris bed breakthrough can be provoked due to interactions with the system or it can occur spontaneously. Re-entrainment due to scouring, which can occur spontaneously, can be described as instability in the debris bed. System feedback is necessary to understand the magnitude of the scouring effect if it occurs. However, the onset of this instability can be investigated separately from the system. Sections 5.2.8, 5.3.1.2.2 and 5.3.2 of this report investigate the onset of scouring for three different capture geometries and a range of p:f ratios. These studies were conducted following predicted flow versus differential pressure response curves that do not consider dynamic system feedback mechanisms.

2.3 REFERENCES

2-1 GL 2004-02, "Potential Impact of Debris Blockage on Emergency Recirculation during Design Basis Accidents at Pressurized-Water Reactors," September 2004.

2-2 10 CFR Part 50 §50.46, "Acceptance Criteria for Emergency Core Cooling Systems for Light Water Nuclear Reactors," 72 Federal Register 49494, August 2007.

2-3 WCAP-16793-NP-A, Revision 2, "Evaluation of Long-Term Cooling Considering Particulate, Fibrous and Chemical Debris in the Recirculating Fluid," July 2013.

2-4 Nuclear Regulatory Commission, "Advisory Committee on Reactor Safeguards Thermal Hydraulic Phenomena Subcommittee Open Session," Official Transcript of Proceedings, Rockville, Maryland, May 2012.

2-5 Bird, R.B. et al., "Transport Phenomena," Revised Second Edition, John Wiley & Sons, 2007.

2-6 Niven, R.K., "Physical Insight into the Ergun and Wen & Yu Equations for Fluid Flow through Packed and Fluidized Beds," Chemical Engineering Science, 56, pp 527 - 534, 2002.

2-7 Davies, C.N. et al., "The Separation of Airborne Dust and Particles," Proceedings of the Institution of Mechanical Engineers, B1, pp 185 - 198, 1952.

2-8 Ingmanson, W.L. et al., "Internal Pressure Distributions in Compressible Mats under Fluid Stress," TAPPI Journal, 42, pp 840 - 849, 1959.

2-9 ASTP-RIGSI191-V03, Revision 1, "South Texas Project Risk-Informed GSI-191 Evaluation Volume 3: CASA Grande Analysis," ADAMS Accession # ML13175A240, June 2013.

2-10 OG-13-218, Enclosure 2, "AREVA Document 66-9199574-000, 'Fiber Bypass Size Characterization Test Report,'" May 2013.

2-11 OG-13-218, Enclosure 1, "AREVA Document 32-9201054-000, 'PWR Strainer Fiber Bypass Length Distribution,'" May 2013.

2-12 Wakeman, R. and Tarleton, S., "Solid Liquid Separation: Principles of Industrial Filtration," Elsevier Inc., 2005.

2-13 Herzig, J.P. et al., "Flow of Suspensions through Porous Media - New Differential Equation for Clogged Beds is Derived," Industrial and Engineering Chemistry, 62 (5), pp 8 - 35, 1970.

2-14 Zamani, A. et al., "Flow of dispersed particles through porous media - Deep bed filtration," Journal of Petroleum Science and Engineering, 69, pp 71 - 88, 2009.

2-15 NEI-04-07, Volume 1, Revision 0, "Pressurized Water Reactor Sump Performance Evaluation Methodology," Nuclear Energy Institute, December 2004.

3 TEST FACILITY DESCRIPTION

3.1 OVERVIEW

The test facility was constructed at the Westinghouse thermal hydraulic test laboratory located in Churchill PA. The design of the test facility supported the test objectives, which included a phenomenological investigation of fiber bed construction and debris bed head loss as function of debris mass transported to the capture geometry. The facility provided for an investigation of the effects of fuel geometry on the fiber bed morphology and head loss. Furthermore, the scale of the facility represented approximately one-quarter of a full-area FA, which allowed numerous parameters to be investigated and a statistical assessment of their importance.

Figure 3-1 shows a schematic of the subscale facility in the test configuration. The design consisted of a 4 inch inner-dimension, square cross-section column that housed the tested capture geometry. The vertical column was fabricated from clear polycarbonate sidewalls to provide optical access. For all testing, flow was injected from the bottom of the test column and directed upwards through the tested capture geometry.

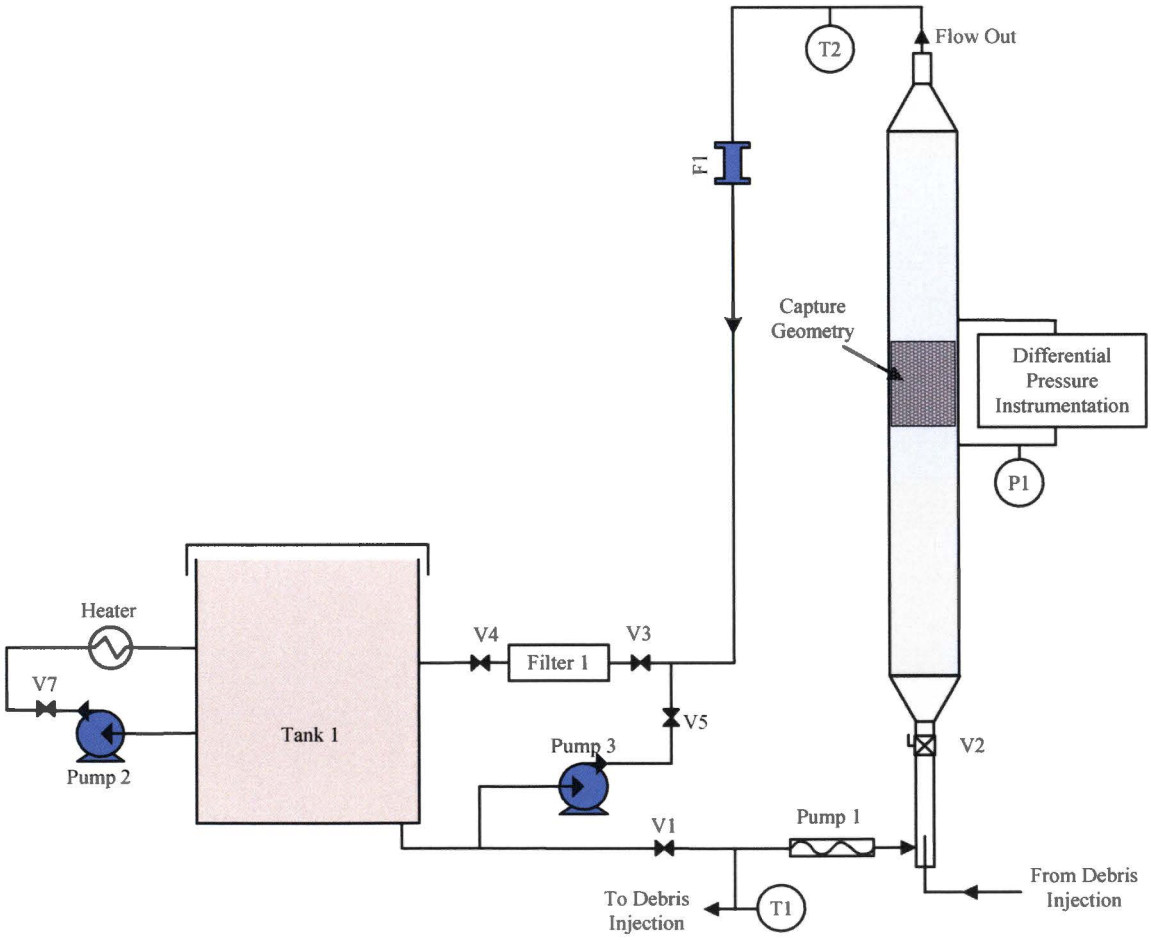

Figure 3-1 Subscale Test Facility Process Flow Diagram

For all testing, the primary flow rate was set with a positive-displacement pump (Pump 1), which was controlled throughout each test using a variable frequency drive. The Pump 1 drive was controlled to follow a predetermined flow rate curve based on differential pressure feedback. The flow rate profile was varied throughout the experimental program to follow predicted core response to debris bed formation, as described in Section 3.3.

As described in Section 3.2, debris injection was supplied using positive-displacement pumps as well. The debris injection flow was combined with the primary Pump 1 flow prior to entering the test section. Debris injection flow rate was held constant throughout each test and was not used for flow control. The debris injection system (DIS), described in Section 3.2, provided a continuous metered addition of debris at a controlled concentration. This allowed the total debris mass delivery to be accurately known at any point during the test.

The design philosophy behind the selection of positive-displacement pumps for main flow control and debris injection was simply for reproducible test control. As demonstrated in Volume 4, the reactor coolant system response to debris collection at the core inlet can be considered neither constant-flow nor constant-head. During the LTCC phase of a LOCA transient, the downcomer collapsed liquid level changes due to the continuous reduction in decay heat and any additional resistance at the core inlet due to the collection of debris. In addition, the diversion of flow through the RV AFPs further reduces flow through the core inlet. This transient process was simulated in the testing by supplying a pressure and flow boundary condition using feedback controls. To avoid transient fluctuations associated with proportional, integral derivative flow control, which would be required using a centrifugal pump and drive, positive-displacement pumps were selected. The specific type of pump selected was a progressive-cavity pump. This type of pump uses a helical stainless steel rotor and form fitting rubber stator to essentially eliminate flow pulsations associated with typical positive-displacement pumps. Inspection of fibrous debris using high frame rate photography and measurement of system pressure indicated that there were no significant pressure pulsations as a result of the selected pump style.

Downstream of the test column, all debris that penetrated the test geometry was collected in a high capture efficiency bag filter (Filter 1). Post-test weight from the bag filter allowed debris penetration to be directly quantified, and the use of filters also significantly reduced the water volume required to run each test while maintaining realistic debris concentrations. Furthermore, it was not required to replace the fluid inventory after each test This dramatically increased the number of tests that could be performed for this program since draining, flushing, filling, reheating, chemical addition and de-aeration of the fluid inventory after each experiment was not required. Test repetitions using the same fluid inventory demonstrated excellent repeatability, which further supported the decision to re-use the inventory. The fluid inventory was replaced only after significant discoloration of the fluid was observed. The discoloration consisted of a yellow tint. It was postulated that the discoloration was due to the dissolution of binder from the fibrous insulation.

An atmospheric tank (Tank 1) was used for chemical mixing and maintained the absolute pressure in the system dependent upon the liquid level. A heating loop was placed in circulation with Tank 1 to maintain the test temperature.

3.2 DEBRIS INTRODUCTION

As described in Section 2.1, the overall methodology adopted as part of this program requires pressure drop as a function of fibrous debris load to evaluate timing of flow distribution through the core inlet and AFPs. To support this, a review of debris introduction methods used for previous studies was completed. This is followed by a description of the DIS used for this program that addresses issues identified with previous work while supporting the overall methodology objectives.

In general, industry testing of sump strainers and fuel components has not included concentration as a controlled variable. However, some efforts have been made to control debris injection such that slugs of debris did not reach the filtering area. For example, NUREG/CR-6917 (Reference 3-1) described a series of tests performed for sump strainer conditions. The strainer inlet conditions were maintained at somewhat controlled concentrations by distributing the debris along a flexible pipe segment and shaking the pipe segment to suspend the debris before initiating flow. However, this method of debris addition likely resulted in an uncontrolled distribution of debris along the pipe segment. In addition, re-circulating debris within the loop would have resulted in a time-varying concentration profile.

The WCAP-16793-NP-A, Revision 2 FA test program (Reference 3-2) controlled the concentration of fibrous debris with manual additions to a tank with uncontrolled mixing patterns. This method of debris addition resulted in non-uniform debris concentrations reaching the test assembly. The variation of concentration with time was likely a saw-tooth pattern in which peak concentrations would be difficult to calculate. Furthermore, since the method of debris addition was manual, the impact on test-to-test variation may have been significant.

To address these issues, a debris addition system that controls the concentration of debris reaching the test article at any point in time was designed. One of the design requirements of the DIS was to allow controlled injections over time intervals consistent with those expected during recirculation mode of a PWR. To meet this objective, an online dilution system that allowed control of debris injection over time intervals of 30 minutes to 300 minutes was designed. These time intervals were selected since 30 minutes is consistent with approximately one sump pool volume turnover for a high ECCS injection PWR and 300 minutes represents a slow delivery of debris to the core inlet up to the point when boric acid dilution measures are typically taken. This design allowed the effect of debris concentration on debris bed head loss to be evaluated as part of the test matrix. Section 3.2.3 provides the injection profiles examined. Although the injection profiles may not be consistent with an actual plant delivery profile, they do allow an assessment of the importance of debris delivery concentration on debris bed head loss.

Figure 3-2 and Figure 3-3 show schematics of the DIS. Debris was injected to the test column with an online dilution system that provided a predetermined concentration feed of particulate and fiber debris. The main components of the DIS included two tanks with mixers, an injection pump, a clean water addition pump, a circulation pump and a 4-way solenoid-operated control valve. Throughout the testing the DIS tanks were interchanged with smaller or larger volume tanks depending on the desired debris injection concentration.

Each tank was stirred with an impeller mounted 15 degrees off axis and centered at one-third of the tank diameter from the bottom of the tank. All piping and fittings within the DIS maintained a 0.5 inch inside diameter (ID) throughout. Clear fluorinated ethylene propylene (FEP) tubing was selected for smooth

inner surface and ability to evaluate potential debris trapping with good optical access. Figure 3-4 shows a photograph of the DIS.

The DIS was operated in either an injection mode, shown in Figure 3-2, or a circulation mode shown in Figure 3-3. During injection, contents from the high concentration tank (HCT) were pumped to the low concentration tank (LCT) and into the test column. During circulation mode, the LCT continued to inject to the test column, while the HCT remained isolated. Turning the 4-way valve shown in Figure 3-2 and Figure 3-3 switched between the injection and circulation mode and modulation of the 4-way valve controlled the dilution rate and injection concentration. In this manner, flow was maintained through all of the DIS tubing at all times, which prevented any settling in the tubing.

Before each test, both tanks were filled with water from the primary test loop, which had already been prepared with the appropriate chemistry. For ideal mixing, the DIS tanks were filled to a depth equal to the tank diameter. Before debris introduction into the system, all pumps were circulated at max flow for a period of time, which purged the DIS of any air pockets. All the previous actions were accomplished with the DIS operating in injection mode. After purging the lines the DIS was switched to circulation mode such that the HCT was isolated from the test loop. Debris was then prepared and added to the HCT. The HCT mixer impeller was turned on at high RPM to disperse the debris homogenously in the tank. During this operation, air bubbles could be intentionally entrained into the tank to enhance mixing. After debris dispersion, the HCT and LCT impellers were set at a low RPM, sufficient to maintain a homogenous debris suspension without settling, but low enough to prevent vortexing and air entrainment in the un-baffled tanks. During this phase the circulation pump continued re-circulating the contents of the HCT, which was isolated from the test loop by the 4-way valve shown in Figure 3-3. This allowed any air transported to the sample lines during the high speed mixing process to be swept out.

Once this process was complete, all three pumps shown in Figure 3-3 were set to a constant flow rate with the DIS still in circulation mode. At this point, no debris had been injected into the test loop. To initiate debris injection, the 4-way valve was turned and DIS switched to injection mode. Debris was pumped from the HCT to the LCT as shown in Figure 3-2. Concurrently, the clean water addition pump was switched from the LCT to the HCT. This prevented debris settling in the circulation loop piping.

The DIS was automatically controlled by a control program after starting each experiment. The software used a predetermined input file that defined cycle timing of the 4-way valve throughout the course of each experiment. Cycling the 4-way valve during the test allowed generation of the desired profile of debris concentration to inject for each experiment. The concentration delivered to the test column was then dependent only on the valve cycle timing, tank dimensions and flow rate.

Throughout the testing effort, several changes were made to the DIS to address debris retention issues that were observed in the early portions of the test matrix. The following sections provide detail on these configuration changes.

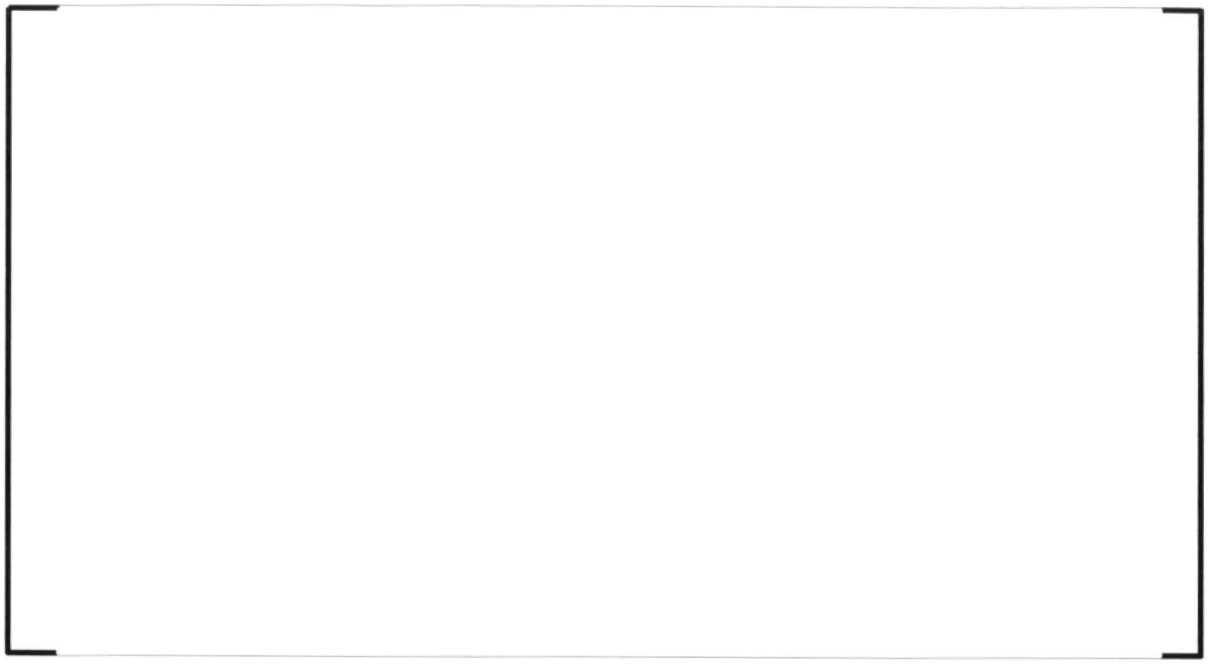

a,c

Figure 3-2 Debris Injection Schematic (Injection Mode Alignment)

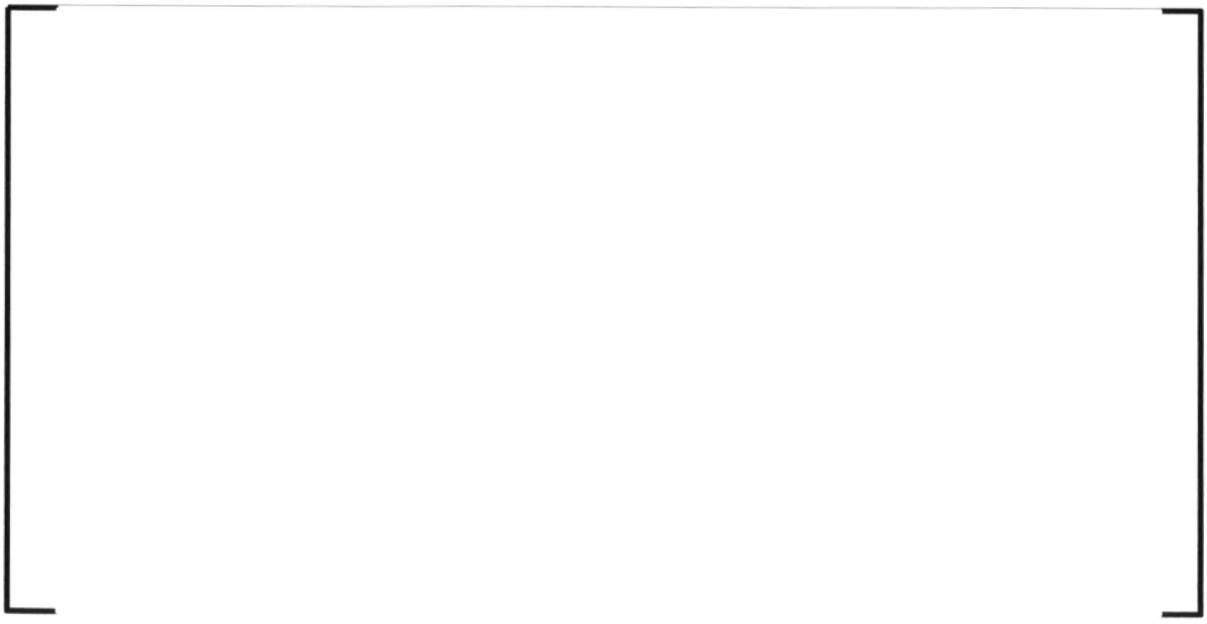

a,c

Figure 3-3 Debris Injection Schematic (Circulation Mode Alignment)

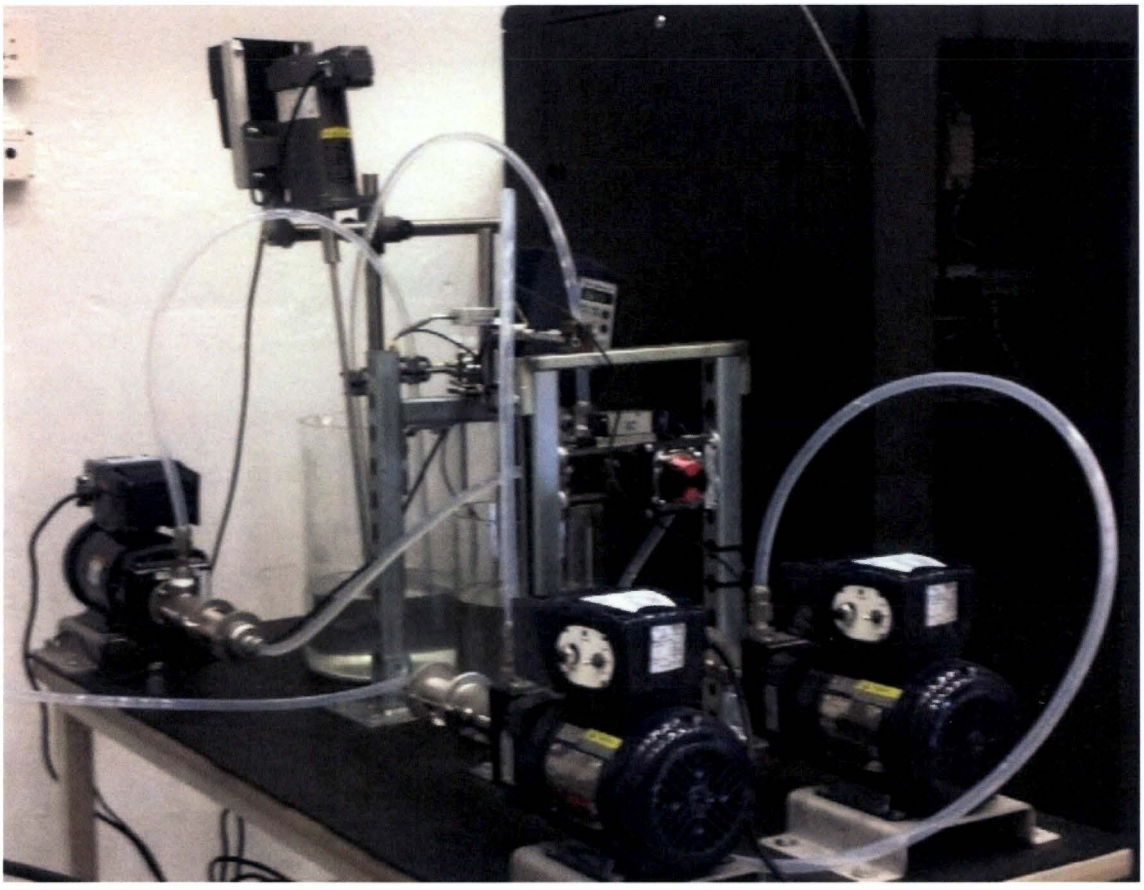

Figure 3-4 Debris Injection System

3.2.1 DIS Configuration 1 (T001 through T036)

For the initial test series, the three DIS pumps were set at a constant volumetric flow rate of [ ][a,c] throughout the duration of each experiment[1]. The HCT was a 20 liter clear glass beaker with 11.22 inch outer diameter and 16.93 inch height. The LCT was a 10 liter clear glass beaker with 8.86 inch outer diameter and 13.38 inch height.

A valve cycle timing routine was used to produce a 30 minute debris injection period. Given the volumetric flow rate, valve cycle timing and tank volumes, the debris injection profile, as shown in Section 3.2.3, was defined for Configuration 1.

[1] Note that slight variations, within 5%, in clean water and circulation pump flow rate were necessary for level control. However, the injection pump flow was always maintained at a constant rate.

During the initial test series, it was noted that some retention of debris occurred within the DIS. As a result, several tests were considered invalid and repeated after the changes described in Section 3.2.2 were made.

3.2.2 DIS Configuration 2 (T037 through T212)

The equipment and operation of the DIS system was modified to address issues associated with debris retention in the DIS. To lower the concentration of debris passing through the pumps, the 20 liter HCT was replaced with a 75 liter tank with 18 inch outer diameter and 30 inch height.

This change in the HCT tank occurred starting at Test T037. In order to maintain similar debris injection concentration profiles, as compared the prior testing, changes were also made to the operation of the DIS. First, the volumetric flow rate through all three DIS pumps was increased to [ ]^{a,c} This was necessary considering the increase in HCT volume.

For the 30 minute injection experiments, valve cycling during the experiment was no longer required. In addition, 30 seconds after starting each 30 minute injection experiment, the clean water pump flow rate was turned off and the HCT level was reduced from 18 inches to 6 inches. At that point, the clean water pump was turned back on through the completion of each experiment.

3.2.3 Debris Delivery Profiles

Calculations were performed to determine the cumulative fiber mass delivered to the test column for each DIS configuration, nominal injection duration (30 minute or 300 minute) and total fiber mass. The calculations assumed homogenous mixing in the HCT and LCT. In addition, a sampling efficiency of 1.0 was assumed for all debris components[2]. This assumption will result in a small error, which was assumed to be negligible for this effort[3].

The transient calculations were carried out in 1 second increments. Results for 12.5 and 25 gram fiber injections are shown in Figure 3-5. The Configuration 2 delivery rates slightly lag the Configuration 1 delivery rates. This was due to the larger volume HCT and HCT drain-down procedure that was implemented for Configuration 2. Within a 30 minute period, for the 30 minute injection cases, the majority of debris was delivered in both Configuration 1 and 2. However, tests were continued until at least 99.9% of the debris, based on the transient calculation, was injected. Figure 3-6 shows results for the Configuration 2, 300 minute injection and Figure 3-7 shows results for the Configuration 2, 30 minute injection experiments considering various fiber loads.

[2] Sampling efficiency is the ratio of concentration in the sample line divided by the concentration of the bulk fluid.

[3] Bench testing, which included sampling of blended NUKON fibers using a 0.5 inch sample line oriented in the same manner as the DIS sample line, demonstrated a sampling efficiency of 0.98 for the conditions examined.

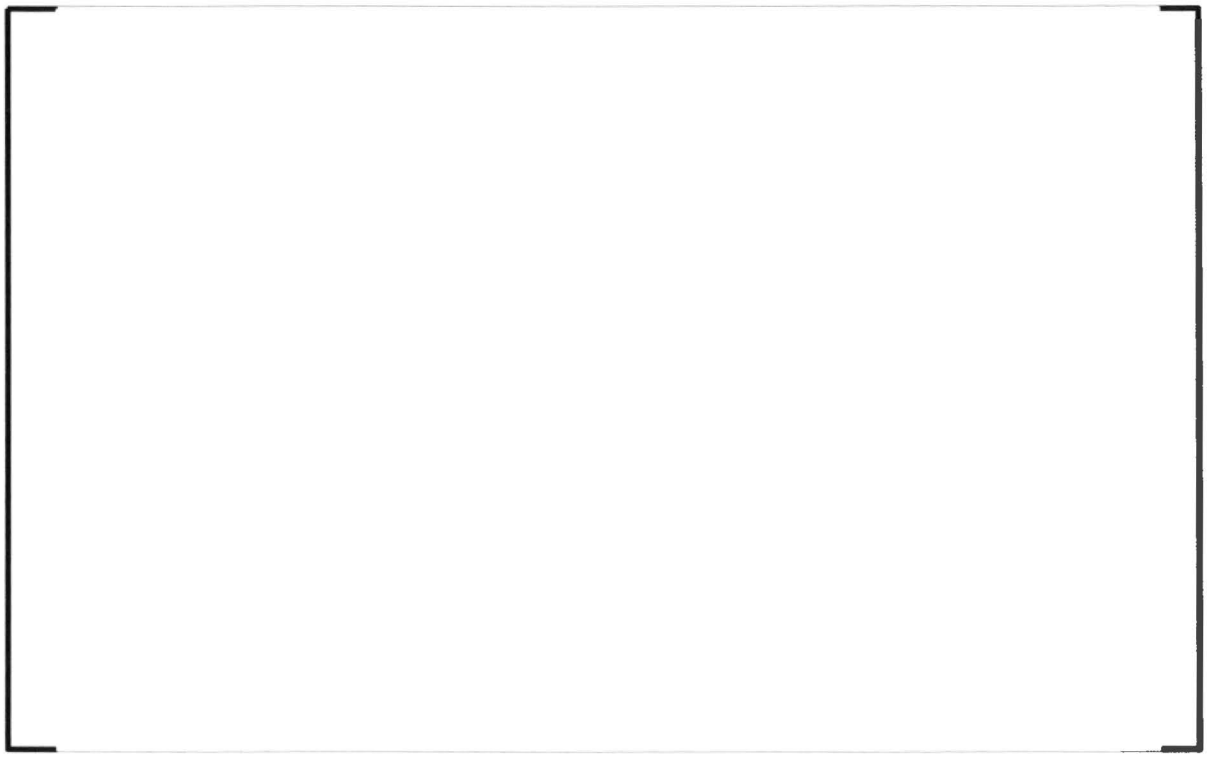

a,c

Figure 3-5 Comparison of Configuration 1 and 2 Debris Injection Profiles

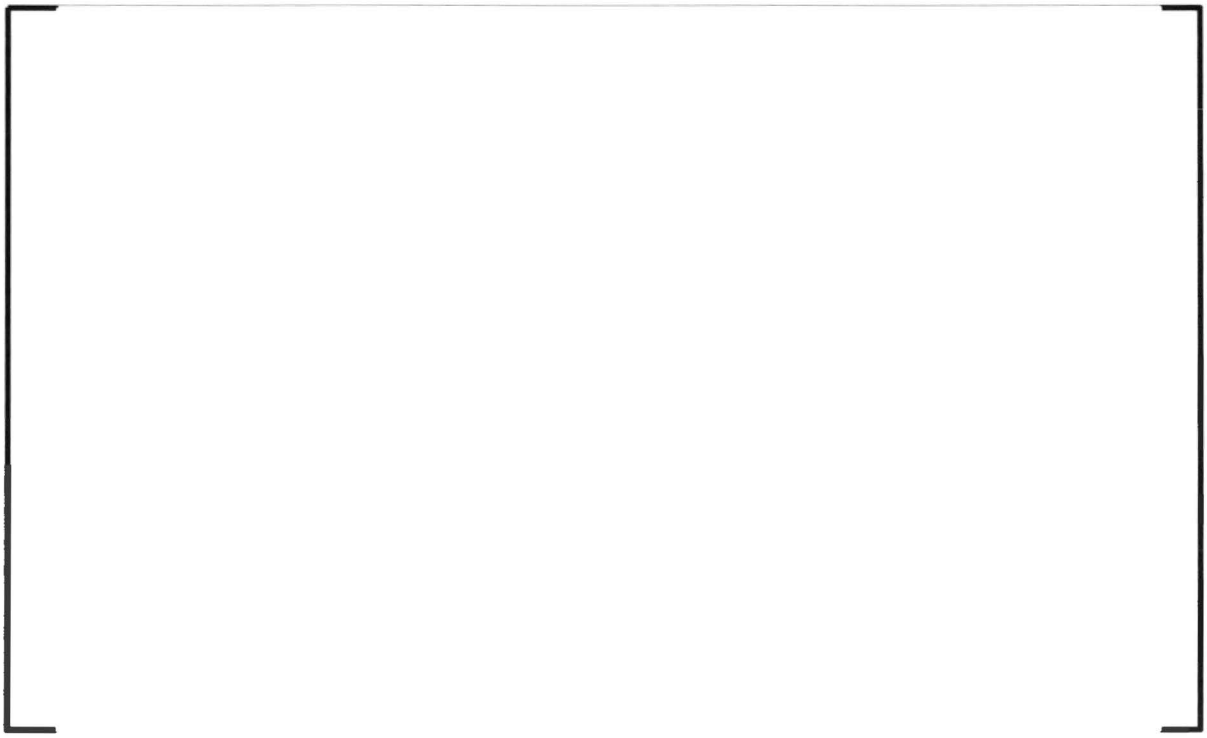

a,c

Figure 3-6 Configuration 2, 300 minute Debris Injection

a,c

Figure 3-7 Configuration 2 Debris Injection Profiles for Entire Range of Fiber Masses Investigated

3.3 FLOW CONTROL

Maintaining representative flow rates through the test section is considered important for several reasons. These can be summarized as follows:

- Debris penetration
  - At high flow rates, it is possible that fiber and particulate penetration and re-entrainment may be higher than at low flow rates. For example, particulate scouring, as described in Section 2.2.5, is driven by increased shear on particles. Higher flow rates may increase the effect of debris scouring.
  - Since there are no existing models to predict particulate penetration through fiber beds as a function of flow rate, particle size, etc., there is no way to scale results from constant flow rate conditions to the actual plant response. Therefore, testing representative plant responses is necessary.
- Scouring and bed breakthrough
  - At high interstitial velocities, fluid shear within the debris bed can reach a point in which scouring and potential bed breakthrough occurs. This can result in a dramatic reduction in

pressure drop across the bed. This process is very chaotic and test-to-test variation after this occurs is very high. Preservation of the flow and pressure boundary conditions is necessary to preserve characteristics of the debris bed, such as porosity and bed compression that influence the onset of scouring.

- Bed compression
  - At increased differential pressure across the debris bed, the fiber mat will compress, which can have a strong influence on the particle capture efficiency of the debris bed. Therefore, it is important to maintain realistic bed compression throughout the experiment such that particle capture efficiency is consistent with post-LOCA conditions.
  - For some cases, bed compression is reversible, and in other cases it is not. Since there is no predictive model available to discriminate between regimes in which the process is reversible or not, it is necessary to follow a representative flow versus differential pressure curve, such that the results do not need to be scaled to other conditions considering bed compression.

Because of the phenomena described above, all testing reported in this document followed representative flow versus differential pressure profiles based on observations from the comprehensive set of analyses documented in Volume 4. The Volume 4 analyses study the impact of varied core inlet resistance on core inlet flow. Based on these analyses, a set of expected core inlet flow response curves was developed for this test program. All curves follow a flow reduction evolution as a function of head loss through the core inlet, starting from different initial flow rates. These initial flow rates have been selected to cover a wide range of ECCS flows during cold leg recirculation. These are shown in Figure 3-8 as Low, Mid, Mid2, High, Final-Low, Final-Mid and Final-High. Note that the flow rates shown in Figure 3-8 are consistent with the flow rates during the scaled testing. To scale these values to conditions representative of a FA, the geometric scaling factors reported in Section 3.5 of this report are necessary.

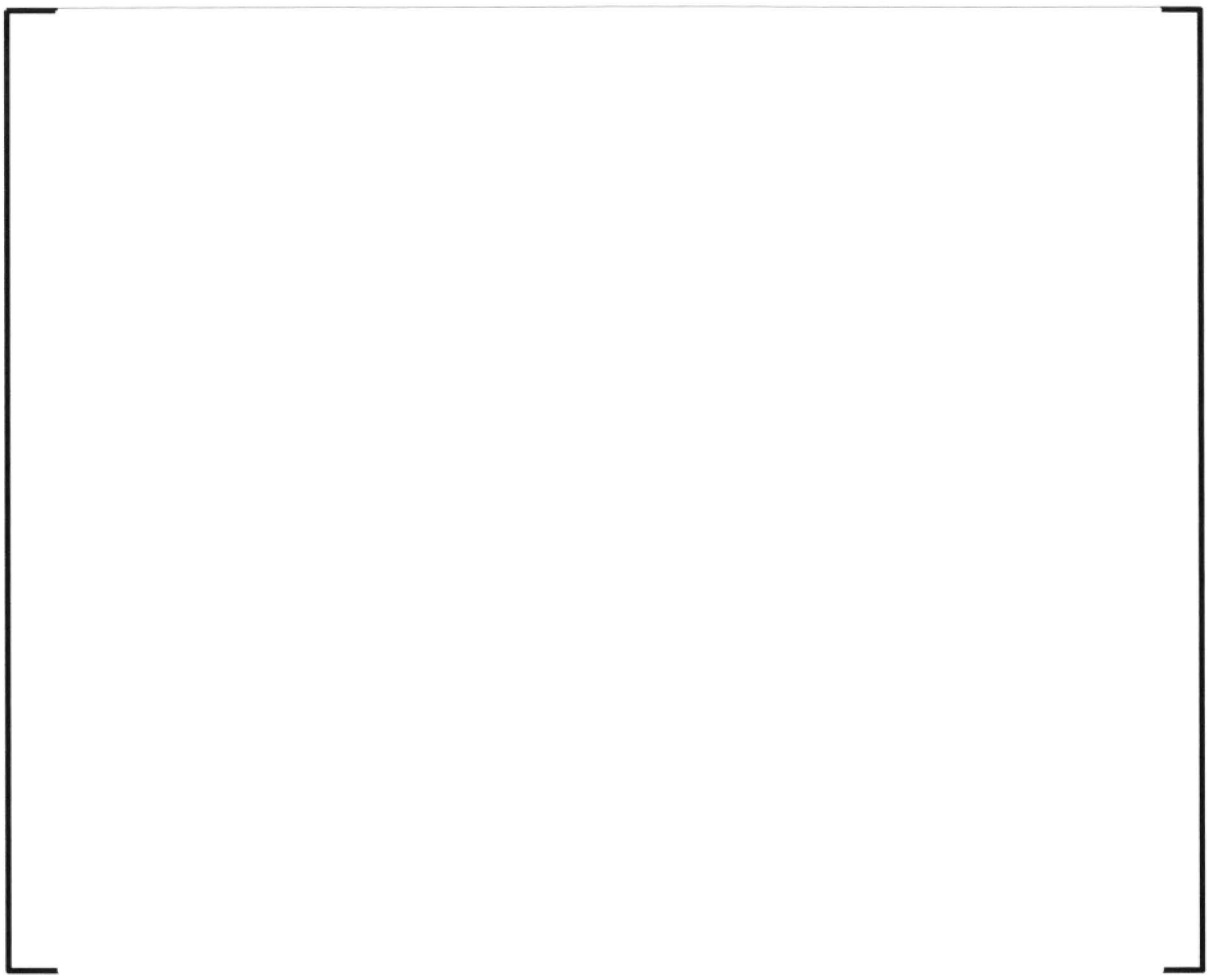
a,c

Figure 3-8 Flow Reduction Curves used for Subscale Testing

The flow reduction versus pressure drop relationship is expressed by the following equation:

$$Q = A \cdot \Delta P^{C} + B \qquad \text{Equation 3-1}$$

where Q is the volumetric flow rate through the test column in units of gpm, ΔP is the pressure drop across the tested component in units of psi and A, B and C are constants. Table 3-1 summarizes the Equation 3-1 constants used throughout the testing. Note that for the Final-Low, Final-Mid and Final-High flow response curves, a portion of the beginning of the response curve was held at a constant flow rate. This represents downcomer filling during the initial stages of the transient. All curves were trimmed at the end to hold a [ ]^{a,c} flow, which is approximately twice what is required to make-up for steam generation / boil-off from the core 20 minutes after the event initiation.

Table 3-1 Flow Response Curve Parameter Summary					
Curve I.D.	**A**	**B**	**C**	**IF dP ≤ 2.5 psid**	**IF dP > 16.84 psid**
Low					
Mid					
Mid2					
High					
Final-Low					
Final-Mid					
Final-High					
Note 1: If dP > 2.6 psid					

a,c

Depending on the plant type, specific characteristics of the ECCS and core inlet geometry, the core inlet flow response to debris bed formation can vary widely for HLB conditions. As resistance to flow at the core inlet increases, coolant begins to fill the downcomer and can eventually flood the cold side RCS piping and portions of the steam generators. In addition, with an increase in flow resistance at the core inlet, a larger portion of the total ECCS flow is diverted through AFPs. Further complicating this issue is the fact that debris transport rate to the vessel can vary depending on the break location and numerous other factors. Finally, variations in plant geometry (e.g., BB flow resistance) and ECCS design make a generic coverage of possible plant responses extremely difficult and potentially overly conservative.

Considering the complexity of the problem all scenarios could not be examined. However, all tested profiles are representative, and could occur during the LTCC phase of a postulated LOCA. By defining a range of flows, the experimental results cover a wide range of conditions. Given the broad range of flow profiles tested, any significant influence of flow response on debris bed formation and resulting head loss can be identified.

3.4 TEST COLUMN

The primary flow was combined with a debris-laden flow in an annular gap region directly upstream of the test column as shown in Figure 3-9. Debris was delivered from the DIS as described in Section 3.2 via a 0.5 inch inner diameter tube to the 1 inch test column inlet. This geometry aided in mixing and provided a uniform distribution of debris entering the test column.


a,c

Figure 3-9 Debris Injection Mixing Upstream of Test Column

Debris was then passed through a custom 1 inch circular to 4 inch inner-dimension, square cross section diffuser as shown in Figure 3-9. This provided a smooth, steep transition to prevent debris from settling on the bottom surface of the diffuser. This geometry also prevented recirculation regions and promoted a uniform debris distribution entering the test column.

Dimensions for the test column are provided in Figure 3-10. The test column was designed to maintain a length-to-diameter (L/D) ratio of 10, corresponding to approximately 40 inches, upstream and downstream of the capture geometry. The first capture geometry used was the grid and rod assembly shown in Figure 3-11. A small section of a FA grid was placed within the grid insert and sealed around the perimeter to prevent bypass around the grid. The grid insert walls remained flush with the clear test vessel sidewalls via a recess installed in the test section sidewalls as shown in Figure 3-11. This prevented debris trapping that could occur with a large lip. Fuel rod simulators and thimble tubes with plugs, that were 20 inches in length, were then installed into the grid assembly. This provided 10 inches upstream and downstream of the grid for flow development in the subchannel region formed by the rods. The grid and fuel rod simulators were made from prototypic materials, while the thimble tubes were simply stainless steel rods.

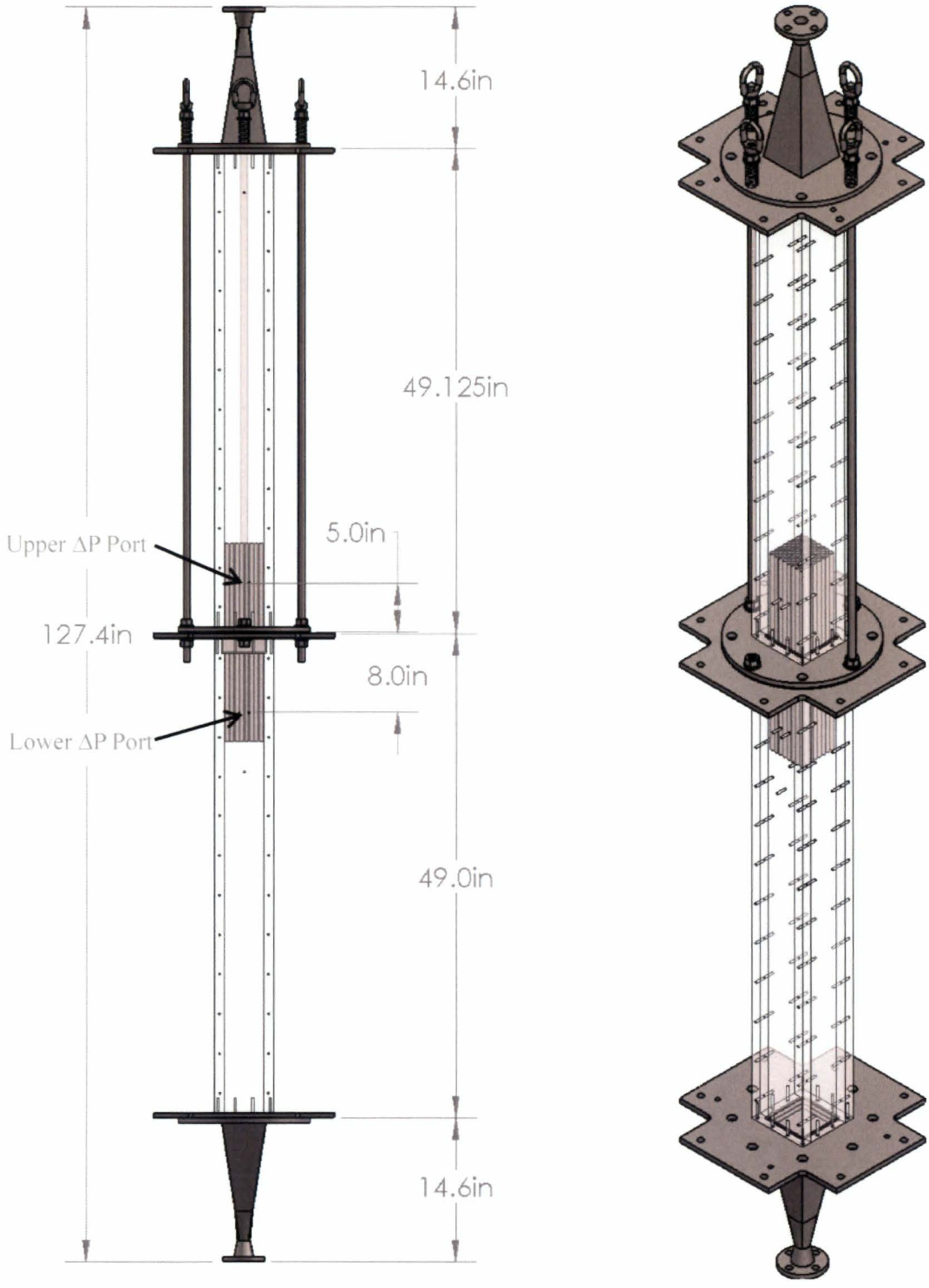

Figure 3-10 Dimensioned Drawing of Test Column

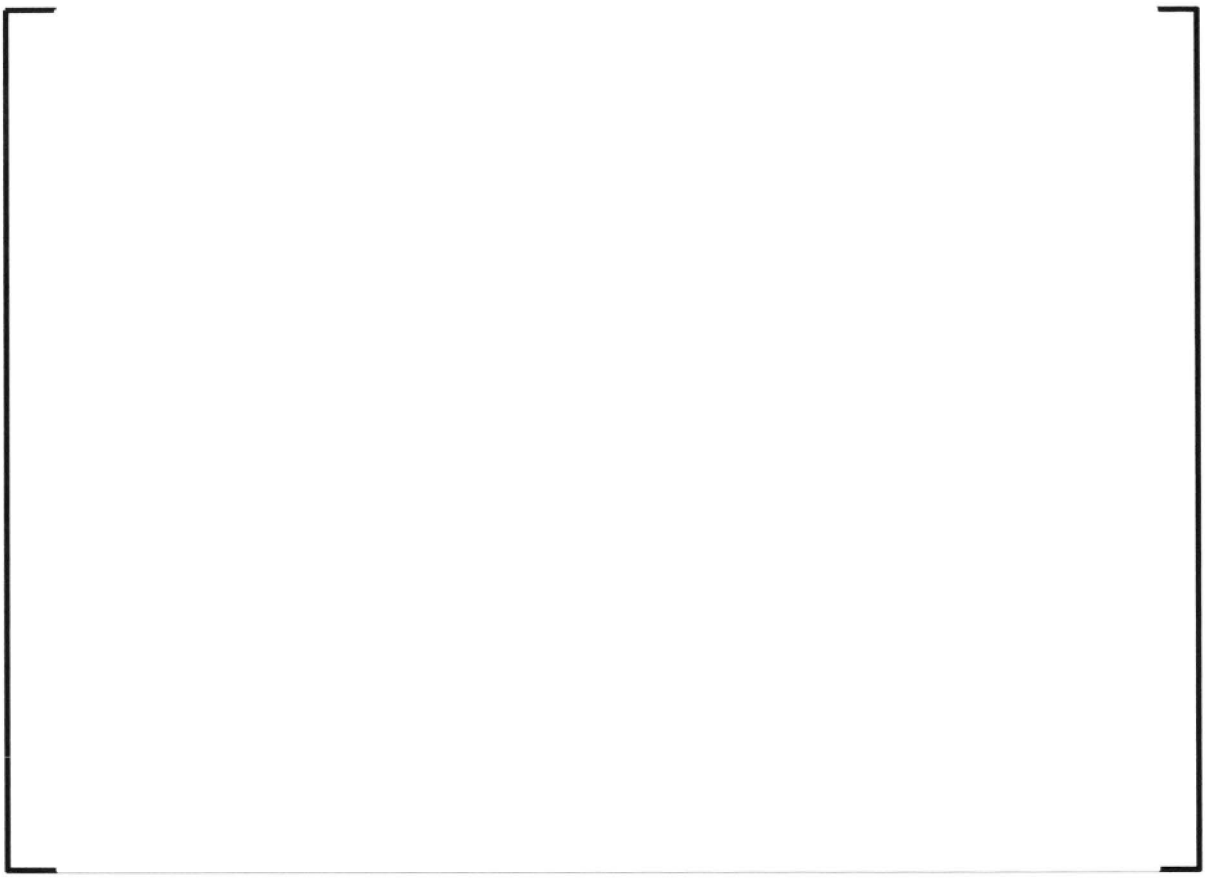

a,c

Figure 3-11 Grid and Rod Assembly Installed in Test Column

Starting at test T140, a new test column of similar dimensions was manufactured to perform core inlet geometry testing. The original test column did not have capabilities to install bottom nozzle (BN) geometry. A schematic of this flow column is shown in Figure 3-12. The updated flow column was similar to the original column in terms of overall dimension and concept. The same diffusers were used at the top and bottom of the flow column to transition from the loop piping to the flow column. The updated test column, like the original, was designed to maintain a L/D ratio of 10 upstream and downstream of the capture geometry.

Major changes to the column included O-rings and custom clamps to seal and secure the column walls. This corrected leaking issues and allowed for higher pressures to be achieved compared to the original test column design. Furthermore, the updated test column design incorporated the ability to install an additional insert for the BN at the interface between the bottom and top sections of the test column.

a,c

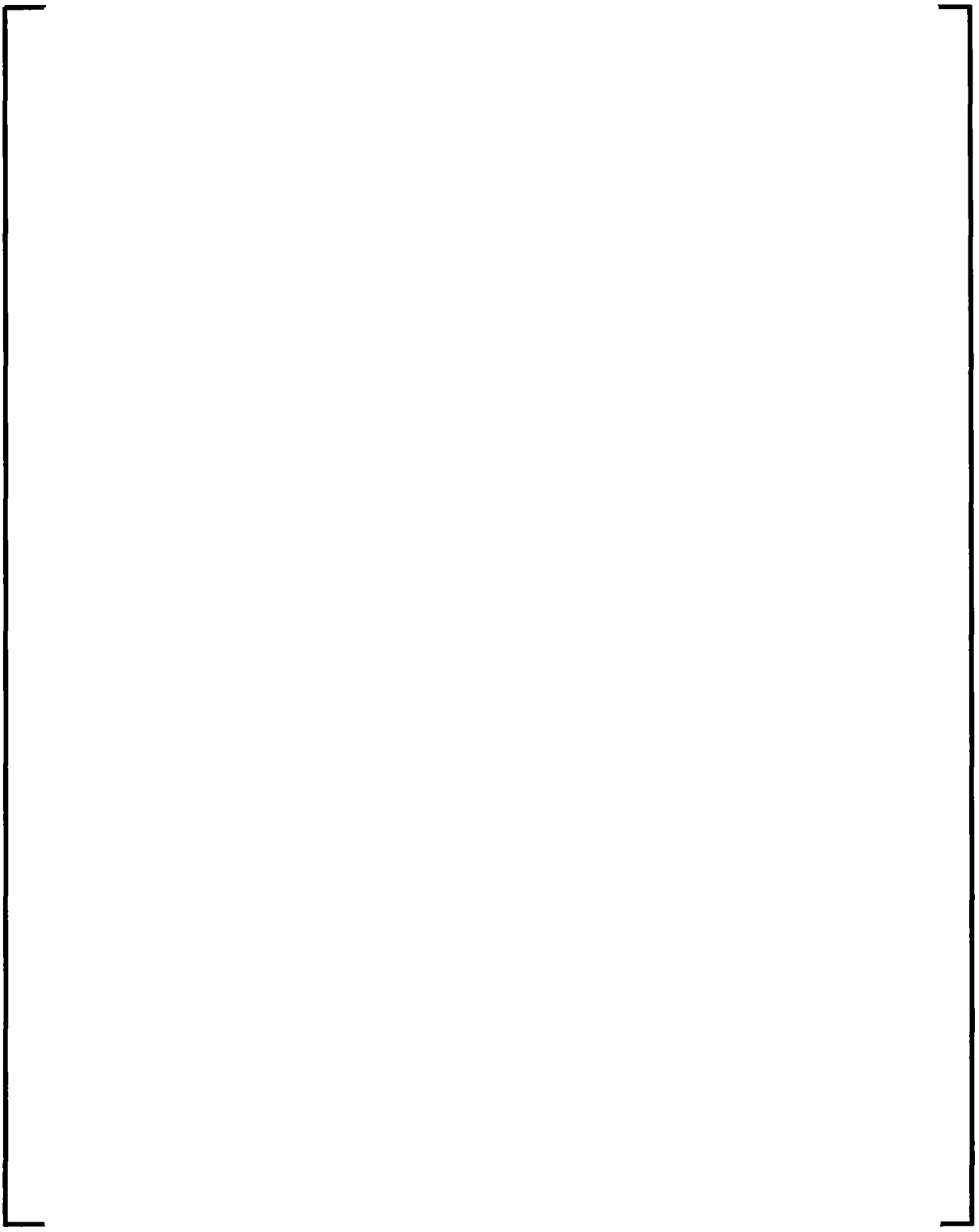

Figure 3-12 Schematic of Updated Test Column for Core Inlet Geometry Testing

3.5 TEST GEOMETRY

The 4 inch inner-dimension square column described in Section 3.4 housed various test geometries throughout the test matrix. Table 3-2 below provides a list of the tested geometries.

Table 3-2	Summary of Test Geometries
ID	**Description**
RFA	Westinghouse RFA single bottom grid with assembly-to-assembly gap in the middle
HMP	AREVA HMP™ single grid with assembly-to-assembly gap in the middle
OFA	Westinghouse OFA single bottom grid with assembly-to-assembly gap in the middle
UFA	Westinghouse UFA single bottom grid with assembly-to-assembly gap in the middle
RFA BN/P-1	Westinghouse RFA BN/P-grid and bottom grid with assembly-to-assembly gap in the middle
RFA BN/P-2	Westinghouse RFA BN/P-grid and bottom grid without assembly-to-assembly gap
FG/HMP	AREVA FUELGUARD™ and first HMP grid without assembly-to-assembly gap

The test matrix was broken into three segments. The first segment, including tests T001 through T139, investigated debris capture associated with a single grid. The second segment, including tests T140 through T212, investigated debris capture at the core inlet and included fuel entrance geometry (e.g., Westinghouse BN or AREVA Inc. FUELGUARD) and one or more grids. The third segment of the test matrix consisted of alternate flow path testing.

3.5.1 Fuel Assembly Grids (T001 through T139)

Initial phenomenological studies considered debris beds formed on FA grids. The single grid was selected for tests T001 through T139 to ensure uniform debris bed construction at a single elevation within the test column. This allowed a direct measure of the debris penetration by measurement of post-test bag filter weights that provided valuable insights into debris bed morphology and mechanisms resulting in debris penetration.

A portion of tests T001 through T139 was used to compare the impact of grid geometry on debris collection and head loss. Variation of fuel rod diameter, pitch-to-diameter ratio and grid strap design were considered in the selection of grids. Table 3-3 provides a summary of important dimensions for the various grids used for these tests. For each grid, the open flow area was calculated using the installed

HMP is a trademark or registered trademark of AREVA. Other names may be trademarks of their respective owners.
FUELGUARD is a trademark or registered trademark of AREVA. Other names may be trademarks of their respective owners.

pitch of the FA and subtracting the area associated with the fuel rods, instrumentation tube and thimble tubes. The grid straps and springs were not considered in the calculation of open flow area.

Table 3-3 Summary of Grids used for Tests T001 through T139

	AREVA 17x17 High Mechanical Performance (HMP)	Westinghouse 17x17 Optimized Fuel Assembly (OFA) bottom grid	Westinghouse 17x17 Robust Fuel Assembly (RFA)		Westinghouse 15x15 Upgraded Fuel Assembly (UFA) bottom grid
			bottom grid	P-grid[1]	
Rod Diam.					
Rod Pitch					
Thimble Tube Diam.					
Inst. Tube Diam.					
Assembly Pitch					
Outer Dimension of Grid					
Gap					
# of Fuel Rods					
# of Thimble Tubes					
# of Instrument Tubes					
Open Area					
Open Area					

a,c

Note 1: The P-grid was not used during Tests T001 through T139, but was shown here since it was used in later testing.

The test grids were cut from prototypic FA grids supplied by each fuel vendor. The grid cuts used for the RFA, OFA and HMP grids listed in Table 3-3 are shown in Figure 3-13. The grid cut shown in Figure 3-13 forms a 4 x 8 section of grid with an outer grid strap on one side. Two of these 4 x 8 grids were placed in the test section and sealed around the periphery with a prototypic gap formed across the center of the geometry. The assembled grid geometry is shown in Figure 3-14. Figure 3-15 through Figure 3-17 show images of the OFA grid assembled in the grid holder with rods and thimble tubes installed. The UFA grid

was prepared similarly to the RFA, OFA and HMP grids. However, for the UFA grid a 4 x 7 section and a 3 x 7 section were used as shown in Figure 3-18. This resulted in the gap being slightly offset from the center of the column.

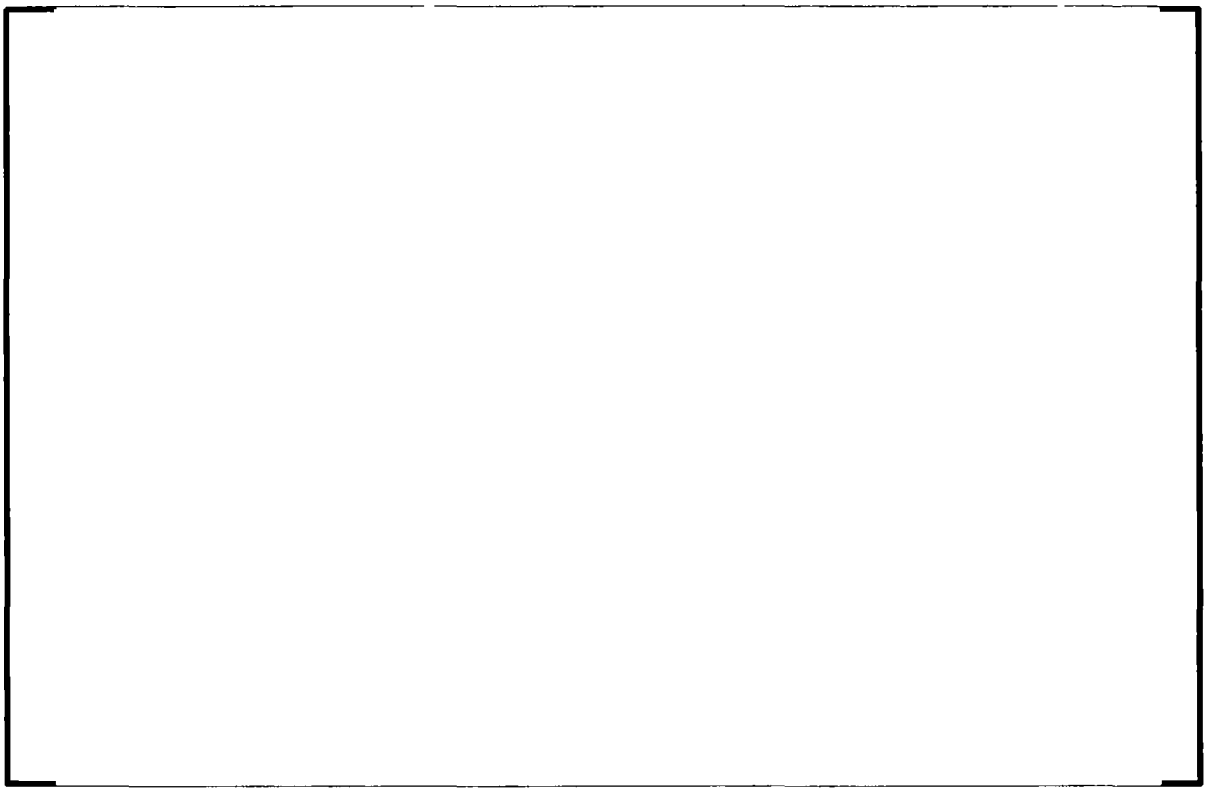

a,c

Figure 3-13 4 x 8 Grid Sections used for RFA, OFA and HMP Testing

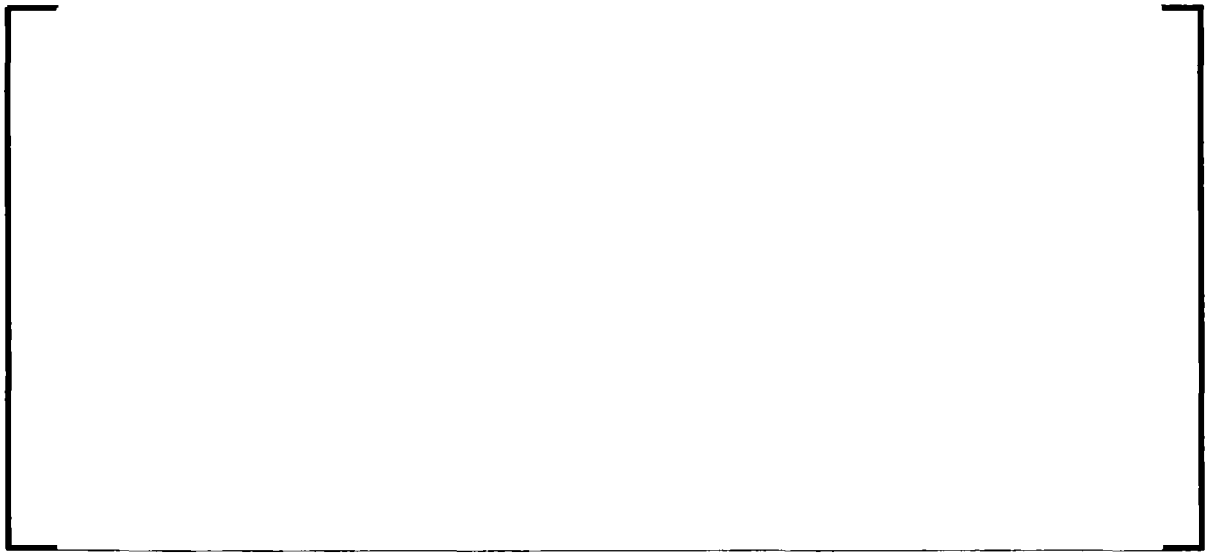

a,c

Figure 3-14 Image of OFA Test Grid Assembly

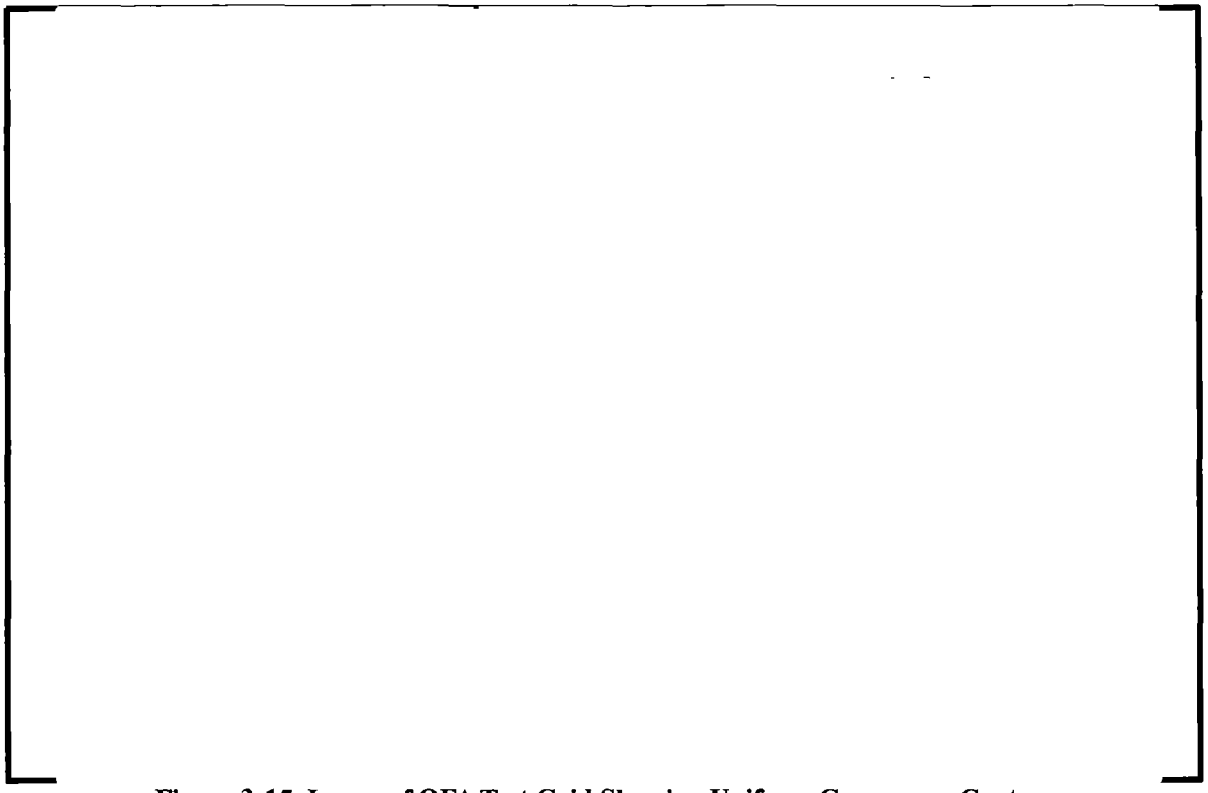

a,c

Figure 3-15 Image of OFA Test Grid Showing Uniform Gap across Center

a,c

Figure 3-16 Image of OFA Test Grid Showing Bottom Portion of Outer Grid Strap in Center

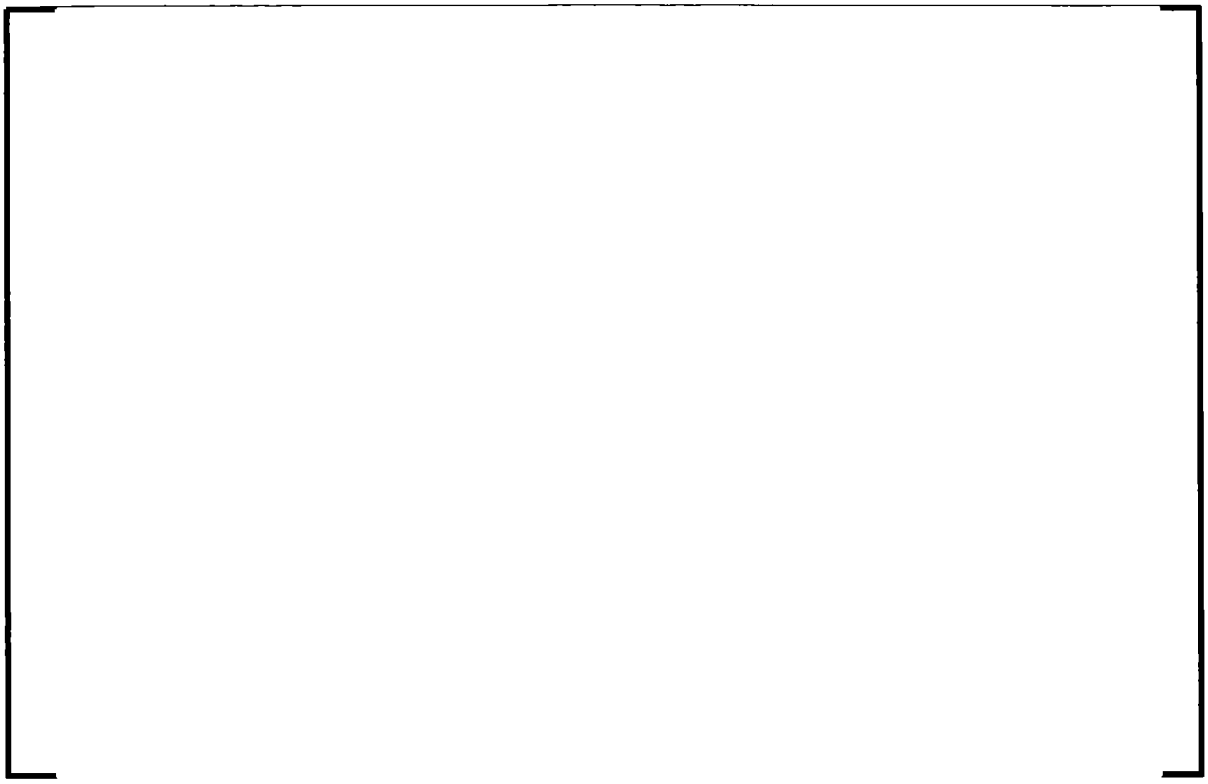

a,c

Figure 3-17 Image of OFA Test Grid Showing Bottom of Grid

a,c

Figure 3-18 3 x 7 and 4 x 7 Grid Sections used for UFA Testing

As shown in Figure 3-14, simulated fuel rods and thimble tubes 20 inches long were installed into the grids. Considering the thimble tubes and fuel rod simulators, the total flow area of each of the test grids was calculated for comparison to the full-area FA data provided in Table 3-3. Table 3-4 below summarizes the results of this calculation. Comparison of Table 3-4 to Table 3-3 indicates that there is an insignificant difference in the open flow area ratio compared to an installed FA. The last row in Table 3-4 presents the open area ratio compared to a full-area FA. This value can be used to scale results from the subscale facility to a full-area assembly.

Table 3-4 Summary of Test Grids used for Tests T001 through T139

	HMP Test Grid	OFA Test Grid	RFA Test Grid	UFA Test Grid
# of Fuel Rods				
# of Thimble Tubes				
Open Area				
Open Area %				
Open Area Ratio Compared to Full-Area Assembly %				

a,c

3.5.2 Westinghouse Core Inlet with Gap (T140 through T151)

Realistic core entrance geometry that included a lower end fitting was examined as part of this program. There were several reasons for extending the experimental data set to this type of geometry. The primary reason was that this geometry can be directly scaled to actual core inlet geometry to conservatively predict plant response. This extension can be performed without the single-grid experimental results if debris penetration through the core entrance geometry is small or insignificant. Initially, it was not clear that this would be the case over a wide range of conditions. However, test results discussed in Section 6.0 demonstrate that there is very little penetration of fibrous debris through the BN for the limiting stable debris bed conditions. When penetration did occur, the combined pressure loss across the lower end fitting and grids was not limiting, as discussed in Section 5.3.

The Westinghouse RFA BN, P-grid and bottom grid were selected for the initial core inlet geometry test series. The RFA grid geometry was shown to be the most restrictive of the Westinghouse grids tested. The selected geometry did not include side skirt flow holes in the BN since these are less common.

The BN geometry is essentially a perforated plate with sides and feet that support the FA by resting on the lower core plate. Comparing the RFA BN design to other Westinghouse fuel designs, the RFA BN maintains [ ]^{a,c} Section 6.2 of this report provides a discussion of the test results in terms of the BN flow hole diameter and open flow area ratio, which demonstrates that the [ ]^{a,c} Table 3-5 provides dimensional information for the BN. Table 3-3 in Section 3.5.1 provides dimensional information for the P-grid and bottom grid.

Table 3-5 Summary of RFA Bottom Nozzle Dimensions		
	Value	**Units**
Assembly pitch		
Outer dimension of BN		
Gap between adjacent nozzles		
BN flow hole diameter		
Total number of BN flow holes		
Total open flow area (flow holes and gap included)		
Open flow area ratio		
BN Top Surface to Bottom of Rods (in)		
BN Top Surface to P-grid Bottom Surface (in)		

a,c

Drawings of the BN insert designed for tests T140 through T151 are shown in Figure 3-19 and Figure 3-20. The tested BN was fabricated from clear polycarbonate and consisted of two BN sections with a prototypic gap in the center of the insert. As a result of this design, the central region of the BN included a portion of the side skirt. Table 3-6 summarizes the tested BN geometry. This is a slight distortion from an installed RFA BN, which has an open flow area ratio of [ ]^{a,c} as shown in Table 3-5.

Table 3-6 Summary of Tested Bottom Nozzle with Gap Dimensions		
Gap between BN sections		
BN flow hole diameter		
Total number of BN flow holes		
Total open flow area (flow holes and gap included)		
Open flow area ratio		
Test column inlet flow area		
Ratio of test column inlet flow area to installed FA inlet flow area[1]		
Note 1: This value used to scale results from test geometry to a single FA in Section 6.5		

a,c

The P-grid insert is shown in Figure 3-21. The grid insert, like the grid insert described in Section 3.5.1, was sealed around the periphery and maintains a prototypic assembly-to-assembly gap in the center. The P-grid insert was designed such that the spacing between the BN and the P-grid was prototypic. By installing the grid and BN as separate spool piece inserts into the test column, precise control of the gap between the P-grid and BN was attained. Figure 3-12 in Section 3.4 shows an image of the BN and P-grid insert installed in the test column.


a,c

Figure 3-19 BN Insert Showing Close-up of Chamfered Gap between Adjacent BN Sections


a,c

Figure 3-20 Schematic of Subscale Facility Bottom Nozzle Insert Showing Flow Hole Pattern

a,c

Figure 3-21 Schematic of New Subscale P-Grid Insert

3.5.3 Westinghouse Core Inlet Central FA Region (T152 through T178)

A center cut of the BN, which underlays an 8 x 8 P-grid cut-out, was used for tests T152 though T178. This change from the geometry described in Section 3.5.2 was made as a result of test observations during tests T140 through T151. During those experiments, non-uniformities were observed in the debris bed as a result of the BN side skirts installed within the center of the test geometry. While non-uniformities would be expected near the BN side skirts in larger scale geometry, there was also a pronounced non-uniformity in the debris bed at the test vessel wall, which would not be considered realistic. Since insignificant debris penetration was observed through the gap formed between adjacent BN sections, it was decided that the side skirts would be eliminated to increase the inlet dimension of the BN flow holes from 2 to 4 inches. In addition to the edge effect minimization, a better effort was made to preserve the open flow area ratio of the tested component, compared to the actual core inlet geometry.

Several options for a BN cut-out from a full-area BN were considered. However, a single cut-out, with the same dimensions of the subscale test column, would not provide an optimal match of the open flow area ratio. Therefore, a design including [ ]^{a,c} flow holes with a diameter of [ ]^{a,c} which is within the tolerance of the Westinghouse RFA BN design drawings, was selected. The design includes blocked areas consistent with the location of thimble tubes within the FA. Table 3-7 shows important dimensions of the tested BN. Figure 3-22 through Figure 3-26 show drawings of the BN and assembled test geometry with grids installed.

Table 3-7 Summary of Tested Bottom Nozzle without Gap Dimensions		
	Value	**Units**
BN flow hole diameter		
Total number of BN flow holes		
Total open flow area		
Open flow area ratio		
Test column flow area		
Ratio of test column inlet flow area to installed FA inlet flow area[1]		
Note 1: This value used to scale results from test geometry to a single FA in Section 6.5		

a,c

a,c

Figure 3-22 Selected Bottom Nozzle Section

a,c

Figure 3-23 Test Section Top View Showing BN Flow Holes with Respect to Simulated Fuel Rods

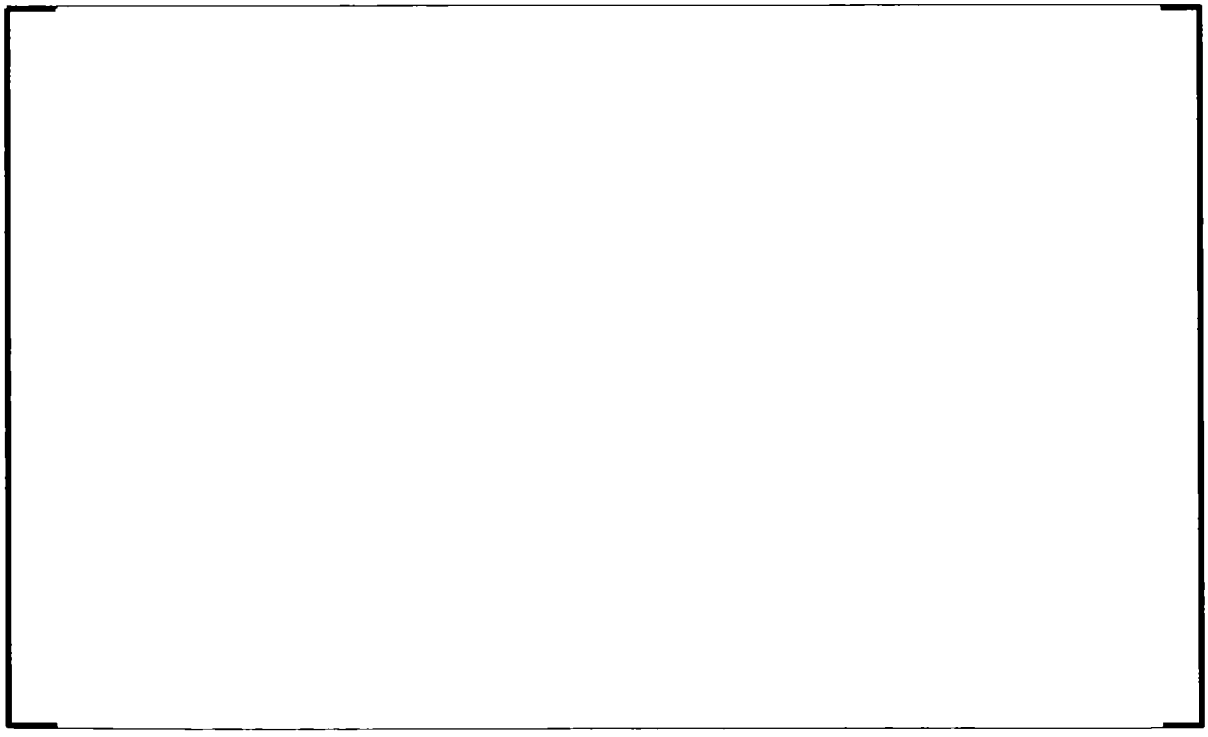

a,c

Figure 3-24 Test Section Bottom View Showing BN Flow Holes with Respect to Grid Straps

a,c

Figure 3-25 Cross-Sectional View of Test Column

a,c

Figure 3-26 8 x 8 Central Region P-Grid Cut-Out

3.5.4 AREVA Core Inlet Central FA Region (T179 through T212)

Similar to the test geometry described in Section 3.5.3, a central section of a prototypic AREVA lower end fitting was utilized in tests T179 through T212. The AREVA lower end fitting is essentially a screen that serves the same purpose of the Westinghouse BN/P-grid combination in that it is intended to provide structural integrity for the FA and is designed to capture debris under normal operating conditions. Above the lower end fitting was the same 8 x 8 rod bundle used for the Westinghouse core inlet geometry tests. The rod bundle contained a central region of a prototypic HMP grid properly distanced from the lower end fitting. The rod bundle also contained a Westinghouse RFA grid at the top of the bundle to provide structural support and to keep the rods aligned.

3.5.5 Alternate Flow Path

After reviewing the hole geometry and flow conditions expected in the AFPs following a LOCA, it was determined that debris blockage of AFPs is highly unlikely. This is because individual AFP holes are large compared to those at the sump strainer or core inlet. Furthermore, velocity through the holes would be relatively high since the combined flow area through the AFP flow holes is very small compared to the total core inlet flow area. Due to the relatively high velocity and large AFP hole size, debris entrainment through the AFP holes is expected, as opposed to blockage.

Some fraction of debris that enters the AFP would be expected to collect within regions where it would not impede flow through the flow passages. For example, the open flow area through a former plate contained in the BB region of a PWR is small compared to the flow area above and below the former plate. The holes in the former plates are spaced far apart and there is a large region of horizontal former plate expected to collect debris either due to settling or separation from the main flow stream. However, as debris accumulates close to the holes, the flow velocity will re-entrain the debris and carry it to the next former elevation within the BB.

To substantiate this, the subscale test facility was used to demonstrate that the flow holes in the AFPs being credited will not become blocked with debris following a LOCA. The testing was accomplished by utilizing inserts that fit into the subscale flow column, with hole dimensions representative of those in the AFPs. Since multiple types of AFPs are credited, depending on specific plant design, and since the size of holes in the AFPs vary across the PWR fleet, two hole sizes were tested over a broad range of flow conditions and debris concentrations.

The AFP test plate consisted of a [ ]^{a,c} thick plate with a single hole in the center of the plate. The plate was installed in the test column in a similar manner to the single-grid insert described in Section 3.5.1. Both [ ]^{a,c} hole diameters were tested with no chamfers. The holes were located in the center of the test column.

3.6 FILTRATION

Downstream of the 1 inch test column outlet, a single bag filter housing and filter insert were placed in-line for capturing all debris that penetrated the test geometry. Due to the requirement to maintain reasonable pressures in the acrylic test column, and considering the small particulate debris filtration requirements, a #2 bag filter and housing were selected. Based on the requirement that the filtration

system should efficiently capture debris with size distributions at or below 10 μm, an Eaton TOPLINE™ filter housing fitted with ACCUGAF™ bag filters was selected. The TOPLINE housing is assembled from cast 304 stainless steel components, which results in a smooth internal surface with no weld seems. The entrance design to the housing essentially eliminates debris trapping locations and the bag seal prevents debris bypass.

All tests used Eaton ACCUGAF polypropylene bag filters. Specifications for the selected bag types are provided in Table 3-8. Bag selection for individual tests was based on injected particle size distribution.

Table 3-8 ACCUGAF Bag Filter Specifications

	Particle Size at Common Removal Efficiencies (μm)				
Filter Model	>60%	>90%	>95%	>99%	>99.9%
AGF-51	0.2	0.6	0.8	1.5	5
AGF-55	1	2	3	5	15

Commercially-available #2 bag filter housings with guaranteed 1μm particulate capture come standard with a 2 inch diameter inlet pipe. As a result, it was necessary to provide additional flow upstream of the bag filter housing such that debris could not settle within the piping entering the housing at the lowest tested flow rates. This was accomplished without generating additional debris capture locations by combining a small flow rate from Pump 3, as shown in Figure 3-1, upstream of the bag filter housing with the primary loop flow. The flow was combined in an annular passage with the primary flow entering on the inner portion of the piping. This prevented the velocity in the bag filter housing inlet from dropping below the settling velocity for entrained debris.

Prior to each experiment, each filter bag was labeled and weighed. Following each experiment, the filter bag was removed from the housing and the wet weight was measured. The filter bags were then placed in a dryer for a period of time until all liquid was evaporated from the bag. At that time the bags were then allowed to stabilize at room conditions and then weighed again. Using the difference in wet weight versus dry weight, and the known concentration of boric acid and buffering agent in the test fluid, the total mass of debris captured in the bag could be calculated. Mass balances, comparing the injected debris mass to the debris mass based on the bag filter weight, showed good agreement. However, due to uncertainty in the test fluid chemical concentrations[4] and dripping of fluid from the bags during drying that was not accounted for, the bag filter mass balance demonstrated a typical uncertainty of approximately 10%. The mass balance discrepancy was calculated for each experiment and varied depending on the debris mass. For experiments with a large debris mass, the mass balance error was much less than 10%.

TOPLINE is a trademark or registered trademark of Eaton Filtration, LLC. Other names may be trademarks of their respective owners.

ACCUGAF is a trademark or registered trademark of Eaton Filtration, LLC. Other names may be trademarks of their respective owners.

[4] Variability in the chemical concentration was due to some evaporation of the test fluid over the course of several days of testing with the same fluid and due to pH adjustments that were made intermittently.

3.7 WATER CHEMISTRY

All testing was conducted starting with de-ionized (DI) water. The main test loop mixing tank was filled with 250 gallons of DI water before filling any other piping segments or the test column. Therefore, the total water inventory in the system was 250 gallons. At standard conditions, this corresponds to a total mass of 944.4 kg of DI water.

The boric acid (H_3BO_3) solution buffered with sodium hydroxide (NaOH) was prepared by adding H_3BO_3 and NaOH to the DI water. The target boron concentration for all testing was 2700 ppm, consistent with industry reported average (Reference 3-3). Two target pH values of 7.0 and 9.0 were set based on the NaOH concentration. In addition, to investigate the effect of different buffer types on the debris bed head loss, tests were also performed at pH of 7.0 using trisodium phosphate (TSP) and sodium tetraborate (NaTB). Bench-top experiments were performed prior to testing to estimate the mass of buffer required for a given pH. During the testing, samples of the water were drawn periodically for pH measurement.

3.8 INSPECTION AND CLEANUP

Back flushing the test loop after each test aided in the loop cleanup process and was also used to characterize debris trapped on the capture geometry. After completion of each experiment, the inlet and outlet of the test column were realigned as shown in Figure 3-27. Pumped flow was initiated and the back flow was directed through a second bag filter housing. During this phase, pulsed air injections were performed, injecting compressed air just below the test geometry, through dedicated taps located on the wall of the test column to aid in breaking up the debris bed.

After back flushing, the upper flange of the test column was disconnected and a pressure washer wand was inserted through the flange into the test column. The pressure washer was used to remove any debris remaining trapped on the test geometry after back flushing. After pressure washing was completed, the configuration was restored and the column back flushed again to force debris dislodged by the pressure washer to the bag filter housing.

If debris was still visible on the test geometry, the geometry was removed from the column and cleaned. Debris removed from the test geometry during this process was collected and filtered using the same bag filter used for back flushing.

Particular attention was made to cleaning and inspection of the DIS. After each test was completed, the content of debris in the DIS tanks was calculated to be lower than 0.1% of the content at the beginning of the test. Such content is negligible in terms of impact on the test results, since it is of the same order of the precision achieved when debris is weighted for addition in the HCT.

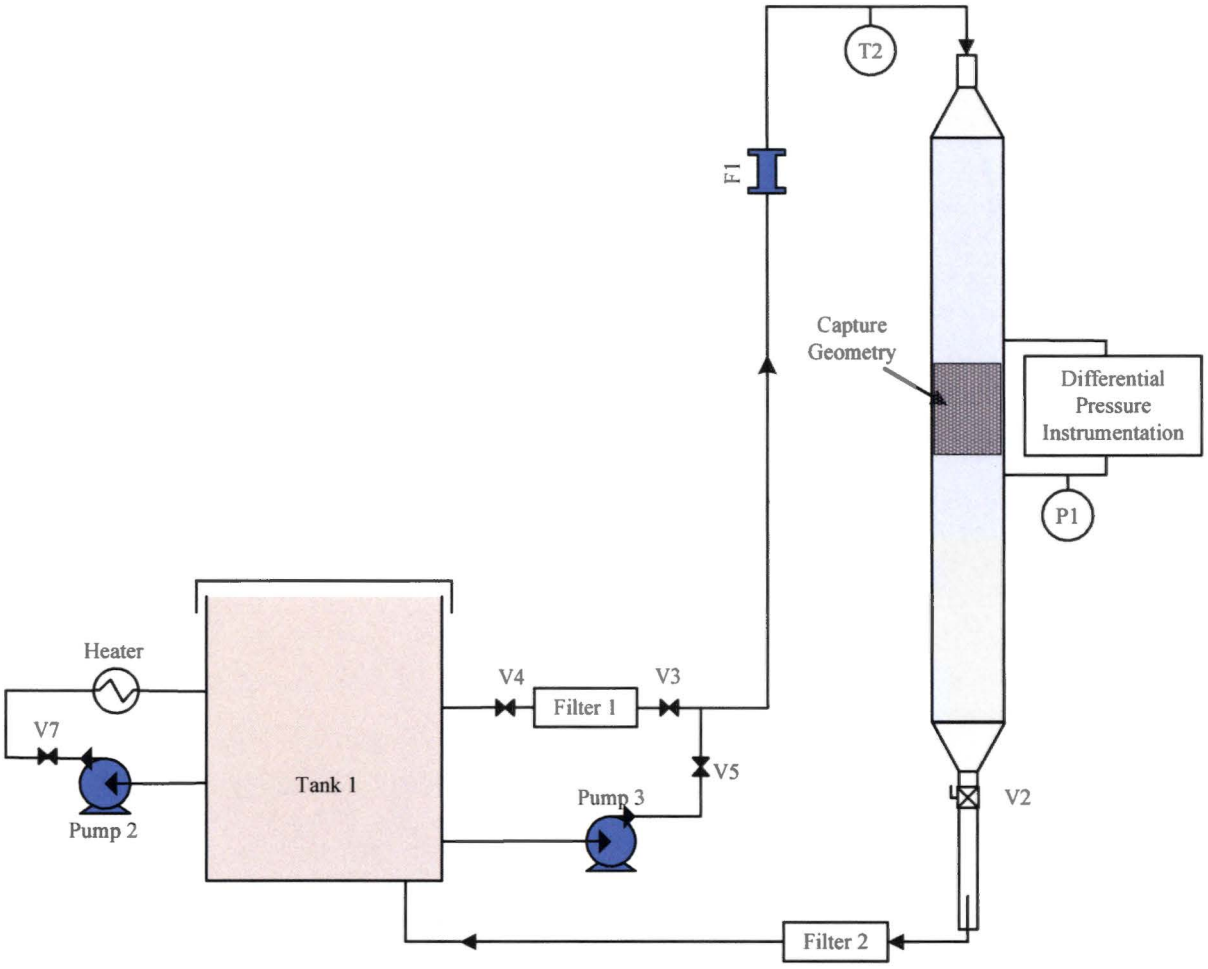

Figure 3-27 Test Loop Flow Diagram for Back-Flushing

3.9 DEBRIS CONSTITUENTS

3.9.1 Fibrous Debris

Although Section 2.2.2 implies that fiber length distribution is not an important factor for head loss, it may be an important factor in the fiber penetration through the fuel geometry as described in Section 2.2.3.

References 3-4 and 3-5 examined sump strainer bypass for a range of conditions applicable to the operating PWR fleet including varied geometry, face velocity, chemistry and agitation. An initial study was performed to compare size distributions of four different types of fibrous debris when prepared utilizing the Nuclear Energy Institute (NEI) pressure washing method (Reference 3-6). The study concluded that fibrous debris length distributions, when prepared using the pressure washing procedure,

were similar for NUKON™ base wool, mineral wool and ceramic fiber types, but a longer length distribution was measured for Temp-Mat material. On this basis, NUKON and Temp-Mat were selected for the Reference 3-4 bypass testing. Results from the Reference 3-4 testing were utilized in Reference 3-5 to develop a model for assessing PWR fleet-wide fiber length distributions downstream of sump strainers.

One of the major complications in investigating the impact of fiber length distribution on head loss was establishing a method for processing NUKON base wool fiber to length distributions in a controlled manner that were representative of the Reference 3-5 results. To approach this problem, it was recognized that a detailed evaluation of the measurement system used to determine fiber length distribution was necessary.

3.9.1.1 Fiber Length Distribution Measurement System Evaluation

The fiber length measurement system consists of all steps and procedures necessary from the initial collection of fiber from a uniformly mixed vessel, sample dilution, filtration and measurement of lengths using a light microscope. Evaluation of the fiber length distribution measurement system included the following:

- Comparison of measured length distribution as a function of measurement count
- Comparison of measured length distribution from three samples drawn from the same prepared batch of fibers to quantify uncertainties associated with sampling.
- Comparison of measured length distribution from three measurements under the light microscope using a single sample to characterize uncertainties associated with length measurement.
- Comparison of measured length distribution from three samples drawn from different batches prepared using the same procedure to characterize batch-to-batch variation.

In total, approximately 20,000 fiber lengths were manually measured as part of the effort.

All results presented here are based on NUKON base wool procured from Performance Contracting Incorporated (PCI) in the form of heat-treated blankets that had been shredded using PCI procedures DPP-01 and DPP-02 (References 3-7 and 3-8). In the heat-treating process PCI takes 24 inch x 48 inch sheets of NUKON base wool and places them on racks (6 feet x 12 feet), which are then pressed against a vertical hot plate. PCI heat treats the NUKON base wool at 572°F ± 100°F for a period of 6 to 8 hours. This process is consistent with that defined in the NEI guidance documented in Reference 3-6. Shredding is then performed to process the insulation blanket into smaller clumps of fibrous insulation.

After receipt of debris processed using the dry shredding method, additional dispersion of fiber clumps was necessary. This was performed by blending the fiber with water using a Waring 4 liter laboratory

---

NUKON is a trademark or registered trademark of Performance Contracting Inc. Other names may be trademarks of their respective owners.

blender and a blender setting of 18,000 RPM. The resultant fiber suspension was dispersed into fines with no clumps visibly present, consistent with the expected form of fiber downstream of a typical sump strainer (Reference 3-5).

Immediately after blending, the contents of the blender were placed into a 20 gallon actively mixed vessel with liquid height equal to the diameter of the vessel. A mixer was placed in the vessel with the mixer impeller located in the center of the vessel, one-third of the water height from the bottom of the vessel. The impeller shaft was tilted 15° off vertical for optimal mixing. Samples were then drawn from the mixed vessel while the vessel was being actively stirred by the impeller.

Results of the sample count study concluded that a minimum of [ ]^{a,c} individual fiber length measurements were required to characterize the distribution. This conclusion was reached by measuring [ ]^{a,c}
Measuring a total of [ ]^{a,c} individual fibers resulted in a measurement uncertainty significantly less than the measurement uncertainty associated with other aspects of the measurement system. This was consistent with the Reference 3-5 conclusions, which were reached independently. Figure 3-28 through Figure 3-30 show the results of this study.

[a,c

Figure 3-28 Length Distributions Plotted in Sets of 100 Measurements

a,c

Figure 3-29 Length Distributions Plotted in Sets of 300 Measurements

a,c

Figure 3-30 Length Distributions Plotted in Sets of 600 Measurements

Comparison of three different samples (S1, S2 and S3) drawn from the same batch L1P1 (Lot 1, Preparation 1) and two separate measurements (M1 and M2) of each sample using the light microscope is shown in Figure 3-31. Over [ ]^{a,c} length measurements were used for each distribution shown in Figure 3-31such that measurement count should not impact the measurement uncertainty.

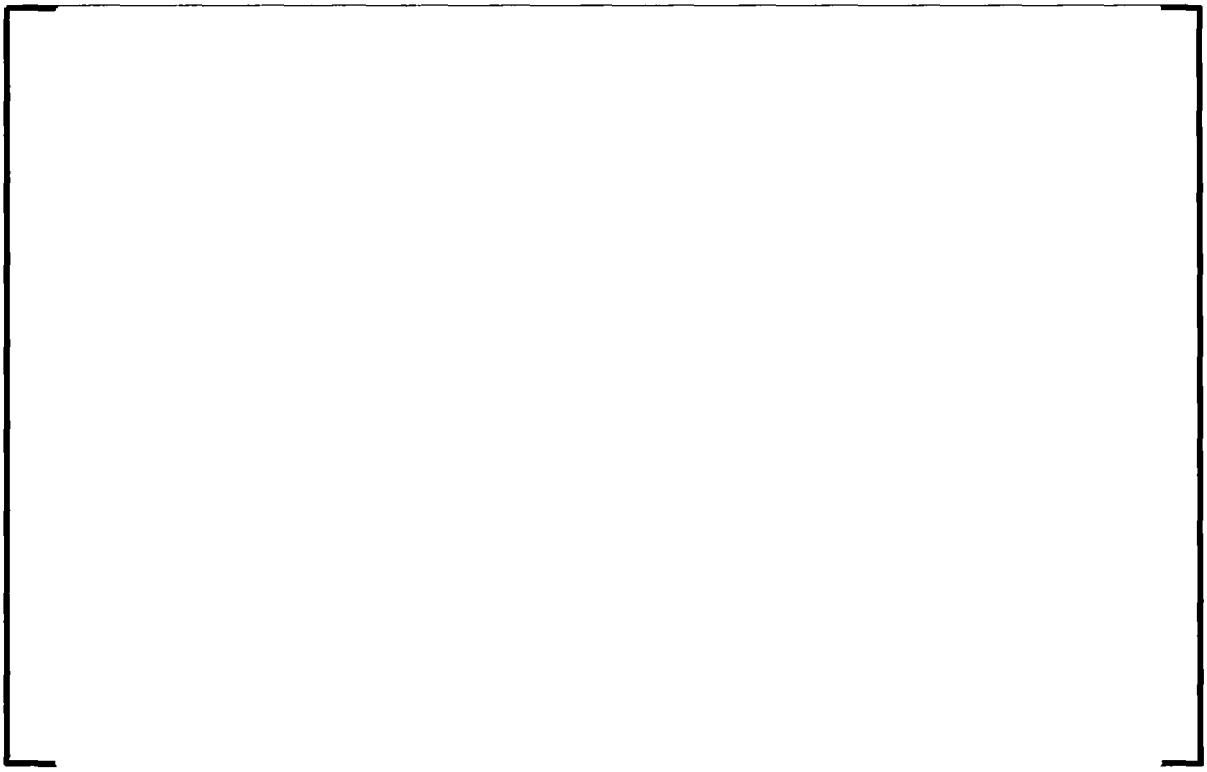

a,c

Figure 3-31 Length Distribution from Three Samples and Two Measurements of Each Sample

Since the uncertainty associated with measurement count is small in comparison, the spread of data shown in Figure 3-31 can be used to approximate the uncertainty in fiber length measurement. Based on Figure 3-31, uncertainty from the sampling process is greater for smaller fibers than long fibers. For fibers at the 90th percentile of each length distribution, the variation did not exceed [ ]^{a,c} For fibers at the 50th percentile of each length distribution, the variation did not exceed [ ]^{a,c} For fibers at the 10th percentile of each length distribution the variation did not exceed [ ]^{a,c}

After investigation of the required sample count and uncertainties associated with sampling and length measurement using the light microscope, an examination of batch to batch variation was conducted. This included comparison of results from three different batch preparation (L2P1, L2P2 and L2P3) using the blender. Results are shown graphically in Figure 3-32. The results are shown along with fleet wide minimum, maximum and mean predicted length distributions based on the Reference 3-5 (Alden Laboratories) model.

Upon review of Figure 3-32, batch-to-batch variation was most significant near the 50th percentile. However, the variation was essentially within the uncertainty due to sampling and length measurement. Nonetheless, since variations in blender blade wear and other factors that can influence batch preparation

were not considered, it was determined that portion of the tests performed as part of this program would include test-specific length distribution analysis.

The fiber blending procedure [

]^{a,c} However, it is noted that the length distribution measurement uncertainty at the 10th percentile was [ ]^{a,c} as described above. Therefore, [

]^{a,c}

a,c

Figure 3-32 Summary of Batch Preparation Results Compared to Fleet Wide Variation

3.9.1.2 Fiber Diameter Distribution

Fiber diameter was measured using a scanning electron microscope (SEM). A total of 30 images similar to Figure 3-33 were captured to develop the basis for the fiber diameter distribution. Results of the fiber diameter measurements are shown in Figure 3-34. The results are based on the measurement of [ ]^{a,c} individual fibers. The measured median diameter was [ ]^{a,c} The 10th and 90th percentiles of the distribution were [ ]^{a,c} respectively.

a,c

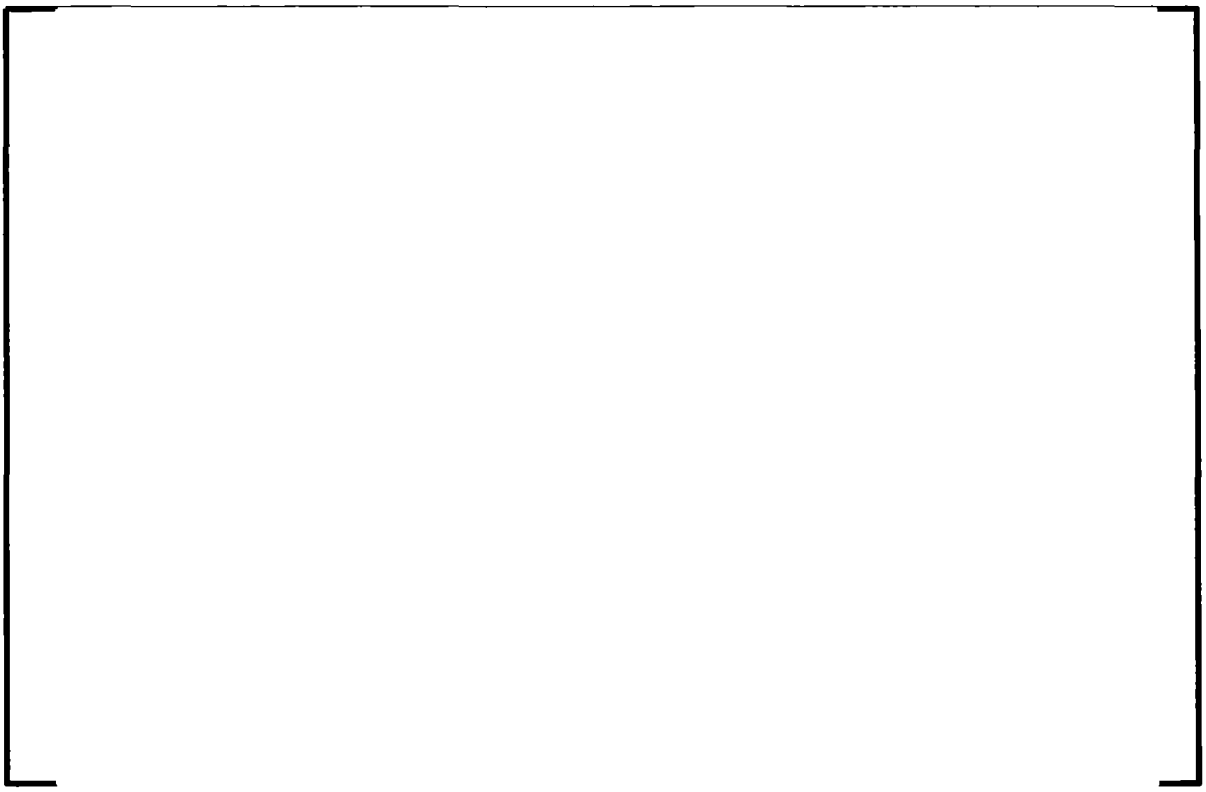

Figure 3-33 SEM Image of NUKON Fiberglass

a,c

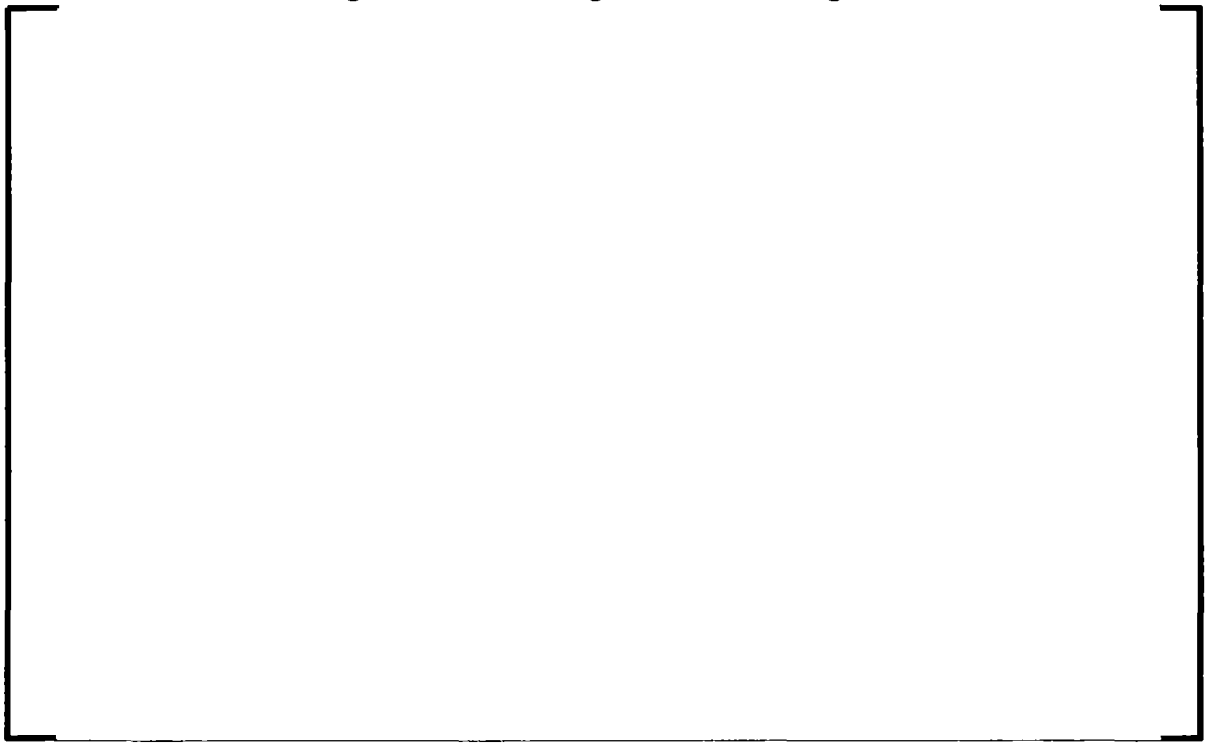

Figure 3-34 NUKON Fiberglass Diameter Distribution

3.9.2 Particulate Debris

Selection of particulate for this program was based on a review of the particle capture mechanisms documented in Section 2.2.4. Primarily, the effects of straining and interception were considered to have the most significant effect. Based on Reference 3-9, the minimum particulate size expected in containment, in significant quantities, is 10 μm. The maximum size particle that could reach the core during recirculation may be several orders of magnitude greater in diameter and is dependent on the settling characteristics of the particle and the particular flow conditions present. However, review of Figure 2-1, considering a nominal fiber diameter of [ ]^{a,c} based on Figure 3-34 and an upper bound porosity of [ ]^{a,c} which is a reasonable upper bound based on experimental observations at low flows with no particulate present, indicates that the effects of straining should be maximized by examining a range of conditions with an upper bound nominal diameter of [ ]^{a,c}

Silicon Carbide particulate debris was selected for this study since it is commercially available in graded sizes. Particulate procured from U.K. Abrasives included nominal size ranges from approximately [ ]^{a,c} as presented in Table 3-9. Values shown in Table 3-9 are based on volume weighted measurements of particle size.

Table 3-9 UK Abrasives Silicon Carbide Volume Based Size Distribution

ID	UK Abrasives ID	Mean Size (μm)	>3%	>25%	>50%	>75%	>94%
A							
B							
C							
J							
I							
E							
H							
F							

a,c

As shown in Table 3-9, the process used to generate a graded size distribution of silicon carbide results in fairly narrow size distributions. However, the size distribution of particulate reaching the core during a post-LOCA event would include a wider range of particulate diameter. Reference 3-10 provides a plant-

specific example of a particulate size distribution that could reach the core considering the wide range of particulate sources that exist in a PWR containment.

To examine conditions that are more representative of PWR containments, two mixed distribution batches of silicon carbide were prepared (D and 1). These batches were prepared using a combination of particulate batches shown in Table 3-9. Table 3-10 and Table 3-11 provide size distribution information for the mixed batches that were prepared.

The Distribution D particulate was simply an equal part mix of the A, B and C particulates. The volume weighted mean particulate diameter of distribution D can be shown to be 11.24 μm based on Table 3-10. Results using distribution D are compared to distributions A, B and C in Section 5.2.6.

The Distribution 1 particulate mix was defined based on test results documented in Section 5.2.6. Evidence was provided that the [ ]^{a,c} particulate resulted in the most restrictive debris bed since these particle sizes maximized the effects of particle straining and packing density. Distribution 1 is a broad size distribution that is weighted more heavily with particulate diameters of [ ]^{a,c} Furthermore, the Distribution 1 particulate also included a tail of smaller particulate in an attempt to further maximize particle packing.

Table 3-10 Mixed Particulate Distribution "D"

Particle ID	Particle Size (μm)	Particle Mass (%)

a,c

Table 3-11 Mixed Particulate Distribution "1"

Particle ID	Particle Size (μm)	Particle Mass (%)

a,c

3.10 INSTRUMENTATION

Table 3-12 provides a list of the instrumentation used for this test program. The location of flow and temperature instrumentation did not change throughout the course of testing. The location of these instruments with respect to the main test facility components is shown in Figure 3-1. The HCT and LCT level sensors monitored tank level continuously throughout each experiment and provided feedback for tank level control.

Table 3-12 Instrumentation Summary

ID #	Description	Type	Range	Nominal Accuracy[1]
F1	Primary flow Rate	Magnetic flow meter	0 - 20 gpm	± 0.25% rate
P1	Upstream pressure	Pressure transducer	0 - 36 psid	±0.1 psi
DP1H	High-range differential pressure	Pressure transducer	0 - 20 psid	±0.1 psi
DP2H	High-range differential pressure	Pressure transducer	0 - 20 psid	±0.1 psi
DP1L	Low-range differential pressure	Pressure transducer	0 - 2 psid	±0.01 psi
Level 1	HCT level	Ultrasonic	0 – 22 in	±0.125 in
Level 2	LCT level	Ultrasonic	0 – 13 in	±0.125 in
T1	DIS inlet temperature	T-type thermocouple	32 - 201°F	± 1.8°F
T2	Downstream temperature	T-type thermocouple	32 - 201°F	± 1.8°F

Note 1: These values account for instrument measurement accuracy and analog to digital converter accuracy.

The location of differential pressure instrumentation was modified throughout the course of the test program. The single-grid (T001 through T139) and AFP experiments utilized DP1H and DP1L to monitor pressure drop across the test component. The relative location of pressure taps with respect to the capture geometry is shown in Figure 3-10. DP2H was not used for the single-grid experiments. Figure 3-35 shows the installation location for DP1H, DP1L and DP2H for the core inlet geometry experiments.

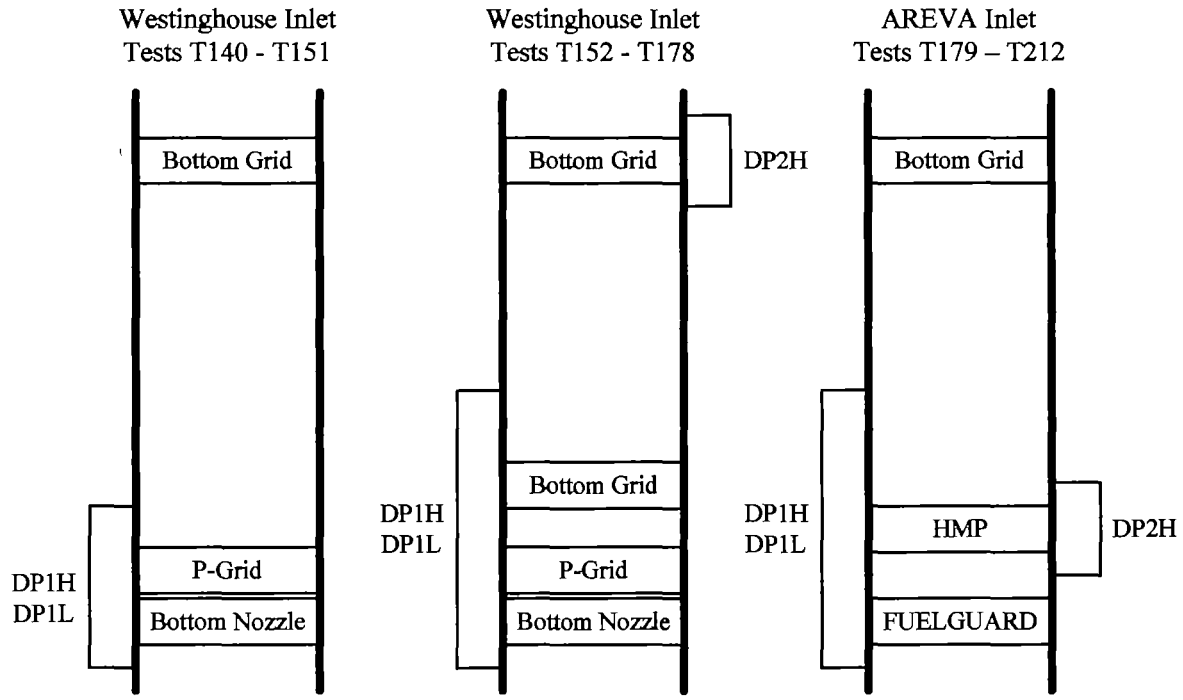

Figure 3-35 Location of Differential Pressure Instrumentation for Tests T140 through T212

3.11 REFERENCES

3-1 NUREG/CR-6917, "Experimental Measurements of Pressure Drop across Sump Screen Debris Beds in Support of Generic Safety Issue 191," Pacific Northwest National Laboratory, 2007.

3-2 WCAP-16793-NP-A, Revision 2, "Evaluation of Long-Term Cooling Considering Particulate, Fibrous and Chemical Debris in the Recirculating Fluid," July 2013.

3-3 LTR-PEP-13-35, Revision 0, "Plant Responses to OG-12-462, Utility Survey Request for GSI-191 Project Inputs (PA-SEE-1090 and PA-SEE-1072)," March 2013.

3-4 OG-13-218, Enclosure 2, "AREVA Document 66-9199574-000, Fiber Bypass Size Characterization Test Report," May 2013.

3-5 OG-13-218, Enclosure 1, "AREVA Document 32-9201054-000, PWR Strainer Fiber Bypass Length Distribution," May 2013.

3-6 Nuclear Energy Institute Generic Procedure, Revision 1, "ZOI Fibrous Debris Preparation: Processing, Storage and Handling," January 2012.

3-7 Performance Contracting Inc. Procedure, DPP-01, Revision 0, "Debris Preparation Procedure for Production of Heat Treated NUKON Base Wool," February 2012.

3-8 Performance Contracting Inc. Procedure, DPP-02, Revision 0, "Debris Preparation Procedure for Producing NUKON Base Wool Fines Debris," February 2012.

3-9 NEI-04-07, Volume 1, Revision 0, "Pressurized Water Reactor Sump Performance Evaluation Methodology," Nuclear Energy Institute, December 2004.

3-10 ALION-REP-AEP-4462-13, Revision 9, "Bypass Debris Characterization Report for D.C. Cook Nuclear Plant Step #2," May 2008.

4 TEST MATRIX

The core entrance geometry head loss test matrix consisted of 212 individual experiments. Of the 212 experiments, there were a total of 88 separate sets of experimental conditions, which are referred to as test series. Only a portion of the 212 experiments are referenced in this report. Experimental results not provided in this report were excluded based on the following criteria:

- Test operator error or test equipment failure
- Results were consistent with all observed trends, but were not necessary to support arguments documented in this report

Under no circumstances were results excluded due to unknown or inexplicable behavior.

All testing was conducted at a fluid temperature of 130°F. In general, the target temperature was maintained within ±5°F at the capture geometry. The following list summarizes the test conditions which were varied as listed in Table 4-1 for each test series:

- Flow control
  - The pressure drop versus flow profile used for the test series to simulate actual core inlet response to formation of a debris bed. The pressure drop versus flow profiles are provided in Section 3.3.
- pH
  - The test fluid pH target value for each experiment. A pH of 7 or 9 was targeted depending on the test series. DI water was prepared with chemical additions to control test pH as described in Section 3.7.
- Buffer
  - The type of buffer used to control pH for each experiment. Depending on the test series, buffer type was either NaOH, TSP or NaTB as descried in Section 3.7.
- Capture geometry
  - The debris capture geometry for each test series. Section 3.5 provides geometric information for each geometry tested. Table 3-2 in Section 3.5 provides a concise summary of the capture geometries tested.
- Fiber load
  - The total mass of fibrous debris injected for each experiment. This value is the actual fiber mass injected during the experiment. Since the test geometry represents approximately one-quarter of a FA, these values are scaled with the appropriate geometric

scaling factors based on information provided in Section 3.5. Section 6.5 provides an example of this scaling calculation for the core inlet test geometry.

- Particle-to-fiber (p:f) ratio
  - The ratio of particle mass to fiber mass injected.
- Particulate size
  - The particulate size distribution for each experiment as documented in Section 3.9.2.
- Injection time
  - The nominal time period over which the majority of debris was injected. This parameter can be used to estimate the average debris concentration transported to the capture geometry for each experimental condition. As described in Section 3.2.3 the total test time does not correspond to the injection time. The total test time continued until 99.9% of debris contained in the DIS was transported to the capture geometry.
- Debris delivery profile
  - The debris delivery profile used to calculate the mass of debris injected at any point during the experiment. The debris delivery profile was calculated for each experimental condition as described in Section 3.2.3. Changes to the DIS configuration, as described in Section 3.2, and changes in the total mass of injected fiber resulted in different debris delivery profiles.

Depending on the test series (1 through 88), 1 to 7 experiments were completed to understand the test-to-test variability over a range of conditions. Test Series 5 and 10 essentially represent the same test condition, only differing by the debris delivery profile. Test Series 5 and 10 represent a baseline condition in which the majority of the single-grid experiments were compared. Noting that the listed test IDs are in chronological order, tests completed as part of Test Series 10 were spaced out over the course of several months to understand the impacts of small changes to the test system that occurred over the course of time.

Table 4-1 Primary Test Matrix

Test Series	Flow Control	pH	Buffer	Capture Geometry	Fiber Load (g)	p:f Ratio	Particulate Size	Injection Time (min)	Debris Delivery Profile	Test IDs
1	Low	7	NaOH	RFA	25	1:1	A	30	1	T001 T002 T003 T004 T005
2	Low	7	NaOH	RFA	25	10:1	A	30	1	T016 T017 T018 T021
3	Mid	7	NaOH	RFA	25	1:1	A	30	1	T006 T007 T008 T009 T022
5	Mid	7	NaOH	RFA	25	10:1	A	30	1	T015 T019 T020
6	High	7	NaOH	RFA	25	10:1	A	30	1	T023 T024 T025 T026
8	Mid	7	NaOH	RFA	12.5	10:1	A	30	3	T029 T030 T031 T032 T033
9	Mid	7	NaOH	RFA	25	0:1	A	30	1	T034 T035 T036
10	Mid	7	NaOH	RFA	25	10:1	A	30	4	T037 T046 T047 T048
11	High	7	NaOH	RFA	25	10:1	A	30	4	T038 T039
12	Mid	7	NaOH	HMP	25	10:1	A	30	4	T040 T042 T043 T044
13	Mid	7	NaOH	RFA	25	10:1	A	300	5	T050 T051 T052 T053 T054
14	Mid	7	NaOH	RFA	25	15:1	A	30	4	T055 T056 T057 T058 T059 T060 T061
15	Mid	7	NaOH	RFA	12.5	30:1	A	30	6	T062 T063 T064 T065
16	Mid	7	NaOH	RFA	25	10:1	B	30	4	T066 T067 T068 T069
17	Mid	7	NaOH	RFA	25	10:1	C	30	4	T070 T071 T097 T110
18	Mid	7	NaOH	RFA	25	10:1	D	30	4	T072 T073 T074 T075
19	Mid	9	NaOH	RFA	25	10:1	A	30	4	T076 T077 T078 T079
20	Mid	7	TSP	RFA	25	10:1	A	30	4	T080 T081 T082 T083
21	Mid	7	NATB	RFA	25	10:1	A	30	4	T084 T085 T086 T087
22	Mid	7	NaOH	UFA	25	10:1	A	30	4	T088 T089 T090 T091
23	Mid	7	NaOH	OFA	25	10:1	A	30	4	T092 T093 T095
24	Mid	7	NaOH	RFA	12.5	10:1	E	30	6	T098 T102
25	Mid	7	NaOH	RFA	12.5	10:1	F	30	6	T099 T103
27	Mid	7	NaOH	RFA	12.5	10:1	H	30	6	T105 T106
28	Mid	7	NaOH	RFA	12.5	10:1	I	30	6	T107 T108
29	Mid	7	NaOH	RFA	12.5	10:1	J	30	6	T109 T111 T112

Table 4-1 Primary Test Matrix

Test Series	Flow Control	pH	Buffer	Capture Geometry	Fiber Load (g)	p:f Ratio	Particulate Size	Injection Time (min)	Debris Delivery Profile	Test IDs
30	Mid	7	NaOH	RFA	12.5	10:1	Dist 1	30	6	T113
33	Low	7	NaOH	RFA	12.5	10:1	Dist 1	30	6	T117
34	Mid2	7	NaOH	RFA	12.5	10:1	Dist 1	30	6	T118 T119 T120
35	Mid2	7	NaOH	RFA	12.5	1:1	Dist 1	30	6	T121 T124
36	Mid2	7	NaOH	RFA	12.5	50:1	Dist 1	30	6	T122 T123 T135
37	Mid2	7	NaOH	RFA	12.5	15:1	Dist 1	30	6	T130 T132
38	Mid2	7	NaOH	RFA	12.5	12:1	Dist 1	30	6	T128 T129
39	Mid2	7	NaOH	RFA	12.5	25:1	Dist 1	30	6	T131 T133
40	Mid2	7	NaOH	RFA	12.5	30:1	Dist 1	30	6	T134
41	Mid2	7	NaOH	RFA	12.5	40:1	Dist 1	30	6	T136
42	Mid2	7	NaOH	RFA	12.5	45:1	Dist 1	30	6	T137 T138 T139
43	Mid	7	NaOH	RFA BN/P-1	25	10:1	A	30	4	T140 T143 T146 T149
44	Mid2	7	NaOH	RFA BN/P-1	12.5	10:1	Dist 1	30	6	T141 T144 T147 T151
45	Mid2	7	NaOH	RFA BN/P-1	12.5	50:1	Dist 1	30	6	T142 T145 T148
46	Mid2	7	NaOH	RFA BN/P-1	12.5	30:1	Dist 1	30	6	T150
47	Final-Mid	7	NaOH	RFA BN/P-2	12.5	10:1	Dist 1	30	6	T152 T161 T163
48	Final-Mid	7	NaOH	RFA BN/P-2	12.5	20:1	Dist 1	30	6	T153
49	Final-Mid	7	NaOH	RFA BN/P-2	12.5	30:1	Dist 1	30	6	T154
50	Final-Low	7	NaOH	RFA BN/P-2	12.5	10:1	Dist 1	30	6	T155
51	Final-Low	7	NaOH	RFA BN/P-2	12.5	20:1	Dist 1	30	6	T156 T162
52	Final-Low	7	NaOH	RFA BN/P-2	12.5	30:1	Dist 1	30	6	T157
53	Final-High	7	NaOH	RFA BN/P-2	12.5	10:1	Dist 1	30	6	T158
54	Final-High	7	NaOH	RFA BN/P-2	12.5	20:1	Dist 1	30	6	T159
55	Final-High	7	NaOH	RFA BN/P-2	12.5	30:1	Dist 1	30	6	T160
56	Final-Low	7	NaOH	RFA BN/P-2	12.5	15:1	Dist 1	30	6	T164 T166
57	Final-Low	7	NaOH	RFA BN/P-2	12.5	12:1	Dist 1	30	6	T165 T167 T170 T176

Table 4-1 Primary Test Matrix

Test Series	Flow Control	pH	Buffer	Capture Geometry	Fiber Load (g)	p:f Ratio	Particulate Size	Injection Time (min)	Debris Delivery Profile	Test IDs
58	Final-Low	7	NaOH	RFA BN/P-2	12.5	5:1	Dist 1	30	6	T169
59	Final-Low	7	NaOH	RFA BN/P-2	8	12:1	Dist 1	30	7	T173 T174 T175
60	Final-Low	7	NaOH	RFA BN/P-2	15	12:1	Dist 1	30	8	T177
61	Final-Low	7	NaOH	RFA BN/P-2	15	10:1	Dist 1	30	8	T178
62	Final-Low	7	NaOH	FG/HMP	12.5	10:1	Dist 1	30	6	T179
63	Final-Low	7	NaOH	FG/HMP	12.5	15:1	Dist 1	30	6	T180
64	Final-Low	7	NaOH	FG/HMP	12.5	20:1	Dist 1	30	6	T181
65	Final-Mid	7	NaOH	FG/HMP	12.5	10:1	Dist 1	30	6	T182
66	Final-Mid	7	NaOH	FG/HMP	12.5	20:1	Dist 1	30	6	T183 T188
67	Final-Mid	7	NaOH	FG/HMP	12.5	30:1	Dist 1	30	6	T184
68	Final-High	7	NaOH	FG/HMP	12.5	30:1	Dist 1	30	6	T185
69	Final-High	7	NaOH	FG/HMP	12.5	40:1	Dist 1	30	6	T186
70	Final-High	7	NaOH	FG/HMP	12.5	20:1	Dist 1	30	6	T187
71	Final-Mid	7	NaOH	FG/HMP	12.5	40:1	Dist 1	30	6	T189
72	Final-Low	7	NaOH	FG/HMP	12.5	40:1	Dist 1	30	6	T192
74	Final-High	7	NaOH	FG/HMP	12.5	15:1	Dist 1	30	6	T193
75	Final-Mid	7	NaOH	FG/HMP	9	35:1	Dist 1	30	9	T194
76	Final-Low	7	NaOH	FG/HMP	9	40:1	Dist 1	30	9	T195
77	Final-Low	7	NaOH	FG/HMP	9	45:1	Dist 1	30	9	T196
78	Final-Low	7	NaOH	FG/HMP	7	50:1	Dist 1	30	10	T197
79	Final-Low	7	NaOH	FG/HMP	7	55:1	Dist 1	30	10	T198
80	Final-Low	7	NaOH	FG/HMP	7	65:1	Dist 1	30	10	T199
81	Final-Low	7	NaOH	FG/HMP	6	75:1	Dist 1	30	11	T200 T203 210
82	Final-Low	7	NaOH	FG/HMP	5	85:1	Dist 1	30	12	T201
83	Final-Low	7	NaOH	FG/HMP	5	40:1	Dist 1	30	12	T202
84	Final-Low	7	NaOH	FG/HMP	5	75:1	Dist 1	30	12	T204

Table 4-1 Primary Test Matrix

Test Series	Flow Control	pH	Buffer	Capture Geometry	Fiber Load (g)	p:f Ratio	Particulate Size	Injection Time (min)	Debris Delivery Profile	Test IDs
85	Final-Low	7	NaOH	FG/HMP	5	50:1	Dist 1	30	12	T205
86	Final-Low	7	NaOH	FG/HMP	5	60:1	Dist 1	30	12	T206 T211 T212
87	Final-Low	7	NaOH	FG/HMP	5	70:1	Dist 1	30	12	T207
88	Final-Low	7	NaOH	FG/HMP	5	65:1	Dist 1	30	12	T208 T209

Table 4-2 summarizes the test conditions used for the AFP testing. Two hole diameters were tested as shown in Table 4-2 and described in Section 3.5.5. The test fluid was boric acid buffered with NaOH. The boric acid concentration was 2,700 ppm and the pH was approximately 7.2. The fluid temperature was 130°F. Fiber was added in three batches of 12.5 g or three batches of 50 g/FA. The second fiber addition included 12.5 g of silicon carbide particulate with a mean diameter of 10.4 μm. The flow rate started at 0.75 gpm and was increased to 2 gpm and finally 4 gpm during the duration of each test.

Table 4-2 Alternate Flow Path Test Matrix

Test ID	Hole Diameter (in)	Flow Rate (gpm)	Total Fiber Addition (g)
1090-AFP-T002	[ ]	[ ]	[ ]
1090-AFP-T003	[ ]	[ ]	[ ]

a,c

5 TEST RESULTS AND DATA ANALYSIS

To gain an understanding of the test facility operation, Section 5.1 reviews results from an individual experiment in detail and also provides a general discussion of potential experimental error sources. The remaining test data analysis presented in this section essentially follows the order in which testing was conducted. The analysis of test results from the single-grid phenomenological experiments is presented first with conclusions from each of the test series comparisons documented. Following the single-grid comparison studies, results for the Westinghouse and AREVA core inlet geometry experiments are presented in Section 5.3.1 and 5.3.2. Finally, results of the alternate flow path study are documented in Section 5.6.

5.1 OVERVIEW OF TEST RESULTS AND POTENTIAL EXPERIMENTAL BIASES

5.1.1 Example of Typical Test Result

Prior to reviewing the parametric study results, it is useful to review individual measurement results from a single experiment to understand the test operation. For this review, the results from test T176 will be examined. Test T176 used the Westinghouse core inlet geometry described in Section 3.5.3. Test T176 was selected [

]^{a,c} The following list summarizes the test conditions for test T176:

- "Final-Low" pressure drop versus flow profile as defined in Figure 3-8 of Section 3.3
- Boric acid solution with NaOH buffered to a pH of 7
- Total fiber mass of 12.5 grams and 150 grams of Distribution 1 particulate
- Fiber and particle injected over nominal period of 30 minutes, following the debris injection profile number 6 shown in Section 3.2.3.

At the start of the experiment, water was circulated through the entire system, including the HCT and LCT, to assure uniform temperatures throughout. The HCT was then isolated for debris addition. Particles and fibers were added to the HCT and the contents uniformly mixed. To start the experiment, the operator initiated the flow pressure feedback routine to set the desired flow curve. At the same time, the DIS 4-way isolation valve was opened, and debris laden flow was transported to the test column.

For test T176, the second DIS configuration was in place. Configuration 2 utilized an HCT drain-down from [ ]^{a,c} level over the initial portion of the test. Figure 5-1 shows the measured HCT and LCT levels compared to the set-points. As shown, the level control was in good agreement with the set-point, indicating that the debris delivery curves shown in Section 3.2.3 are applicable. At the conclusion of the test, the HCT tank was completely drained as shown in Figure 5-1.

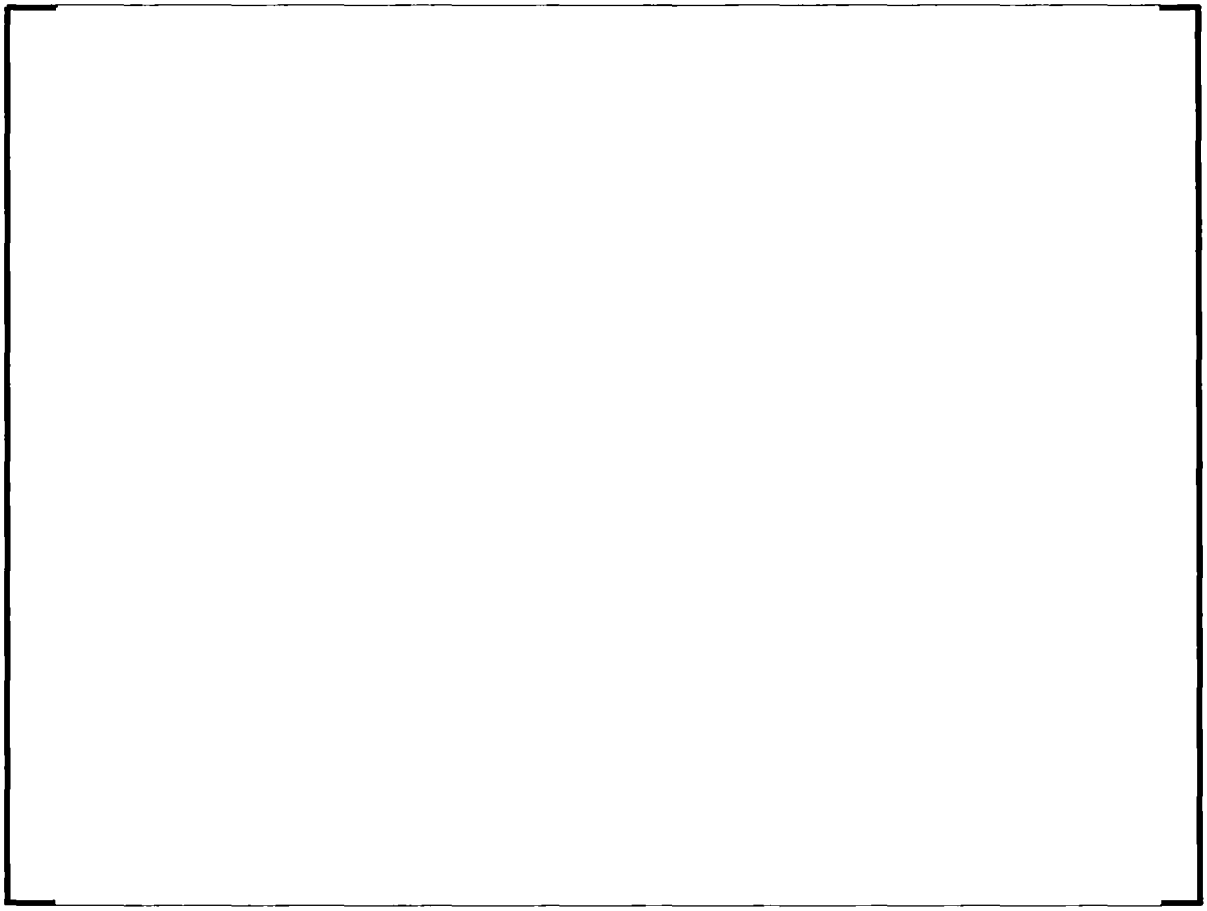

a,c

Figure 5-1 Test T176 Measured DIS Tank Levels Compared to Level Setting

As debris collected on the grids, the pressure drop was monitored across the core inlet geometry and a downstream grid for these experiments as shown in Figure 3-35 of Section 3.10. Figure 5-2 shows the result of these measurements. For tests T176, the pressure drop exceeded 2 psi, at which point the low-range differential pressure transducer was over range. However, measurements from the low-range sensor provided increased accuracy for the low range and also provided independent confirmation of the high-range pressure transducer operation. For test T176, there was no debris bed formed on the downstream grid, and the high-range DP2 did not register a pressure drop.

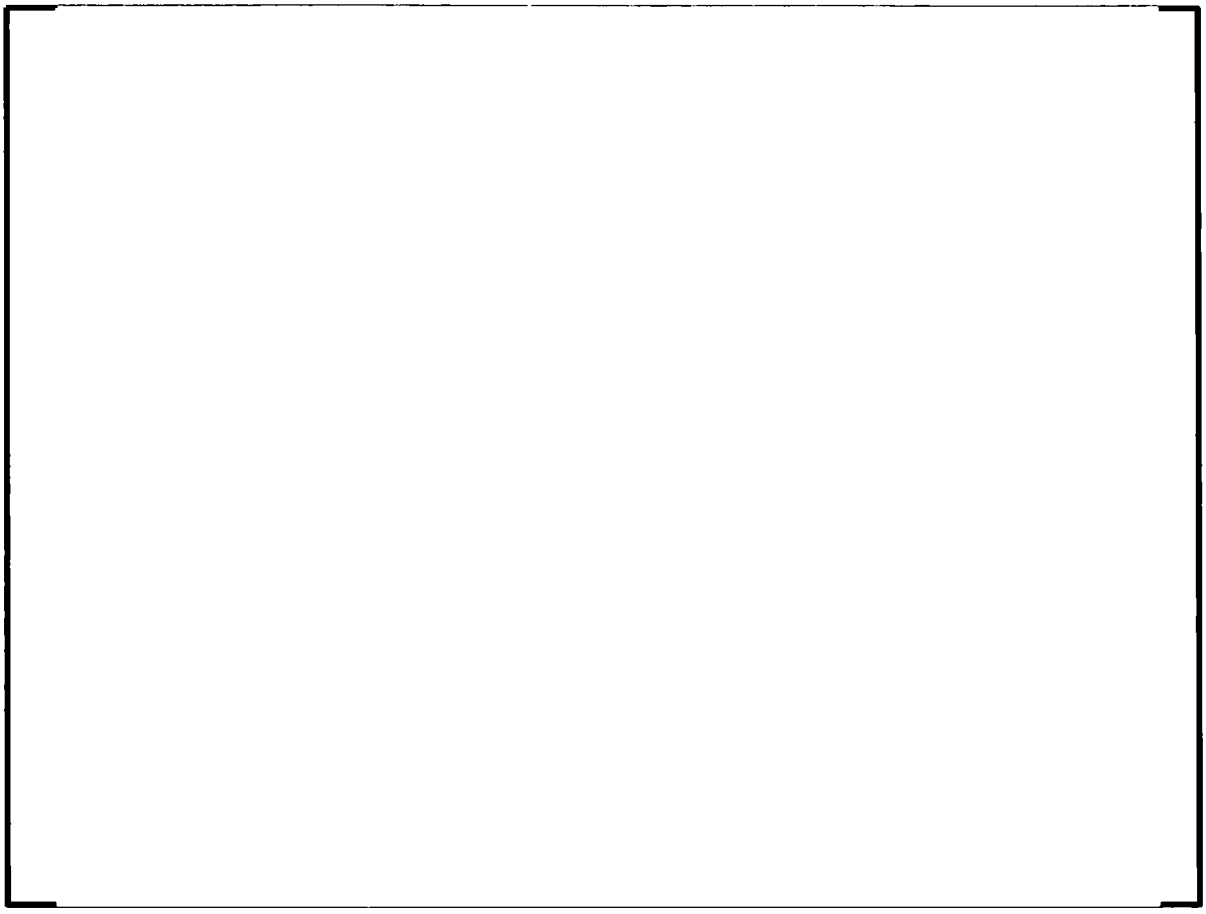

a,c

Figure 5-2 Test T176 Measured Pressure Differentials

Figure 5-3 shows results of the measured gage pressure directly upstream of the grid. The pressure transducer was located at an elevation approximately 1 foot below the capture geometry and measured pressure entering the capture geometry with respect to the ambient pressure. This measurement was used to confirm that the static pressure did not fall below ambient conditions such that non-condensable gas dissolution could occur.

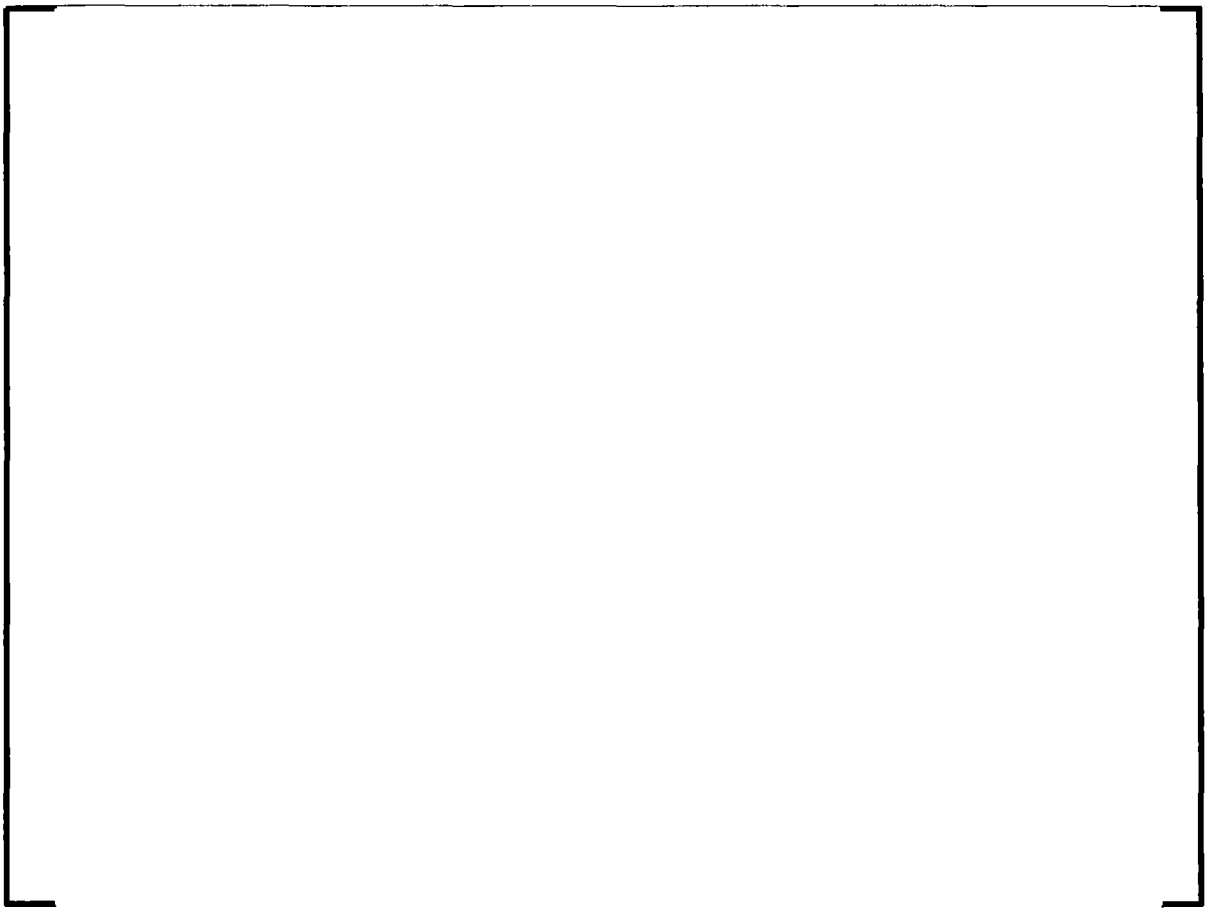

a,c

Figure 5-3 Test T176 Measured Gage Pressure

Figure 5-4 shows results from the DIS inlet and test column outlet thermocouple measurements. At the start of the experiment, the upstream and downstream measurements agree within 2°F. This demonstrates the good insulating characteristics of the thick polycarbonate test column walls. As the HCT begins to release contents into the test system, flow of clean water to the DIS is ceased for a period of time, and the DIS inlet temperature drifts since the thermocouple is in a stagnant region during this period. Once the DIS drain-down is complete and clean water injection to the DIS commences again, the DIS inlet temperature resumes reading the inlet test fluid temperature. This behavior only occurred for the DIS Configuration 2 experiments that implemented the drain-down procedure. The result is that the inlet temperature to the test column must be inferred during the period of time that the HCT was draining. In this case, the results simply show that the test column inlet temperature remained constant at 130°F, which demonstrates high precision control to the inlet temperature setting of 130°F.

The test column outlet temperature, shown in Figure 5-4, does show a "real" decrease in temperature as the DIS injects its contents. This was due to the relatively long residence time of fluid within the DIS, which did not contain heaters or insulation. The result was a temperature drop up to 5°F. Note that test T176 followed the "Final-Low" flow profile. For flow profiles with higher flow rates (e.g., "Final-Mid" and "Final-High"), the temperature drop due to DIS injection was negligible.

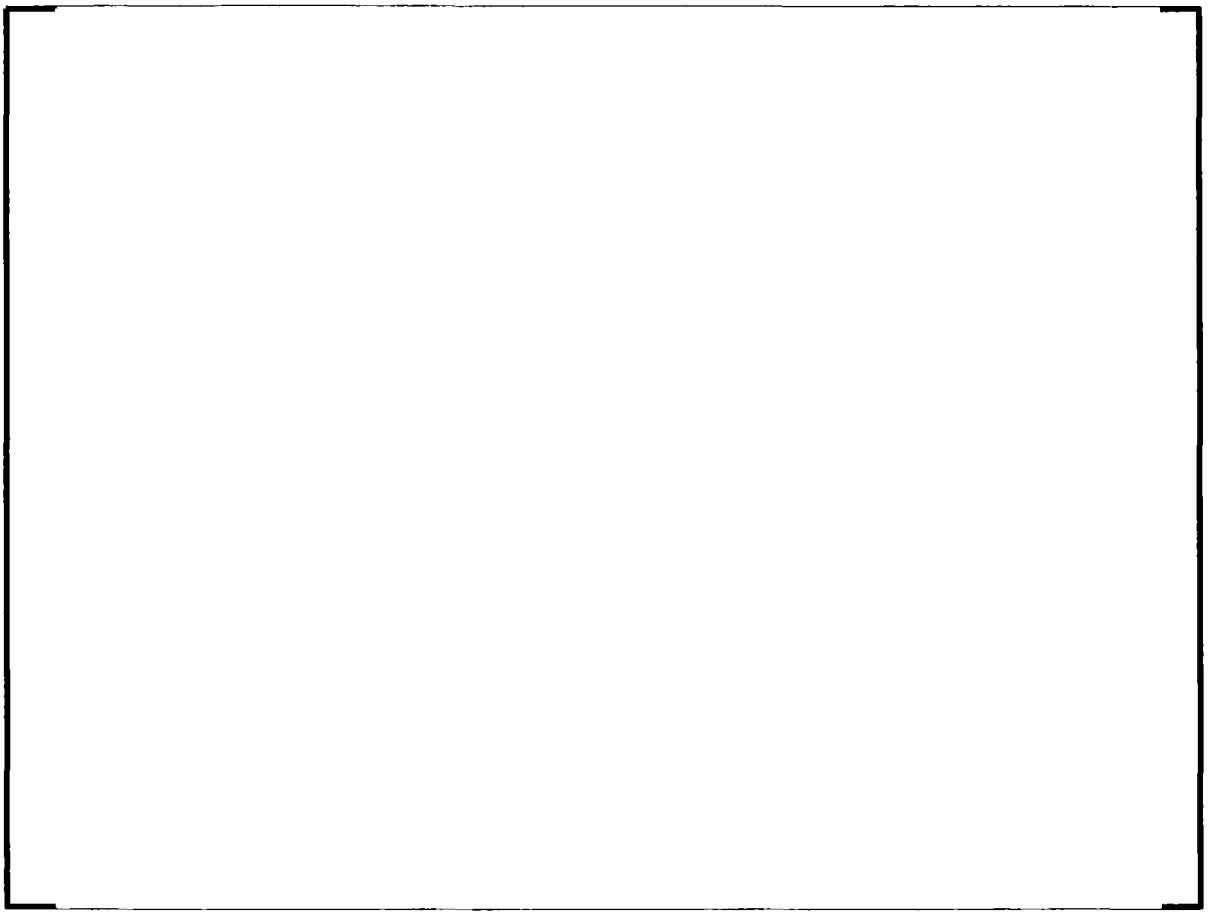

a,c

Figure 5-4 Test T176 Measured Test Column Outlet and DIS Inlet Temperatures

Figure 5-5 shows the flow rate setting and measured flow rate as a function of pressure drop. The flow rate setting is based on the "Final-Low" pressure drop versus flow profile as defined in Figure 3-8 of Section 3.3. As shown, the measured flow rate compared to the setting was within the flow rate measurement accuracy for the entire duration of the experiment.

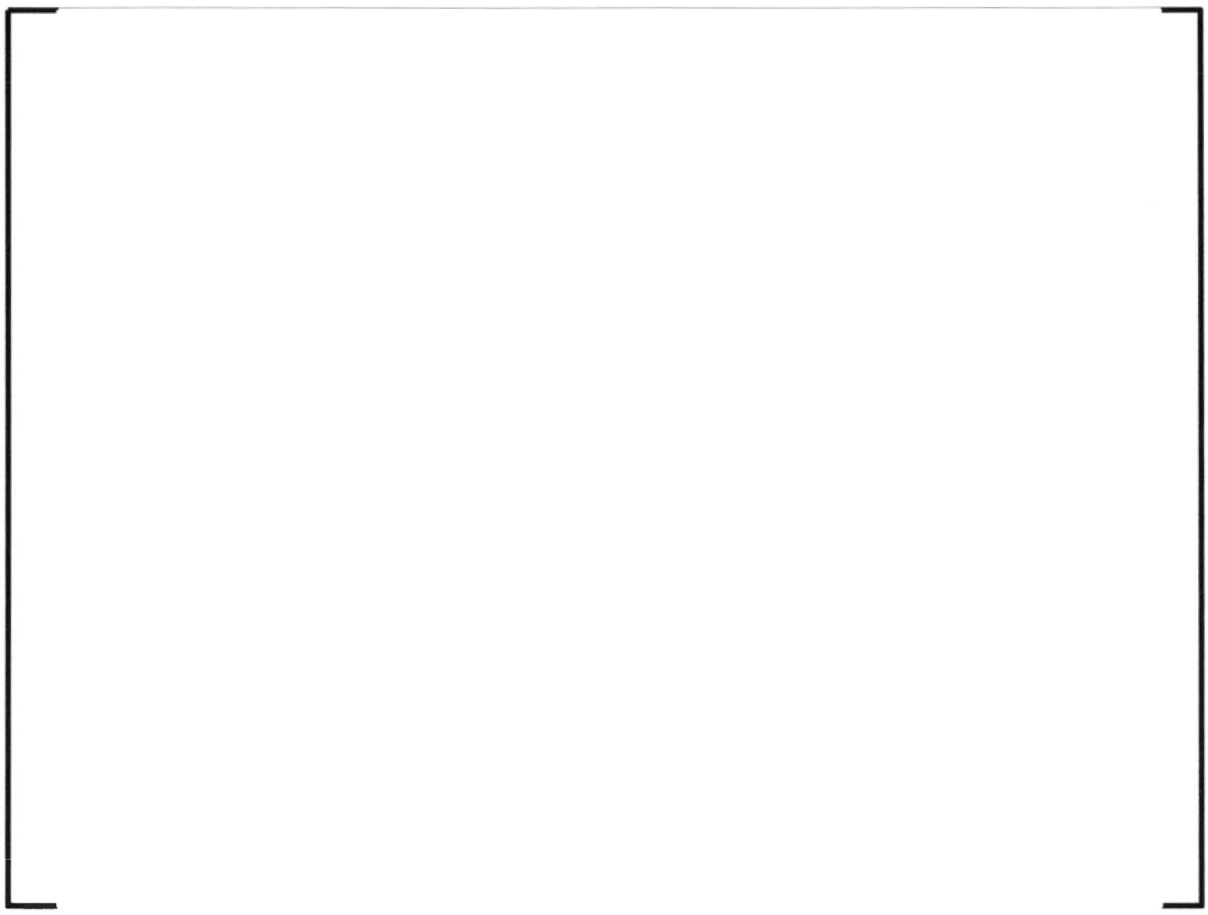

a,c

Figure 5-5 Test T176 Flow Rate Setting and Measured Flow Rate Comparison

5.1.2 Sources of Uncertainty and Experimental Bias

Significant measures were taken to control non-condensable gas dissolution during this program. Procedures were in place to assure that adequate time to preheat the facility was available and that the dissolved gas content had stabilized at the test temperature. Design features, such as downstream filtration to raise the static pressure in the test column and assure that the test geometry elevation was below the main feed tank elevation, were implemented. Nonetheless, some dissolution was observed during the experiments. During early experiments, it was determined that heat generation within the main progressive-cavity pump was leading to dissolution of gas within the pump. This was unforeseen and is a result of the positive-displacement pump selection, which requires direct contact with high frictional heat generation between the rotor and stator. To mitigate this issue, a throttle valve was installed directly downstream of the pump to elevate the static pressure within the pump. This was somewhat of a tradeoff since frictional heating would also increase due to increased loads on the pump shaft. Non-condensable gas dissolution was also observed in the DIS tubing. The DIS tanks were maintained at atmospheric pressure and suction lines from the DIS tanks were allowed to rise above the tank level. Some dissolution of gas occurred due to the slight drop below ambient pressure. Rather than changing the configuration for a tank bottom withdrawal, it was agreed to leave the sample lines exiting the top of the DIS vessels to avoid debris packing in the sample lines associated with tank bottom withdrawal and to avoid debris

collection locations associated with a tank bottom penetration. It is noted that the amount of non-condensable gas dissolution was insignificant based on visual observation. In general, control of non-condensable gas dissolution was very good, with static pressures held above ambient pressures in the test geometry inlet. However, intermittently throughout the experimental program, some bubbles were observed to collect over time on the upstream debris bed surface. It is likely that there is no impact associated with the level of observed non-condensable gasses because these bubbles were only observed near the end of each experiment.

After changing to DIS Configuration 2, it was necessary to implement a HCT drain-down procedure as described in Section 3.2.3. The initial design of the DIS was aimed at maintaining ideal mixing in the HCT and LCT. However, with reduced level, the ideal ratio of liquid level to tank diameter was not maintained. Near the end of some experiments, particle settling was observed in the outer region of the HCT bottom. To avoid incomplete transport of particulate debris, a procedure was implemented to pulse the mixer near the end of the experiments to re-entrain the settled particles into the mixed suspension. This slightly skewed the delivery rate of particulate, resulting in some experimental bias.

During the single-grid experiments, some fiber agglomerations were observed to collect on the bottom of the simulated fuel rods. Figure 5-6 provides an example image of this fiber capture. Although measures were taken to avoid fiber agglomerations with the fiber preparation procedure and design of the DIS tubing with annular mixing injection geometry, agglomerations were still present. It is postulated that some of the observed experimental variability was due to the buildup of agglomeration on the bottom of the simulated fuel rods. However, this source of variability was only present for the single-grid experiments and is not applicable to the core inlet geometry experiments.

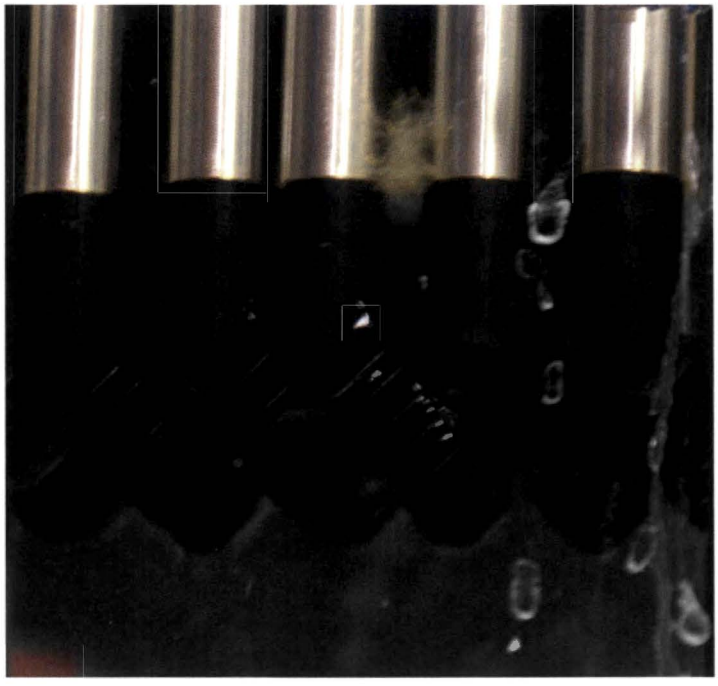

Figure 5-6 Example Image of Fiber Agglomerations on the Bottom of Simulated Fuel Rods

Overall, control of the experiments as part of this test program was very good compared to previous core inlet debris blockage test programs. Variability due to fiber agglomeration on the bottom of the simulated fuel rods for the single-grid studies and dissolution of non-condensable gas was evaluated by completing numerous test repetitions throughout the course of the program. In some cases, the test repetitions were completed over the course of weeks and months to assess modifications to the test facility as described in Section 4. The 2σ standard deviation, which is reported for all data sets in which multiple tests were conducted, can be used to quantify these effects.

Steps were taken to minimize experimental bias, which would not be captured by repeat test statistics. However, the impact of particulate settling that occurred with Configuration 2 of the DIS was not identified until after a majority of the testing was complete. Section 5.3.1.2.2 shows the impact of this bias to be small for the relatively low p:f ratios examined, and within the 2σ uncertainty due to random error. However, Section 5.3.2 shows this effect to be more pronounced for high p:f ratios. To address this bias, a high number of p:f ratio experiments with variable total fiber mass were included in the test matrix. Results of these test are described in Section 5.3.2 and show that the experimental bias can be accounted for by comparison of results at different total fiber mass and different p:f ratios to determine the onset of debris bed instability.

5.2 SINGLE GRID PHENOMENOLOGICAL STUDIES

5.2.1 Test Facility DIS Configuration (Test Series 5 and 10)

As described in Section 3.2, significant modifications to the DIS were made throughout the course of testing. To evaluate the impact of these changes, Test Series 10 was performed after the modifications were complete. All Test Series 10 experimental conditions, with the exception of the configuration change, were consistent with Test Series 5 experiments, which were conducted prior to the configuration change.

Results for differential pressure as a function of time for all tests as part of Test Series 5 and 10 are shown in Figure 5-7 and Figure 5-8 respectively. The same results are also shown as a function of injected fiber mass in Figure 5-9 and Figure 5-10. The individual test results were averaged for each test series and the averaged results are shown along with the raw data for each test. In addition, the 2σ standard deviation, based on repeat test results, is shown using error bars in each figure.

A direct comparison of the averaged results is shown in Figure 5-11. As demonstrated in Figure 5-11, there was an insignificant difference in the results obtained from Configuration 1 versus Configuration 2 of the DIS. Considering the significant difference in operating procedures and debris injection system volume between the two configurations, this result provides strong evidence that there was insignificant experimental bias associated with the debris injection method for the conditions examined.

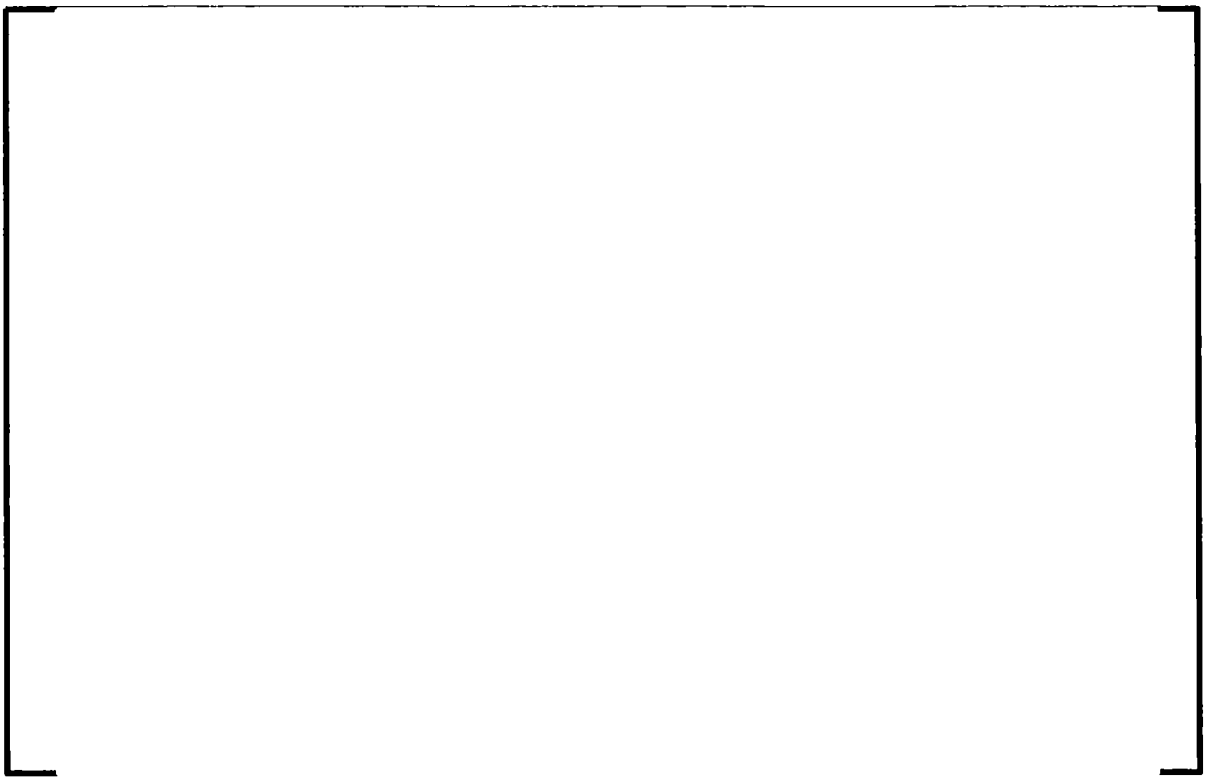

a,c

Figure 5-7 Test Series 5 Pressure Differential as a Function of Time

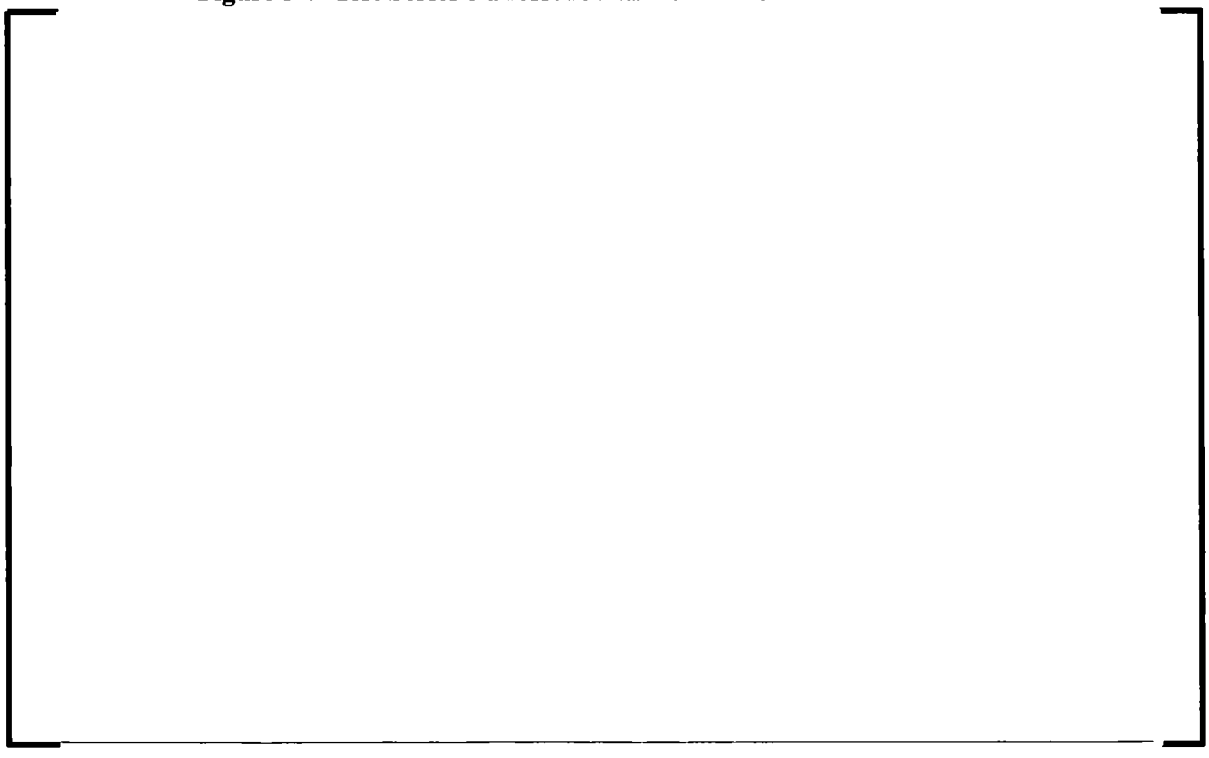

a,c

Figure 5-8 Test Series 10 Pressure Differential as a Function of Time

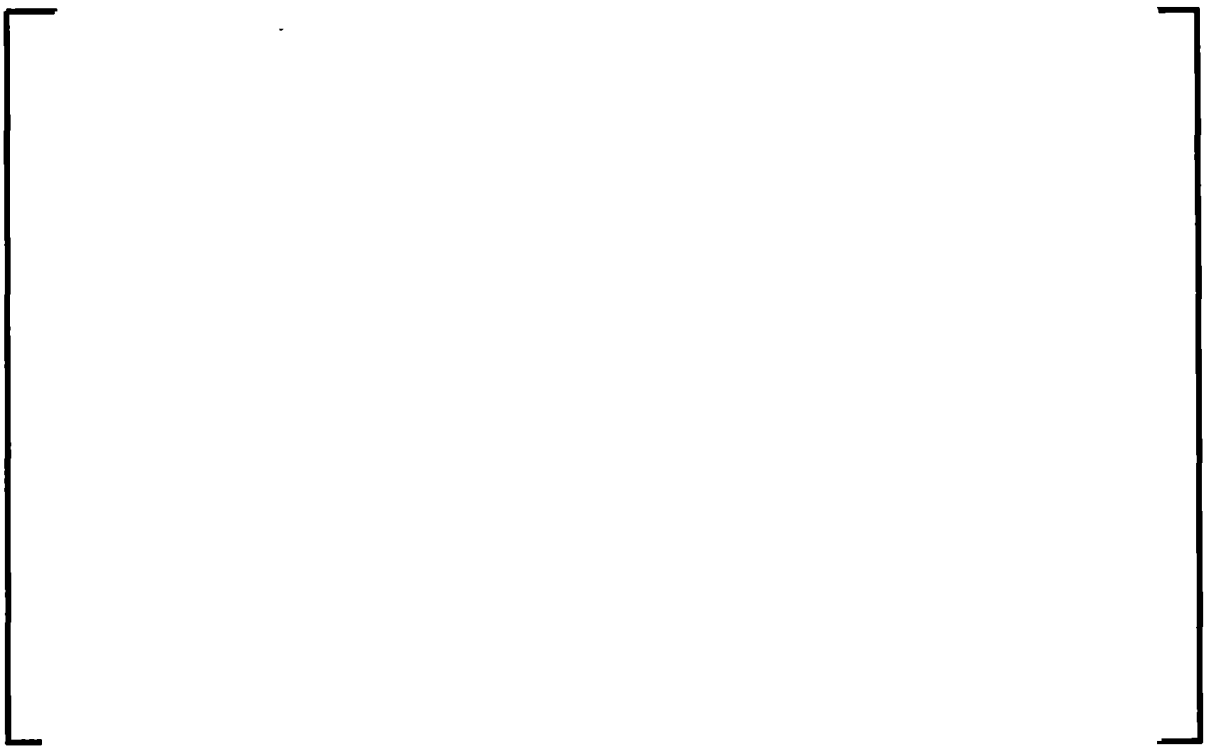

a,c

Figure 5-9 Test Series 5 Pressure Differential as a Function of Injected Fiber Mass

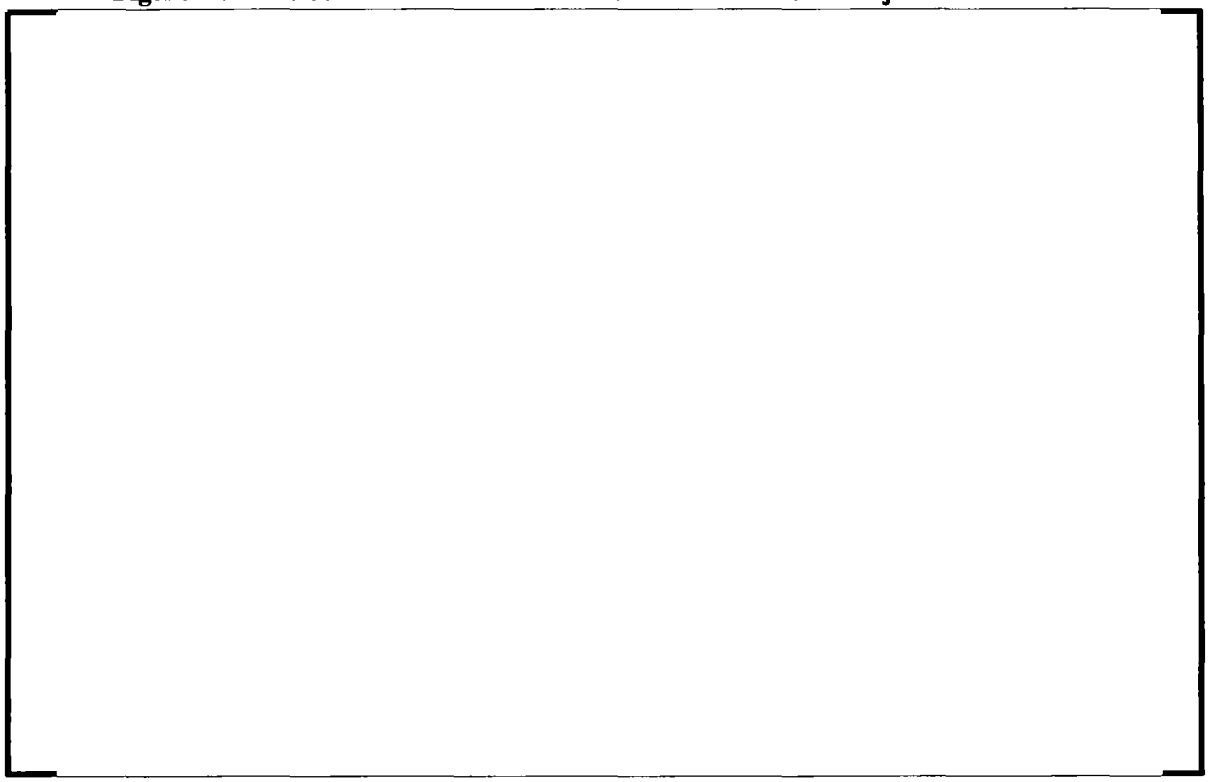

a,c

Figure 5-10 Test Series 10 Pressure Differential as a Function of Injected Fiber Mass

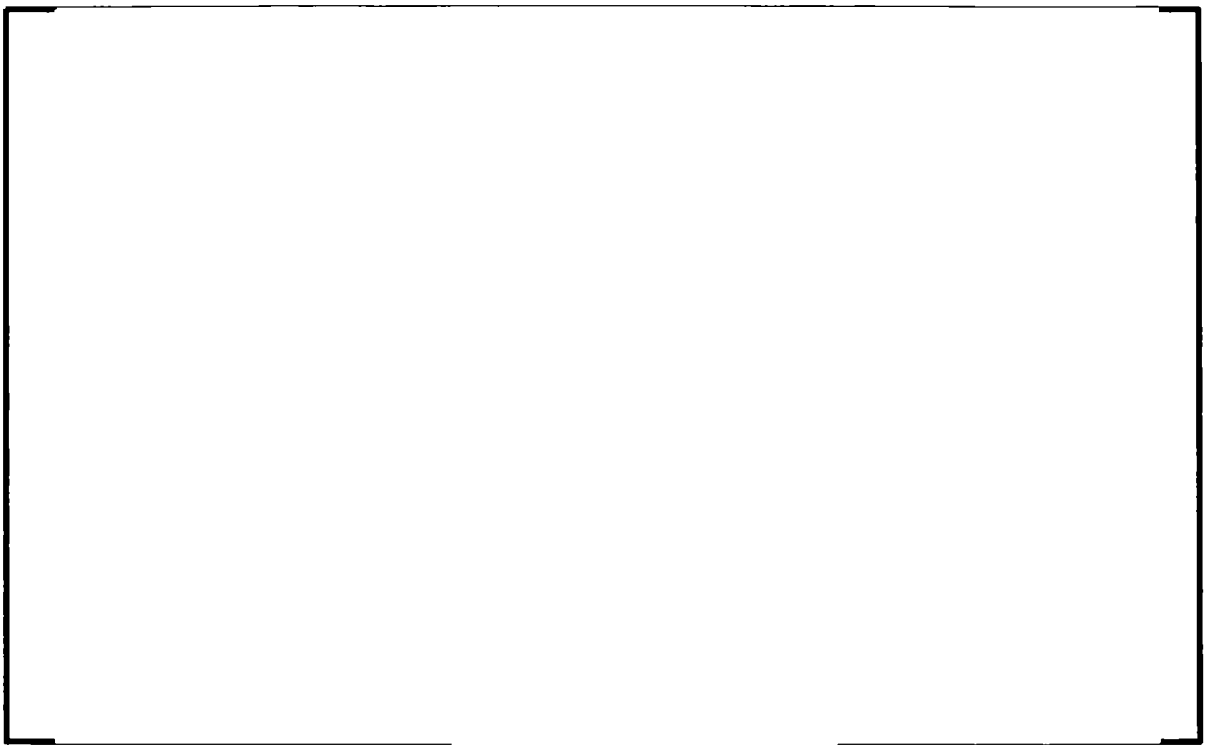

a,c

Figure 5-11 Test Series 5 and 10 Average Pressure Differential as a Function of Injected Fiber Mass

5.2.2 Debris Concentration (Test Series 10 and 13)

To investigate the impact of debris concentration on pressure drop, Test Series 13 was completed with injection duration of 300 minutes, as compared to Test Series 10 in which the injection duration was 30 minutes. These injection durations were selected to encompass the expected range of delivery rates that would occur in a PWR considering differences in ECCS injection flows and sump volumes. All variables other than injection duration remained the same for Test Series 13 compared to Test Series 10.

Figure 5-12 shows the Test Series 13 pressure drop as a function of time, which can be compared directly to Figure 5-8 in Section 5.2.1. The shape of the pressure drop curve, as a function of time, is very different. This is a result of the different debris injection profiles that were used to attain the 30 minute and 300 minute injection durations as discussed in Section 3.2.3. Figure 5-13 shows the differential pressure results for Test Series 13 as a function of fiber mass injected and Figure 5-14 shows a comparison of Test Series 13 to Test Series 10. As shown in Figure 5-14, [

]^{a,c}

a,c

Figure 5-12 Test Series 13 Pressure Differential as a Function of Time

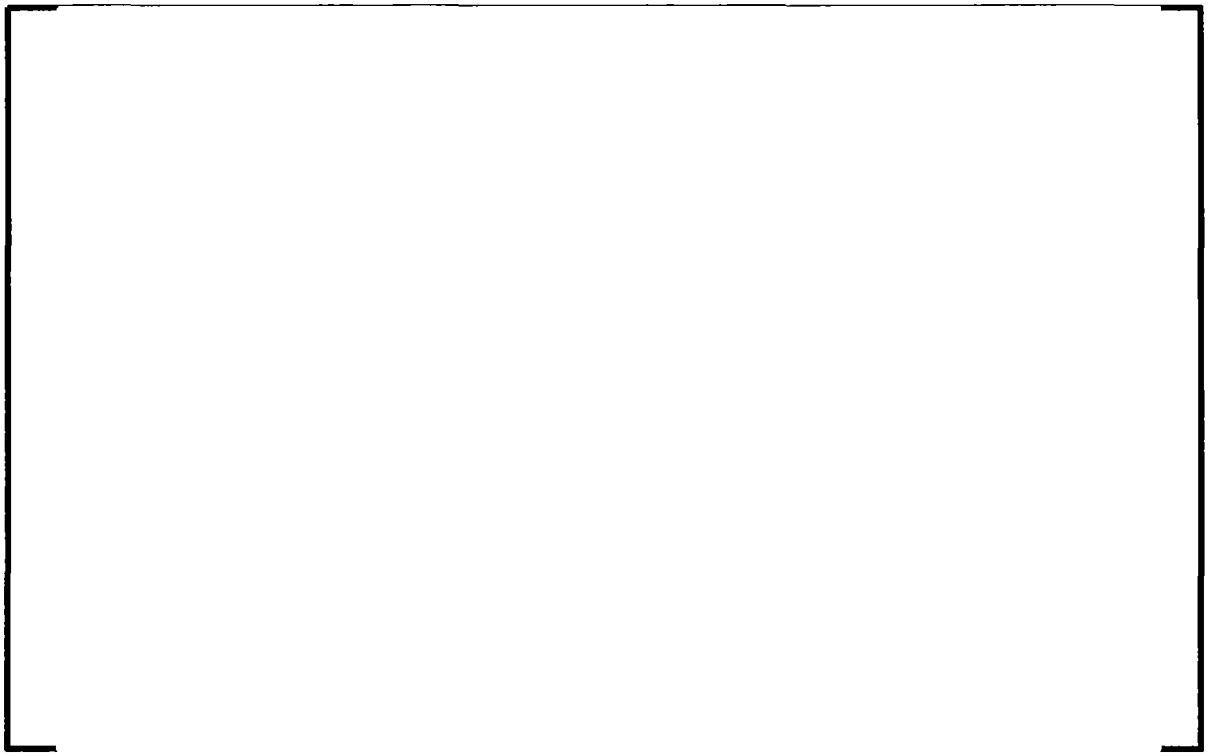

a,c

Figure 5-13 Test Series 13 Pressure Differential as a Function of Injected Fiber Mass

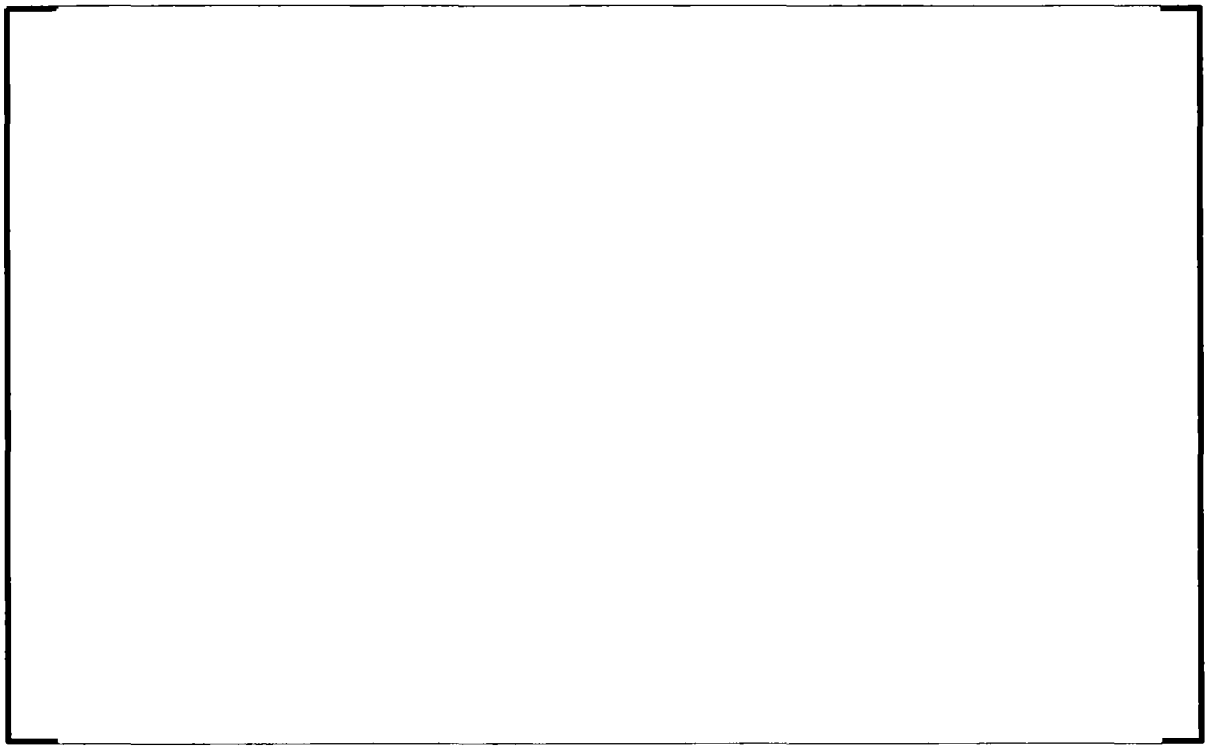

a,c

Figure 5-14 Test Series 10 and 13 Average Pressure Drop as a Function of Injected Fiber Mass

5.2.3 Fiber Mass (Test Series 8 and 10)

To investigate the impact of total injected fiber mass on pressure drop, Test Series 8 was conducted using 12.5 grams of fiber, as compared to Test Series 10 in which 25 grams of fiber was injected. This comparison also confirmed the injection characteristics of the DIS. All variables other than total injected fiber mass remained the same for Test Series 8 compared to Test Series 10.

Figure 5-15 shows the pressure drop as a function of time, which can be compared directly to Figure 5-8 in Section 5.2.1. The shape of the pressure drop curve, as a function of time, is similar since the same injection duration was used, although the magnitude of the pressure drop is significantly different. Figure 5-16 shows the differential pressure results for Test Series 8 as a function of fiber mass injected and Figure 5-17 shows a comparison of Test Series 8 to Test Series 10. As shown in Figure 5-17, results from the 12.5 versus 25 gram fiber injection were in excellent agreement. This test series comparison demonstrates the validity of the assumptions used to calculate the fiber mass injected at any point during the experiment, as described in Section 3.2.3.

a,c

Figure 5-15 Test Series 8 Pressure Differential as a Function of Time

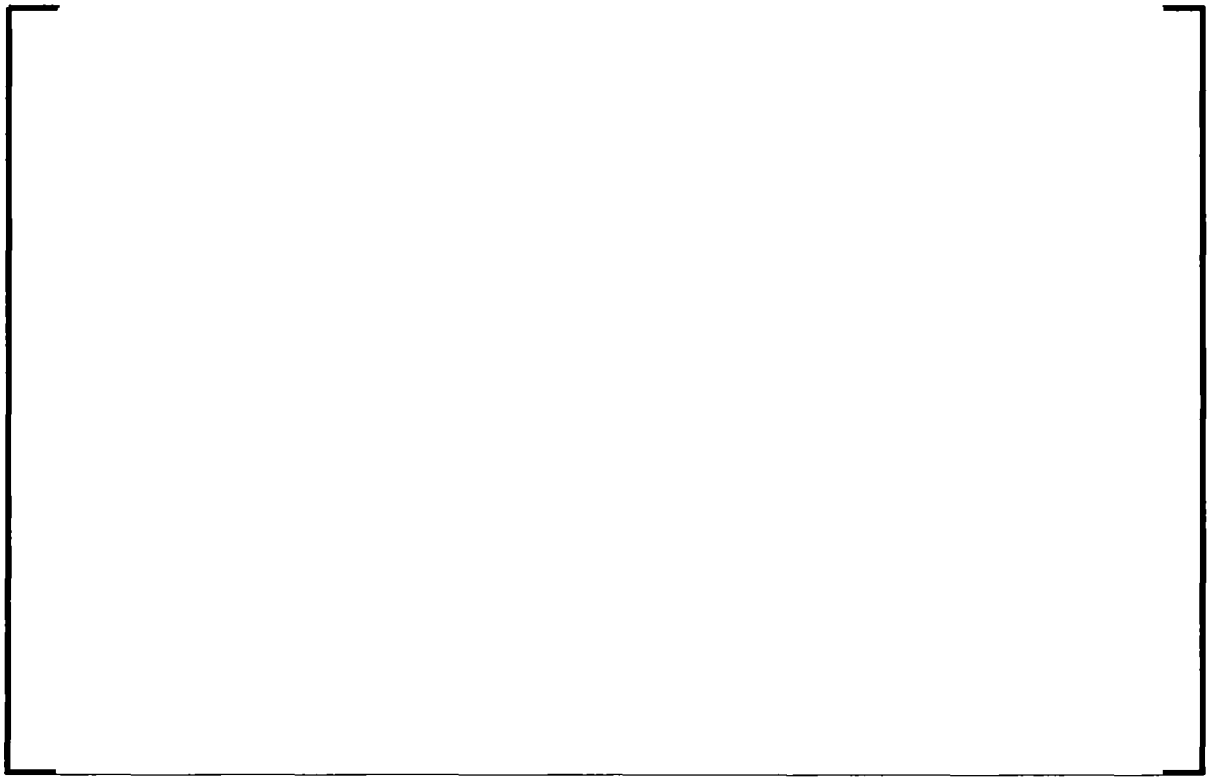

a,c

Figure 5-16 Test Series 8 Pressure Differential as a Function of Injected Fiber Mass

a,c

Figure 5-17 Test Series 8 and 10 Average Pressure Differential as a Function of Injected Fiber Mass

5.2.4 Water Chemistry (Test Series 10, 19, 20 and 21)

The purpose of this parametric was to investigate the influence of water chemistry on debris bed pressure drop. Referring to Section 2.2.4, there was some question as to whether different solution chemistries could impact capture and retention of small particulate within the fibrous debris bed. The parametric included three different buffers (NaOH, TSP and NaTB) commonly used to control containment sump pH and a range of pH (7.0 and 9.0) using the NaOH buffer. All variables other than water chemistry remained the same for Test Series 19, 20 and 21 compared to Test Series 10.

Figure 5-18 shows the results of the buffer type parametric at pH 7.0, and Figure 5-19 shows results of the pH parametric using NaOH buffered solution. The test results indicate [

]^{a,c}

This study provides evidence that sump chemistry has [

]^{a,c}

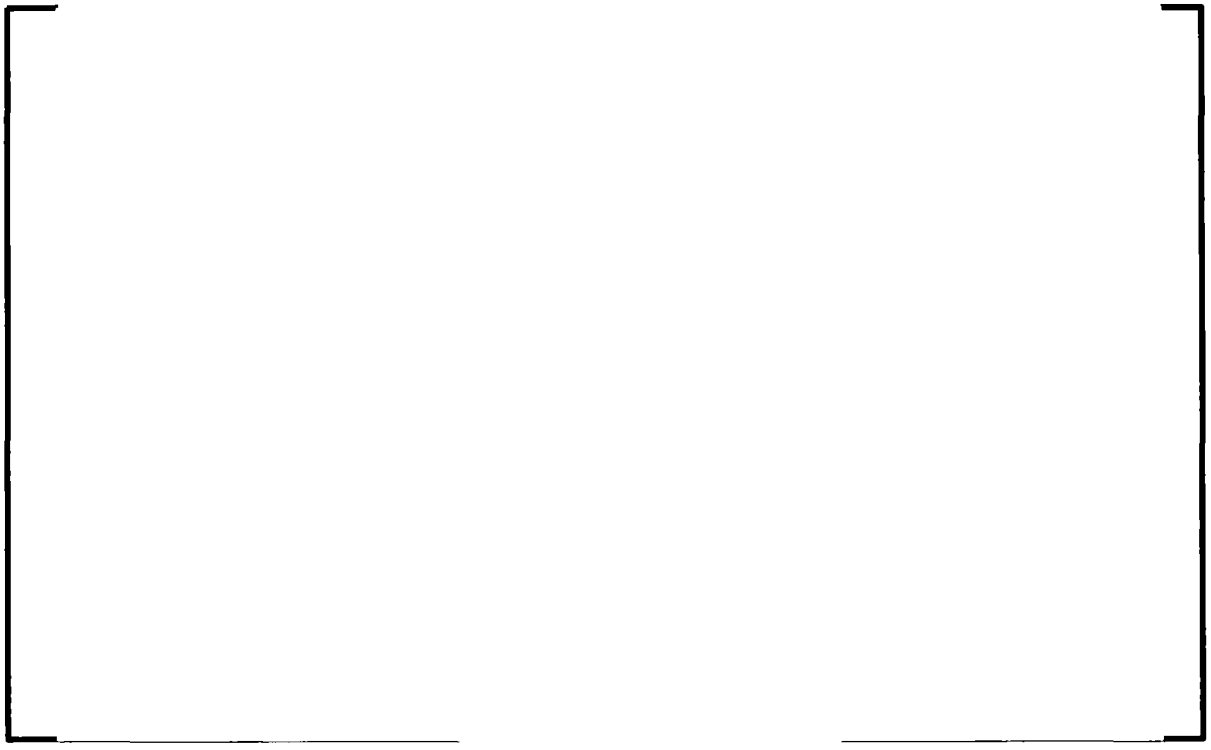
a,c

Figure 5-18 Test Series 10, 20 and 21 Average Pressure Drop as a Function of Injected Fiber Mass


a,c

Figure 5-19 Test Series 10 and 19 Average Pressure Drop as a Function of Injected Fiber Mass

5.2.5 Grid Geometry (Test Series 10, 12, 22 and 23)

The grid geometry parametric was completed to study the effects of capture geometry on head loss. As described in Section 3.5.1, the selected grids encompassed variation in open flow area, rod diameter and pitch. Figure 5-20 shows results of the comparison study. Comparing the open flow areas reported in Section 3.5.1, the results followed the expected trend as shown with the arrow in Figure 5-20. [ ]^{a,c} Figure 5-21 shows the measured capture efficiency as a function of open flow area from Table 3-4 for each of the tests conducted as part of this investigation. The results indicate [ ]^{a,c}


a,c

Figure 5-20 Test Series 10, 12, 22 and 23 Pressure Drop as a Function of Injected Fiber Mass

a,c

Figure 5-21 Test Series 10, 12, 22 and 23 Capture Efficiency Results

5.2.6 Particulate Size Distribution (Test Series 8, 10, 16 - 18 and 24 - 29)

Several test series were performed to examine the impact of particulate size distribution on debris bed head loss. Variations in mean particulate size, including narrow and broad distributions, were examined. As described in Section 3.9.2, the upper bound of the tested size distribution range was aimed at capturing conditions in which essentially complete straining of particulate would occur.

Figure 5-22 shows results for the A, B, C and D particulate distributions provided in Section 3.9.2. Clearly, over this range of particle sizes, increasing mean particle diameter resulted in increased pressure drop with all other variables held constant.

Figure 5-23 shows results for the E, F, H, I and J particulate distribution experiments. A maximum pressure drop of 25 psi was reached using the type J, [ ]^{a,c} mean particle size. Particulate size distributions above [ ]^{a,c} resulted in lower pressure drops. This result can be explained by considering the effects of particulate capture efficiency and packing density. For increasing particle sizes, the capture efficiency increases to the point when all particulate is essentially captured. Above this size distribution, it would be expected that the capture efficiency would remain high, but the packing density of particulate would decrease due to the larger particle size. Therefore, a maximum pressure drop should exist considering the effects of packing density and capture efficiency. The peak pressure drop observed at a [ ]^{a,c} mean particle diameter can therefore be considered a maximum of these two effects combined.

Figure 5-24 shows the same results as Figure 5-23 with the x-axis narrowed to show only the first portion of the test. These results are very instructive for explaining the impacts of varied particulate capture efficiency and packing density. Results from the [ ]^{a,c} experiments are the first to show an initial increase in pressure drop. At a 3 gram fiber load, the [ ]^{a,c} particulate reached a pressure drop of 0.2 psi, while results for decreasing particulate sizes showed a decreasing differential pressure trend at a 3 gram fiber load. This indicates that particle capture efficiency due to straining is the dominant mechanism resulting in head loss, in the early stages of bed development. As fiber and particle loads increase throughout each experiment, the pressure drop trend changes due to increased packing density. Near the end of the set of experiments, the peak pressure drop occurred during the [ ]^{a,c} mean particle size experiments.

Figure 5-25 shows the peak pressure drop measured for each experiment as part of the particle size study. Results for each experiment are shown in Figure 5-25 as compared to Figure 5-22 through Figure 5-24 which show test series averaged results with error bars. Figure 5-25 shows a peak differential pressure at the [ ]^{a,c} mean particle size with results at [ ]^{a,c} of similar magnitude, but slightly lower on average. At the end of each experiment, the main flow rate was shut off and the test section flow rate was reduced to the DIS flow rate of [ ]^{a,c} Figure 5-26 shows the differential pressure at this flow rate for comparison to Figure 5-25. As shown, the trend is consistent, with maximum pressure drop occurring for the [ ]^{a,c} mean particle size.

Figure 5-27 shows the measured total capture efficiency for all experiments as part of the particulate size distribution study. The total capture efficiency results are based on post-test bag filter weights as described in Section 3.6. At [ ]^{a,c} mean particle size, which corresponds to the peak pressure drop shown in Figure 5-25, the capture efficiency is only 50%. Increasing particle size results in increased capture efficiency up to a particulate size of [ ]^{a,c} For particles [ ]^{a,c} and larger, straining and interception combine for essentially complete particulate capture. The total capture efficiency does not reach 100% due to some particle and fiber penetration during the early stages of bed development.

All tests conducted as part of the particle size distribution study were conducted at a p:f ratio of 10:1 using the "Mid" flow curve defined in Section 3.3. Considering increased p:f ratio, it is reasonable to assume that the trends demonstrated here could change. Section 5.2.8 examines the influence of variable p:f ratio.


a,c

Figure 5-22 Pressure Drop as a Function of Injected Fiber Mass for Particle Size A, B, C and D


a,c

Figure 5-23 Pressure Drop as a Function of Injected Fiber Mass for Particle Size E through J

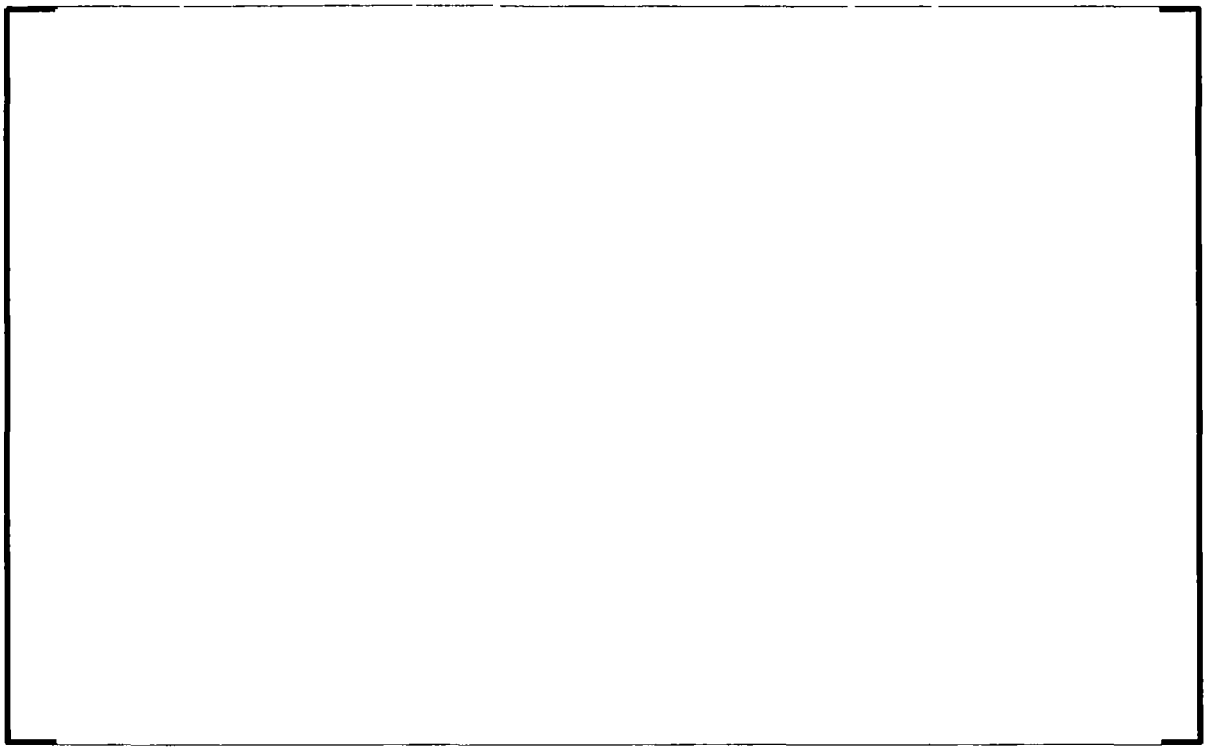

a,c

Figure 5-24 Pressure Drop as a Function of Fiber Mass for Particle Size E through J (Zoomed)

a,c

Figure 5-25 Maximum Pressure Differential as a Function of Particle Size Distribution

a,c

Figure 5-26 Pressure Differential at 0.75 gpm as a Function of Particle Size Distribution

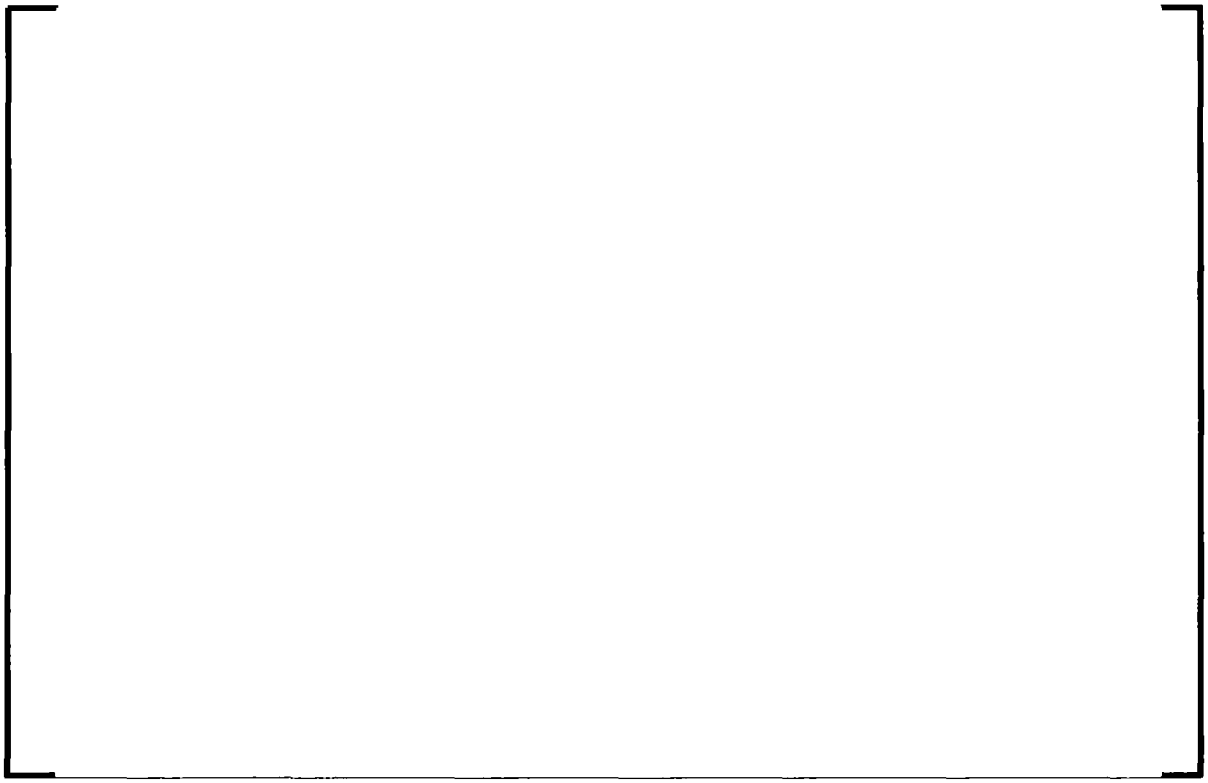

a,c

Figure 5-27 Total Capture Efficiency Based on Post-Test Filter Bag Weights

5.2.7 Flow Rate (Test Series 2, 10, 11, 30, 33 and 34)

The flow rate parametric was completed to study the effects of fluid velocity on head loss. As expected, test results show that flow rate has a significant impact on overall head loss across a debris bed. Figure 5-28 shows head loss results plotted as a function of cumulative fiber load for three different initial flow rates. For Test Series 2, 10 and 11, a mean particulate size of 10 μm (Distribution A in Table 3-9) was used and the p:f ratio was 10:1. As the figure shows, for the same debris load, the pressure drop across the debris bed increases with increasing flow.

Similarly, Figure 5-29 shows the same plot from three test conditions conducted using the Distribution 1 particulate size distribution. For Test Series 30, 33 and 34, 12.5 g of fiber was used with a p:f ratio of 10:1. As the figure shows, the pressure drop behavior is similar to the flow variations performed using the smaller particulate size; the pressure drop across the debris bed increases with increasing flow. However, the magnitude of the pressure drop is much greater for the larger particle size.

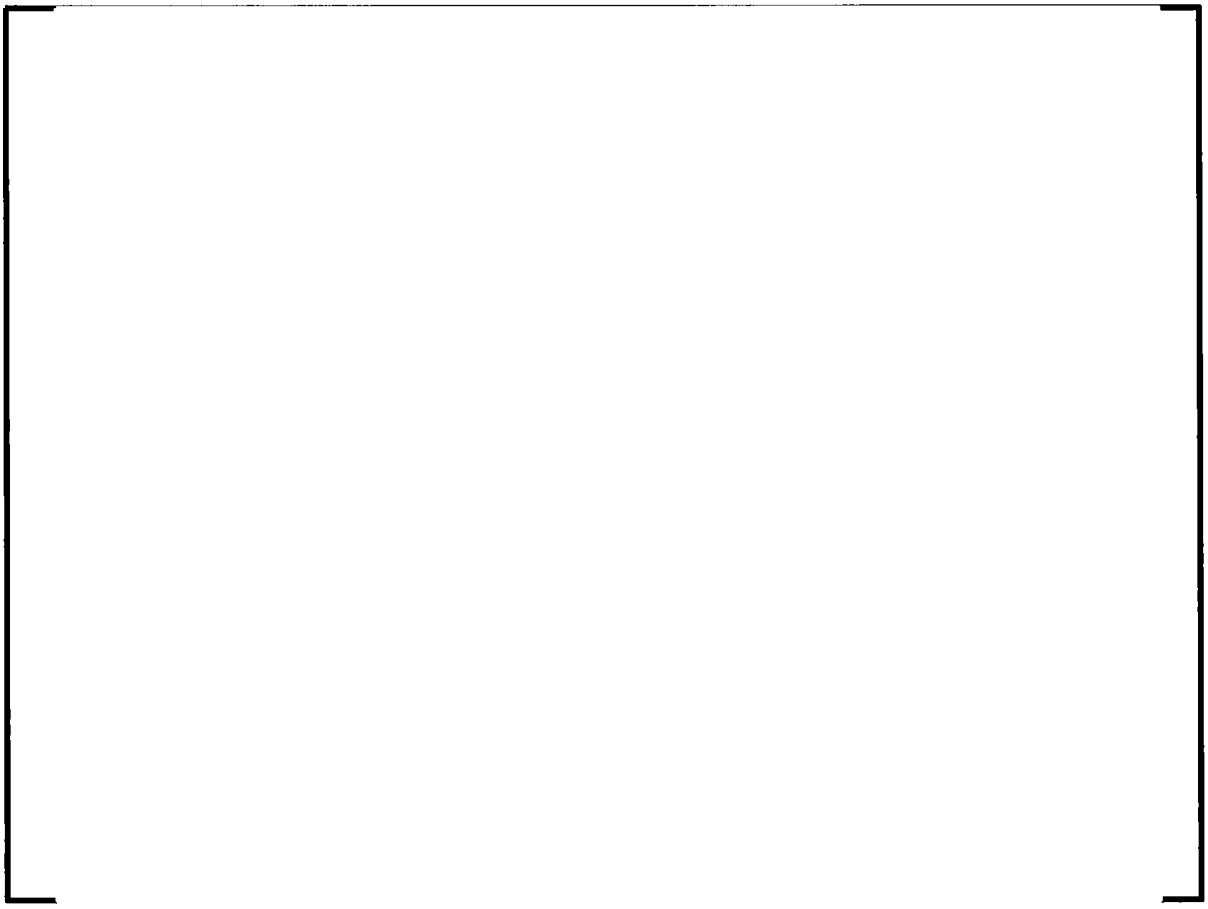

a,c

Figure 5-28 Test Series 2, 10 and 11 Pressure Differential as a Function of Injected Fiber Mass

a,c

Figure 5-29 Test Series 30, 33 and 34 Pressure Differential as a Function of Injected Fiber Mass

5.2.8 P:F Ratio (Test Series 3, 9, 10, 14, 15 and 34 through 42)

An initial parametric study that included Test Series 3, 9, 10, 14 and 15, aimed at evaluating the impact of p:f ratio, was performed using the 10 μm particulate. Figure 5-30 shows results of this study. For the range of p:f ratio studied, 0:1 through 30:1, the pressure drop increased with increasing p:f. Note that the 30:1 condition had a total injected fiber mass of 12.5 grams as compared to 25 grams for all other results shown in Figure 5-30. This was due to difficulties suspending the large mass of particulate at this condition in the small HCT. This was one of the reasons that the DIS system was modified to increase the HCT volume for follow-on testing as described in Section 3.2.

The increase in pressure drop as a function of p:f ratio for the 10 μm particulate shown in Figure 5-30 is marginal considering the large range of p:f ratios examined. This can be explained by evaluating the capture efficiency results shown in Figure 5-31 and Figure 5-32. Figure 5-31 shows the total capture efficiency based directly on the post-test bag filter weights for a range of p:f ratios. The total capture efficiency accounts for both fibrous and particulate debris penetration. Figure 5-31 shows a capture efficiency ranging from [ ]^{a,c} which corresponds to a fiber only condition. This represents a range of [ ]^{a,c} grams of fibrous debris penetration. Assuming the fibrous debris penetration mass is independent of the particle loading, the results at a 0:1 p:f ratio can be extended to estimate the component of the total capture efficiency that is attributable to

fiber penetration. This estimate is provided in Figure 5-31 and Figure 5-35 for fibrous debris penetration values of [ ]^{a,c} grams and is referred to as the estimated component of total capture due to fiber. The difference between the total capture efficiency, which is taken directly from the filter bag measurements, and the estimated component of total capture due to fiber represents the estimated particle capture efficiency. The estimated particle capture efficiency is shown in Figure 5-32. Figure 5-32 shows that [

]^{a,c}

Upon completion of the particulate size distribution study documented in Section 5.2.6, an additional p:f ratio parametric was performed, inclusive of Test Series 34 through 42. This p:f ratio parametric used information gathered during the Section 5.2.6 size distribution study to define the particulate size. For these studies, Distribution 1 particulate, as defined in Section 3.9.2, was utilized. As shown in Section 3.9.2, Distribution 1 particulate is a broad size distribution that is weighted more heavily with particulate in the range of [ ]^{a,c} based on the Section 5.2.6 conclusions. Furthermore, the Distribution 1 particulate also included a tail of smaller particulate in an attempt to further maximize particle packing.

Figure 5-33 shows results of the p:f ratio study using the Distribution 1 particulate. Comparison of Figure 5-33 to Figure 5-30 shows the expected order of magnitude increase in pressure drop due to the larger particulate size. For p:f ratios of 25:1, 30:1 and 40:1 the pressure drop exceeded the design pressure of the test column and the pump was shut off. At a p:f ratio of 50:1, the debris bed became unstable at a pressure drop near 3 psi and the maximum pressure drop did not exceed 7 psi for the remainder of the experiment. Based on these observations, it is suggested that the mechanism for breakthrough and instability of the debris bed was due to particulate scouring as described in Section 2.2.5.

Figure 5-34 shows results at a p:f ratio of 45:1 from Test Series 42. These results were not shown in Figure 5-33 since bed breakthrough was observed during T137 and T139, but not during T138. During test T138, the pump speed was reduced near the end of the experiment to prevent over-pressurizing the test column. This indicates that a p:f ratio of 45:1 represents a transition from a stable to an unstable debris bed for this set of test conditions.

Figure 5-35 shows the total capture efficiency, based on post-test bag filter weights, for all tests conducted as part of Test Series 34 through 42. As shown in Figure 5-35, a transition occurs at a p:f ratio of 45:1. At a p:f ratio of 45:1, only 2 of the 3 experiments as part of Test Series 42 resulted in breakthrough of the debris bed. To better understand the capture efficiency results, the particle only capture efficiency was also calculated using the same method as described above. Figure 5-36 shows the estimated particle capture efficiency. Comparison of Figure 5-36 to Figure 5-35 shows that the high total capture efficiency observed at low p:f ratio is attributable to fiber capture, while the particle capture efficiency only increases with increasing p:f ratio until debris bed breakthrough occurs.

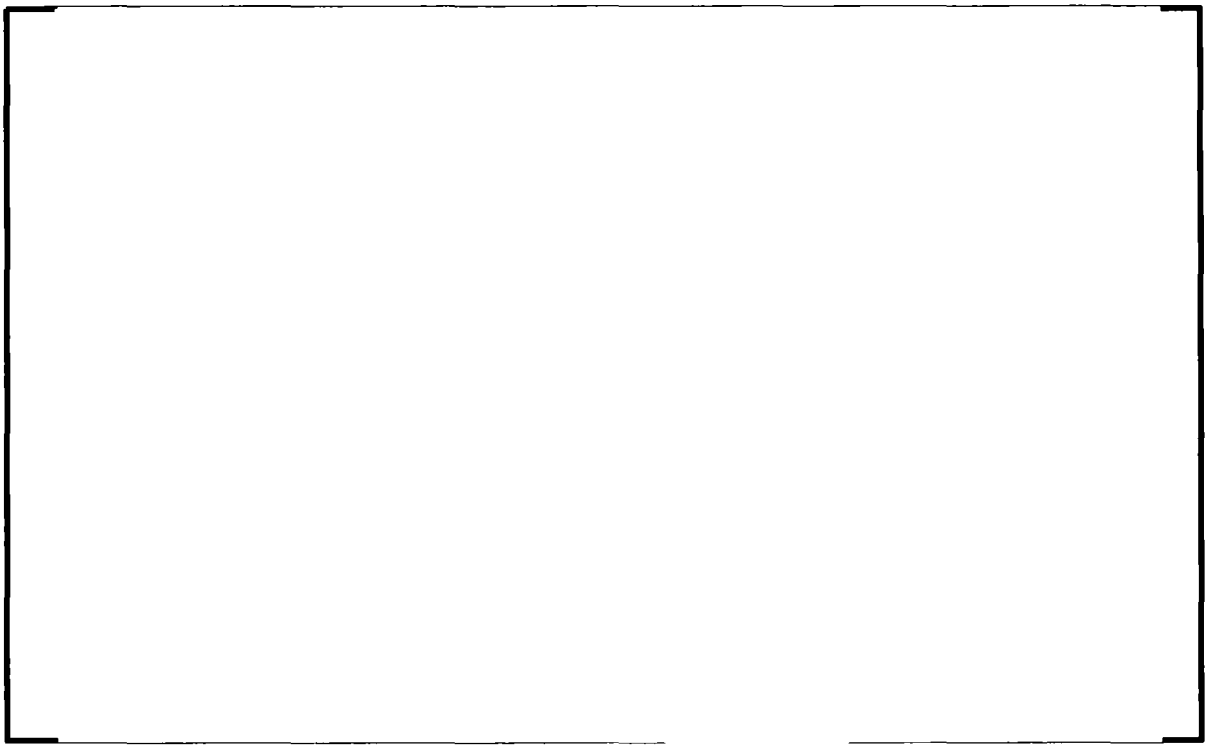

a,c

Figure 5-30 Test Series 3, 9, 10, 14 and 15 p:f Ratio Results for 10 μm Particulate

a,c

Figure 5-31 Test Series 3, 9, 10, 14 and 15 Total Capture Efficiency versus Injected p:f Ratio

a,c

Figure 5-32 Test Series 3, 9, 10, 14 and 15 Particle Capture Efficiency versus Injected p:f Ratio

a,c

Figure 5-33 Test Series 34 through 41 p:f Ratio Results for Distribution 1 Particulate

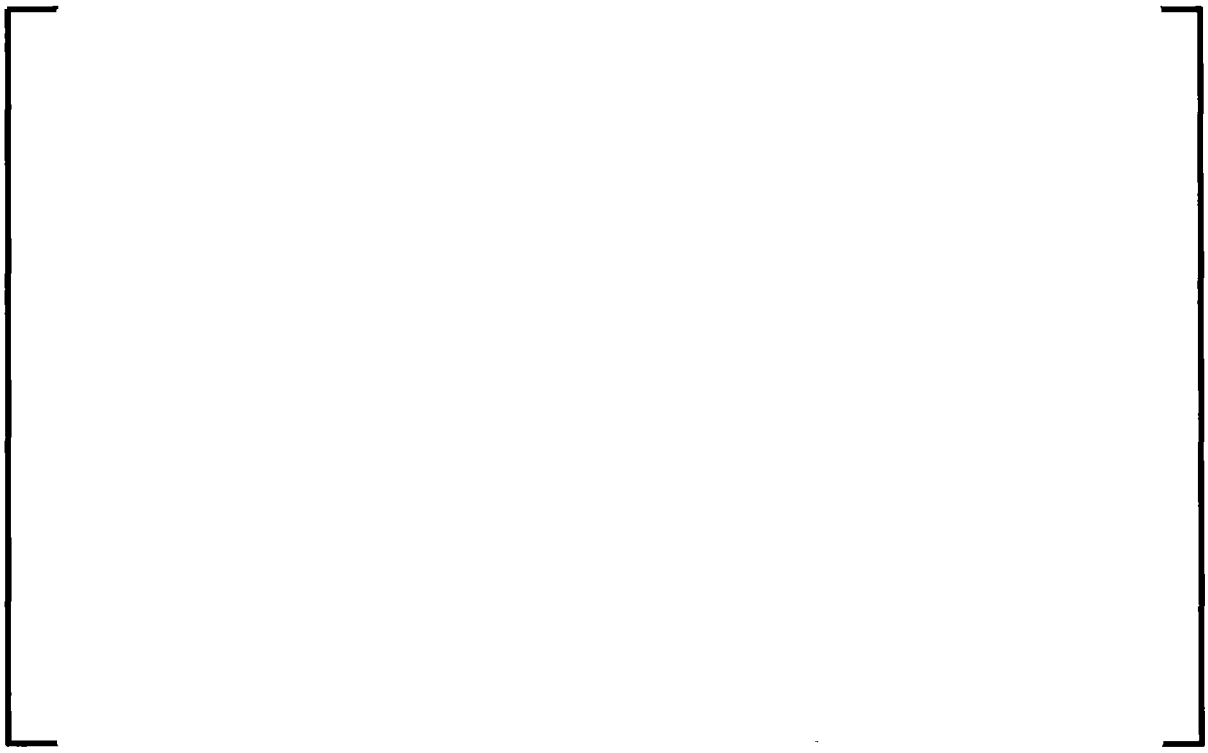

a,c

Figure 5-34 Test Series 42 p:f Ratio 45:1 Results for Distribution 1 Particulate

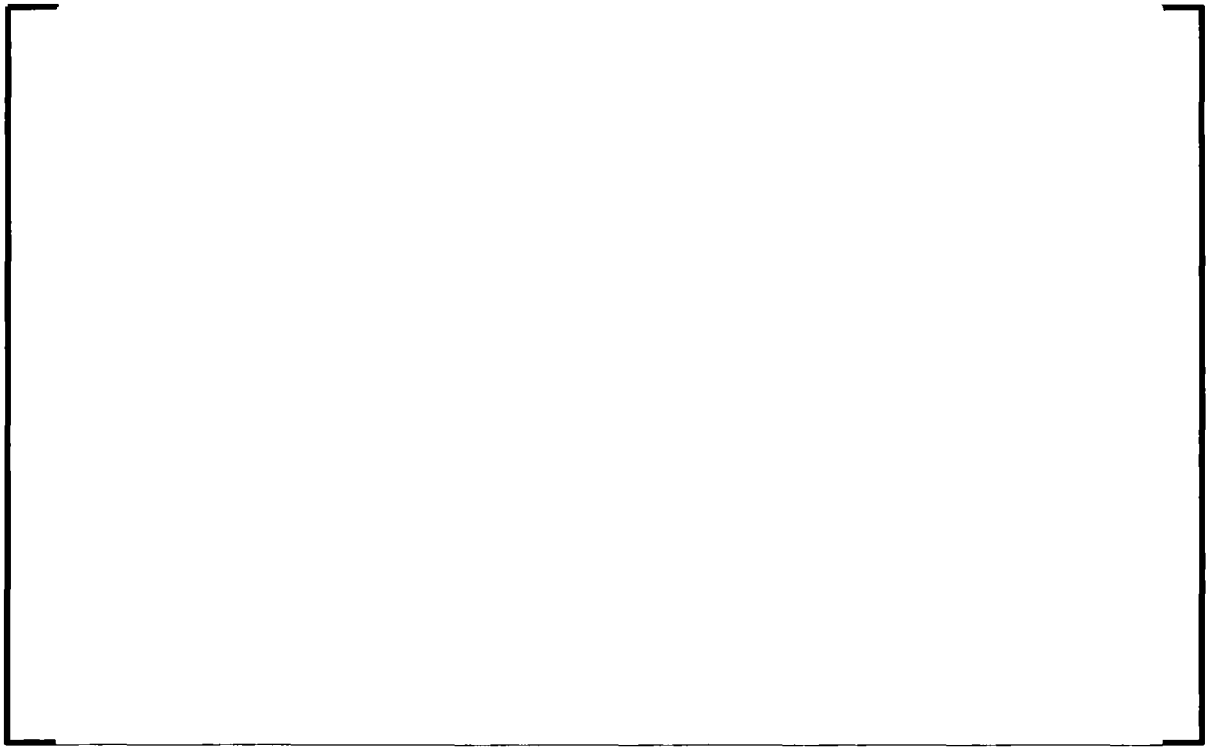

a,c

Figure 5-35 Test Series 34 through 42 Total Capture Efficiency versus Injected p:f Ratio

a,c

Figure 5-36 Test Series 34 through 42 Particle Capture Efficiency versus Injected p:f Ratio

5.3 CORE ENTRANCE GEOMETRY PARAMETRICS

Following the single-grid studies, several experiments were performed using Westinghouse and AREVA core inlet geometry, as described in Section 3.5.3 and 3.5.4. The Westinghouse results are presented in Section 5.3.1 and the AREVA results are presented in Section 5.3.2.

5.3.1 Westinghouse Core Entrance Geometry Results

5.3.1.1 Core Entrance Geometry with Adjacent FA Gap Simulated (Test Series 43 through 46)

Test Series 43 pressure drop results as a function of cumulative fiber load from the 10 μm particulate size distribution test condition were collected at a p:f ratio of 10:1. For comparison, these results are shown in Figure 5-37 along with the single RFA grid Test Series 10 that was operated using the same flow profile, debris load and particle size distribution. Four tests were performed for Test Series 43. Figure 5-37 indicates that the 2σ standard deviation was much greater for the core inlet geometry than for the single grid. [

]^{a,c}

The Test Series 44 pressure drop results as a function of cumulative fiber load from the Distribution 1 particulate size test condition were collected at a p:f ratio of 10:1. For comparison, these results are shown

in Figure 5-38 along with the single RFA grid Test Series 34 that was conducted using the same flow profile, debris load and particle size distribution. Four tests were completed as part of Test Series 44. Figure 5-38 indicates that the 2σ standard deviation was much greater for the core inlet geometry than for the single grid. [

]^{a,c}

The Test Series 46 pressure drop results as a function of cumulative fiber load from the Distribution 1 particulate size test condition were collected at a p:f of 30:1. For comparison, these results are shown in Figure 5-39 along with the single RFA grid Test Series 40 that was operated using the same flow profile, debris load and particle size distribution. Uncertainty bands are not shown for these test series, since only one experiment was completed for each test condition. Figure 5-39 indicates that [

]^{a,c}

The Test Series 45 pressure drop results as a function of cumulative fiber load from the Distribution 1 particulate size test condition were collected at a p:f of 50:1. For comparison, these results are shown in Figure 5-40 along with the single RFA grid Test Series 34 that was operated using the same flow profile, debris load and particle size distribution. Three tests were completed as part of Test Series 45. Figure 5-40 indicates that the 2σ standard deviation was similar for the core inlet geometry compared to the single grid. [

]^{a,c}

Comparing the core entrance to the single-grid test results presented in this section showed [

]^{a,c}

Comparing the core entrance to the single-grid test results, with respect to debris bed breakthrough, the core entrance geometry exhibited bed breakthrough [

]^{a,c}

[

]^{a,c}

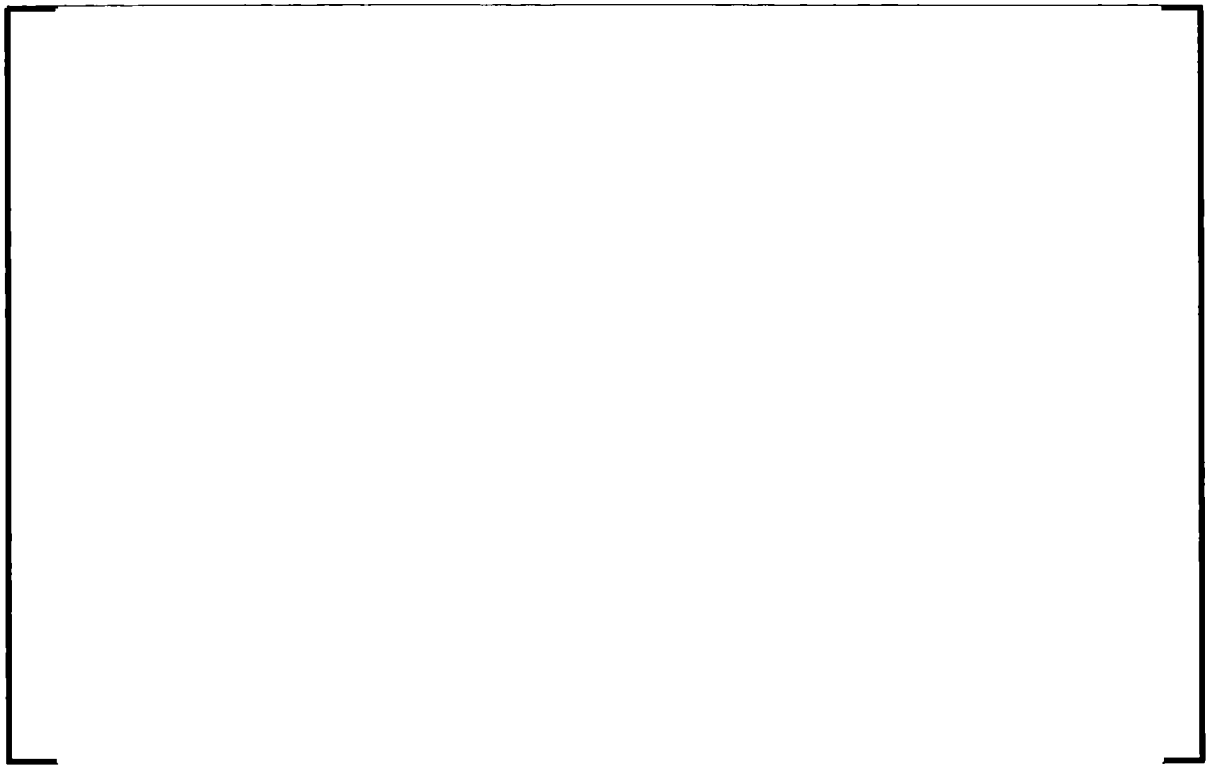
a,c

Figure 5-37 10 μm Particulate Size Baseline with Core Inlet Geometry

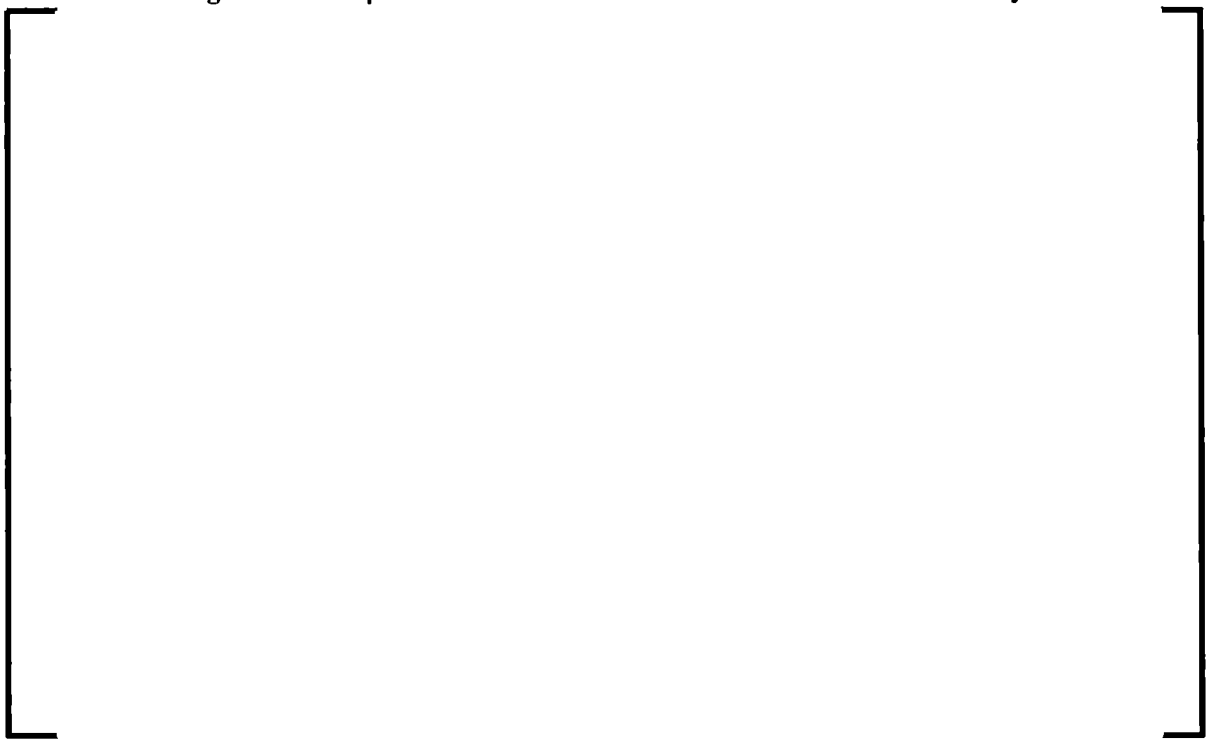
a,c

Figure 5-38 Distribution 1 Particulate Size, p:f = 10:1 with Core Inlet Geometry

a,c

Figure 5-39 Distribution 1 Particulate Size, p:f = 30:1 with Core Inlet Geometry

a,c

Figure 5-40 Distribution 1 Particulate Size, p:f = 50:1 with Core Inlet Geometry

5.3.1.2 Core Entrance Geometry with Central FA Region Simulated (Test Series 47 through 61)

As described in Section 3.5.3, a center cut of the BN, which underlays an 8 x 8 P-grid cut-out, was used for tests T152 though T178. This change was made as a result of test observations during tests T140 through T151 as described in Section 3.5.3. Furthermore, additional pressure taps were installed to measure pressure drop across the RFA bottom grid installed downstream of the BN as described in Section 3.10.

To better understand the impact of the gap formed between adjacent FAs, results from the core entrance geometry testing with gap simulated are compared to results from central fuel assembly region testing. This comparison is discussed in Section 5.3.1.2.1. Finally, results of the parametric study performed with the central FA core entrance geometry are discussed in Section 5.3.1.2.2.

5.3.1.2.1 Comparison of Core Entrance Geometry with Gap to Central FA Region

For test series included in this portion of the overall test matrix, the flow profiles were modified as discussed in Section 4. This was due to the availability of updated information as part of the work performed to support Volume 4. As a result, direct comparison of the central region core entrance geometry test series to the core entrance geometry results with gap centered in the test section, following the same differential pressure and flow boundary condition, was not possible. Nonetheless, reasonable comparison can be made using the "Mid2" and "Final-Low" flow profiles provided in Figure 3-8 of Section 3.3.

Figure 5-41 shows the comparison of core entrance geometries at a p:f of 10:1. Test Series 44 included core entrance geometry with a gap centered in the test section and Test Series 50 included a central FA region of the core inlet geometry. Comparison of these two test series indicates [

]^{a,c}

Figure 5-42 shows the comparison of core entrance geometries at a p:f of 30:1. Test Series 46 included core entrance geometry with a gap centered in the test section and Test Series 52 included a central FA region of the core inlet geometry. Comparison of these two test series indicates [

]^{a,c}

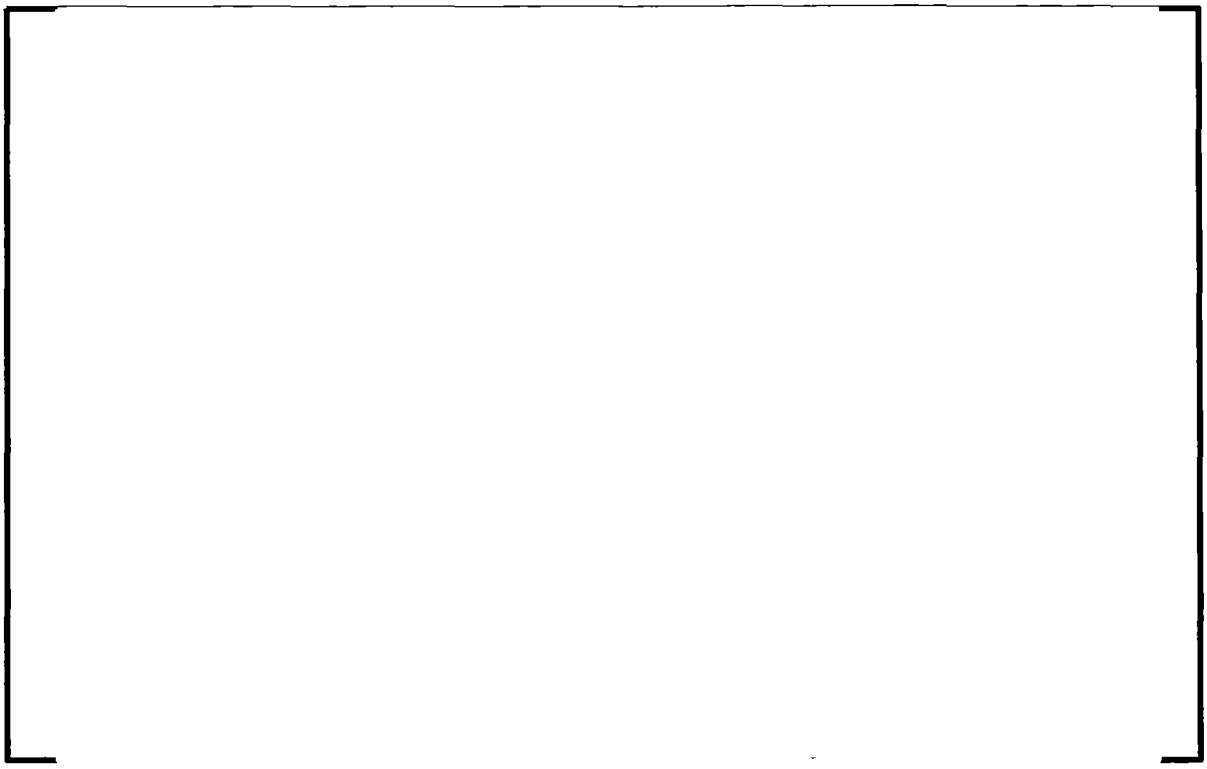

a,c

Figure 5-41 Comparison of Core Entrance Geometry with and without Gap at p:f = 10:1

a,c

Figure 5-42 Comparison of Core Entrance Geometry with and without Gap at p:f = 30:1

5.3.1.2.2 Flow Rate and p:f Ratio Parametric Study

As described in Section 5.2.8, unstable debris beds were observed at a p:f ratio of 50:1 during the single-grid studies, but not at lower p:f ratios. This transition was only investigated for a single flow and differential pressure profile. In addition, Section 5.3.1.1 discusses a comparison of the core entrance geometry and single-grid results and demonstrates a significant shift in the p:f ratio resulting in transition from unstable to stable debris beds for the same flow and differential pressure profile. Since a stable debris bed results in a more restrictive condition, a thorough investigation of the boundary between stable and unstable conditions was undertaken for the core inlet geometry. This study focused on p:f ratio and flow rate profile as the primary variables impacting the transition.

Figure 5-43 and Figure 5-44 show results of the p:f ratio study performed following the "Final-Low" flow profile provided in Section 3.3. Error bars are shown only for the Test Series 51, 56 and 57 results since repeats were not performed as part of the other test series. The results show [

]^{a,c}

Results following the "Final-Mid" and "Final-High" flow profiles are shown in Figure 5-45 and Figure 5-46. [

]^{a,c}

Considering the significance of the [

]a,c

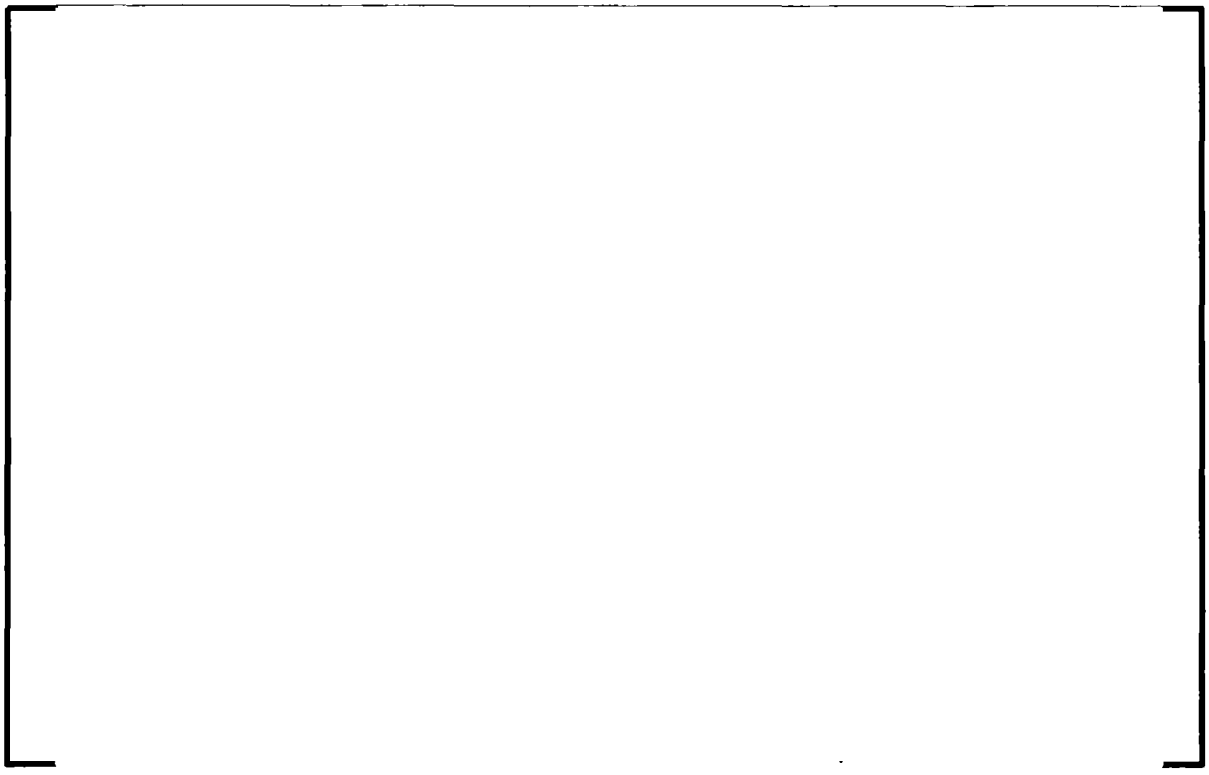

Figure 5-43 Core Inlet Geometry p:f Ratio Results following "Final-Low" Flow Profile

a,c

Figure 5-44 Core Inlet Geometry p:f Ratio Results following "Final-Low" Flow Profile (Zoomed)

a,c

Figure 5-45 Core Inlet Geometry p:f Ratio Results following "Final-Mid" Flow Profile

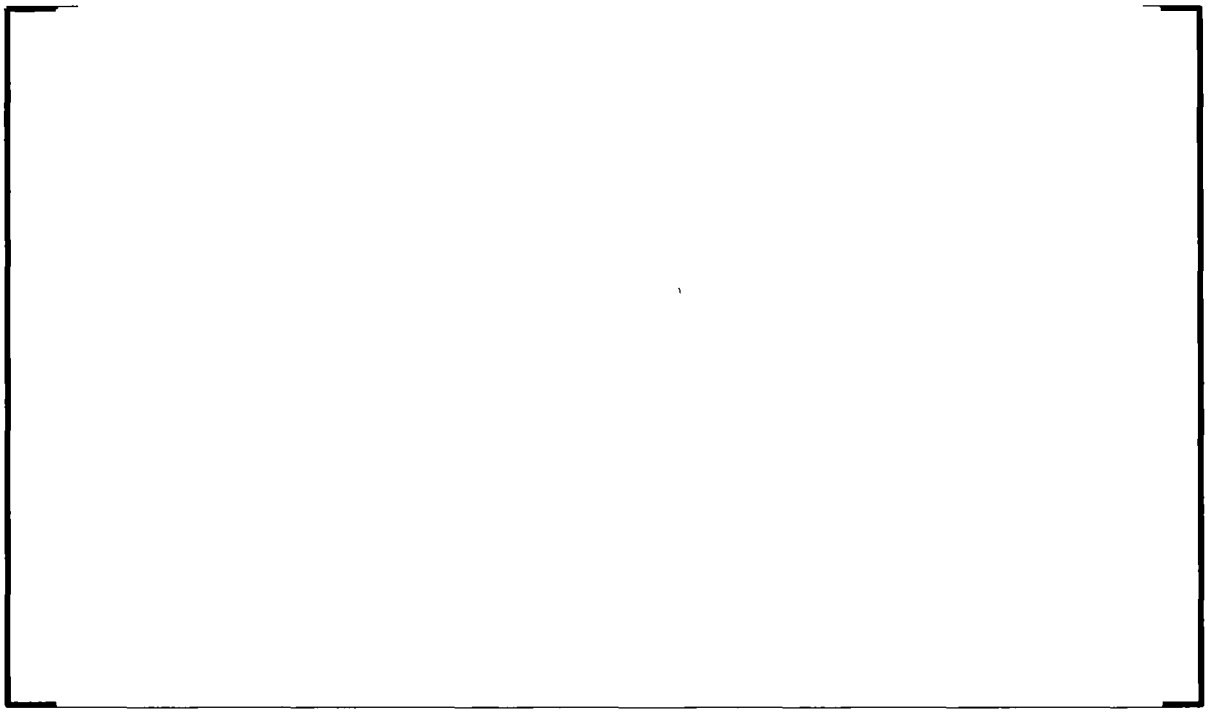

a,c

Figure 5-46 Core Inlet Geometry p:f Ratio Results following "Final-High" Flow Profile

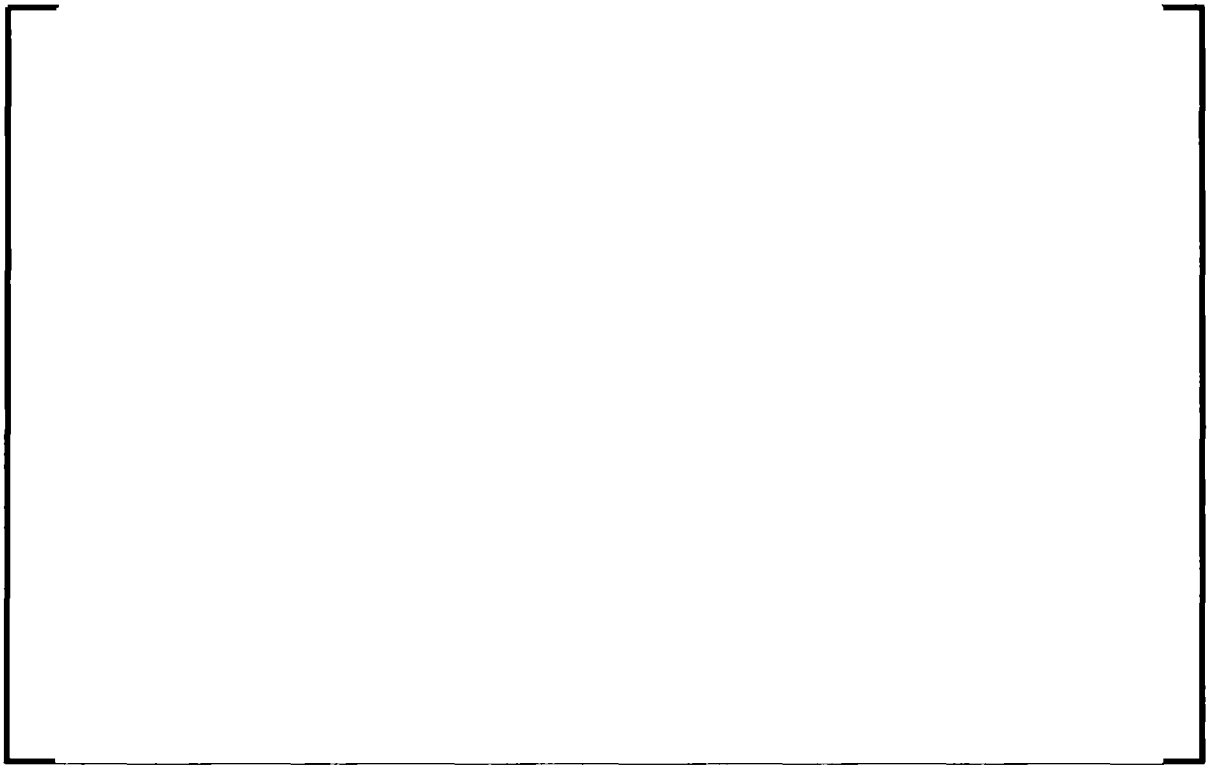

a,c

Figure 5-47 Core Inlet Geometry p:f = 12:1 Results following "Final-Low" Flow Profile

5.3.2 AREVA Core Entrance Geometry Results

For the Westinghouse BN, unstable debris beds were observed at [

]^{a,c} Given the significant differences in the AREVA FUELGUARD core inlet geometry compared to the Westinghouse BN, a similar study investigating the effect of p:f ratio and flow profile was completed for the AREVA FUELGUARD core inlet geometry described in Section 3.5.4.

Figure 5-48 through Figure 5-50 show results of the p:f ratio study performed following the "Final-Low" flow profile provided in Section 3.3. The results show [

]^{a,c}

A number of the experiments conducted using the Areva core inlet geometry resulted in conditions that exceeded the test column maximum allowable operating pressure similar to what occurred during some of the Westinghouse RFA grid studies as shown in Figure 5-33. This required the main pump speed to be reduced. For test results shown in this section, when the pressure drop exceeded 20 psi, followed by a sharp decrease in pressure drop, this was due to main pump speed reduction and not debris bed breakthrough.

For the "Final-Low" results shown in Figure 5-48 through Figure 5-50, [

]^{a,c}

After examination of the "Final-Low" flow profile results, it is apparent that the differential pressure trends are dissimilar when comparing results from the same p:f ratio at reduced total fiber mass. For lower total fiber load, results at the same p:f ratio indicate higher pressure drop. Figure 5-51 through Figure 5-54 show comparisons at different total fiber mass at the 40:1, 50:1, 65:1 and 75:1 p:f ratio conditions respectively. [

]^{a,c}

The differential pressure trend with total fiber load is consistent with the observed trend shown in Figure 5-47 for the Westinghouse BN experiments. [

]^{a,c}

To address bias [

]^{a,c}

Results following the "Final-Mid" and "Final-High" flow profiles are shown in Figure 5-56 and Figure 5-57. [

]a,c

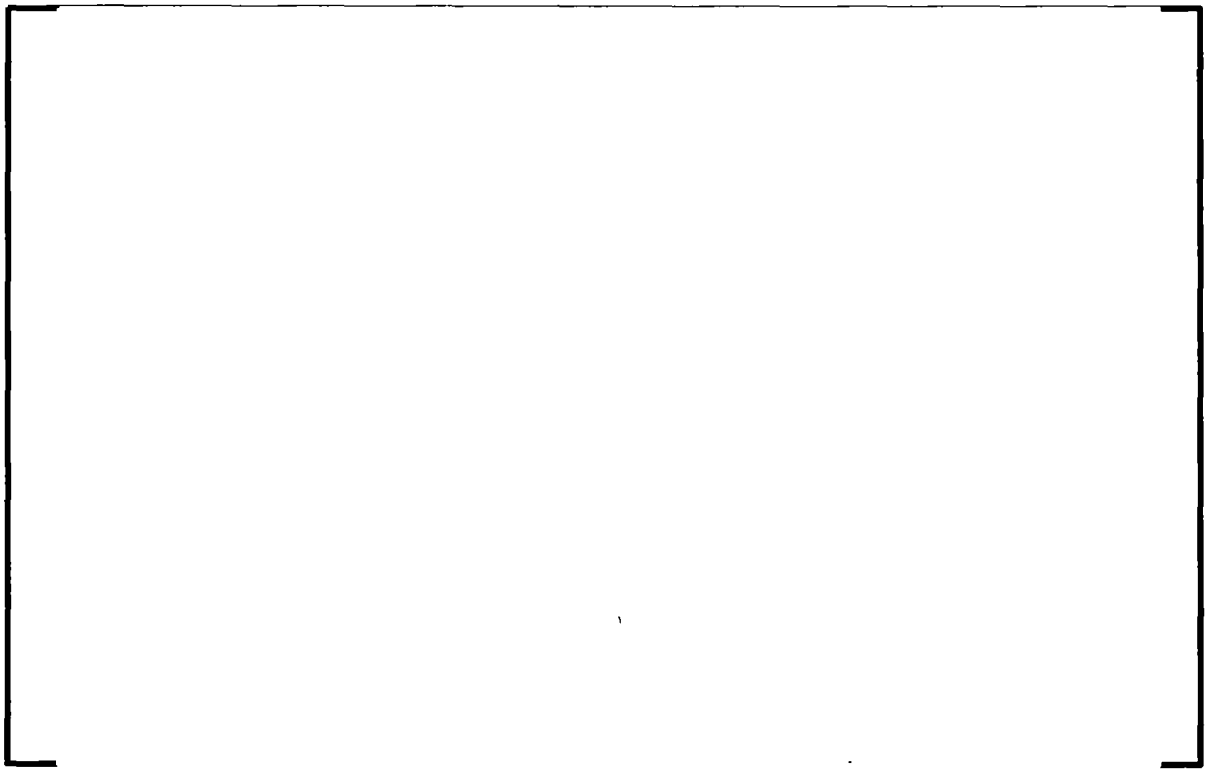

a,c

Figure 5-48 AREVA Core Inlet Low p:f Study Results following "Final-Low" Flow Profile

a,c

Figure 5-49 AREVA Core Inlet Intermediate p:f Study Results following "Final-Low" Flow Profile

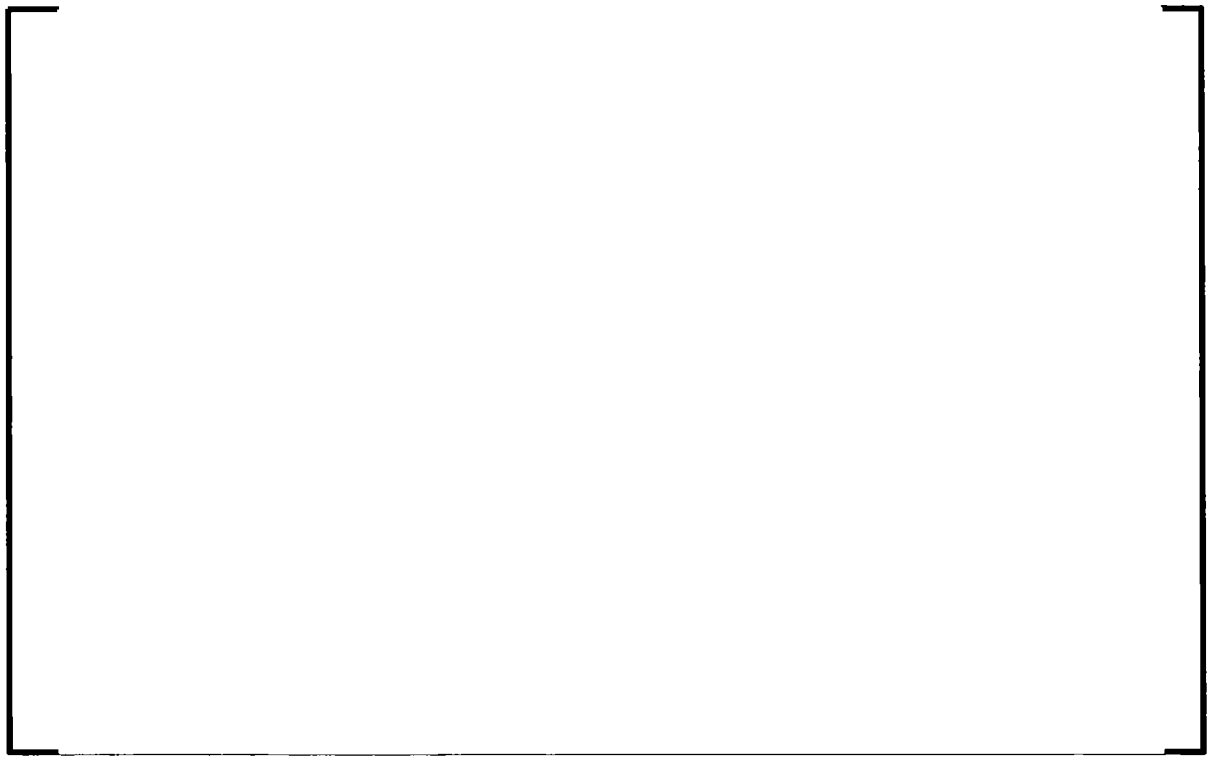

a,c

Figure 5-50 AREVA Core Inlet High p:f Study Results following "Final-Low" Flow Profile

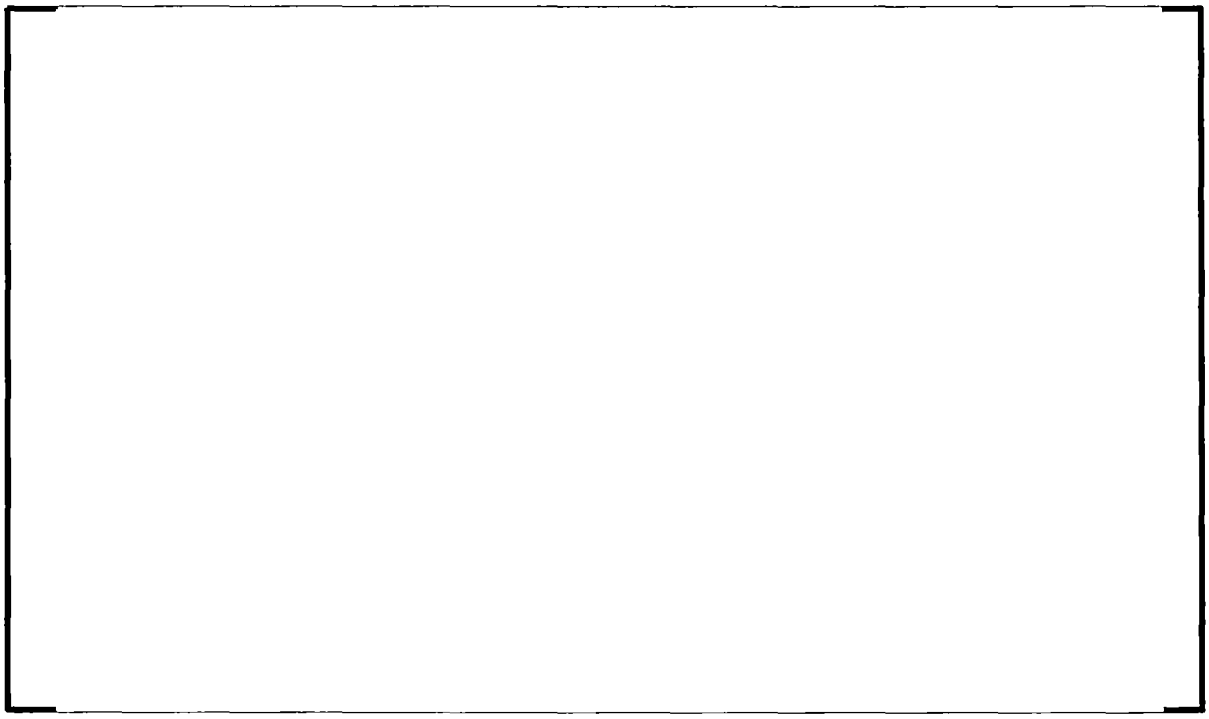

a,c

Figure 5-51 AREVA Core Inlet p:f = 40:1 Results following "Final-Low" Flow Profile

a,c

Figure 5-52 AREVA Core Inlet p:f = 50:1 Results following "Final-Low" Flow Profile

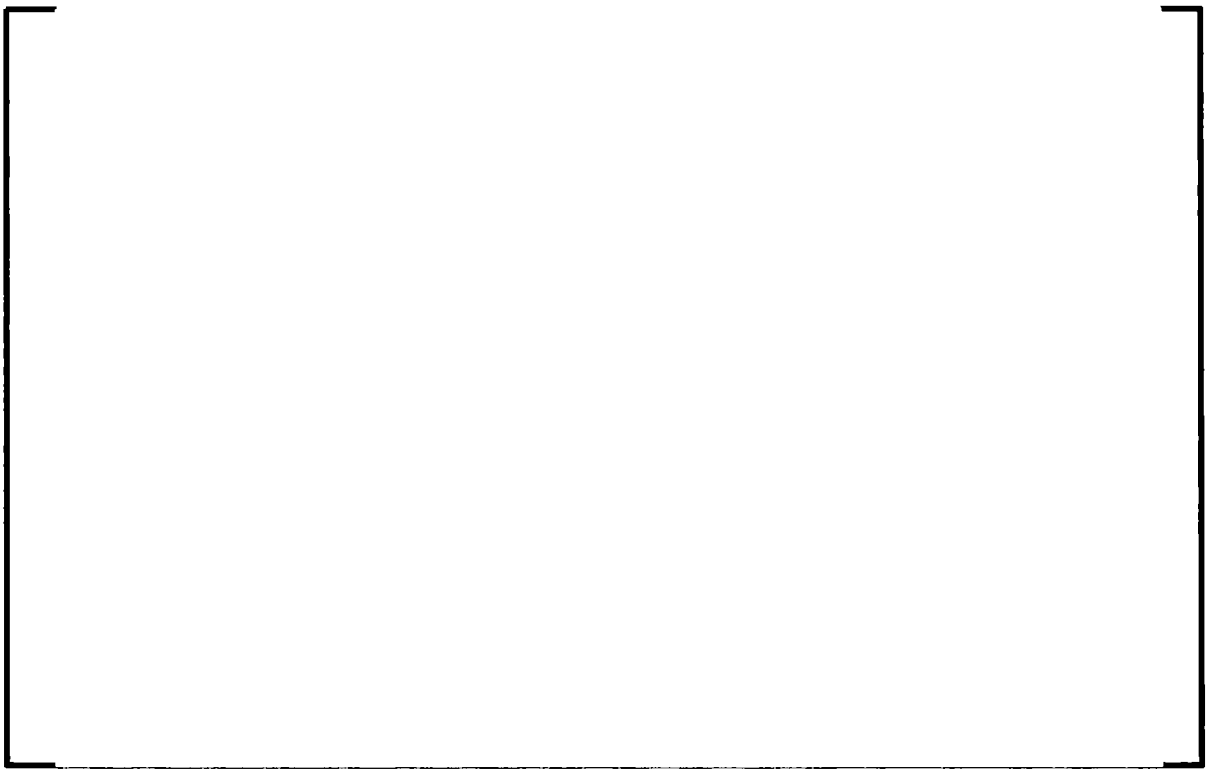

a,c

Figure 5-53 AREVA Core Inlet p:f = 65:1 Results following "Final-Low" Flow Profile

a,c

Figure 5-54 AREVA Core Inlet p:f = 75:1 Results following "Final-Low" Flow Profile

a,c

Figure 5-55 AREVA Core Inlet Limiting Conditions following "Final-Low" Flow Profile

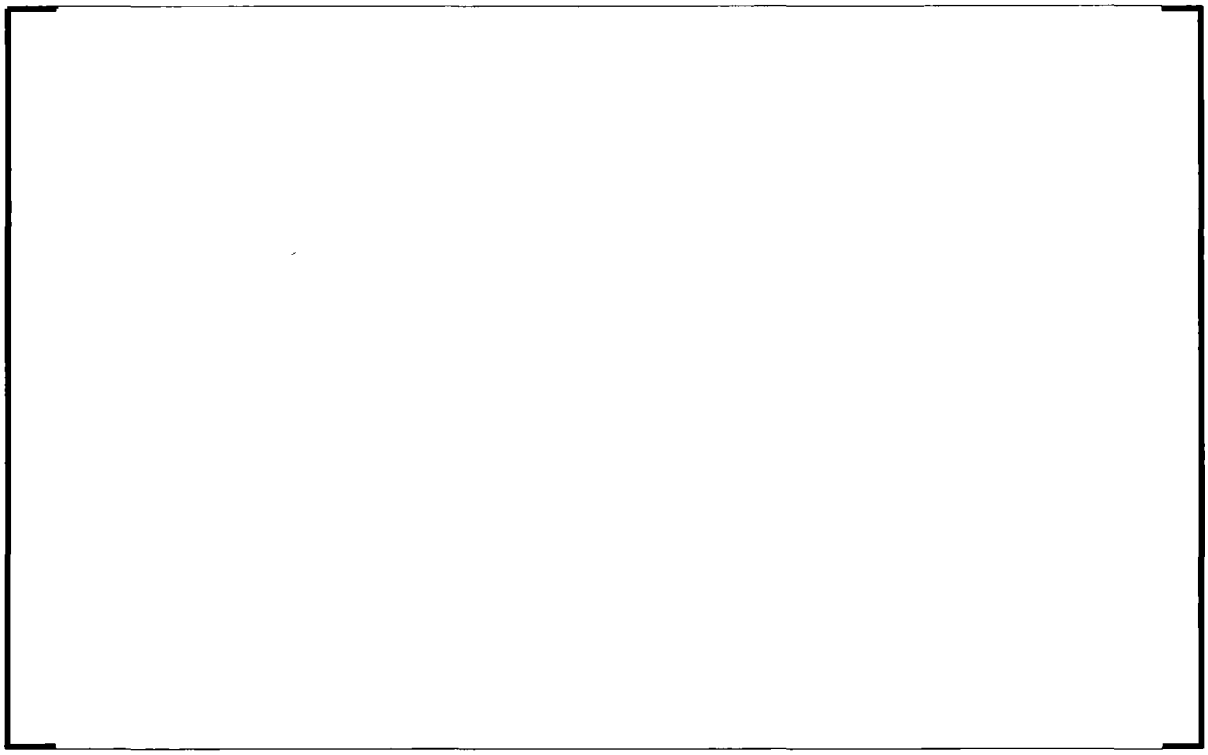

a,c

Figure 5-56 AREVA Core Inlet p:f Study Results following "Final-Mid" Flow Profile

a,c

Figure 5-57 AREVA Core Inlet p:f Study Results following "Final-High" Flow Profile

5.4 COMPARISON OF TEST RESULTS TO MODEL PREDICTION

Using the capture efficiency and bed thickness measurements, it was possible to estimate the volume average debris bed porosity. Due to uncertainty in bag filter weights, as described in Section 3.6, non-uniformities in the interior of the debris bed, assumptions necessary to estimate the particle and fiber penetration based on total capture efficiency and bed thickness measurements inaccuracy, the accuracy associated with porosity calculation is considered to be within ±30%. Acknowledging this uncertainty, there is still value associated with examining the porosity results since they can provide useful insights into the mechanisms resulting in pressure loss through the debris bed.

Figure 5-58 shows the subscale test results, including grid and lower end fitting experiments, compared to the Equation 2-11and Equation 2-13 model predictions[1]. Only test results in which bed breakthrough did not occur are shown. Based on Figure 5-58, it is clear that the Blake-Kozeny formulation of the viscous term, Equation 2-2, which is used as input to the Ergun equation, Equation 2-11, is insufficient to predict

[1] There were several assumptions necessary to calculate the void length scale, as defined in Equation 2-6, for the combined particulate and fibrous debris bed. These assumptions were not presented since results of this evaluation do not impact the limiting conditions, shown in Figure 6-1, used as input to the Volume 1 analysis.

the observed data trends. Equation 2-13 accounts for the influence of variable debris bed porosity on the viscous loss term, and explains the observed trends.

It should be noted that the predictions shown in Figure 5-58 require knowledge of the debris capture efficiency and bed thickness. Measured results were used to calculate these values. A complete pressure loss model would include a capture efficiency model and a model to account for compressibility of the debris bed, which were not developed as part of this effort. Nonetheless, the model predictions provide confidence in the data set, further evidence of localized bed breakthrough and [

]^{a,c}

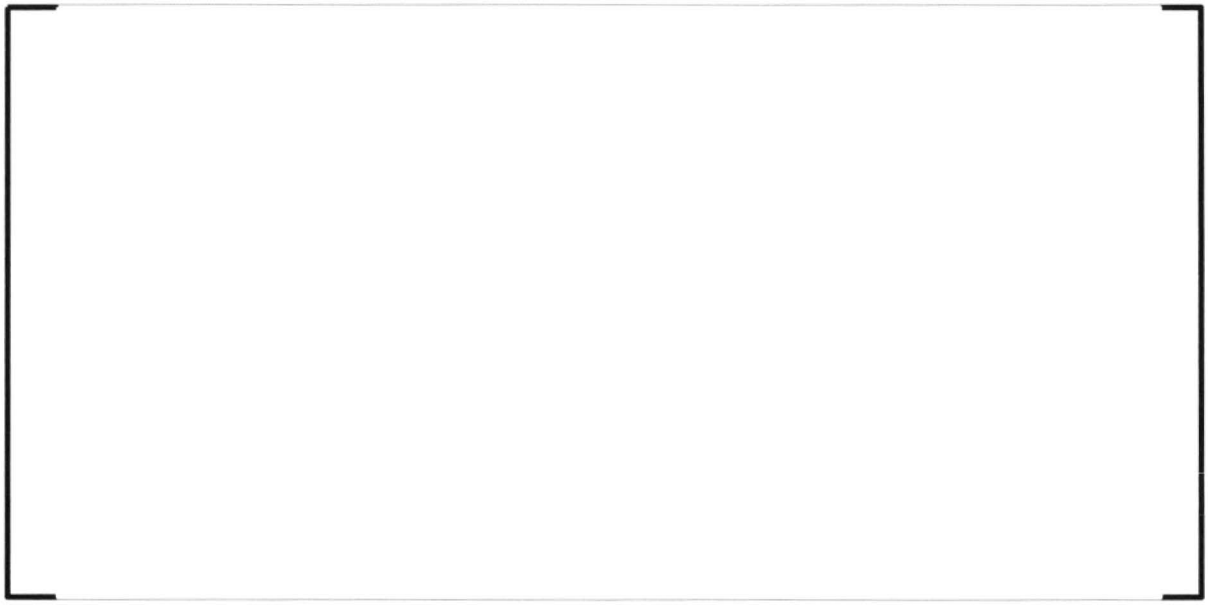

a,c

Figure 5-58 Comparison of Measurements (Excluding Unstable Bed Results) to Model Predictions

5.5 EVALUATION OF FIBER LENGTH MEASUREMENT RESULTS

Fiber length distribution was measured for several test series to assure that the length distribution was within the expected range of conditions predicted by the Reference 5-2 model. Fiber samples were drawn from the HCT prior to the addition of particulate while the HCT was being actively mixed by the impeller. After a several-step dilution process, the fiber suspension was passed through a small filter paper, which was then placed under a light microscope for image analysis. Figure 5-59 and Figure 5-60 show an example of the image analysis before and after length measurement, respectively. These results were taken from test T005. [

]^{a,c}

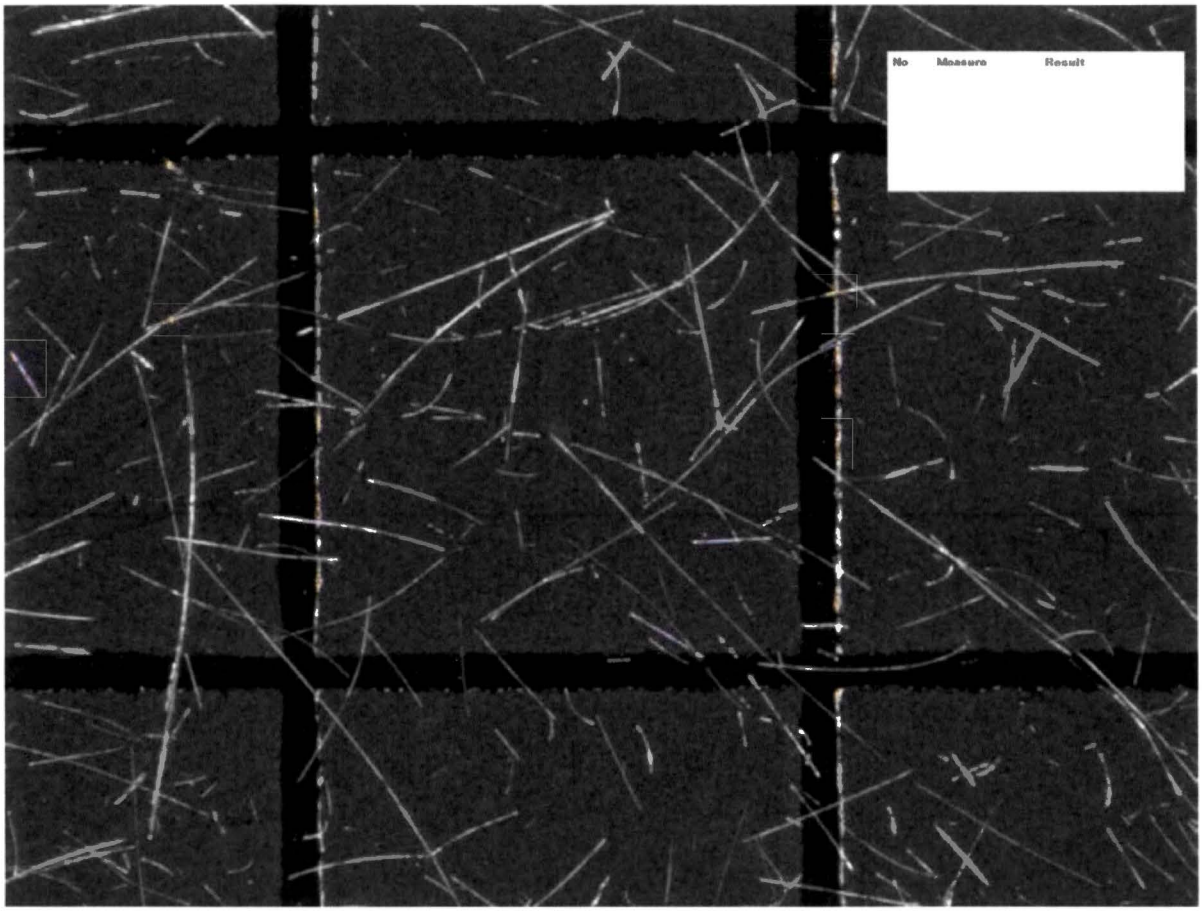

Figure 5-59 Test T005 Fiber Sample

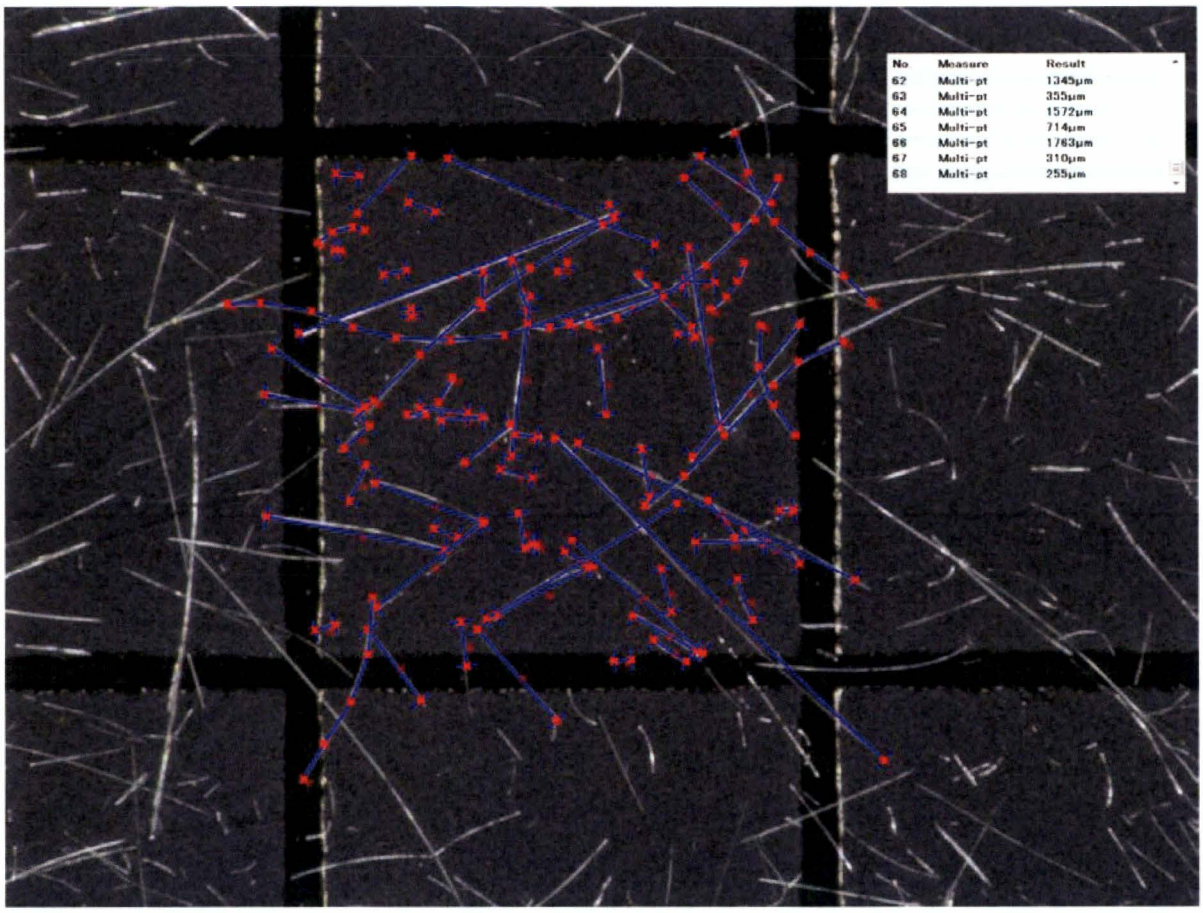

Figure 5-60 Test T005 Fiber Sample with Length Measurements Shown

For a majority of the test series, the fiber length distribution was fairly well controlled within the test series. Figure 5-61 through Figure 5-65 show fiber length distributions measured for Test Series 1 through 6. The measured length distributions are shown alongside the target length distributions as discussed in Section 3.9.1. The results were consistent and repeatable within these test series. The results demonstrate that the target fiber length distribution range was met for Test Series 1 through 6.

Figure 5-66 and Figure 5-67 show results from Test Series 57 and 59, which represent the limiting condition examined during the Westinghouse core inlet experiments. Figure 5-68 shows a comparison of the 10th, 50th and 90th percentile of the measured length distributions to the maximum measured pressure drop for each test as part of Test Series 57. Review of the measured fiber length distributions showed [

]^{a,c}

In conclusion, [

]^{a,c}

Considering this result, in addition to conclusions drawn in Section 2.2.2, it can be concluded that [

]a,c

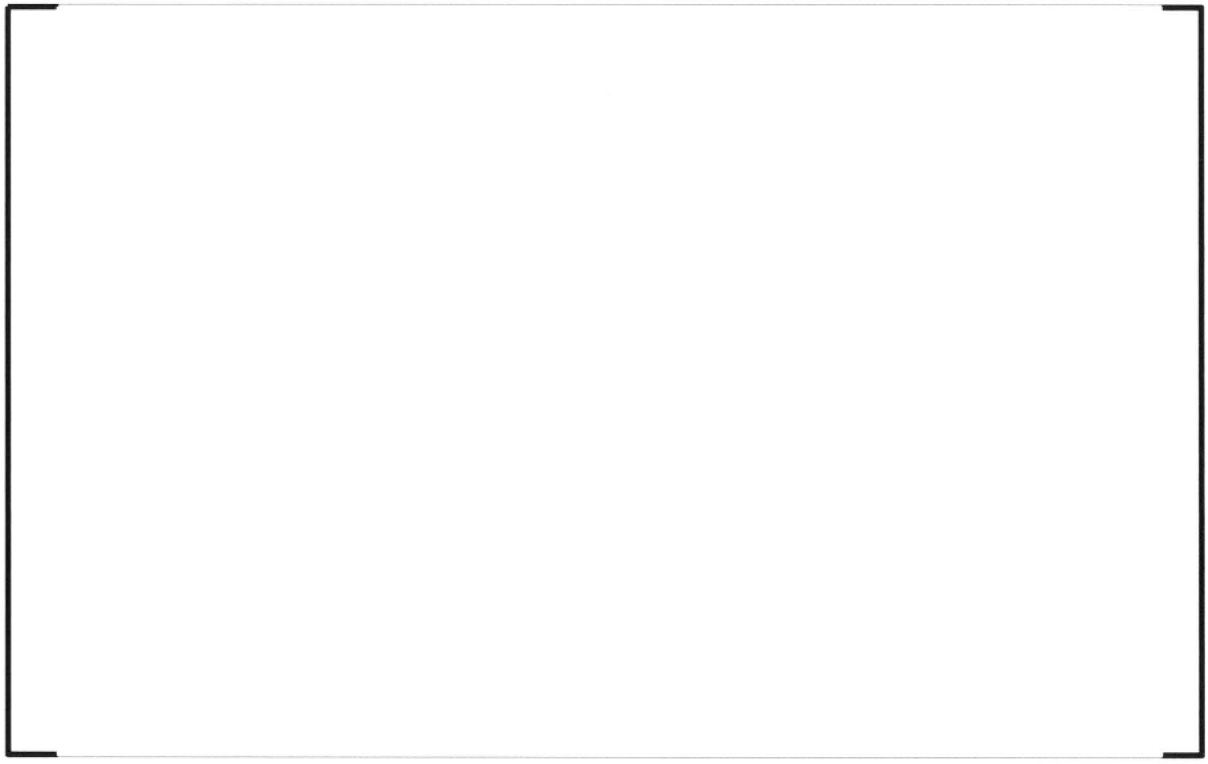

a,c

Figure 5-61 Test Series 1 Cumulative Fiber Length Distributions

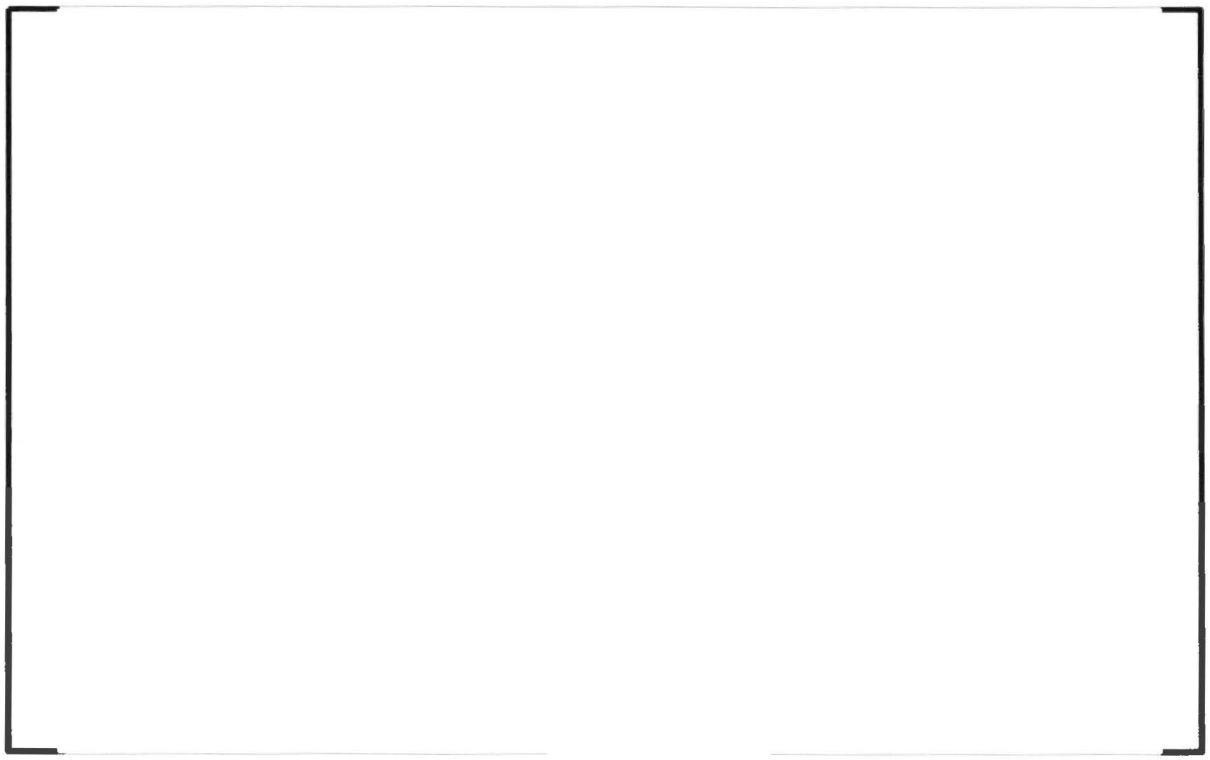

a,c

Figure 5-62 Test Series 2 Cumulative Fiber Length Distributions

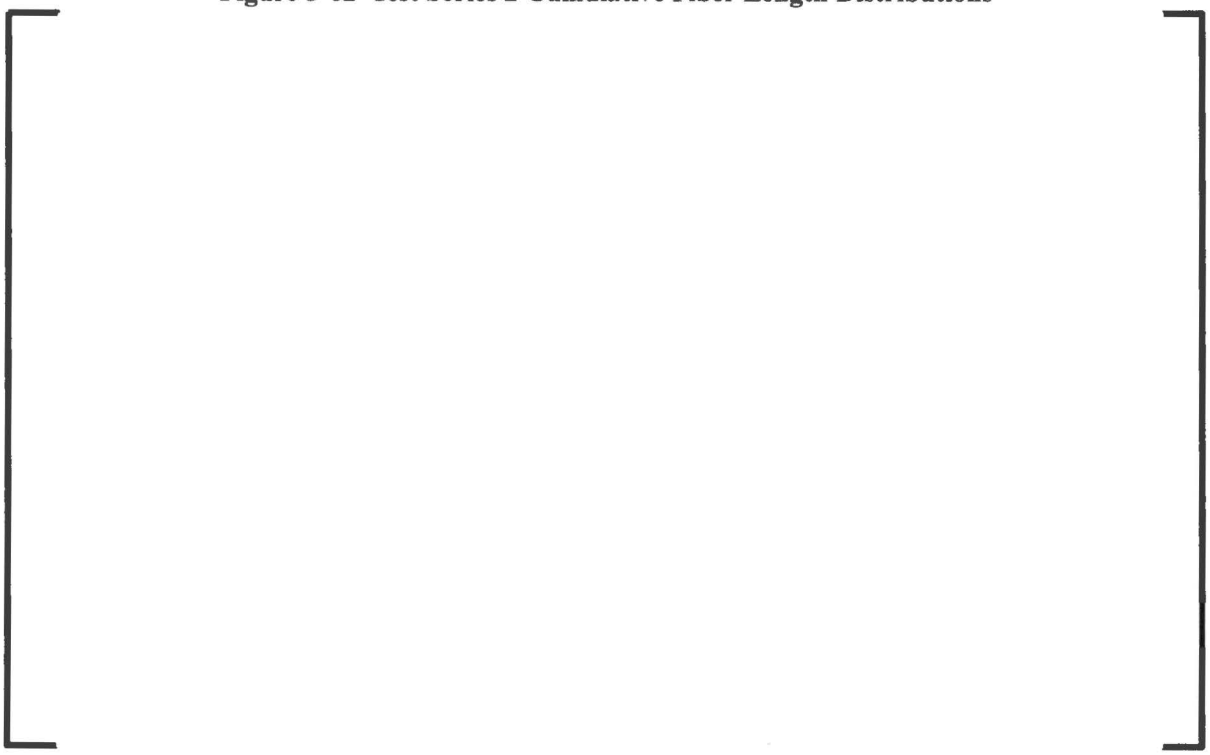

a,c

Figure 5-63 Test Series 3 Cumulative Fiber Length Distributions

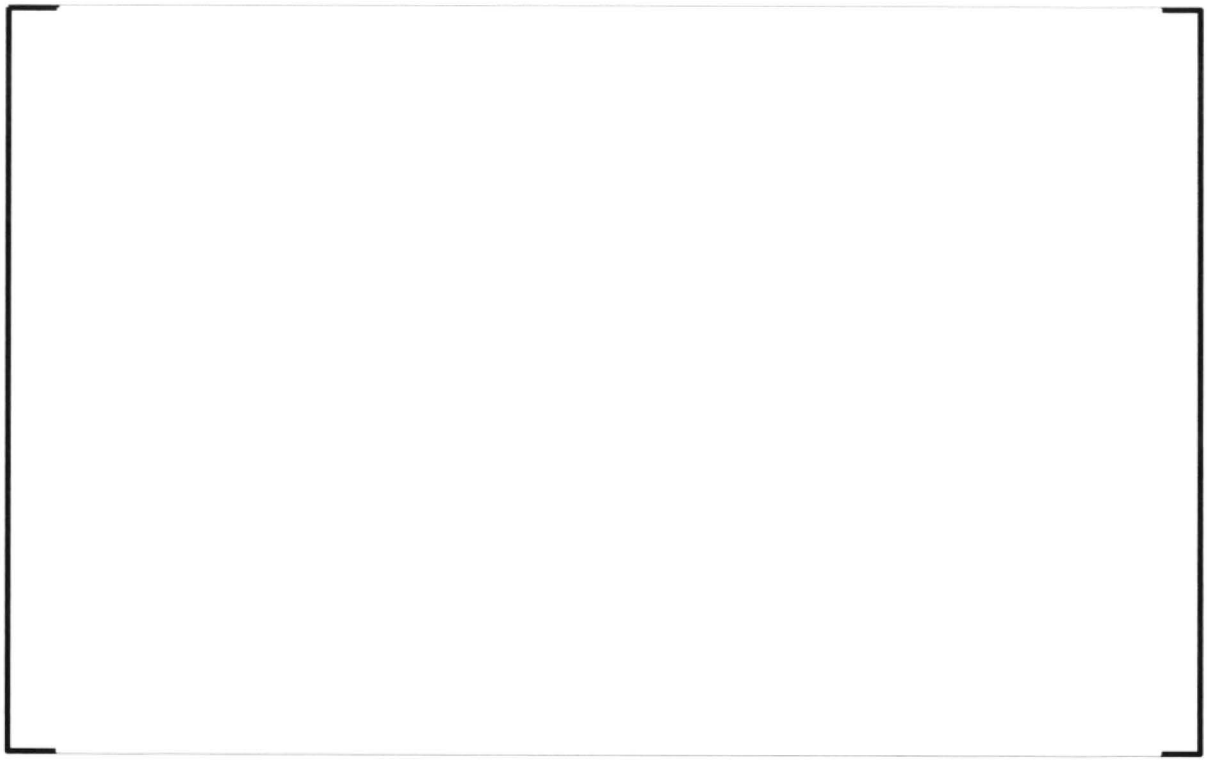

a,c

Figure 5-64 Test Series 5 Cumulative Fiber Length Distributions

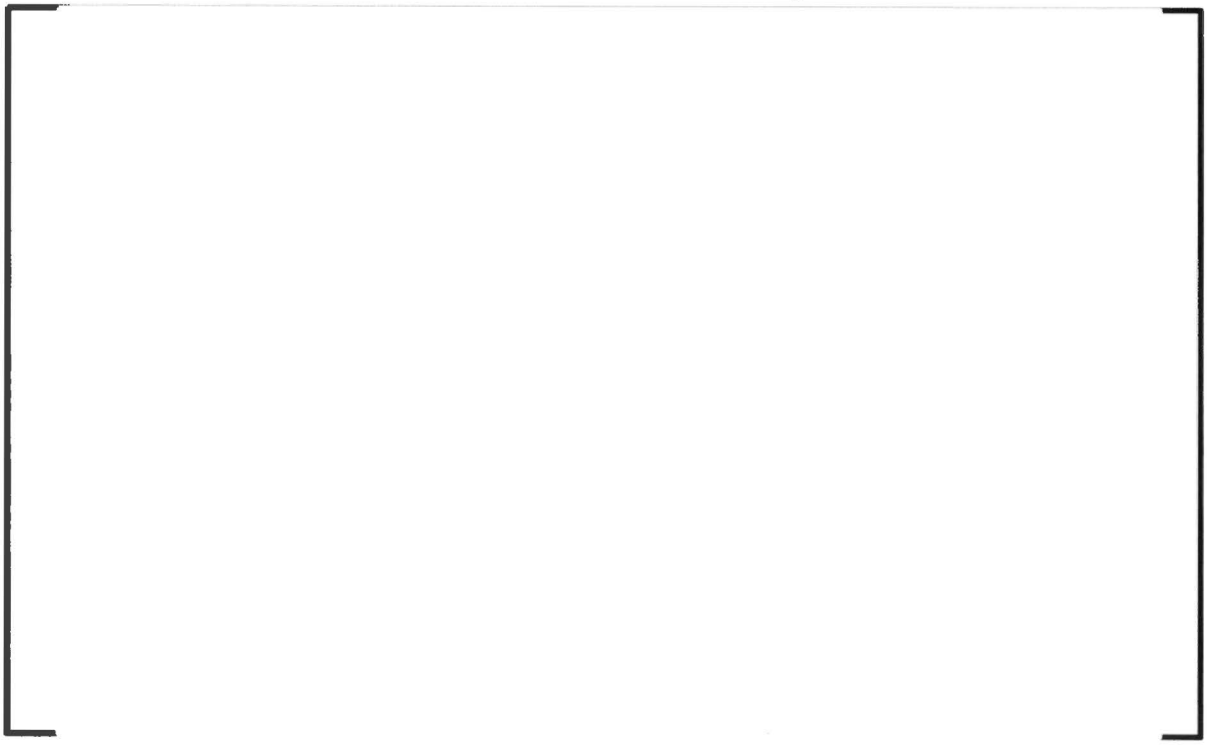

a,c

Figure 5-65 Test Series 6 Cumulative Fiber Length Distributions

a,c

Figure 5-66 Test Series 57 Cumulative Fiber Length Distributions

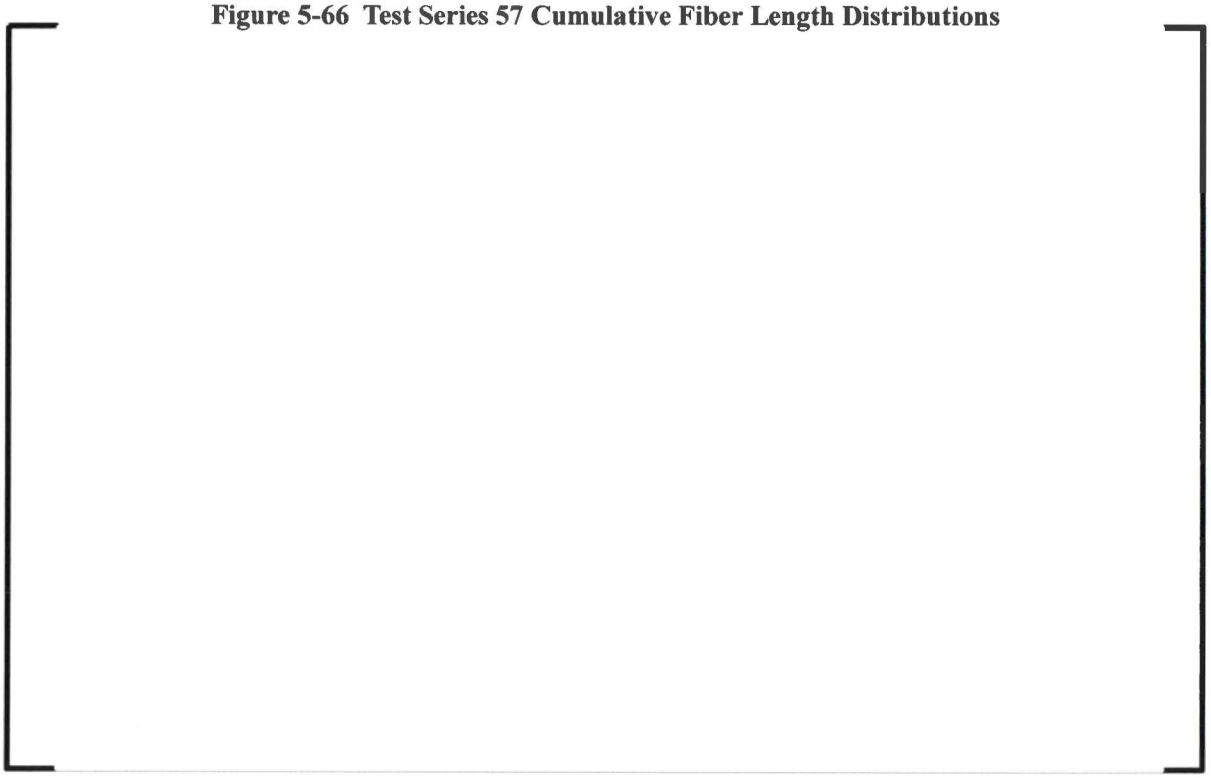

a,c

Figure 5-67 Test Series 59 Cumulative Fiber Length Distributions

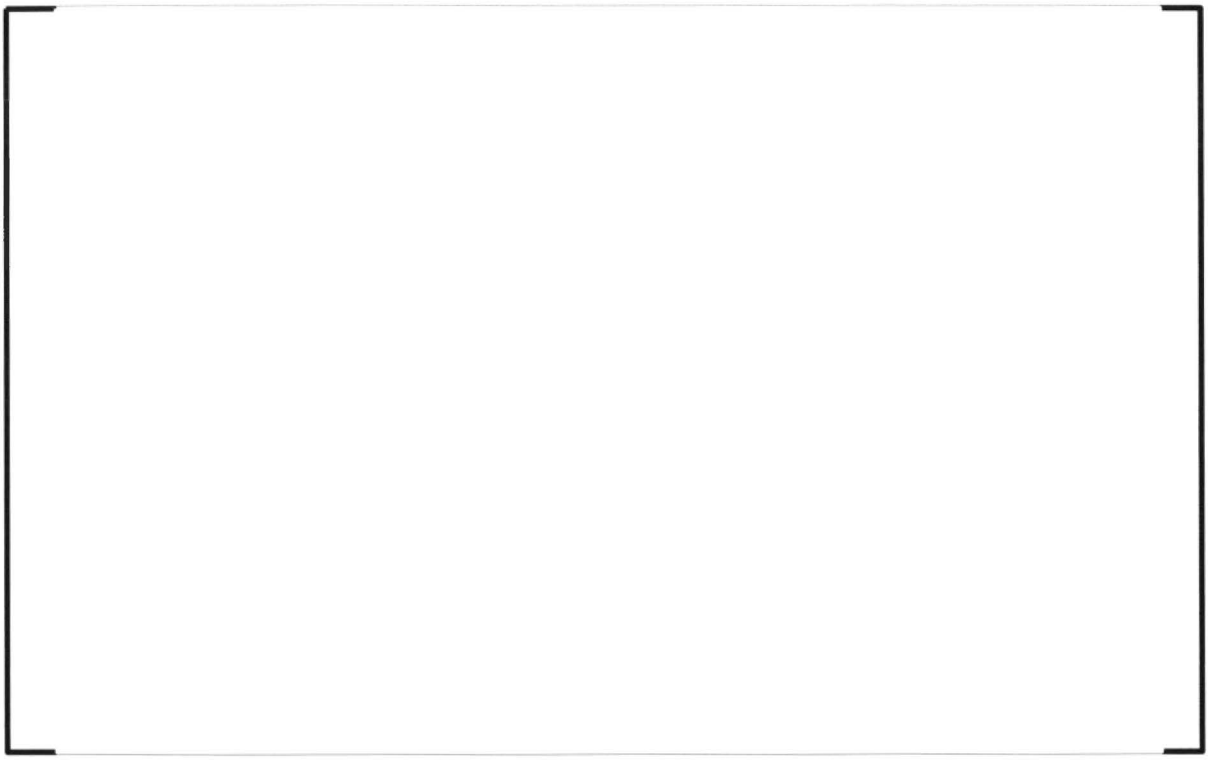

a,c

Figure 5-68 Test Series 57 Comparison of Length Distribution to Measured Pressure Drop

5.6 ALTERNATE FLOW PATH RESULTS

The AFP tests conducted confirmed that debris is not expected to block the flow passages within the AFPs considered in the Volume 1 methodology. Debris that approached the test plate far from the hole tended to accumulate on the underside of the plate, while debris that approached the plate near the hole was swept through the hole. This behavior is illustrated in Figure 5-69, which shows the test plate at the end of test 1090-AFP-T003.

The measured pressure drop showed no indications of increased losses due to the accumulation of debris on the plate during the entire duration of the tests. Figure 5-70 shows the flow rate and pressure drop evolution from test 1090-AFP-T002. As expected, the pressure drop across the test plate increases as the flow rate increases. This is due to the increased minor losses through the hole in the test plate. The pressure drop trend with flow was confirmed by predicting the measured pressure drop using the following relation:

$$\Delta P = \frac{1}{2} K \rho v^2 \qquad \text{Equation 5-1}$$

where ρ is the fluid density, K the minor loss coefficient, and v the superficial velocity. For an abrupt area change, $K = 1.4$. Density at atmospheric pressure and 130°F is 61.6 lbm/ft^3 and the velocity is calculated for the three flow conditions using the hole flow area provided in Section 3.5.5. The result is three predicted pressure drop values. The predicted pressure drops are compared to the measured

pressure drops in Figure 5-71. As the figure shows, the measured pressure drops are within 5% of the predicted values.

Figure 5-72 shows the flow rate and pressure drop evolution from test 1090-AFP-T003. Similar to 1090-AFP-T002, the pressure drop across the plate increases as flow rate increases. Similar pressure drop predictions were made using Equation 5-1 for this test. Figure 5-73 shows that the measured pressure drops compare well with the predicted values.

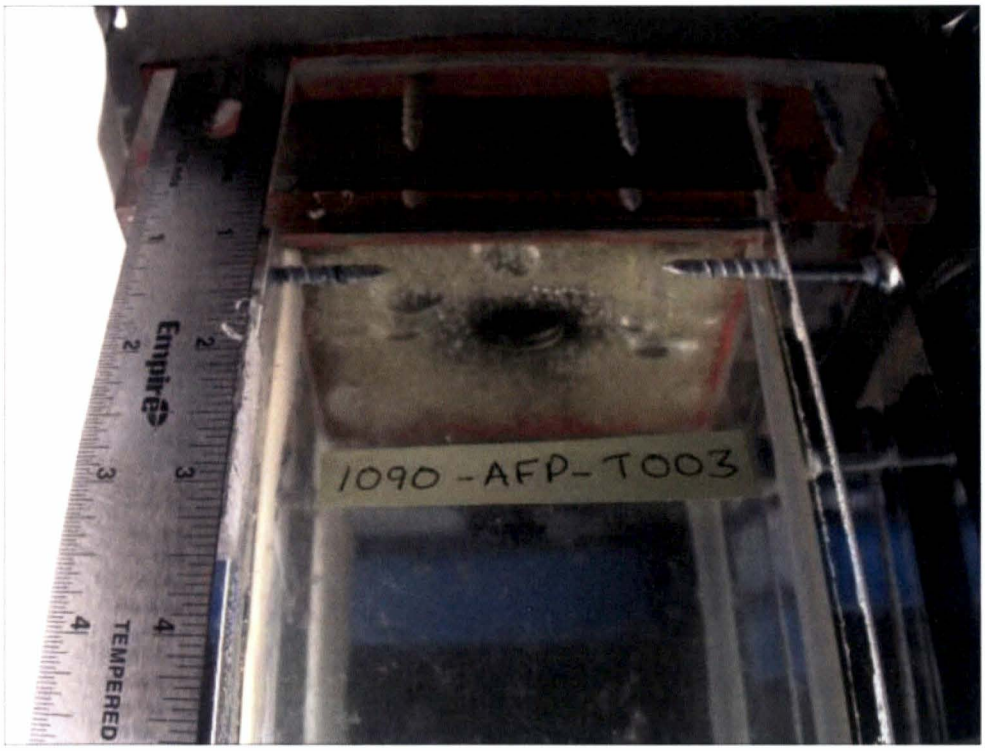

Figure 5-69 Image from the End of AFP Test 1090-AFP-T003

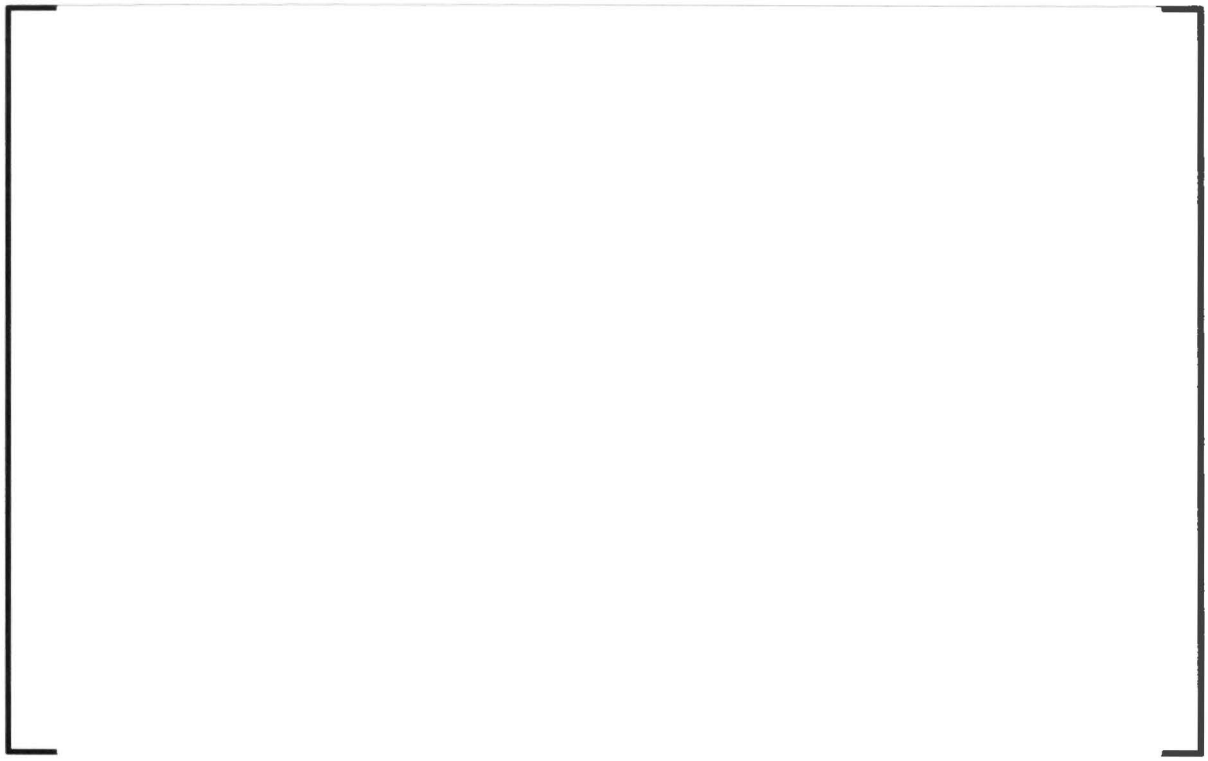

a,c

Figure 5-70 Flow Rate and Pressure Drop Evolution from AFP Test 1090-AFP-T002

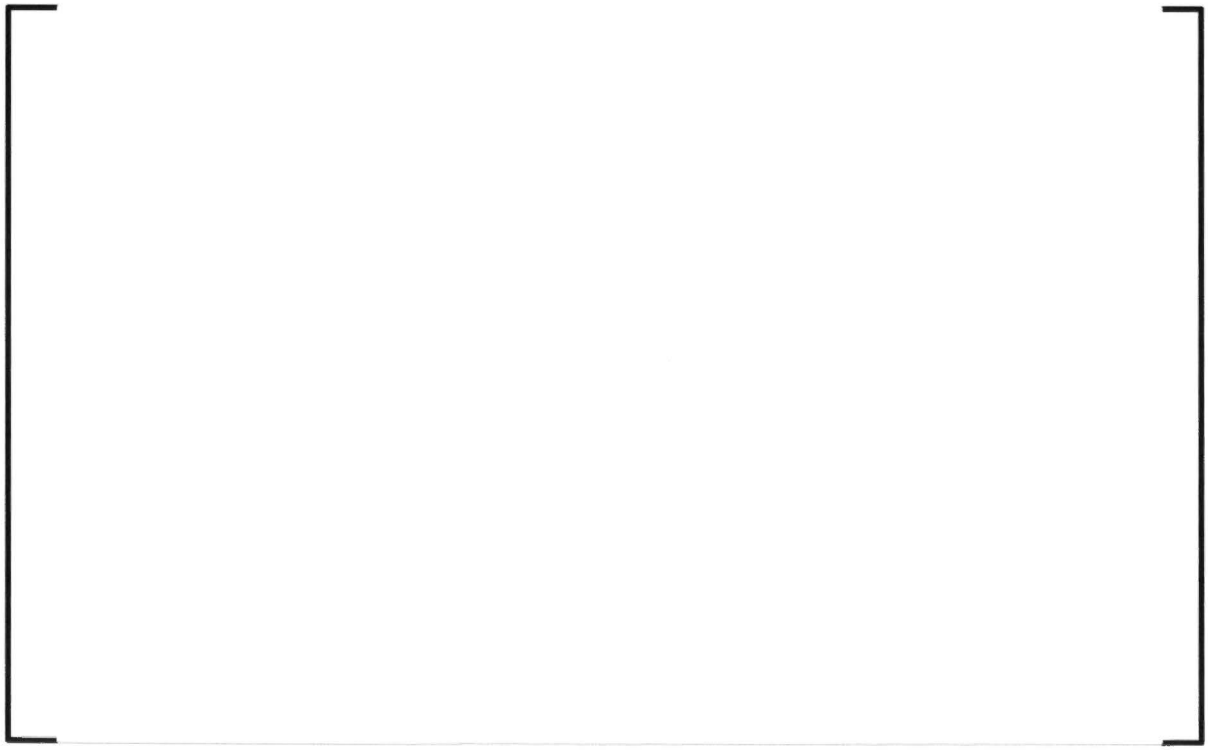

a,c

Figure 5-71 Measured versus Predicted Pressure Drop from AFP Test 1090-AFP-T002

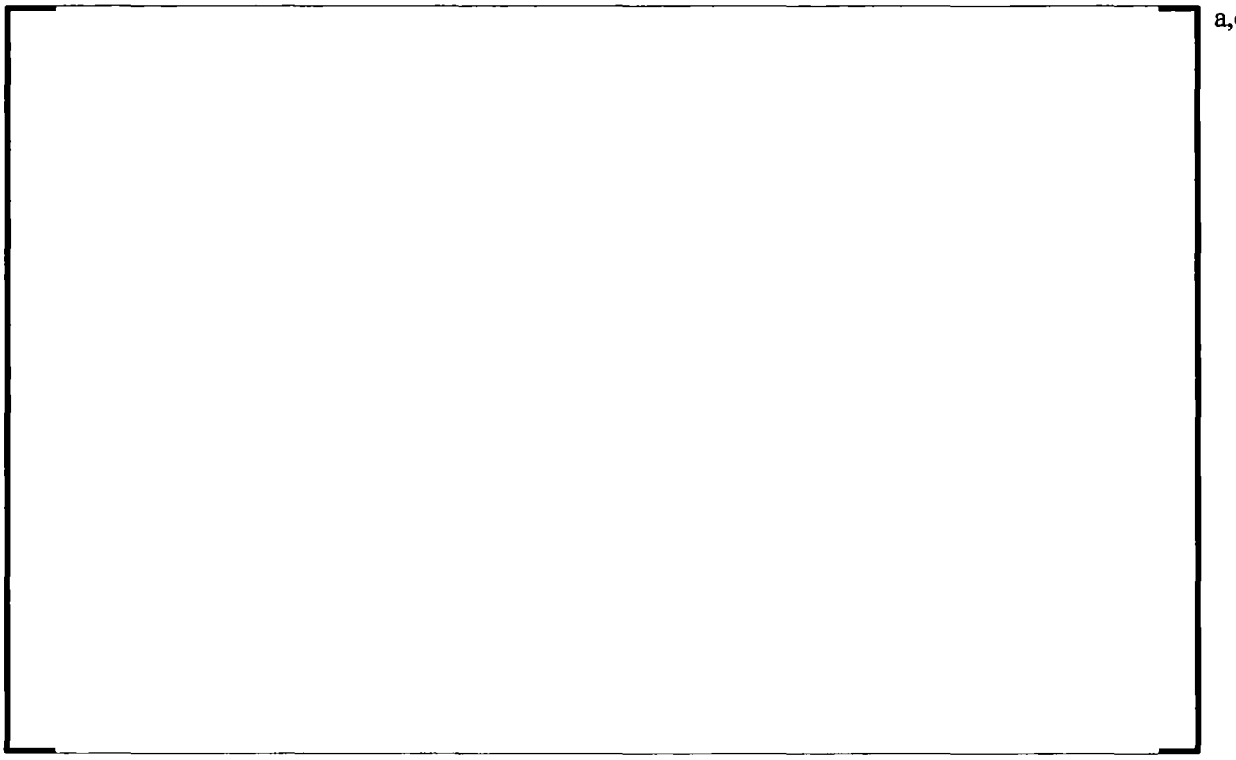

a,c

Figure 5-72 Flow Rate and Pressure Drop Evolution from AFP Test 1090-AFP-T003

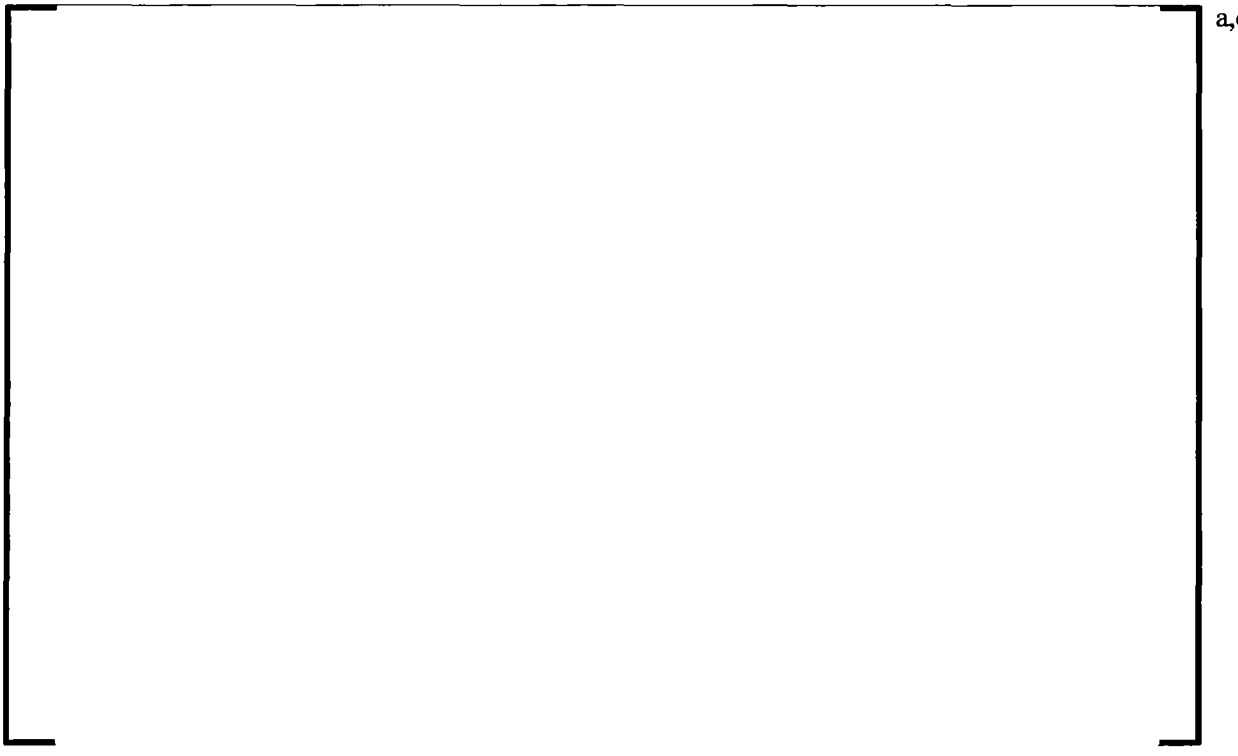

a,c

Figure 5-73 Measured versus Predicted Pressure Drop from AFP Test 1090-AFP-T003

5.7 REFERENCES

5-1 NEI-04-07, Volume 1, Revision 0, "Pressurized Water Reactor Sump Performance Evaluation Methodology," Nuclear Energy Institute, December 2004.

5-2 OG-13-218, Enclosure 1, "AREVA Document 32-9201054-000, PWR Strainer Fiber Bypass Length Distribution," May 2013.

6 APPLICABILITY OF TEST RESULTS TO PWR CORE INLET

The intent of this evaluation is to demonstrate that the subscale facility core inlet experiments, which represent an approximately one-quarter segment of a full-area FA cross section, preserve the dominant physical phenomena that influence pressure drop at the core inlet due to debris bed formation. The evaluation considers geometric, kinematic and dynamic similarities of the test facility as compared to a PWR core. For important physical phenomena that were not represented in the experiments, arguments are presented that demonstrate that experimental results obtained from the subscale facility can be considered a conservative representation with respect to pressure drop. Finally, geometric information from Section 3.5.3 and 3.5.4 are used to scale results from the Westinghouse and AREVA core inlet geometry experiments to a single FA scale, since this is the typical scale used by nuclear utilities to analyze core inlet head loss.

6.1 DEBRIS BED WALL BOUNDARY CONDITION

Space between adjacent assemblies installed in a PWR core result in long narrow gaps, which are approximately 0.04 inches wide, and gap intersections that may affect debris bed morphology and head loss. Previous testing documented in Reference 6-1 simulated this gap with a FA centered in the test vessel with a gap of approximately [

]^{a,c} at the bottom grid location. This resulted in a wall boundary condition instead of a symmetry condition, which was an unevaluated distortion of the test results.

In addition to the flow field differences at the boundary, capture geometry near the edge of the test assembly in this Reference 6-1 configuration was different than the prototypical case. The flat wall of the test vessel did not provide a ledge for fiber to capture, potentially leading to weak spots and increased fiber penetration through the debris bed around the periphery of the fuel grid which would not exist in a prototypic core. Boreholes formed at the periphery of the grid under some test conditions performed in Reference 6-1 and it is not clear that this behavior was representative.

Based on these observations, the subscale facility eliminated the wall gap and placed the gap in the central region of the test column to assure a realistic representation of the gap geometry. Test observations from the single grid and core inlet geometry with simulated gap indicated [

]^{a,c}

The subscale facility test section is enclosed by a smooth-walled test column. Very close to the wall of the test column, packing of particles and fibers is different from that at the interior of the channel. As the diameter of the flow column is reduced, this effect becomes more pronounced to the point that at very small diameters, the overall characteristics of the bed can no longer be considered similar to those of an unperturbed bed in a larger system. This problem is encountered in scaling packed-bed reactors and much research has been completed in this area for particle beds (References 6-2 through 6-4). In general, it has

been shown that maintaining a test section to debris constituent diameter ratio of 10 - 20 sufficiently minimizes this wall effect. It is ideal to minimize the dimensions of the subscale facility for practical purposes. Therefore, the edge effects associated with the test geometry walls were considered when sizing the facility.

To consider wall effects, the length scales of particulate and fibrous debris that bypass the sump were considered. Fibrous debris that is not filtered by typical sump strainers has been shown to have length distributions ranging from microns on the low end to millimeters on the high end as discussed in Section 3.9.1. Considering a 5 mm long fiber suggests that test geometry greater than 3.75 inches results in insignificant wall effects. Therefore, a square test section with 4 inch cross section was selected for the subscale facility. This dimension is sufficient to minimize wall effects associated with the test vessel.

It is noted that the wall effect should be well pronounced within the FA subchannels and grid structure. Within the FA, the rod pitch results in a length scale between rods that is less than 10 to 20 fiber lengths. Therefore, the subscale facility uses prototypic rod geometry in the vicinity of the FA grid.

6.2 DEBRIS BED PROPERTIES

To obtain similarity between the tested debris bed and what could occur locally at the core inlet to a PWR, consideration of the governing equation for flow through porous media is needed. Dimensional analysis of the pressure drop equation under consideration is provided in Section 2.2.1 and 2.2.2. The dimensionless pressure drop is represented by Reynolds number, Re, and Galileo number, Ga, both based on debris constituent diameter as well as bed porosity as defined by Equation 2-9 and Equation 2-10.

Considering prototypic debris dimensions, the Reynolds number and Galileo number are automatically preserved, assuming that the superficial velocity and debris bed porosity are preserved. By minimizing the edge effects discussed in Section 6.1 and maintaining prototypic superficial velocity throughout the experiment using the approach described in Section 3.3, the in-bed Reynolds number and Galileo number are preserved.

For Westinghouse fueled PWRs, some variation exists in the core inlet design. The tested RFA BN had [ ]^{a,c} flow holes and an open flow area ratio of [ ]^{a,c} The [

]^{a,c}

6.3 INLET BOUNDARY CONDITION

Properties of the capture geometry inlet flow field can influence the structure of a debris bed in several ways. Primarily, non-uniform transport of debris to the capture geometry can influence uniformity of the debris bed. For instance, consider flow turning and separation as flow passes through the lower core plate flow holes. This can cause some non-uniformity of the debris bed collected at the BN. This type of behavior was observed in the Reference 6-1 testing and could occur in a PWR core. Furthermore, these

effects could also occur at a larger scale. For example, consider flow turning associated with the downcomer to lower plenum transition. It is likely that a fraction of the debris transported to the core would be held up in circulation regions near this transition and remain separated, without transporting to the core inlet capture region.

For the purposes of this program, the effect of lower core plate flow holes were neglected, assuming that non-uniformities would result in less restrictive debris beds. Neglecting the lower core plate flow holes provided the most simplistic capture geometry representative of the core inlet, such that the impact of individual parameter could be evaluated with confidence. Consideration of large-scale phenomena requires simulation of core flow patterns. These effects would be difficult or impossible to consider at a small scale as discussed in Section 6.4.

6.4 EVALUATION OF RCS DYNAMICS

Dynamic similarity of the test facility as compared to a PWR core was not attempted as part of this effort. Two-phase instabilities as a result of boiling in the upper region of the core and loop seal piping that may exhibit chugging behavior may exist during recirculation phase. These phenomena would act to perturb the debris bed in a manner that would reduce capture efficiency and increase debris penetration. Multi-dimensional effects, such as those driven by radial core power distribution, would result in complex flow fields in the core that would promote non-uniformities in debris beds should they form. Given this information, it is highly unlikely that the restrictive debris beds examined as part of this experimental effort could form. Nonetheless, due to the relatively low state of knowledge associated with the RCS response to LTCC scenarios and feedback mechanisms due to debris bed formation, a solution approach which considers the possibility of uniform debris bed formation was selected.

6.5 SCALING CORE INLET TEST RESULTS TO FUEL ASSEMBLY SCALE

To simplify application of the subscale data sets to the evaluation of PWR core inlet geometry, the subscale results are scaled to a full-area FA scale, which is the typical scale used for in-vessel core inlet blockage analyses by the operating PWR fleet.

Considering the 4 inch by 4 inch cross section of the subscale test column, and the [ ]^{a,c} installed pitch of the Westinghouse RFA BN and AREVA FUELGUARD core inlet geometries, the area ratio between the subscale facility and the single FA is [ ]^{a,c} Superficial velocity through the debris bed was consistent with the range of expected conditions in a PWR. A maximum pressure drop, with respect to superficial velocity profile, was found with the "Final-Low" flow profile. Therefore, for a simplified, bounding assessment of the core response to debris bed formation as a function of fibrous debris load, results from [ ]^{a,c} can be scaled using the scaling factor of [ ]^{a,c} The scaled results are shown in Figure 6-1. The same scaling factor can be used to scale the flow rate profiles provided in Section 3.3.

a,c

Figure 6-1 Limiting Conditions Scaled to Single FA

Note that the scaling factor of [ ]^{a,c} is only applicable to fuel designs with an installed pitch of [ ]^{a,c} inches. For other fuel designs, the scaling factor must be adjusted to account for the installed pitch.

All testing was conducted at a temperature of 130°F, which is relatively low considering the early stages of hot leg recirculation examined as part of this study. Considering the effects of increased temperature, [

]^{a,c}

6.6 REFERENCES

6-1 WCAP-16793-NP-A, Revision 2, "Evaluation of Long-Term Cooling Considering Particulate, Fibrous and Chemical Debris in the Recirculating Fluid," July 2013.

6-2 Bear, J., "Dynamics of Fluids in Porous Media," Dover Publications Inc., New York, Dover Edition, 1988.

6-3 Di Felice, R. and Gibilaro, L., "Wall Effects for the Pressure Drop in Fixed Beds," Chem Eng. Sci. 59, 3037-3040, 2004.

6-4 Chu, S. and Ng, K., "Flow in Packed Tubes with a Small Tube to Particle Diameter Ratio," AIChE Journal, Vol. 35, Issue 1, 148-158, 1989.

7 SUMMARY OF RESULTS AND CONCLUSIONS

Results of this testing define limiting conditions for the collection of debris on core inlet fuel components. The results of this testing will be used as input to the overall methodology that allows PWR licensees to calculate a plant-specific in-vessel fibrous debris limit. Debris bed resistance data collected in the subscale facility is used to relate a physical debris quantity to the limiting core inlet resistances determined in the TH analyses as described in Volume 1.

Experiments documented in Section 5.2.6 define a limiting particle size distribution that resulted in the worst-case pressure drop through a fibrous debris bed developed using NUKON fibers. The existence of a peak particle size distribution was predicted to exist over the range of tested conditions based on measured fiber diameters and analysis of the effective pore size in a fibrous debris bed. Experiments confirmed the existence of a particle size distribution with an approximately [ ]^{a,c} mean diameter, which maximized the effects of straining and particle packing. Pressure drop associated with [ ]^{a,c} particulate was observed to result in an order of magnitude lower pressure drop than the [ ]^{a,c} mean diameter particulate.

Measured fiber length distributions demonstrated that fiber lengths used during the testing were consistent with those expected to transport to the core inlet following a LOCA. [

]^{a,c}

A thorough literature review identified scouring as localized debris bed instability. Debris bed breakthrough observed during the single-grid and core inlet experiments was attributed to the scouring instability. [

]^{a,c}

The scaling analysis considered debris bed morphology and edge effects associated with the test vessel wall. Near the vessel wall, a region of distorted porosity can form due to the influence of the wall on debris packing. Results from the literature review indicated that edge effects can be considered negligible when the vessel dimensions are large with respect to the debris constituents forming the porous debris bed. Based on the scaling evaluation, it was concluded that the geometric scale of the subscale facility was sufficient to minimize edge effects. Experimental observations confirmed the size of the rim to be small with respect to the test column dimension. The scaling evaluation also demonstrated that the dominant physical phenomena expected to drive debris bed head loss were either preserved, or in the cases of dynamic, system effects and multi-dimensional flows, conservatively neglected. Using the flow area ratio between the subscale and a full-area FA, it is possible to relate the subscale debris load to that of a full-area FA. Figure 6-1 in Section 6.5 provides the limiting conditions identified for the Westinghouse BN and AREVA FUELGUARD core inlet geometries scaled to a single FA scale for reference purposes.

Two subscale tests were conducted to investigate the ability of debris to block the flow passages within the AFPs considered in the methodology described in Volume 1. The tests were conducted using two hole sizes and a range of flow rates representative of the conditions expected within the AFPs. As expected, the

tests confirmed that debris will not block the flow passages within the AFPs. Debris that approaches the test plate far from the hole tended to accumulate on the underside of the plate, while debris that approached near the hole in the plate was transported through the hole. The primary reason for this behavior is due to the acceleration of the flow as it goes through the hole. The pressure drops measured during the test increased with increasing flow and it was shown that the magnitude of the pressure drop could be reasonably predicted using the simple relation provided by Equation 5-1.

APPENDIX A: REQUESTS FOR ADDITIONAL INFORMATION AND RESPONSES

The RAIs addressed herein were provided to the Pressurized Water Reactor Owners Group (PWROG) via the following document. NRC Correspondence, "Request for Additional Information Re: Pressurized Water Reactor Owners Group Topical Report WCAP-17788, 'Comprehensive Analysis and Test Program for GSI-191 Closure' (TAC No. MF6536)," June 2016, ADAMS Accession Nos. ML16105A197 and ML16105A200.

RAI-6.1

Describe the development of the flow vs. dP curves used in the test program to realistically or conservatively represent the conditions of a full scale core. The U.S. Nuclear Regulatory Commission (NRC) staff understands that the flow vs. dP inputs to the testing were developed from a full core model and applied to a partial fuel assembly. How was it determined that application of results that are averaged over a large area can be applied to the test facility without introducing significant uncertainty that could result in non-conservative conclusions?

Response

All testing reported followed representative flow versus differential pressure profiles based on observations from the comprehensive set of analyses documented in WCAP-17788, Volume 4. The WCAP-17788, Volume 4 analyses studied the impact of varied core inlet resistance on core inlet flow. Based on these analyses, a set of realistic core inlet flow response curves was developed for this test program. All curves follow a flow reduction evolution as a function of head loss, starting from different initial flow rates. These initial flow rates have been selected to cover a wide range of ECCS flows during cold leg recirculation. The flow reduction curves are shown in WCAP-17788, Volume 6, Figure 3-8 as Low, Mid, Mid2, High, Final-Low, Final-Mid and Final-High.

The first set of flow control curves (Low, Mid, Mid2, High) used in the subscale head loss single grid parametric testing was based on the thermal-hydraulic analyses completed to support development of the parameters K_{max} and t_{block}, which are input parameters used in the hot leg break in-vessel debris evaluation. In these analyses, rapid buildup of debris at the core inlet was simulated. As a result, the timing associated with activating the alternate flow path (AFP) and diverting flow from the core inlet to the AFP was very fast. Based on this response, the original flow control curves decayed as debris began to collect and create a measureable pressure drop across the debris bed.

The average core inlet velocity following core inlet blockage from Westinghouse upflow Case 3A and Case 3B is shown in Figure RAI-6.1-1. The figure shows that the inlet velocity quickly reduces from the total ECCS flow, which is assumed to go through the core prior to core inlet blockage. When the core inlet resistance reaches a constant value the inlet velocity is just below boil-off and core cooling is maintained by a combination of flow through the core inlet and flow through the barrel/baffle channel.

For Case 3A, the total ECCS flow is equivalent to a core inlet velocity of 0.54 ft/s. The core inlet resistance reaches a constant value 4800 seconds after the postulated LOCA. At this time, using Appendix K decay heat and assuming saturated inlet conditions at atmospheric pressure, the flow at the core inlet required to make-up for boil-off is 0.03 ft/s. At this time, the simulations predict a core inlet flow velocity of 0.026 ft/s which is approximately 13 percent less than boil-off. For Case 3B, the total ECCS flow is equivalent to a core inlet velocity of 0.24 ft/s. The core inlet resistance reaches a constant value 8580 seconds after the postulated LOCA. At this time, using Appendix K decay heat and assuming saturated inlet conditions at atmospheric pressure, the flow at the core inlet required to make-up for boil-off is 0.026 ft/s. The simulations predict a core inlet flow velocity which is equal to boil-off.

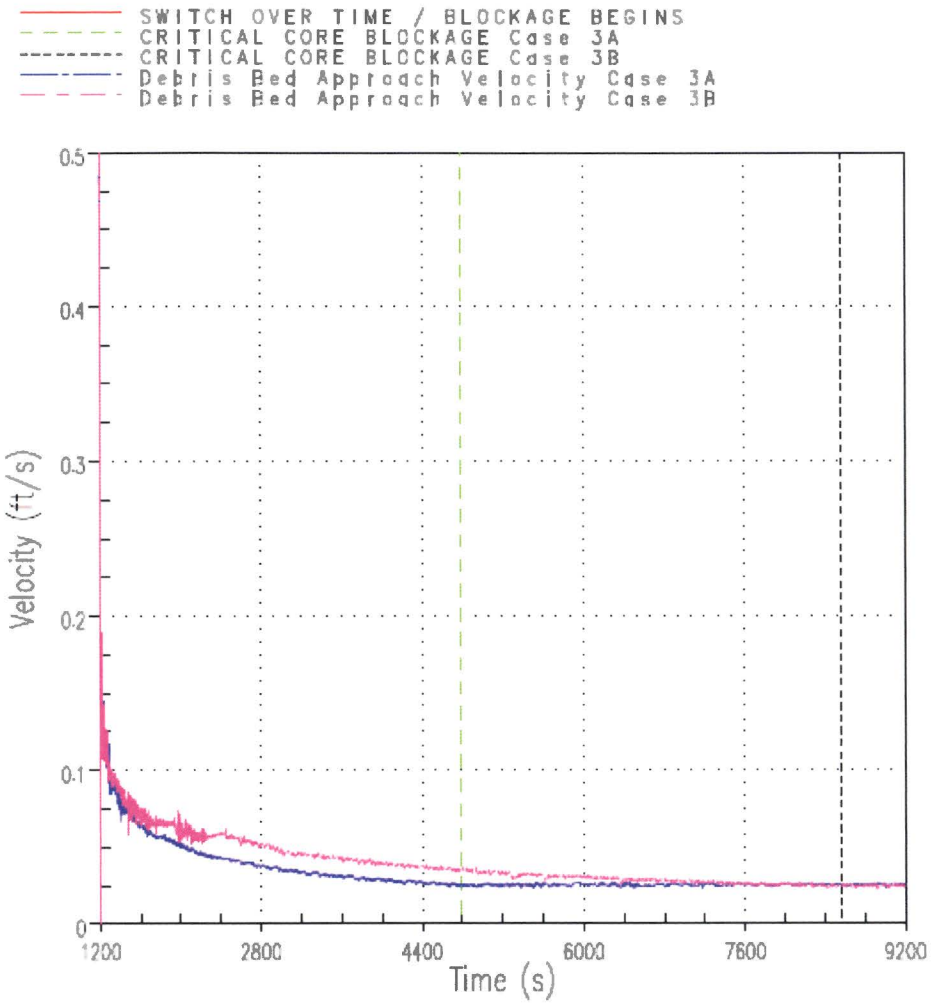

Figure RAI-6.1-1 Core Inlet Velocity during Core Inlet Blockage

Figure RAI-6.1-2 shows the core inlet velocity plotted as a function of pressure drop across the debris bed for Cases 3A and 3B. The figure shows similar curves for both cases. Based on this observation, it was determined that testing could be conducted independent of time and ECCS flow rate. However, it should be noted that the initial ECCS flow rate is different in both cases until a marginal head loss is reached at the core inlet. Therefore, the initial flow rate was varied in the subscale testing before starting the flow reduction transient.

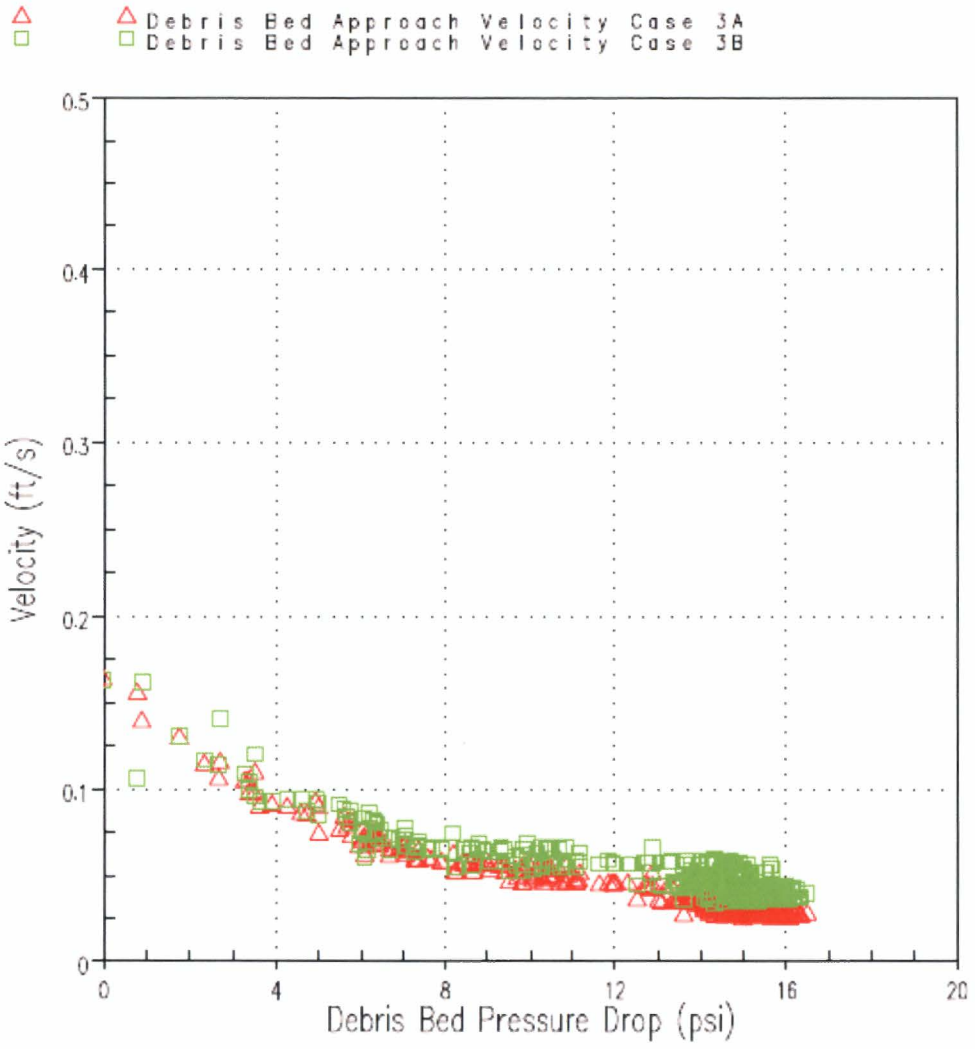

Figure RAI-6.1-2 Debris Bed Approach Velocity as a Function of Debris Bed Pressure Drop

After defining the first set of flow curves, additional thermal hydraulic analyses were completed that simulated debris buildup at the core inlet that progressed more slowly in time to define the parameters K_{split} and m_{split}, which are input parameters used in the hot leg break in-vessel debris evaluation. Analysis of these simulations allowed for a more detailed look at the flow response early in the transient. These simulations are more consistent with the buildup rates observed in the subscale testing and are therefore more appropriate for defining flow control curves for the final limits testing (Final-Low, Final-Mid, and Final-High). The primary difference between the flow responses seen in the two sets of thermal hydraulic analyses is that the activation of the AFP is delayed in time due to the slower buildup of debris at the core inlet. Based on that observation, the final limits flow control was held constant at the initial flow rate until a pressure drop of 2.5 psid is measured across the debris bed. After this point, the flow rate is reduced as a function of increasing pressure drop. Another key difference between the original flow control and the flow control defined for the final limits testing is that the three flow control curves decay to the same final flow rate; [ ]^{a,c}

The core inlet flow response to debris bed formation can vary widely for hot leg break conditions depending on the plant type, specific characteristics of the ECCS, and core inlet geometry. As resistance to flow at the core inlet increases, coolant begins to fill the downcomer and can eventually flood the cold side RCS piping and portions of the steam generators. In addition, with an increase in flow resistance at the core inlet, a larger portion of the total ECCS flow is diverted through AFPs. Finally, variations in plant geometry (e.g., barrel/baffle flow resistance) and ECCS design make a generic coverage of possible plant responses extremely difficult and potentially overly conservative.

Considering the complexity of the problem, all scenarios could not be examined. However, all tested profiles are realistic and could occur during the LTCC phase of a postulated LOCA. By defining a range of flows, the experimental results cover a wide range of conditions. Given the broad range of flow profiles tested, any significant influence of flow response on debris bed formation and resulting head loss were identified.

The application of averaged core inlet velocities from a core-wide model to determine the subscale flow profiles is appropriate given the effect of core inlet blockage on core inlet velocity. In the WCAP-17788, Volume 4 thermal hydraulic analyses, core inlet resistance due to the accumulation of debris is applied uniformly across the entire core inlet. This uniform application of debris across the core inlet may not be realistic as it is expected that debris will accumulate proportional to the flow through the core inlet. As seen in WCAP-17788, Volume 4, thermal hydraulic analyses completed without the simulation of core inlet blockage demonstrate that there will be some flow distribution at the core inlet. In fact, it is possible that downflow could exist at the inlet to peripheral fuel assemblies. However, application of a uniform blockage across the entire core in the simulations is conservative since this scenario will lead to the highest head loss across the entire core inlet. As the results in WCAP-17788, Volume 4 demonstrate, the application of uniform core inlet resistance under large hot leg break conditions leads to a uniform velocity profile across the entire core inlet. As such, the average core inlet velocity is representative of the entire core inlet and is applicable to a scaled down test facility that creates a uniform blockage.

RAI-6.2

Provide a comparison between the results of the WCAP-17788 test program and the WCAP-16793 test program (pre-chemical results). Are any tests (including informational or preliminary tests that may not have been included in the test report) comparable from a debris loading and test velocity perspective? If so, how do the results compare? The NRC staff recognizes the differences in test methods and conditions between the two programs, but concluded that a comparison of the new testing to testing under somewhat similar but larger scale conditions could provide additional justification for use of a smaller scale test facility.

Response

Given the large differences in test methods and conditions between the WCAP-17788 program and the WCAP-16793-NP-A, Revision 2 (Reference RAI-6.2-1) program, a direct comparison of pressure drop results is difficult. The following major differences between the two test programs are identified:

- Debris Addition Procedure – In the subscale testing, fibrous and particulate debris was injected into the test section concurrently and the debris addition was once-through (i.e., debris that did not capture during the first pass through the test section was not recirculated through the test section). In the full-area fuel assembly testing (WCAP-16793), particulate debris was added first followed by fibrous debris and the debris was recirculated through the test section until a stable pressure drop was achieved.
- Flow Control – In the subscale testing, the flow rate through the test section was reduced as the measured pressure drop across the debris bed increased. In the full-area testing, the flow rate was held constant throughout the test.
- Test Geometry – In the subscale testing, only two spacer grids were installed downstream from the bottom nozzle. Further, the test geometry was sealed against the flow housing walls such that debris bypass around the test geometry was minimized. In the full-area fuel assembly testing (WCAP-16793), 4-5 grids were installed above the bottom nozzle, and a gap was maintained around the test section and flow housing which promoted debris bypass.

Despite the differences, by examining the trends and behavior observed in the two test facilities, it is possible to draw conclusions that support additional justification for use of a smaller test facility. While not explicit or exact, for tests conducted with similar debris loadings and test velocities, discrepancies between the pressure drop results can be explained by the differences described above.

Table RAI-6.2-1 provides a comparison of several tests from the two programs completed with similar test conditions. The following sections provide a discussion of each test comparison.

<u>WCAP-17788 Test Series 44 versus WCAP-16793 Test No. CIB42</u>

As shown in Table RAI-6.2-1, subscale Test Series 44 (TS44) was conducted with debris loading of 56 grams per fuel assembly (g/FA) and a particulate loading of 560 g/FA (particulate-to-fiber ratio = 10 (p:f = 10)). Comparatively, WCAP-16793 CIB42 was conducted with debris loading of 50 g/FA and a particulate loading of 50 g/FA (p:f = 1). As such, the fibrous debris loadings are comparable but the total injected particulate load is an order of magnitude higher in the subscale test series.

TS44 was conducted with a variable flow velocity. The test began at a flow velocity of 0.8 ft/s and ended with a flow velocity of 0.05 ft/s. CIB42 was conducted with a constant flow velocity of 0.07 ft/s, which is in the range of flow velocities used in TS44.

Four tests were completed at the TS44 test conditions and a single bed was formed on the upstream surface of the Westinghouse bottom nozzle in every test. CIB42 consisted of a single test and two debris beds were formed.

Table RAI-6.2-1 shows that the pressure drop measured in TS44 was more than 3 times higher compared to CIB42, which can be attributed to the facts that: (1) the p:f ratio was higher in TS44, and (2) a single debris bed formed in TS44 compared to multiple beds in CIB42.

WCAP-17788 Test Series 48 versus WCAP-16793 Test No. CIB43

As shown in Table RAI-6.2-1, subscale test TS48 was conducted with debris loading of 56 grams per fuel assembly (g/FA) and a particulate loading of 560 g/FA (p:f = 10). Comparatively, WCAP-16793 CIB43 was conducted with debris loading of 50 g/FA and a particulate loading of 750 g/FA (p:f = 15). As such, the fibrous debris loadings are comparable and the particulate load was higher in CIB43.

TS44 was conducted with a variable flow velocity. The test began at a flow velocity of 0.13 ft/s and ended with a flow velocity of 0.1 ft/s. CIB 43 was conducted with a constant flow velocity of 0.07 ft/s, which is lower than the flow velocity in TS44 across the entire test duration.

One test was completed at the TS48 test conditions and two debris beds were formed. The majority of the debris collected on the upstream surface of the Westinghouse bottom nozzle with some debris collecting on the upper spacer grid. CIB43 consisted of a single test and four debris beds were formed.

Table RAI-6.2-1 shows that the overall test section pressure drop measured in TS48 was higher than the total fuel assembly pressure drop obtained in CIB43 even though twice as many debris beds were formed in CIB43. However, the pressure drop measured across the bottom nozzle in TS48 was more than two times higher compared to CIB43.

WCAP-17788 Test Series 55 versus WCAP-16793 Test No. CIB02

As shown in Table RAI-6.2-1, subscale test TS55 was conducted with debris loadings of 56 grams per fuel assembly (g/FA) and a particulate loading of 1680 g/FA (p:f = 30). Comparatively, CIB02 was conducted with debris loading of 53 g/FA and a particulate loading of 1361 g/FA (p:f = 25). As such, the debris loadings are comparable with the particulate load in TS55 only slightly higher.

TS55 was conducted with a variable flow velocity and had a starting flow velocity of 0.23 ft/s and an ending velocity of 0.17 ft/s. CIB02 was conducted with a constant flow velocity of 0.2 ft/s, which is in the range of flow velocities used in TS55.

One test was completed at the TS55 test conditions and two debris beds were formed. The majority of the debris collected on the upstream surface of the Westinghouse bottom nozzle with some debris collecting on the upper spacer grid. CIB02 consisted of a single test and four debris beds were formed.

Table RAI-6.2-1 shows that the overall test section pressure drop measured in TS55 is just over 2 psid less than the total fuel assembly pressure drop measured in CIB02. The bottom nozzle pressure drop is more comparable with the measured pressure drop from TS55 being approximately 1 psid higher.

WCAP-17788 Test Series 59 versus WCAP-16793 Test No. CIB30

This comparison is provided at a low flow condition. TS59 was conducted with a total fibrous debris load of 35 g/FA; however, the comparison is made at the point in the test where the total injected fibrous debris load is 18 g/FA, which is the same fibrous debris loading used in CIB30. Assuming that the particulate injection is uniform with the fibrous debris, the particulate load at this point in the test is approximately 216 g/FA (p:f = 12:1). CIB30 was conducted with a particulate load of 270 g/FA (p:f = 15:1). As such, the debris loadings are comparable with the particulate load in CIB30 only slightly higher.

TS59 was conducted with a variable flow velocity and had a starting flow velocity of 0.06 ft/s and the flow velocity at a fibrous debris loading of 18 g/FA is 0.06 ft/s. CIB30 was conducted with a constant flow velocity of 0.01 ft/s, which is lower than the flow velocity in TS59.

Three tests were completed in TS59 and in all tests a single debris bed was formed on the upstream surface of the Westinghouse bottom nozzle. In CIB30 a single debris bed on the bottom nozzle was also formed. Table RAI-6.2-1 shows that the measured pressure drop at 18 g/FA in TS59 is comparable to the measured pressure drop from CIB30 even though the flow velocity in TS59 is higher.

WCAP-17788 Test Series 83 versus WCAP-16793 Test No. 2-FG-FPC

As shown in Table RAI-6.2-1, subscale test TS83 was conducted with debris loadings of 21.5 grams per fuel assembly (g/FA) and a particulate loading of 860 g/FA (p:f = 40). Comparatively, 2-FG-FPC was conducted with debris loading of 18 g/FA and a particulate loading of 810 g/FA (p:f = 45). As such, the debris loadings are comparable.

This comparison is made at the end of TS 83 when the main column flow pump was turned-off and the only source of flow through the test column was from the debris injection pump. As shown in Table RAI-6.2-1, the resulting flow velocity at this point in TS 83 is comparable to the constant flow velocity used in 2-FG-FPC.

Both tests in this comparison used the same AREVA lower end fitting (bottom nozzle), and the fibrous and particulate debris quantities were similar. However, results from the two tests are different. In TS 83, a single debris bed formed on the lower end fitting, while in test 2-FG-FPC, no debris accumulated on the lower end fitting, and a single debris bed formed on the first spacer grid. This comparison illustrates that the subscale test setup and procedures, using the AREVA fuel components, promoted debris capture on the lower end fitting, which results in a higher pressure drop than what was observed in the WCAP-16793 test program.

Conclusions

As demonstrated by the comparisons presented above, it is difficult to directly compare pressure drop results from the WCAP-17788 program to the WCAP-16793 program because of differences between the test methods and test conditions. However, it is possible to explain the discrepancies in the comparisons by understanding the differences between the two test programs. As such, it is possible to reach conclusions that support additional justification that use of the subscale test facility results in overall head loss results that are conservative relative to the WCAP-16793 test program:

- TS44 resulted in a higher pressure drop compared to CIB42, which can be attributed to two factors: (1) a single debris bed was formed on the surface of the bottom nozzle, and (2) the particulate load was higher. Although the initial flow velocity was higher in TS44, a single debris bed was still formed at the bottom nozzle. This behavior indicates that fibrous debris is less likely to penetrate through the subscale core entrance geometry and/or bypass through the gap between the test section and flow housing which results in a higher pressure drop across the bottom nozzle. Similarly, TS83 resulted in a higher pressure drop compared to 2-FG-FPC because a single debris bed was able to form on the lower end fitting. In test 2-FG-FPC, no debris accumulated on the lower end fitting.
- In TS48, which had a higher flow rate compared to TS44, multiple debris beds were formed within the test section. CIB43 which was conducted with similar debris loads also formed multiple debris beds. The overall test section pressure drops measured in TS44 and CIB43 are comparable; however, the pressure drop across the bottom nozzle was higher in TS48 compared to CIB43. This result further demonstrates that the subscale facility tends to capture more debris at the bottom nozzle.
- Subscale test TS55 was also conducted with a high flow rate and formed multiple debris beds, similar to CIB02. In this comparison, the overall pressure drop was higher in CIB02 but again, the bottom nozzle pressure drop was higher in TS55. Similar to the other comparisons made, this trend

indicates that more debris captures on the upstream surface of the bottom nozzle in the subscale testing compared to the WCAP-16793 testing. This can be attributed to the gap between the test section and the flow housing walls in the WCAP-16793 testing. The fact that the overall fuel assembly pressure drop is higher in CIB02 could be attributed to the recirculation of particulates. Since the subscale testing used a once-through debris addition technique, particulates that did not capture in the debris bed on the first pass-through would not have had another chance to be captured in the resulting debris bed and increase the pressure drop. The filter bag data from TS55 indicates a significant quantity of particulate penetration, which indicates that the in-bed particulate load (i.e., the particulate load that captured in the debris bed) is significantly less than the injected particulate load. Using the filter bag data, the in-bed particulate load from this test is estimated to be 206 g/FA (p:f = 3.67). Given the constant recirculation, it is reasonable to assume that more particulate was captured in CIB02 resulting in a higher total fuel assembly pressure drop.

- In TS59, pressure drop measurements made at 18 g/FA were selected to make a comparison to one of the WCAP-16793 low flow rate tests conducted with similar debris loadings. As the comparison indicated, the pressure drops were comparable even though the flow velocity in TS59 was higher, which would indicate that the pressure drop should be higher. Similar to the previous comparison, this discrepancy can be attributed to the capture efficiency of particulates and the fact that the in-bed particulate load is expected to be higher in CIB30.

The subscale head loss program concluded that for a system with the same amount of debris, a single debris bed results in a worse overall pressure drop compared to multiple debris beds. The comparisons provided above support this conclusion. Both test programs have demonstrated that increased particulate load tends to promote fibrous debris penetration thus resulting in the formation of multiple debris beds. In the WCAP-16793 test program, the particulate load is added first. As such, the highest particulate concentrations are present when fibrous debris is added to the test column resulting in a higher propensity to distribute the fiber across multiple elevations. The subscale debris addition in this regard is more conservative because a concurrent fiber and particulate debris addition reduces the particulate concentration during the early stages of the test. This is relevant in the comparison of TS44 and CIB42. Even though TS44 was conducted with a total injected p:f ratio 10 times higher than CIB42, a single debris bed was formed that resulted in a higher overall pressure drop across the test section.

Both test programs indicate that increased flow velocities tend to promote debris penetration and bypass. As such, the flow reduction used by the subscale test program reduces these effects and promotes formation of a debris bed in a single location, which has been shown to lead to the highest head losses due to more compaction of the debris bed. This is relevant in the comparison of TS48 to CIB43. Even though TS48 had a higher flow velocity more debris was able to collect on the bottom nozzle which resulted in a higher head loss. This trend can also be attributed in part to differences in the test section which are discussed next.

The subscale test column, with its test section sealed against the flow housing wall does not allow bypass around the test section capture geometry as it did in the WCAP-16793 test program. This design promotes debris capture on the bottom nozzle, thus creating a more conservative scenario.

Table RAI-6.2-1 Comparison of Subscale Test Results to Full-Area Fuel Assembly Test Results

Subscale Test Facility (WCAP-17788)						Full-Area Test Facility (WCAP-16793)					
Test Series	Fiber Load (g/FA)	Particulate Load (g/FA)	Flow Velocity at Pressure Drop (ft/s)	Max Pressure Drop (psid)		Test No.	Fiber Load (g/FA)	Particulate Load (g/FA)	Flow Velocity (ft/s)	Max Pressure Drop before Chemical Addition (psid)	
				Total Test Section	Bottom Nozzle					Total Fuel Assembly	Bottom Nozzle
44	56	560	0.05	9.1	9.1	CIB42	50	50	0.07	2.66	2.35
48	56	560	0.1	5.9	5.4	CIB43	50	750	0.07	3.78	1.49
55	56	1680	0.17	4.4	3.6	CIB02	53	1361	0.2	6.65	2.54
59[1]	18	216	0.06	0.3	0.3	CIB30	18	270	0.01	0.32	0.32
83	21.5	860	0.02[2]	0.78	0.78	2-FG-FPC	18	810	0.02	0.111	0.002

Notes [1] Conditions taken at point in test when 18 g/FA fiber was injected into the test section.

[2] This flow velocity and the corresponding pressure drop were measured at the end of the test when the main column flow pump was turned-off and the only source of flow through the column was provided by the debris injection pump.

References

RAI-6.2-1 WCAP-16793-NP-A, Revision 2, "Evaluation of Long-Term Cooling Considering Particulate, Fibrous and Chemical Debris in Recirculating Fluid," July 2013.

RAI-6.3

Provide an example of how the total mass of debris captured in the filter bags was determined (ref. Section 3.6). Please describe the relative magnitude associated with the predominant sources of uncertainties. Discuss the significance of the total debris mass measurement uncertainty in terms of the experimental program conclusions. Significant uncertainties would include the potential for lost debris, fluid lost from the bags resulting in loss of dissolved chemicals, and fluid chemical concentrations.

Response

The subscale test loop featured two in-line polypropylene filter bags for the purpose of capturing particulate and fibrous debris. One filter bag and housing was placed downstream of the test column to capture and quantify debris that penetrated the test section capture geometry. A second filter bag and housing was used during the back flushing process after each test to quantify debris that had collected on the test section capture geometry.

Prior to each test, two new filter bags were weighed dry, and the mass of each bag recorded. It should be noted that there was no need to pre-dry the filter bags before use since polypropylene has practically no hygroscopic properties. One filter bag was placed in the downstream housing, while the other bag was placed in the back flush filter housing. After the test was performed, the wet mass of each bag filter, along with any captured debris from the test, was measured and recorded. Prior to removing the filter bags from the housing, compressed air was used to remove any excess liquid from the filters. The downstream and back flush filter bags were then placed in an oven and dried to remove any remaining moisture. The dried filter bags were then weighed and the mass recorded.

The test solution, a boric acid (H_3BO_3) solution buffered with either sodium hydroxide (NaOH), sodium tetraborate (NaTB), or trisodium phosphate (TSP), introduced additional mass to the filter bags in the form of chemical solute. As a result, the approximate mass of chemical solute was calculated and subtracted from the post-test dry filter mass based on the post-test wet filter mass and the known chemical concentrations of the test solution.

To determine the total solute mass captured in the bag filter, the approximate mass of solution retained in the filter was determined by taking the difference between the post-test wet and dry masses. The resultant mass of solution was then used to determine the mass of each chemical constituent by multiplying the evaporated solvent mass by a ratio of the recorded mass of the chemical constituent from the test procedures to the mass of 250 gallons of deionized (DI) water (solvent). The total captured solute mass was calculated as the sum of the chemical constituent masses. Buffering solutions were created in large batches, and the same test solution was often used for multiple tests. The chemical addition records for each batch were used in the determination of the corresponding test solution masses.

With the collected solute mass known, the total mass of particulate and fibrous debris collected by each bag filter was calculated by subtracting the solute mass and the pre-test filter mass from the post-test dry filter mass. The collection error for each test was quantified by comparing the sum of debris collected in the downstream and back flush filters to the total injected debris mass recorded in the test procedure for each test. To check the validity and error associated with this collection methodology, a baseline test was run in which no debris was injected. The resultant error associated with the calculation of the final debris mass

was determined to be 1.91 percent for this baseline test. The measured and calculated values associated with the baseline test are documented in Table RAI-6.3-1 below.

Table RAI-6.3-1 Baseline Test Filter Bag Results

Test	Filter ID	Initial Mass (g)	Wet Mass (g)	Dry Mass (g)	Water Mass (g)	Solute Mass (g)	Collected Debris Mass (g)	Nominal Debris Mass (g)	Injected Debris Mass (g)	% Error
Baseline	1	255.58	598.38	260.33	338.05	5.44	-0.69	0.00	0.00	1.91
	2	259.17	556.01	264.36	291.65	4.69	0.50			

For each test, the collection error was calculated and documented. Generally, the sample collection error was found to be less than 10 percent. The average error was found to be 6.67 percent, while the median error was 4.45 percent, and the mode error was 2.03 percent. A distribution of the calculated test sample errors is provided in Figure RAI-6.3-1. While the majority of tests were found to have an error of less than 10 percent, some tests were found to have errors of greater than 10 percent.

The largest source of uncertainty associated with the bag filters can be attributed to the subtraction of the solute mass and the potential for lost debris. It was noted that during the drying process that solute was beginning to collect on the oven walls which would have reduced the dry weight and thus the estimated quantity of debris. It is also recognized that the solution concentrations prepared would increase during the duration of testing due to evaporation from the supply tank, which would also reduce the estimated quantity of debris collected in the bag filters. Also, early in the test program, debris collection within the debris injection system (DIS) was identified. Corrective actions were taken to eliminate the collection of debris within the DIS and during the final limits testing, very little debris collection was identified in the DIS such that there was a high level of confidence that all the prepared debris was being injected into the test section.

The filter bag debris mass measurement uncertainty did not significantly impact the program conclusions. The most important factor in terms of debris mass was that the prepared debris mass was accurate and that it is all transported to the test section. The debris mass prepared for each test was very accurate and was not influenced by the factors that lead to uncertainty associated with the filter bag masses. For all final limits tests conducted, it was confirmed by inspection after each test that practically all the debris prepared in the high concentration tank (HCT) was transported through the DIS to the test section.

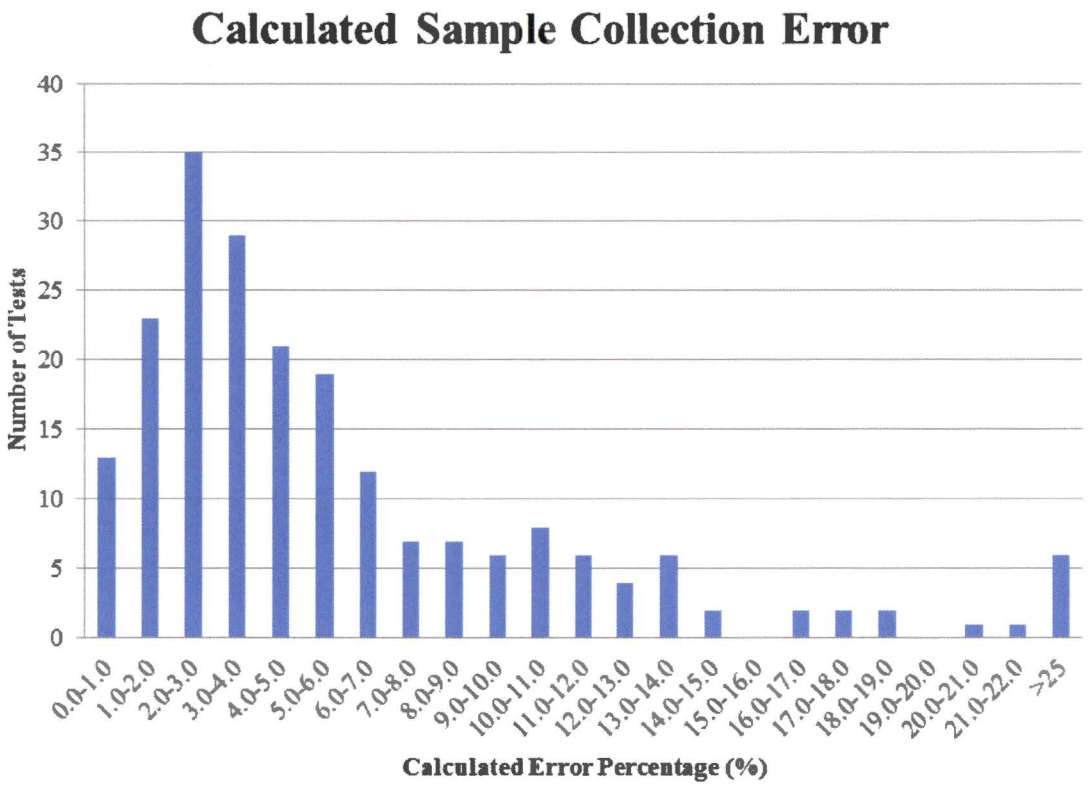

Figure RAI-6.3-1 Calculated Sample Collection Error

RAI-6.4

Table 4-2 shows the test matrix for Alternate Flow Path (AFP) testing.

a. Provide a justification for the fiber amounts used. Describe how this amount of fiber bounds all four plant categories.
b. Section 4 states that the amounts were added on a per fuel assembly basis. Why is the amount of fiber per fuel assembly important to the AFP evaluation?
c. Provide information on how the debris was introduced during the AFP tests. Was it introduced all at once or introduced over time intervals?
d. Two hole sizes were tested over a range of flow conditions. There are AFPs in CE and Westinghouse upflow plants that are smaller diameter and/or flow area than the hole sizes tested. How are the hole dimensions tested representative of the AFP geometries in all four plant categories in Volume 4? Provide the geometries and dimensions of all credited AFPs for each plant category and the associated flow area. Justify that the test geometries provide acceptable bounding results for debris capture at the openings. In the response, consider the effects of velocity through the openings in combination with geometry effects and range of fiber sizes.

Response

a. As stated in WCAP-17788 Volume 6 Section 3.5.5, blockage of the alternate flow paths (AFPs) is not expected to occur given the dimensions of the AFP passages and the flow rate through them. The credited AFP passages have dimensions that are larger than the range of fiber sizes expected to enter the AFPs. The objective of the AFP testing was to demonstrate that flow passages with dimensions larger than the constituent fiber size would not block by showing that there is no mechanism for debris capture that will allow fibrous debris to bridge a dimension that is larger than the range of fiber lengths expected to enter the AFPs. As such, it is not necessary that the total amount of fibrous debris used in the testing bound all four plant categories.

   As illustrated in WCAP-17788 Volume 6 Figure 5-69, debris that approached the test plate far from the open hole tended to accumulate on the underside of the plate, while debris that approached the plate near the hole was swept through the hole leaving a ring around the hole that was free of debris. Had additional fibrous debris continued to be added to the test, the same behavior would continue.

   Although it is not a requirement that the fibrous debris quantities used in the AFP testing bounded all four plant categories, the amount of debris chosen for the AFP testing was selected to be representative of the debris amounts expected to transport through the AFPs credited in the four plant categories.

   The total in-vessel fibrous debris limit defined for the hot leg break scenario, which is the scenario that credits AFPs, is [ ]^{a,c} The Combustion Engineering (CE) System 80 nuclear steam supply system (NSSS) has the most fuel assemblies; 241. The Westinghouse 3-loop NSSS has the least fuel assemblies; 157 (the Westinghouse upper plenum injection NSSS does not credit AFPs). As such, the total in-vessel fibrous debris limit for all plants has a range of [ ]^{a,c} Considering that the initial accumulation of debris is at the core inlet only, it is reasonable to assume that [ ]^{a,c} or approximately [ ]^{a,c} will accumulate at the core inlet prior to activation of the AFP. After activation

of the AFP, debris is split between the core inlet and the AFP and it is reasonable to expect that half the debris entering the reactor vessel, after activation of the AFP, will transport through the AFP.

Based on these reasonable assumptions, the CE System 80 NSSS would be expected to transport approximately; [ ]^{a,c} of fibrous debris through the AFP. Similarly, the Westinghouse 3-loop NSSS would be expected to transport approximately; [ ]^{a,c} of fibrous debris through the AFP. The Westinghouse 4-loop and Babcock and Wilcox (B&W) NSSS designs would be somewhere in between. Considering this to be a reasonable representation of the range of fibrous debris expected to pass through the AFP for all four plant categories, a value of 7500 g was chosen for the AFP testing. This value is justified considering that the value chosen is a reasonable fibrous debris amount that is representative of all plant categories. Further, the AFP testing did not need to bound the maximum amount of fiber that could potentially transport through the AFPs credited for all plant categories, because the debris amounts introduced did not induce any pressure drop in the AFP holes, nor was there any indication of debris accumulation. Significantly more debris could have been tested with the same result.

The amount of fibrous debris used in the subscale AFP testing was determined by scaling the amount of debris transported through the AFPs by the flow area. Review of Table RAI-6.4-2 through Table RAI-6.4-5 indicates that 2100 – 4900 in^2 envelopes the total AFP area for all plant categories. Dividing the limits of this range by the subscale flow area produces a range of scaling ratios of approximately 131 – 307. Dividing the total fibrous debris amount calculated for the AFP testing, 7500 g, results in a scaled total fibrous debris amount for the AFP testing; 7500/131 = 57.3 g to 7500/307 = 24.4 g. As such, the 37.5 g total fibrous debris addition used in the AFP testing is a reasonable value that is representative of the actual fibrous debris amount expected to transport through an AFP. Information regarding the addition of these debris batches is provided in the response to RAI-6.4c.

b. Section 4 states, "Fiber was added in three batches of 12.5 g or three batches of 50 g/FA." There is no importance with regard to the fiber amount added being reported on a per fuel assembly basis. In terms of scaling to fibrous debris amounts transported through the AFP, either the actual debris load added in the subscale facility, three batches of 12.5 g, or the amount reported on a per fuel assembly basis can be used provided the correct flow area is applied (i.e., the subscale flow area or the per fuel assembly flow area). The intent of providing the amount of fiber added on a per fuel assembly basis was to provide a direct comparison of the amount of fiber added in the AFP testing to the amounts of fiber added in core inlet head loss testing, which are generally reported in the topical report on a per fuel assembly basis.

c. Debris was added in three batches as a function of time. Each addition included 12.5 g of fibrous debris and the second addition included 12.5 g of particulate debris. Figure RAI-6.4-1 shows the cumulative debris loads from the two AFP path tests as a function of time. As shown in the figure, each batch of debris was allowed to completely deplete prior to the next addition of debris. Table RAI-6.4-1 provides the times at which the debris additions were made.

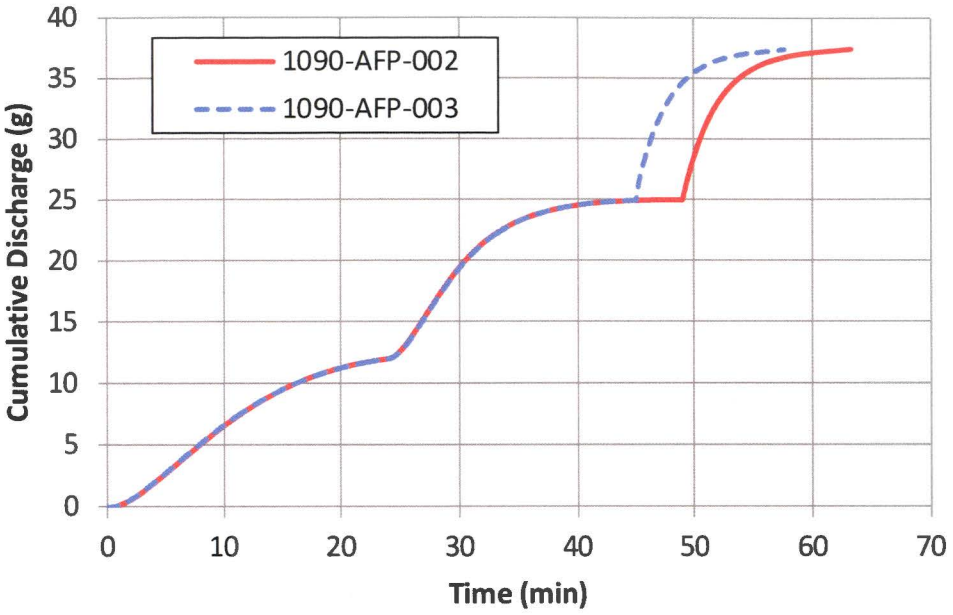

Figure RAI-6.4-1 Cumulative Fiber Discharge used in the Alternate Flow Path Tests

Table RAI-6.4-1 Summary of Debris Addition Times used in the Alternate Flow Path Tests

Action	1090-AFP-T002	1090-AFP-T003
First Debris Addition	start of test	start of test
Second Debris Addition	24 minutes	24 minutes
Third Debris Addition	49 minutes	45 minutes
Test Completed	64 minutes	58 minutes

d. In the subscale AFP testing, a [ ]^{a,c} were tested. The geometries and dimensions of the plant AFP paths vary by vendor and plant design. Table RAI-6.4-2 through Table RAI-6.4-5 summarize the AFP geometries for the Westinghouse upflow, Westinghouse downflow, CE, and B&W plant categories, respectively. The tables provide the limiting dimensions and flow areas through the AFPs.

As shown in the Table RAI-6.4-2, the Westinghouse upflow plant category consists of 3- and 4-loop converted and design upflow plants. The design upflow units have baffle bolt cooling holes while the converted upflow units do not. One design upflow unit contains core barrel bolt cooling holes, which are similar to the baffle bolt cooling holes. The other former plate holes are through holes with no obstructions. Also provided in Table RAI-6.4-2 are the minimum hole dimensions through the former plates along with the minimum total area through the formers and the total barrel/baffle flow area. The former plate hole dimensions and calculated flow areas are representative of the upstream and downstream surfaces of the former plates and do not consider obstructions from baffle or core barrel bolts. The smallest hole dimension in Westinghouse 4-loop converted upflow units is [ ]^{a,c} The smallest hole dimension in Westinghouse 4-loop design upflow units is [ ]^{a,c} which does not consider the baffle or core barrel bolts. The smallest hole dimension in Westinghouse 3-loop converted upflow units is [ ]^{a,c} The smallest hole dimension in Westinghouse 3-loop design upflow units is [ ]^{a,c} These dimensions are all considerably larger than the range of fiber lengths expected to enter the AFPs and are bounded by the dimensions of the AFP test geometries. WCAP-17788 Volume 6 Figure 3-32 provides the length distribution of fiber expected to enter the reactor vessel. As shown in the figure, the majority of fiber is less than 1mm, or 0.0394 in., which is an order of magnitude smaller than the former plate holes contained in the Westinghouse upflow plant designs.

Figure RAI-6.4-2 shows the geometry of the baffle bolt, or core barrel bolt, cooling holes contained in the Westinghouse 3-loop design upflow units. The Westinghouse 4-loop design upflow units are similar except that the former plate holes are slightly larger. As shown in the figure, not all holes provide baffle bolt cooling and there are also gaps, chamfers, and stress reliefs that create open flow area through the former. These fractions of open area are considered when determining the total flow area through the former. This flow area is considerable and equates to [ ]^{a,c} equivalent diameter holes.

Also shown in Figure RAI-6.4-2 are the dimensions necessary to calculate the clearances through the baffle bolt cooling holes when the baffle bolt is in place. This clearance is approximately [ ]^{a,c} which is approximately half of the maximum fiber length expected to transport through the AFP and is smaller than the [ ]^{a,c} diameter hole tested in the subscale AFP testing. However, bounding the clearances through these holes is not required as they are not the only passages that exist through the former plates. Further, the reduction in flow area through this clearance produces an increased flow velocity. The AFP testing demonstrated that increased velocity resulted in higher efficiency debris transport through the flow passage. As such, these holes are not expected to block with debris and since they are not the only flow passages through the former plates, it was not necessary to test this hole type in the AFP testing.

Table RAI-6.4-3 summarizes the AFPs in the Westinghouse downflow plant category. The Westinghouse downflow plant category consists of 3- and 4-loop plants. The AFP credited in the

Westinghouse downflow plant category are the upper head spray nozzles (UHSNs) which are characterized by the flow area through the UHSNs. All but two Westinghouse downflow units have smaller flow areas through the UHSNs, which are defined as T-hot plants. The smallest hole size through the T-hot plant design is [ ]^{a,c} The other Westinghouse downflow units have larger flow areas through the UHSNs, which are defined as T-cold plants. The smallest hole size through the T-cold plant design is [ ]^{a,c} These dimensions are all considerably larger than the range of fiber lengths expected to transport through the AFPs and are bounded by the AFP test geometries.

Table RAI-6.4-4 summarizes the AFPs in the CE plant category. The CE plant category is similar to the Westinghouse upflow plant category in that they are considered upflow plants with a channel that runs parallel to the core. This channel is referred to as the reactor vessel shroud and has an inlet below the active core and an outlet above the active core, similar to the barrel/baffle channel in the Westinghouse upflow plant category.

CE plant designs are unique in that the shroud ribs (equivalent to former plates in the Westinghouse designs) do not extend to the core barrel. A gap exists across the entire length of the shroud channel between the shroud ribs and the core barrel. As shown in Table RAI-6.4-4, the smallest shroud gap is [ ]^{a,c} Many of the CE plant designs also contain slots and/or holes in the shroud ribs. These are all through slots/holes with no obstructions. One plant contains a shroud slot that is [ ]^{a,c} However, this unit also has holes in the shroud which are [ ]^{a,c} gap between the shroud ribs and core barrel. As such, it is not required to demonstrate that the [ ]^{a,c} shroud slots will not block with debris since there are other passages through the AFP that are bounded by the tested geometries. Further, the [ ]^{a,c} dimension is considerably larger than the range of fiber lengths expected to pass through the AFP such that they are not expected to block with fiber.

Table RAI-6.4-5 summarizes the geometries through the AFPs for the B&W plant designs. This table also provides the areas through the AFPs. The baffle design for all of the B&W plants is the same.

Flow into the baffle region is through holes on the periphery of the lower grid rib section. [

]^{a,c}

There are 8 former plates in the baffle region. Seven of these plates are identical and have [ ]^{a,c} The total area through these former plates is [ ]^{a,c} The plate at the mid-plane level has [

]^{a,c} This mid-plane former plate also has a [ ]^{a,c} The total area through the mid-plate former plate is [ ]^{a,c}

At the top of the baffle, flow out of this region is through holes on the periphery of the upper grid rib section. There are [ ]^{a,c}

There are also flow paths through the baffle plates into the core that consist of LOCA holes and slots. There are [

]^{a,c}

The minimum dimension through these components is [ ]^{a,c}

As discussed above, there are only two instances in which the credited AFP geometries are not explicitly bounded by the [ ]^{a,c} hole tested in the AFP testing. These two instances are the baffle bolt and core barrel bolt cooling hole clearances contained in Westinghouse design upflow plants and the single CE unit that has [ ]^{a,c} slots in the shroud ribs. It is not necessary to demonstrate through testing that these geometries will not block with debris since these geometries are larger than the range of fiber sizes expected to enter the AFP and because there are other, larger, flow passages contained in these AFPs that are bounded by the subscale AFP testing. Further, smaller holes equate to higher flow velocities through the openings. The subscale testing has shown that increased flow velocity increases the efficiency of fibrous debris entrainment. Since these flow passages are smaller than what was tested, the flow velocity will increase such that the entrainment process is expected to keep these passages free of fibrous debris.

Given the dependence on flow velocity through the AFP, it is important to ensure that the flow rates considered in the AFP testing are representative of those in the prototypic AFPs. For all plant categories, flow through the credited AFPs effectively starts at zero and increases as core inlet resistance increases. The three flow rates tested in the subscale facility were 0.75, 2, and 4 gpm. Below 0.75 gpm, it was difficult to maintain fibrous debris transport through the vertical subscale test column.

Table RAI-6.4-6 provides the Reynolds numbers calculated for the subscale test column and the two hole dimensions used in the AFP testing. The table shows that the subscale column Reynolds number varied between approximately 900 – 4800 which includes the laminar flow regime through the transition to a turbulent flow regime. The Reynolds number for the AFP holes tested was varied approximately 6100 – 98000 which is in the turbulent flow regime.

Table RAI-6.4-6 also provides the Reynolds numbers calculated for the various Westinghouse and B&W AFPs. In the calculation, three flow rates were considered; 25, 75, and 125 gpm. These flow rates were selected because the calculated Reynolds numbers for these flows agree well with the calculated Reynolds numbers used in the subscale AFP testing. The Reynolds number is calculated based on the flow area upstream of the former plate flow holes or the UHSNs and the flow area through the former plate flow holes or UHSNs. As the table shows, the Reynold number upstream from the former plates or UHSNs compares well with the Reynolds numbers calculated for the subscale column. Similarly, the Reynolds number calculated based on the former plate or UHSN flow area compares well with the range of Reynolds numbers calculated for the subscale AFP tests.

This comparison is shown graphically in Figure RAI-6.4-3. The figure plots the plant AFP Reynolds number as a function of the tested AFP Reynolds number. Figure RAI-6.4-4 provides the same comparison zoomed in such that the comparison at lower Reynolds numbers can be seen more clearly. As indicated by the figures, the majority of plant AFP flow conditions are reasonably

represented by the AFP testing. Some of the plant former plate Reynolds numbers calculated at the 25 gpm flow rate are shown to be less than those tested. This is acceptable considering the fact that the plant AFP flow rate will continue to increase as the transient progresses such that the plant AFP Reynolds number will increase to the point that it is represented by the AFP testing.

CE AFPs were not considered in this evaluation since these AFPs include a gap around the shroud ribs and core barrel that is not representative of the holes used in the AFP testing. As this gap is significantly larger than the range of fiber sizes expected to transport through the AFP, it is not necessary to include the Reynolds number comparison since this gap will not block with debris under any flow condition.

Table RAI-6.4-2 Summary of Westinghouse Upflow Barrel/Baffle Alternate Flow Paths

Plants	No. Loops	BB Design / Baffle Bolt Cooling Holes	Smallest Hole Diameter (in)	Former Flow Area (in^2)	BB Flow Area (in^2)
McGuire 1&2	4	Converted Upflow / No			
Watts Bar 1&2, Diablo Canyon 2	4	Converted Upflow / No			
Byron 1&2, Braidwood 1&2, Catawba 1&2, Vogtle 1, Seabrook 1, Millstone 3, Wolf Creek, Callaway, Comanche Peak 1&2	4	Design Upflow / Yes: 109 standard holes, 104 baffle bolt cooling holes per former			
Vogtle 2	4	Design Upflow / Yes: 53 standard holes, 184 baffle and core barrel bolt cooling holes per former			
STP 1&2	4	Design Upflow / Yes: 109 standard holes, 104 baffle bolt cooling holes per former			
Farley 1&2, V. C. Summer, North Anna 1	3	Converted Upflow / No			
Shearon Harris 1, Beaver Valley 2	3	Design Upflow / No, Former 1. Yes, Formers 2-8, 107 standard holes, 120 baffle bolt cooling holes			

a,c

Table RAI-6.4-3 Summary of Westinghouse Downflow Barrel/Baffle Alternate Flow Path

Plants	No. Loops	Upper Head Spray Nozzle Design	Smallest Hole Diameter (in)	UHSN Flow Area (in^2)	Upper Downcomer Flow Area (in^2)
D.C. Cook 1&2, Indian Point 2&3, Diablo Canyon 1, Salem 1&2	4	T-Hot	[			a,c
Sequoyah 1&2	4	T-Cold			
North Anna 2[1], Surry 1&2, H.B. Robinson 2, Turkey Point 3&4	3	T-Hot			]

Note [1] North Anna Unit 2 is now a converted upflow configuration that is equivalent to North Anna Unit 1 in Table RAI-6.4-2.

Table RAI-6.4-4 Summary of Combustion Engineering Shroud Alternate Flow Paths

Plants	Shroud Design	Holes in Lower Core Support Plate	Smallest Hole Diameter (in)	Flow Area (in^2)	Shroud Flow Area (in^2)
Palisades	Upflow	Yes			
Fort Calhoun	Upflow	Yes			
St Lucie 1, Calvert Cliffs, Millstone 2, Waterford 3	Upflow	No			
St Lucie 2	Upflow	No			
ANO 2	Upflow	No			
Palo Verde 1,2&3	Upflow	No			

a,c

Table RAI-6.4-5 Summary of B&W Alternate Flow Paths

Plant	Plant Type	Smallest Hole Diameter (in)	Former Plate Flow Area (in^2)	Baffle Flow Area (in^2)
Oconee 1, 2, 3 TMI-1 ANO-1 DB-1	B&W	[		a.c]

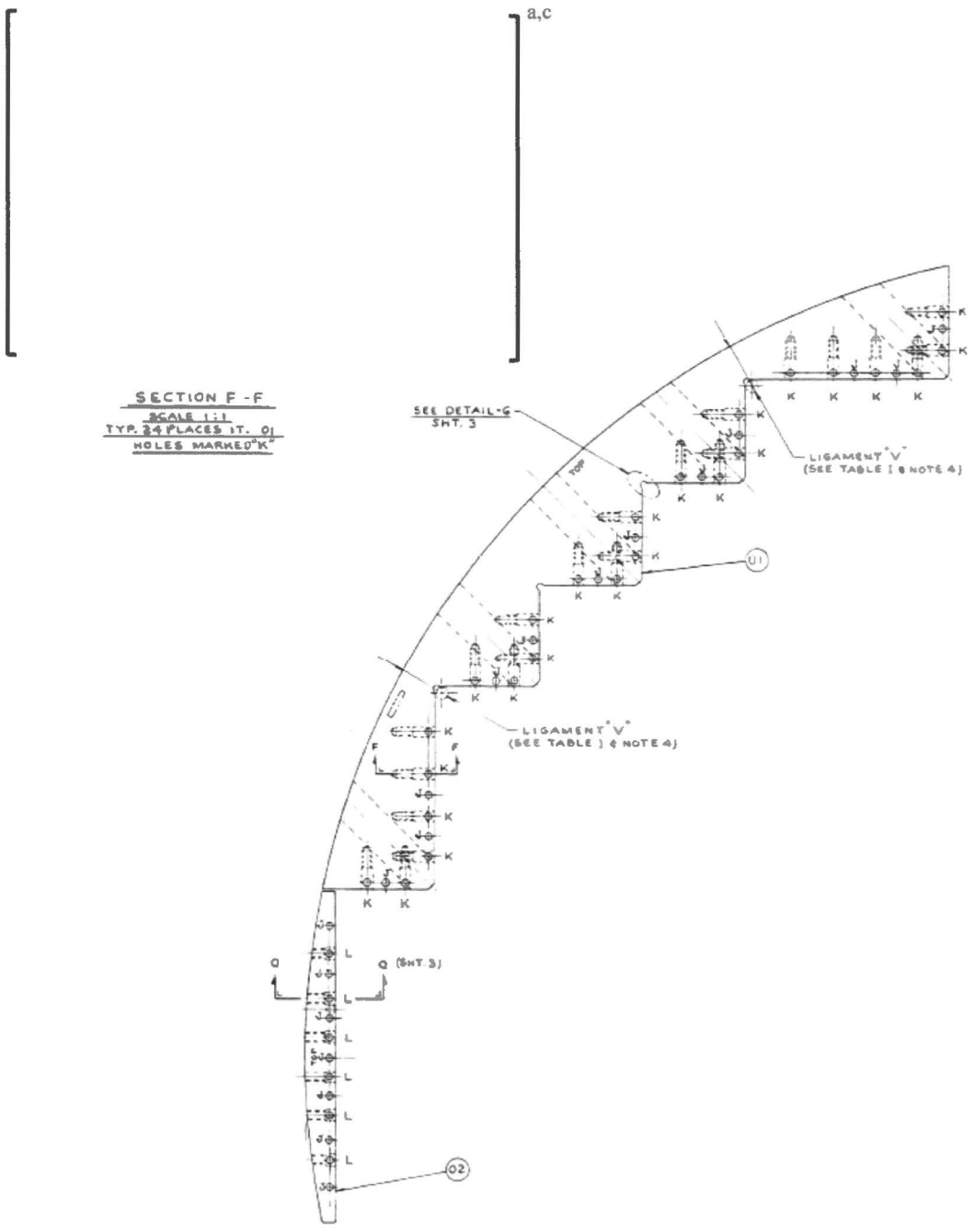

Figure RAI-6.4-2 Typical Westinghouse 3-Loop Design Upflow Former Plate with Baffle Bolt Cooling Holes

Table RAI-6.4-6 Comparison of Reynolds Numbers from Alternate Flow Path Testing to Plant Conditions

Plant Type	Geometry	Flow Rate = 0.75 gpm	Flow Rate = 2 gpm	Flow Rate = 4 gpm
		Re	Re	Re
Subscale Facility	Test Column	904	2410	4821
	[ ]^{a,c} Hole Diameter	18413	49102	98205
	[ ]^{a,c} Hole Diameter	6138	16367	32735
Plant Type	**Geometry**	**Flow Rate = 25 gpm**	**Flow Rate = 75 gpm**	**Flow Rate = 125 gpm**
		Re	**Re**	**Re**
Westinghouse 4-Loop Converted Upflow	BB Channel	1036	2763	4490
	Former Plate	3369 – 5513	8983 – 14700	14598 – 23888
Westinghouse 4-Loop Design Upflow	BB Channel	1037	2766	4495
	Former Plate	3094 – 3442	8250 – 9179	13405 – 14916
Westinghouse 3-Loop Converted Upflow	BB Channel	901	2703	4505
	Former Plate	5407	16221	27034
Westinghouse 3-Loop Design Upflow	BB Channel	1081	2883	4685
	Former Plate	3466	9243	15020
Westinghouse 4-Loop Downflow, T-hot	Upper Downcomer	993	2648	4303
	UHSNs	23445	62519	101593
Westinghouse 4-Loop Downflow, T-cold	Upper Downcomer	993	2648	4303
	UHSNs	5332	14219	23106
Westinghouse 3-Loop Downflow, T-hot	Upper Downcomer	1105	2947	4789
	UHSNs	21506	57351	93195
B&W	BB Channel	877	2631	4384
	Mid-plane Former Plate	1279	3836	6394
	Other Former Plates	2390	7169	11948

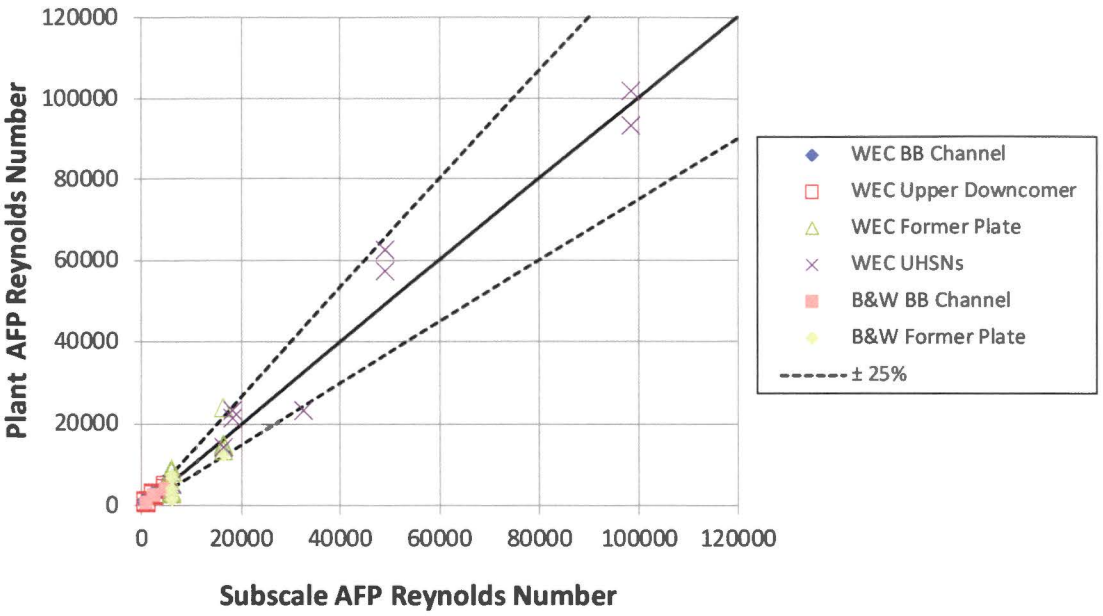

Figure RAI-6.4-3 Alternate Flow Path Reynolds Number Comparison

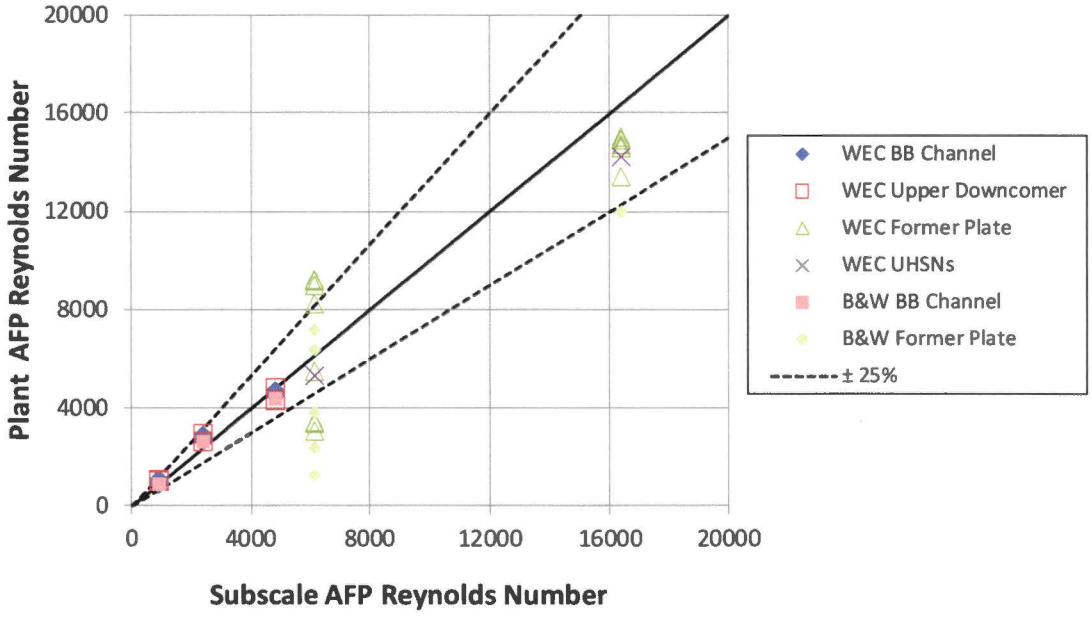

Figure RAI-6.4-4 Alternate Flow Path Reynolds Number Comparison (Zoomed-in)

RAI-6.5

Figure 3-35 shows two of the dP sensors sensing lines across the bottom nozzle, p-grid, and a bottom grid. Verify the accuracy of this configuration. Was any dP attributed to build up at the bottom "bottom grid?"

Response

The test configuration for Tests T152 through T178 is correct as shown in Figure 3-35. The DP1L and DP1H pressure instrumentation spanned the bottom nozzle, P-grid, and bottom grid. Based on visual inspection of the bottom grid during testing, debris collection on the bottom grid was not observed. Therefore, no portion of the recorded pressure drop results was attributed to debris collection on the bottom grid. This trend is consistent with the WCAP-16793-NP-A, Revision 2 (Reference RAI-6.5-1) test program which also did not observe significant debris capture on the first grid above the P-grid.

References

RAI-6.5-1 WCAP-16793-NP-A, Revision 2, "Evaluation of Long-Term Cooling Considering Particulate, Fibrous and Chemical Debris in Recirculating Fluid," July 2013.

RAI-6.6

Some of the plots of head loss vs. time indicate that head loss is increasing at the termination of the test. Discuss whether the tests were allowed to run until a stable head loss was achieved. If not, how was it determined that adequate data had been collected to ensure valid results were obtained for the overall evaluation?

Response

The subscale test procedure defines two criteria for test termination: (1) the test time is greater than or equal to 75 minutes and (2) the pressure drop trend is flat or almost flat. The first termination criterion is based on the debris delivery profiles described in WCAP-17788, Volume 6, Section 3.2.3. Based on these calculations, more than 99.9 percent of the total debris source has been injected prior to 75 minutes. Since all of the debris has been injected, additional significant head loss increase is not expected.

The second termination criterion, as written in the procedures, is to determine if the pressure drop trend was "flat" by looking at the rate of pressure drop increase over the last two minutes of the test. If the rate of change over the two minute interval was less than 0.05 psid per minute then the pressure drop trace was determined to be flat (i.e., the pressure drop was stable) and the test was terminated. For example, Figure RAI-6.6-1 shows the pressure drop results from Test T176 over the last two minutes of the test. The end points of the red line correspond to the data points used to determine the pressure drop rate of increase. At 73 minutes the pressure drop is approximately 15.56 psid, and at 75 minutes the pressure drop is approximately 15.61 psid. Therefore, the rate of pressure drop increase is 0.025 psid per minute over the last two minutes of the test.

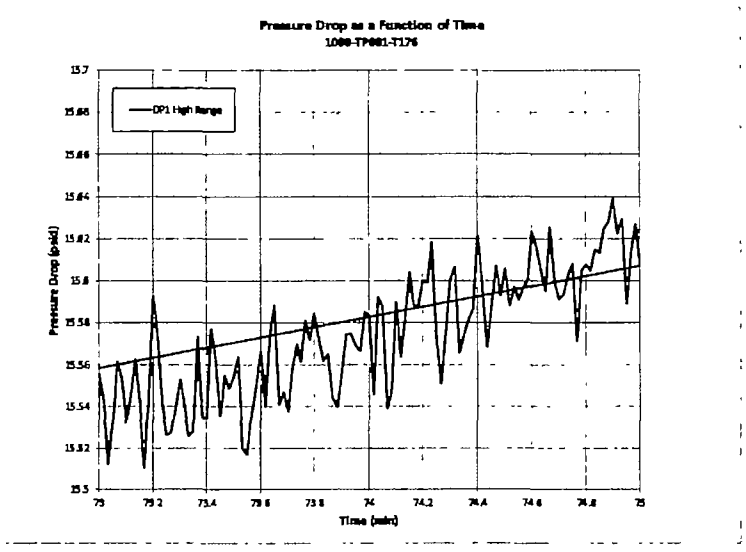

Figure RAI-6.6-1 Pressure Drop Data from the Last Two Minutes of Test T176

RAI-6.7

Define the term "estimated component of total capture due to fiber" in Figures 5-31 and 5-35.

Response

The term "estimated component of total capture due to fiber" used in WCAP-17788, Volume 6, Figures 5-31 and 5-35 represents the anticipated capture efficiency level attributed to the creation of the fiber bed assuming that no particulate debris is captured and assuming a fibrous debris penetration between [ ]^{a,c} independent of p:f ratio. The fibrous debris penetration values were assumed based on the fibrous debris quantity collected during fiber only tests. The estimated component of total capture due to fiber, E, is shown in the form of an equation below:

$$E = \frac{(M_f - M_{fp})}{(M_f + M_p)} \times 100,$$

where,

E = Estimated component of total capture due to fiber (percent),
M_f = Fiber mass (g),
M_{fp} = Assumed mass of fibrous debris penetration (between [ ]^{a,c} (g),
M_p = Particulate mass (g).

A curve is provided for the estimated component of total capture due to fiber at both the [ ]^{a,c} bound of the assumed fibrous debris penetration.

WCAP-17788, Volume 6, Section 5.2.8 will be revised as identified below:

The increase in pressure drop as a function of p:f ratio for the 10 µm particulate shown in Figure 5-30 is marginal considering the large range of p:f ratios examined. This can be explained by evaluating the capture efficiency results shown in Figure 5-31 and Figure 5-32. Figure 5-31 shows the total capture efficiency based directly on the post-test bag filter weights for a range of p:f ratios. The total capture efficiency accounts for both fibrous and particulate debris penetration. Figure 5-31 shows a capture efficiency ranging from [ ]^{a,c} *which corresponds to a fiber only condition. This represents a range of* [ ]^{a,c} *grams of fibrous debris penetration. Assuming the fibrous debris penetration mass is independent of the particle loading, the results at a 0:1 p:f ratio can be extended to estimate the component of the total capture efficiency that is attributable to fiber penetration. This estimate is provided in Figure 5-31 and Figure 5-35 for fibrous debris penetration values of* [ ]^{a,c} *grams and is referred to as the estimated component of total capture due to fiber. The difference between the total capture efficiency, which is taken directly from the filter bag measurements, and the estimated component of total capture due to fiber represents the estimated particle capture efficiency. The estimated particle capture efficiency is shown in Figure 5-32. Figure 5-32 shows that* [

]^{a,c}

RAI-6.8

Figure 5-39 shows that at a particulate-to-fiber (p/f) ratio of 30:1, the grid has a much higher head loss than the prototypical inlet geometry. At a p/f of 10:1, the bottom nozzle produced limiting head loss. At a p/f of 50:1, both the grid and bottom nozzle had about the same head loss. Justify that the conclusion in Section 5.3.1.1, that the core entrance geometry showed a more significant pressure drop than the single grid geometry. Could the grid result in limiting headloss for some conditions as appears to be the case illustrated in Figure 5-39?

Response

Testing showed that a single grid could result in higher or equivalent head loss. However, a single grid is not prototypic of an in-plant scenario as there is always a core inlet geometry (bottom nozzle) upstream from the grid which will act to either limit the amount of debris which can reach the grid or disrupt the flow of debris to the grid, hindering the formation of a uniform debris bed on the grid.

The test results with Westinghouse core inlet geometries presented in WCAP-17788, Volume 6, Section 5.3.1.2.2 showed that the collection of fiber on the bottom nozzle resulted in minimum debris penetration and capture on the downstream grid(s). For the "Final-Low" experiments presented in this section, no appreciable pressure drop was measured across the downstream grid for any of the test series results (Test Series 58, 61, 57, 56, 51, and 52). The "Final-Mid" and "Final-High" experiment results presented in Section 5.3.1.2.2 did result in some debris penetration and bed formation on the downstream grid; however, as shown in Figures 5-45 and 5-46, the pressure drops measured across the downstream grid for these test series (Test Series 47, 48, 49, 53, 54, and 55) were significantly lower than those measured across the inlet geometry (bottom nozzle). As such, for the range of tested flow conditions, a uniform fiber bed capable of acting as an efficient particulate filter was not able to form on the downstream grid, and the debris collection, which created the high head loss seen in the high p:f ratio single-grid tests, was not possible. This illustrates the importance of the bottom nozzle in dictating the formation of the fiber bed.

For the AREVA core inlet geometry test results presented in WCAP-17788, Volume 6, Section 5.3.2, while more appreciable pressure drops were measured across the downstream grid in the "Final-Mid" and "Final-High" flow profile tests shown in WCAP-17788, Volume 6, Figures 5-56 and 5-57, respectively, these pressure drops were significantly lower than those measured during the "Final-Low" experiments which featured stable debris bed formation. As discussed in WCAP-17788, Volume 6, Section 5.3.2, the pressure drop measured at the downstream grid location for the "Final-Low" tests was insignificant. Therefore, these test results support the conclusion that debris bed formation on the core inlet geometry at the "Final-Low" flow condition is limiting with respect to pressure drop.

WCAP-17788, Volume 6, Section 5.3.1.2.2 will be revised as identified below:

Figure 5-43 and Figure 5-44 show results of the p:f ratio study performed following the "Final-Low" flow profile provided in Section 3.3. Error bars are shown only for the Test Series 51, 56 and 57 results since repeats were not performed as part of the other test series. The results show [

]^{a,c}

Results following the "Final-Mid" and "Final-High" flow profiles are shown in Figure 5-45 and Figure 5-46. [

]^{a,c}

RAI-6.9

In Figures 5-47 and 5-51, it appears that lower fiber loads result in higher head losses when p/f ratios and other test parameters are maintained constant. The results are discussed on pages 5-35 and 5-39. The conclusion is that there may have been experimental bias that caused this result (Debris Injection System (DIS) tank mixing/particulate settling), but the theory could not be confirmed. The trend of increasing head loss at lower fiber loads appears to be consistent across several tests. If the potential causes were as discussed, would the results have been more random? Explain how the stronger bias with increasing p/f ratio explains the particulate settling theory. Explain how lower fiber loads can result in higher head losses.

Response

As described in WCAP-17788, Volume 6, Section 5.1.2, after changing to DIS Configuration 2, it was necessary to implement a high concentration tank (HCT) drain-down procedure as described in WCAP-17788, Volume 6, Section 3.2.3. The initial design of the DIS was aimed at maintaining ideal mixing in the HCT and LCT. However, with reduced level, the ideal ratio of liquid level to tank diameter was not maintained. Near the end of some experiments, particle settling was observed in the outer region of the HCT bottom. To avoid incomplete transport of particulate debris, a procedure was implemented to pulse the mixer near the end of the experiments to re-entrain the settled particles into the mixed suspension. This slightly skewed the delivery rate of particulate, resulting in some experimental bias.

As shown in WCAP-17788, Volume 6, Figure 5-1, the HCT tank is drained from approximately 18 in. to 6 in. during the first 18 minutes of each experiment that was completed with DIS Configuration 2. During this drain-down period, the ideal ratio of liquid level to tank diameter was not maintained. As such, it is expected that some particulate settling occurred during the first 18 minutes of each test. Once the HCT tank reached the 6 in. level, the mixer was pulsed in approximately 2 minute intervals to maintain the particulate in suspension. During the 18 minute drain-down period it can be expected that the larger particulates tended to settle more readily than the smaller ones. Based on this theory, the particulate size distribution injected at the beginning of each experiment would have been biased toward smaller size particles and the size distribution injected at the end of the test would have been biased toward larger size particles.

The subscale head loss program has demonstrated that larger particulates will be captured in a fibrous debris bed at a higher efficiency and that higher in-bed particulate loads result in higher head losses. Considering the theory described above regarding the bias in particulate size distribution, it can be expected that the rate of pressure drop increase during the drain-down period would be slower compared to the time period after the drain-down because less particulates would be captured in the debris bed during the drain-down period.

However, particulate capture is a complex process and depends on other factors besides particulate size. Another main contributor to particulate capture is the debris bed morphology. As more fibrous debris is injected into the subscale test section, the debris bed increases in thickness, and the particulate capture efficiency improves significantly. Eventually, the debris bed will become thick enough that all particulates will be captured in the debris bed regardless of size. Also related to the debris bed

morphology, as particulates are captured within the debris bed, the pore sizes of the debris bed decrease, and thus, the debris bed will capture particulates, especially smaller size particulates, more efficiently.

Considering the above discussion, a complete understanding of the trends observed in WCAP-17788, Volume 6, Figures 5-47 and 5-51 is not possible given the limited set of experimental data. However, an understanding of the physical processes occurring during the experiments can be used to explain that any experimental bias associated with DIS tank mixing and particulate settling will be more systematic than random. Further, experiments conducted with lower fibrous debris loads would be expected to experience a stronger bias due to the particulate setting theory.

WCAP-17788, Volume 6, Figure 5-47 presents head loss results from Test Series 59, 57, and 60, all conducted with a 12:1 p:f ratio and fibrous debris loads of 8 g, 12.5 g, and 15 g, respectively. Assuming that the HCT drain-down procedure has minimal impact on the fibrous debris injection rate, WCAP-17788, Volume 6, Figure 3-7 can be used to determine the injected fiber quantity at the time the HCT drain-down period ends (18 minutes). Based on WCAP-17788, Volume 6, Figure 3-7, at 18 minutes, Test Series 59 has injected 4.8 g fiber, Test Series 57 has injected 7.5 g of fiber, and Test Series 60 has injected 9 g of fiber. As described previously, debris beds with a higher fibrous debris loading will capture particulate more effectively. Since Test Series 60 has the highest fibrous debris load at the time the HCT has finished draining, this test will have the highest particulate capture efficiency. As such, any experimental bias related to the settling of larger particulates in the HCT will be minimized. Conversely, Test Series 59 has only injected 4.8 g of fiber at the time the HCT finishes draining; thus, it will have the lowest particulate capture efficiency and the head loss will be impacted the most by the delayed arrival of larger particulates.

The same behavior can be seen in WCAP-17788, Volume 6, Figure 5-51, which presents head loss results from Test Series 83, 76, and 72, all conducted with a 40:1 p:f ratio and fibrous debris loads of 5 g, 9 g, and 12.5 g, respectively. Based on WCAP-17788, Volume 6, Figure 3-7, at 18 minutes, Test Series 83 injected 3 g of fiber, Test Series 76 injected 5.4 g of fiber, and Test Series 72 injected 7.5 g of fiber. The pressure drop transient for Test Series 72 shows that the rate of pressure drop increase had increased sharply before 7.5 g of fiber had been injected; therefore, any delayed injection of larger particulates would have a minimal effect of the head loss. Conversely, the pressure drop from Test Series 83 does not begin to increase until after 3 g of fiber had been injected.

Although the above discussion does not confirm the particulate settling theory with absolute certainty, it does explain why any bias due to particulate settling in the HCT during the drain-down procedure would be expected to be more systematic as opposed to random. It also suggests that a stronger bias would occur during tests conducted with smaller fibrous debris loads and provides an explanation as to why tests conducted with lower debris loads can result in higher head losses.

RAI-6.10

Provide the basis for the assumption that sensitivities conducted with the single grid geometry are valid for the core inlet geometry cases. For example, in the parametric study of head loss vs. fiber mass, it was not apparent from the test results that the single grid tests reflected a similar response when compared to the tests with the core inlet geometry. Some of the conclusions from the single grid sensitivities were not confirmed in tests with core inlet geometries.

Response

The single grid sensitivity tests were intended to identify important parameters; the specific parameters investigated were the DIS configuration, debris concentration, total injected fiber mass, coolant chemistry, grid flow area, particulate size, flow rate, and p:f ratio. The intent of these parametric studies was to investigate and identify which variables were important to pressure drop generation and which were negligible using consistent grid geometry. Those variables that were identified as being important to the generation of a pressure drop were considered in the final geometry testing featuring multiple core inlet geometries and multiple grid designs. To support this approach, the assumption was made that the basic relationships observed during the single grid sensitivities remain applicable for test configurations with core inlet geometries.

The single grid tests provided a common basis for which to test different variables using the same capture geometry and to observe the effects of each variable on pressure drop. The single grid geometry has been shown to promote bed formation more readily than the more complex core inlet geometries, and therefore, allowed for more consistent fiber bed formation. This was important because, while the parametric studies were performed using a single grid, the primary focus was to observe the relationship of each variable with respect to a consistent fiber bed and its formation. Because the relationships observed during the parametric study are primarily attributed to the fiber bed itself and what promotes its formation, not the capture geometry, then these relative relationships hold true with a fiber bed formed on a core inlet geometry as well as a single grid. Therefore, it was determined that additional confirmation of the single grid sensitivity test results, with each core inlet geometry, was not required. Further, the only single grid sensitivities not explicitly confirmed in the core inlet geometry tests were coolant chemistry (pH and buffer type) and particulate size.

The single grid results concluded that coolant chemistry has only a secondary effect with regard to debris bed formation and head loss. There are two factors that coolant chemistry can have on debris bed formation and head loss: (1) the coolant chemistry can impact particulate capture and retention mechanisms as described in WCAP-17788, Volume 6, Section 2.2.4, and (2) the coolant chemistry physical properties can directly influence the pressure drop (see WCAP-17788, Volume 6, Equation 2-5). In the case of fluid properties, the differences in viscosity and density between the solutions tested in the subscale program indicate that this is a minimal effect. In the case of capture and retention mechanisms, water chemistry is only important when particulates are much smaller than those considered in the subscale testing. The results of the single grid coolant chemistry parametric study confirmed that coolant chemistry had little to no effect on the formation of debris beds and the resulting head loss over the range of conditions investigated. As such, there was no need to confirm this result using a core inlet geometry.

With regard to particulate size, the single grid sensitivities concluded that particulate size can have an important effect on head loss since larger particulates will capture in a fibrous debris bed with a higher efficiency. This same behavior would occur regardless of the capture geometry used to form the debris bed.

The example provided, comparing the parametric study of head loss vs. fiber mass using the single grid to those performed using the core inlet geometry, is discussed in detail in the response to RAI-6.9. The response to RAI-6.9 addresses sources of bias in the test results with the core inlet geometry which skew the results away from those shown in the parametric study. This is because the head loss vs. fiber load study performed with the single grid results used DIS Configuration 1 which maintained a constant level in the HCT tank such that ideal mixing was maintained and particulate settling was minimized. Further, the single grid study used a single 10 micron particulate size. The smaller particulate size would have been less likely to settle in the HCT tank. If particulate settling did occur, the experimental bias would have been less significant since the particulates had a uniform size distribution.

RAI-6.11

Table 3-6 provides a dimension of the tested bottom nozzle with a gap. The open flow area ratio is larger than the open flow area ratio of the Robust Fuel Assembly (RFA) Bottom Nozzle as reported in Table 3-5. How is this potential non-conservatism accounted for in the test results?

Response

The tested bottom nozzle with a gap was used to investigate the gap geometry effect on head loss. [

]^{a,c} This behavior supports the conclusion made in RAI-6.2 that the gap between the test section of the flow housing wall present in the WCAP-16793-NP-A, Revision 2 test program may have [ ]^{a,c}

Results from this testing were also compared to single grid results. Comparing the bottom nozzle with a gap to the single-grid test results showed [

]^{a,c}

Given this observation, a second bottom nozzle geometry representing a central region (no gap) was designed and used for the final limits testing. The open flow area ratio for the design without a gap is provided in WCAP-17788, Volume 6, Table 3-7. As shown in the table, the open flow area ratio of this design is less than the open flow area ratio of the RFA bottom nozzle reported in WCAP-17788, Volume 6, Table 3-5. As such, this potential non-conservatism is not a concern in the final limit test results that are used to determine the limiting core inlet resistance.

RAI-6.12

For the AFP tests, results show that pressure drop across the plate increases as flow rate increases. As shown in Figure 5-71, the data from test 1090-AFP-T002 compares with high accuracy to the relationship in Equation 5-1. On the other hand, the data from test 1090-AFP-T003 (Figure 5-73) do not fit the relationship well. How was the relationship in Equation 5-1 determined to be applicable to the test conditions?

Response

The PWROG disagrees with the statement that the data from Test 1090-AFP-T003 does not fit the WCAP-17788, Volume 6, Equation 5-1 relationship well. The data from Test 1090-AFP-T003 (WCAP-17788, Volume 6, Figure 5-73) compares with the relationship in WCAP-17788, Volume 6, Equation 5-1 with the same order of accuracy as the data from Test 1090-AFP-T002 (WCAP-17788, Volume 6, Figure 5-71). In fact, two of the three data points from Test 1090-AFP-T003 are in better agreement with WCAP-17788, Volume 6, Equation 5-1 compared to the Test 1090-AFP-T002 data. Table RAI-6.12-1 shows the measured pressure drop, the predicted pressure drop using WCAP-17788, Volume 6, Equation 5-1, and the absolute difference. As shown in the table, the prediction of the Test 1090-AFP-T003 data using WCAP-17788, Volume 6, Equation 5-1 is reasonable. WCAP-17788, Volume 6, Figures 5-71 and 5-73 present the comparison in terms of relative difference and since the pressure drop scale on WCAP-17788, Volume 6, Figure 5-73 is two orders of magnitude smaller compared to WCAP-17788, Volume 6, Figure 5-71, the comparison (in terms of relative difference) "appears" worse.

Instrument accuracy of the pressure transducers used to collect the AFP pressure drop data are shown in WCAP-17788, Volume 6, Table 3-12. 1090-AFP-T002 pressure drop measurements were collected using DP1H, and 1090-AFP-T003 pressure drop measurements were collected using DP1L. As seen in
Table RAI-6.12-1, the differences between the measured and predicted pressure drops are within the accuracy of the instruments used to collect the data.

WCAP-17788, Volume 6, Equation 5-1 is the standard formulation for calculating pressure drop due to minor losses. These losses represent additional energy dissipation in the flow, usually caused by secondary flows like the ones induced by an abrupt area change. Although the minor loss coefficient, K, is constant in WCAP-17788, Volume 6, Equation 5-1, it varies with different flow conditions. Factors affecting the value of K include: the exact geometry of the abrupt area change, the flow Reynolds number, and proximity to other components that influence the flow field. The value of K was chosen to be 1.4, which is typical for flow through an abrupt area change. Given that all the pressure drop predictions fall within the measurement accuracy of the instruments, there is no need to vary K to account for changes in Reynolds number or the specific geometries used in the AFP testing. As such, the WCAP-17788, Volume 6, Equation 5-1 relationship, and more importantly, the minor loss coefficient selected is applicable to the AFP test conditions.

Table RAI-6.12-1 Summary of Pressure Drop Results from the Alternate Flow Path Testing			
Test Number	**Measured dP (psid)**	**Predicted dP (psid)**	**Difference (psid)**
T002	0.220 (±0.1)	0.223	+0.003
T002	1.560 (±0.1)	1.589	+0.029
T002	6.330 (±0.1)	6.357	+0.027
T003	0.0028 (±0.01)	0.0030	+0.0002
T003	0.0210 (±0.01)	0.0200	-0.001
T003	0.0880 (±0.01)	0.0780	-0.010